Technische Universität München

Fakultät für Chemie

Multimodal and Non-Invasive Imaging Techniques for a Multiparametric Characterization of Tumor Biology

Christian Hundshammer

Vollständiger Abdruck der von der Fakultät für Chemie der Technischen Universität München zur Erlangung des akademischen Grades eines

Doktors der Naturwissenschaften (Dr. rer. nat.)

genehmigten Dissertation.

Vorsitzender:		Prof. Dr. Bernd Reif
Prüfer:	1.	Prof. Dr. Steffen J. Glaser
	2.	Prof. Dr. Axel Haase

Die Dissertation wurde am 20.11.2018 bei der Technischen Universität München eingereicht und durch die Fakultät für Chemie am 14.02.2019 angenommen.

Meinen Eltern

I. Abstract

The globalized world is threatened by the growing number of non-communicable diseases such as cancer. Besides the imperative to reduce the exposure to cancer risk factors, a primary goal of cancer prevention is an early diagnosis and a patient-specific characterization of the malignant state. Ideally, this allows for a tailored treatment planning and an effective follow-up, which are basic concepts of today's precision medicine.

Non-invasive imaging techniques such as computed tomography (CT), positron emission tomography (PET), single photon emission tomography (SPECT) and magnetic resonance (MR) imaging have been developed at the end of the 20th century and have become sophisticated machines that deliver qualitative and quantitative information about diseases. Hybrid imaging techniques combine two or more of these methods and yield a new imaging modality that generates complementary information and has multiple synergistic advantages.

PET/MR is one of the most advanced hybrid techniques on the market. It combines the possibilities to acquire metabolic images with high specificity and sensitivity in the anatomic context with high resolution and excellent soft-tissue contrast. In addition, cutting edge MR technologies such as diffusion-weighted imaging (DWI) and magnetic resonance spectroscopic imaging (MRSI) of hyperpolarized (HP) probes respectively enable the quantification of tumor cellularity and metabolic processes in real-time and without further exposure to ionizing radiation.

The Warburg effect is one of the main hallmarks of tumors. It describes the observation that tumors consume high levels of glucose and process it by aerobic glycolysis rather than oxidative phosphorylation even under normoxic conditions. As consequence of the Warburg effect, tumors produce an excess of lactate in their cytosol, which is co-exported with protons and which finally leads to an acidification of the extracellular space.

This work is structured as follows presenting multimodal and non-invasive imaging techniques like hyperpolarized MRSI and PET/MR to characterize the Warburg effect in greater depth:

- The first study quantitatively analyzes the correlation of the augmented glucose uptake and the glucose reduction via pyruvate to lactate in a pre-clinical breast cancer model in rats. Measurements were conducted on a state-of-the-art clinical PET/MR, which allows the simultaneous imaging of metabolic data with ^{18}F-fluordesoxyglucose (FDG)-PET and HP ^{13}C-pyruvate MRSI while providing anatomic details. Furthermore, diffusion-weighted imaging was used to quantify the effect of variable tumor cellularity on the quantification of image-derived metabolic data.

- Acidification of the extracellular space can be quantified non-invasively by MRSI using hyperpolarized pH sensor molecules, which is summarized in a review of the contemporary literature. The work reveals that hyperpolarized ^{13}C-labelled zymonic acid is the only chemical shift based pH sensor that has been applied *in vivo* so far.

- A further part of this work demonstrates that the hyperpolarized signal lifetime of zymonic acid can be prolonged by deuterium enrichment of the stably attached protons. This enables sensitivity-enhanced pH imaging with temporal resolution *in vitro* and *in vivo*.

- Finally, natural amino acids and their derivatives are analyzed and systematically characterized as a new class of chemical shift based pH sensor molecules. ^{13}C-diaminopropionc acid (DAP) and ^{13}C-serine amide (SA) are non-toxic and exhibit a high pH sensitivity. However, future studies should seek to prolong the hyperpolarized signal lifetime of DAP and SA for instance by deuterium enrichment before they could be used to measure the lactate acidification of tumors.

The methods developed in this thesis are based on cutting edge hybrid imaging technologies that combine PET, MR, hyperpolarized metabolic mapping and hyperpolarized pH *in vivo* imaging to quantify tumor biology in greater depth. In principle, these techniques can be translated to bigger tumor models paving the way for an individual patient care.

II. Kurzzusammenfassung

Die globalisierte Welt wird durch die steigende Zahl nicht-übertragbarer Krankheiten wie Krebs bedroht. Neben der Notwendigkeit die Exposition gegenüber Krebsrisikofaktoren zu minimieren, sind eine frühe Diagnose und eine Patienten-spezifische Charakterisierung des malignen Zustands ein primäres Ziel der Krebsprävention. Im besten Fall führt dies zu einer maßgeschneiderten Therapieplanung und einer effektiven Nachverfolgung des Krankheitsverlaufs, was fundamentale Konzepte der heutigen Präzisionsmedizin darstellt.
Nicht-invasive Bildgebungstechniken wie Computertomographie (CT), Positronen-Emissions Tomographie (PET), Einzelphotonen-Emissionscomputertomographie (SPECT) und Magnetresonanztomographie (MRI) haben sich gegen Ende des 20. Jahrhundert entwickelt und sind heutzutage technisch ausgefeilte Geräte, die qualitative und quantitative Informationen über Krankheiten liefern können. Hybride Bildgebungstechniken kombinieren zwei oder mehrere dieser Methoden, wodurch eine neue Bildgebungsmodalität entsteht, die komplementäre Informationen liefert und eine Vielzahl von synergistischen Vorteilen aufweist.
PET/MR ist eine der fortschrittlichsten Hybridtechniken, die momentan auf dem Markt verfügbar ist. Sie kombiniert die Möglichkeiten, metabolische Bilder mit hoher Spezifität und Sensitivität in einem anatomischen Kontext mit hoher Auflösung und exzellenten Weichteilkontrast zu akquirieren. Zusätzlich ermöglichen innovative MR Technologien wie Diffusions-gewichtete Bildgebung (DWI) und magnetresonanz-spektroskopische Bildgebung (MRSI) hyperpolarisierter (HP) Proben eine Quantifizierung entweder der Tumorzellularität oder metabolischer Prozesse in Echtzeit und ohne weitere Exposition gegenüber ionisierender Strahlung.
Der Warburg Effekt ist eines der wichtigsten metabolischen Kennzeichen von Tumoren. Er beschreibt die Beobachtung, dass Tumore große Mengen Glukose aufnehmen und diese eher durch aerobe Glykolyse als durch oxidative Phosphorylierung prozessieren, selbst wenn ausreichend Sauerstoff zur Verfügung steht. Als Konsequenz des Warburg Effekts produzieren Tumore in ihrem Zytosol einen Überschuss an Laktat, das mit Protonen exportiert wird was letztendlich zu einem Ansäuern des extrazellulären Milieus führt.
Diese Arbeit ist wie folgt aufgebaut und präsentiert multimodale und nicht-invasive Bildgebungstechniken wie hyperpolarisiertes MRSI und PET/MR zur Charakterisierung des Warburg Effekts.

- Die erste Studie analysiert die quantitative Korrelation der erhöhten Glukoseaufnahme und Glukosereduktion via Pyruvat zu Laktat in einem präklinischen Brustkrebsmodell in Ratten. Die Messungen wurden an einem neuartigen klinischen PET/MR Gerät durchgeführt, das eine simultane

Bildgebung metabolischer Daten mit ^{18}F-Fluordesoxyglucose (FDG)-PET und HP ^{13}C-Pyruvat MRSI sowie die Aufnahme anatomischer Details erlaubt. Des Weiteren wurden Diffusions-gewichtete Bilder akquiriert, um den Effekt einer variablen Tumorzellularität auf die Quantifizierung metabolischer Daten zu untersuchen, die aus Bildern generiert wurden.

- Das Ansäuern des extrazellulären Raums kann mit nicht-invasivem MRSI hyperpolarisierter pH Sensormoleküle quantifiziert werden, was in einem Review der aktuellen Literatur zusammengefasst wurde. Diese Arbeit verdeutlicht, dass ^{13}C-markierte Zymonsäure der einzige pH Sensor ist, der auf chemischen Verschiebungsänderungen basiert und bisher *in vivo* verwendet wurde.

- Ein weiterer Teil dieser Arbeit zeigt, dass die Lebenszeit des hyperpolarisierten Signals von Zymonsäure verlängert werden kann, indem man fest eingebaute Protonen mit Deuteronen anreichert. Dies erlaubt eine *in vitro* und *in vivo* pH-Bildgebung mit zeitlicher Auflösung und gesteigerter Sensitivität.

- Schließlich wurden noch Aminosäuren und deren Derivate als neue Klasse von pH-Sensoren basierend auf chemischen Verschiebungsänderungen systematisch analysiert und charakterisiert. ^{13}C-Diaminopropionsäure (DAP) und ^{13}C-Serinamid (SA) sind nicht giftig und besitzen eine hohe pH-Sensitivität. Jedoch sollten zukünftige Studien darauf fokussieren die hyperpolarisierte Signallebenszeit von DAP und SA zum Beispiel durch Deuterierung zu verlängern, bevor diese verwendet werden können um eine Laktatansäuerung von Tumoren zu messen.

Die in dieser Arbeit verwendeten Methoden basieren auf innovativen Technologien, die PET, MR, hyperpolarisierte metabolische und hyperpolarisierte *in vivo* pH Bildgebung miteinander kombinieren, um die Tumorbiologie genauer zu quantifizieren. Im Prinzip können diese Techniken auf größere Tumormodelle übertragen werden, was den Grundstein für eine individuelle Patientenfürsorge legt.

Table of Contents

1. Introduction

1.1 The Global Burden of Non-Communicable Diseases

> "We…the United Nations [(U.N.)]…[a]cknowledge that the global burden and threat of non-communicable diseases constitutes one of the major challenges for development in the twenty-first century which undermines social and economic development throughout the world."[1]
>
> United Nations, September 2011

Chronic or non-communicable diseases (NCD) caused 41 out of 58 million (71%) deaths in 2016 worldwide and mortality rates are projected to increase to 52 million by 2030. Diabetes, cancers, respiratory and cardiovascular diseases were the foremost representatives that were responsible for more than 80% NCD-related deaths.[2] This global epidemic is placing heavy strains on individuals, health care systems and whole nations. Furthermore, NCDs will not only cost millions of lives and cause an "untold suffering". They will prospectively yield a global economic loss of US$ 47 trillion for the time between 2011 and 2030.[3]

In 2011, leading U. N. politicians committed their Governments to fight this "global crisis". Based on the right for everyone to attain "the highest standard of physical…health", they claimed a "primary…responsibility of Governments [to prevent] and control" non-communicable diseases and acknowledged that there was an "urgent need for preventive measures, screening [and] treatment".[1] In 2014, the UN reviewed and reaffirmed key aspects of 2011 to further intensify national and global actions. The most recent "General Assembly Meeting on the Prevention and Control of Non-Communicable Diseases" took place in September 2018, which reveals the worldwide imperative to reduce unnecessary premature deaths.

Primary prevention and control of NCDs includes the identification of their etiology and nation-wide promotion programs to strengthen the awareness of risk factors. This will ideally lead to a global reduction of exposure to tobacco consumption, harmful use of alcohol, pollution, obesity and an increase of physical activity. Secondary prevention involves diagnosis and treatment both at an early stage to halt or slow down disease progression. Screening programs for people at elevated risks are necessary and require modern techniques that allow an accurate diagnosis at affordable prices and ready availability. With regards to treatment, modern science is aiming to address (epi)-genetic, molecular and cellular parameters on a quantitative base. This is already triggering the development of efficient treatment strategies that are tailored to individual phenotypes. Thus, patient-specific treatment is already a central goal of

today´s precision medicine and is going to be an integral part of tomorrow´s health care systems.[4]

1.2 Epidemiology and Etiology of Cancer

Cancers are responsible for nearly one in six deaths globally and the second most common NCD besides cardiovascular diseases. When taken as single entity, cancer mortality outranks other non-communicable diseases such as ischemic heart disease and stroke, which respectively caused 7.0 and 6.3 million deaths in 2011. More than 14 million new cancer cases were diagnosed in 2012, while lung and prostate cancers had the highest incidence rates among men (34.2 and 31.1 per 100,000, respectively). Among women, breast cancer had by far the highest incidence rate followed by colorectal cancer (43.3 and 14.3 per 100,000, respectively).[5] However, world-wide cancer incidents vary with the degree of development expressed by the human development index (HDI), which is a measure of life expectancy, access to education and wealth. In developed countries, lung and stomach cancers as well as “cancers of affluence” like breast, prostate and colorectal cancers are most prevalent with highest mortality rates (**Figure 1.1A-B**). In contrast, the “top five” cancers in rather poor and developing countries are lung, breast, liver, stomach and colorectal cancers (**Figure 1.1C-D**) and more than one fourth of them is related to infections. Furthermore, more than 60% of all cancers occur in less developed countries of the African, Asian, Central and South American continent and these regions account for more than 70% of the global cancer-related deaths.[5]

Within the next two decades, the global burden of cancer will rise drastically (by more than 40%) as incidences positively correlate with population growth and progressive senescence. In addition, developing countries tend to adapt lifestyle risk factors of industrialized nations with flourishing wealth. The most critical risk factor for at least fourteen different types of cancer is first- and second-hand tobacco consumption, e.g active and passive intake of tobacco products that contain several thousands of carcinogenic and mutagenic substances. Routine alcohol consumption and the harmful use of alcohol is a socially tolerated habit of higher developed countries. It mainly accounts for cancers of organs that are in direct contact to harmful components of alcoholic beverages like ethanol and its metabolite acetaldehyde. Interestingly, several meta-studies have shown a positive dose-response correlation of alcohol intake and incidences of prostate and breast cancers that are highly prevalent in developed countries (e.g. Europe).[5]

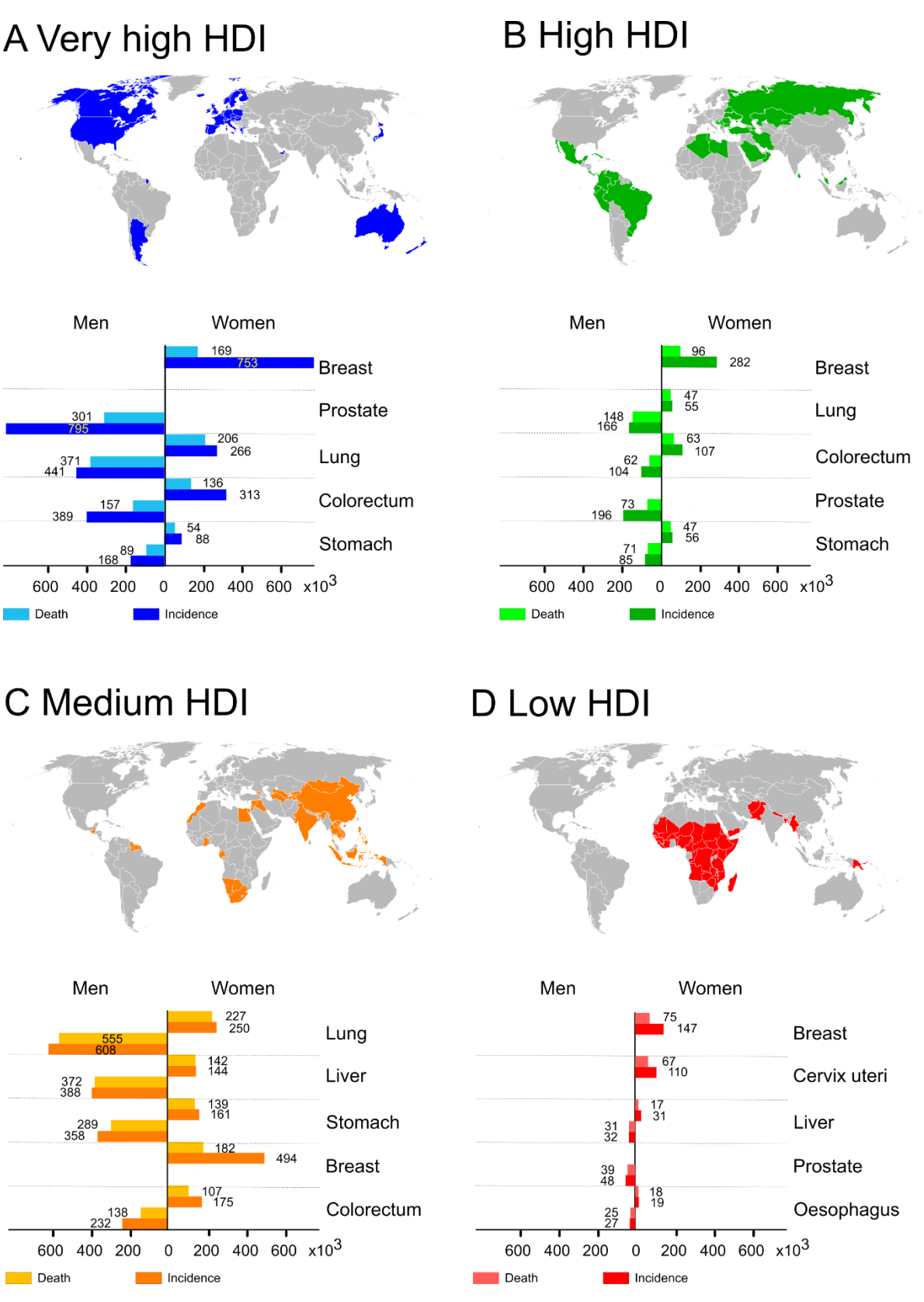

Figure 1.1. Cancer incidence and mortality in 2012 for different human development indices (HDIs). (A) Very high HDI countries are depicted in blue in the map of the world. Cancer incidence and mortality rates of the "top-five" cancers are given in the bar plot below for men and women. **(B)**, **(C)** and **(D)** are respective world maps and bar plots for high, medium or low HDI, respectively depicted in green,

orange and red. The figure was created according to reference [5]. (Copyright information: The world maps are license free as part of the public domain).

Clearly, an unhealthy diet, obesity and lack of physical activity are imminent problems for a majority of the world population that are not only causing NCDs like diabetes, but are also related to several types of cancers. Important risk factors of women are the usage of specific oral contraceptives and reproductive factors that might change with affluence such as nulliparity, pregnancy at late age (> 30) or a short period of lactation. Finally and for the sake of comprehensiveness, environmental pollution (air, soil, water), radiation (UV, X-ray), occupational exposure to carcinogens (e.g.: asbestos) and some pharmaceutical drugs should be mentioned as further cancer etiologies that affect both, developing and developed countries.[5]

1.3 Invasive and Non-Invasive Technologies for Secondary Cancer Prevention

Secondary cancer prevention involves an early detection of lesions, a patient-specific phenotyping and an individualized and targeted therapy.
Evidence based diagnosis and characterization of tumor-specific markers are steadily evolving and allow for the qualitative and quantitative assessment of tumor biology. Some cancers are already encoded in the DNA of individuals or might arise from epigenetic heredity or epigenetic changes. For such lesions, high throughput-genome sequencing is a useful diagnostic tool to detect genetic pre-dispositions.
Classical biopsy is an invasive, but reliable method to sample tissues for characterization not only by histology. At the expression level, tumor parameters can be quantified with techniques like immunohistochemistry, flow cytometry, enzyme linked immunosorbent assays, enzyme activity assays or mass spectrometry. Beyond, easily accessible body fluids like blood and urine often contain quantifiable tumor markers. A prominent example is the prostate-specific antigen (PSA) that can be elevated in prostate cancer patients. In addition, liquid biopsy is a relatively young approach to sample, amplify and identify tumor RNA and DNA that circulate in the blood of cancer patients.
In contrast to these (minimal-)invasive strategies, imaging modalities are rather non-invasive.
Ultrasound, computed tomography (CT), single photon emission computed tomography (SPECT), positron emission tomography (PET) and magnetic resonance imaging (MRI) have been developed throughout the 20th century and have become sophisticated machines that nowadays are routinely used for diagnosis, biopsy guidance, staging, treatment planning and follow-up of cancers.[6-9] However, each

individual modality has its pros and cons with regards to sensitivity, specificity, throughput, cost and patient safety.[9]

Ultrasound uses pulsed sound waves that are sent into a patient and reconstructs images from echoes reflected by tissues and organs. The technique is used for biopsy supported diagnosis, detection and follow-up of several tumors that are rather exposed at the surface of the body such as tumors of the breast[10], thyroid[11] and testicles[12]. In addition, brachial[13], colorectal[14] and vaginal[15] endoscopic ultrasound is applied for specific indications. One main drawback of ultrasound is a fairly low signal-to-noise ratio, but the use of sound waves is rather safe, devices are very flexible, portable and very cost-effective compared to CT, SPECT, PET and MRI.

CTs generate X-rays that transmit through a patient and record attenuated beams by circumferential detectors. Image reconstruction is performed by computer algorithms that calculate and visualize different attenuation values relative to the water density of tissues and thus generate contrast. The first axial single-slice CTs were commercialized in the 1970s and they have steadily been developed. The earliest machines consisted of only one X-ray emitter and detector, which required sequential lateral motion and rotation of the equipment. Obviously, this procedure implied long scan times, which were drastically reduced by the introduction of multi-slice helical CTs that today allow whole-body imaging within less than half an hour.[16] In clinical oncology, CT is applied for screening, biopsy guidance, staging and follow-up of a variety of entities such as retroperitoneal, bone, breast (e. g. mammography) and lung cancers.[17] However, the soft-tissue contrast of CT is rather low and it is therefore hardly used in the brain. Furthermore, repeated and frequent CT radiation might increase the risk for cancer[18], even though developments are steadily focussing on reducing CT doses, e.g. for repeated low-CT screening of patients with increased risk of lung cancer.[19]

PET and SPECT are molecular imaging techniques that rely on the decay of a radionuclide emitting a single γ-ray or a positron. In PET, the emitted positrons travel short distances due to their kinetic energy until they annihilate with electrons. This annihilation event creates two photons in (nearly) opposite direction that are detected by scintillators at coincidence. In contrast, SPECT probes only emit a single γ-ray that is recorded with γ-cameras rotating around the subject to obtain spatial localization.[20] Since coincidence detection is not possible with SPECT, a collimator is necessary to reject scattered γ-rays, which is the main reason why SPECT has a lower sensitivity than PET.[21]

For PET, relatively short-lived isotopes like ^{11}C, ^{13}N, ^{18}F, or ^{124}I are produced on site with a fairly expensive cyclotron or in case of ^{68}Ga with a generator.[22] Subsequently, these radionuclides are chemically incorporated in molecules that are either metabolized, taken up by transporters or that bind to specific receptors. Another possibility is their chelation with molecules or antigens that bind to surface receptors

that are specifically overexpressed in tumors. At this point, ^{18}F-fluordesoxyglucose (FDG) should be mentioned as the oncologic gold-standard to image the augmented glucose uptake of a vast number of tumors.[23] FDG-PET is one main focus of this work and is therefore explained in more detail in **chapter 2**.

SPECT uses isotopes with a rather long half-live like ^{67}Ga, ^{67}Cu, ^{99m}Tc,^{111}In or ^{123}I that are processed similarly to PET agents after generation.[24] One advantage of SPECT and PET is their ability to image and quantify a large variety of biochemical processes in tumors with very low tracer doses in the picomolar range, even though radiation exposure might not be lower than that of CT.[22, 25] For both, SPECT and PET, a vast majority of different tracers have been developed over the last couple of decades, which allow sophisticated insights into tumor biology as well as a high clinical throughput for diagnosis, staging, monitoring of treatment and follow-up.[22, 24]

In contrast to SPECT and PET, MRI has a rather low sensitivity and specificity, but is free of ionizing radiation and has an excellent soft tissue contrast. A detailed physical background of MRI will be given in **chapter 3**. In principle, the variable environment and changing densities of water in different tissues can be used to create contrast, which can be further enhanced by lanthanide-based contrast agents. Furthermore, diffusion-weighted imaging (DWI) and perfusion imaging respectively allow the direct assessment of cell density and perfusion, which can be helpful to assess several stages of tumor growth. In addition, bulk water is not the only “chemical” that creates a great variety of contrasts in MR. Heteronuclei are naturally abundant (^{31}P) or can be stably enriched (^{13}C) in endogenous or exogenous biosensors or metabolic probes. Their resonance signals can be measured and quantified with magnetic resonance spectroscopic imaging (MRSI), even though this is only rarely applied in clinical routine. For instance, the concentration measured by ^{1}H-spectroscopy of metabolites like N-acetyl aspartate, choline, citrate, creatine, lactate and myoinositol could be altered in malign states of the brain, breast, the gastrointestinal tract and the prostate. Furthermore, altered lipid concentrations may indicate treatment induced tumor necrosis.[26]

Besides proton MRSI, ^{31}P-spectroscopy can be used for diagnosis, treatment monitoring and metabolic characterization of lesions of the brain, breast, prostate and liver. Main metabolites that show altered concentrations in the malign state are structural membrane precursors like phospholipids and energy source molecules like inorganic phosphate, nucleoside phosphates and phosphocreatine.[27]

Another application of MRSI for tumor characterization is the quantification of tumor pH with endogenous or exogenous sensors bearing protons or heteronuclei that exhibit pH sensitive nuclear magnetic resonance (NMR) properties. Tumors acidify their extracellular milieu, which is a consequence of the Warburg effect combined with hypoxia and ischemia.[28, 29] A comprehensive overview of this topic is given in

chapter 2 and **chapter 4** and pH imaging will be a major part of this work as shown in **chapter 5, chapter 6** and **chapter 7**.
In addition, sophisticated methods like chemical exchange saturation transfer (CEST) use naturally occurring molecules or probes to characterize pathologies. In principle, CEST irradiates the NMR signal of the probes with a frequency-selective pulse during which the probes exchange protons with bulk water.[30] This leads to a decrease of the water signal, which is used to generate contrast. Applications in oncology are for example glucoCEST,[31, 32] and amide proton transfer (APT) CEST.[33] These methods respectively address elevated glucose uptake and reduced pH, which is observed for many tumors (**chapter 2**).
Nevertheless, the main pitfall of classical MRSI is the fact that it suffers from the low intrinsic sensitivity of magnetic resonance. MR therefore either requires high probe doses or long scan times.
The invention of hyperpolarization techniques such as spin exchange optical pumping (SEOP) and dissolution dynamic nuclear polarization (DNP) that respectively enhance the signals of noble gases and ^{13}C-labelled probes (among other spin-½ nuclei) has shifted these limits. On the one hand, hyperpolarized (HP) gases allow for a functional characterization of the lung and detection of lung cancers.[34] On the other hand, several hyperpolarized ^{13}C-labelled metabolites like pyruvate or ^{13}C-labelled pH sensors hold promise to be translated to the clinic for diagnosis, early treatment response monitoring, tumor stratification, treatment planning and outcome prediction of cancer patients.[35, 36] Hyperpolarized pyruvate - the gold standard of ^{13}C-imaging - in combination with commercial polarizers operating at sterile conditions[37] is already used in human studies.[38, 39] Obviously this implies that the technique holds promise to provide complementary information to other modalities without any further radiation exposure. Hyperpolarized MRSI will be a main focus of this work (**see chapters 4, 5, 6** and **7**). Theoretical aspects are given in **chapter 3**.

1.4 Hybrid Imaging Modalities

Each presented imaging modality has its limitations and advantages and is not superior, but rather complementary to the others. Therefore, a sequential or simultaneous combination of the methods is highly beneficial for cancer patient care with regards to screening, diagnosis, staging, restaging, treatment monitoring, treatment planning and follow-up.[40] In general, a hybrid imaging modality is the combination of two or more imaging technologies ideally yielding a new fusion modality with multiple synergistic advantages. The most obvious is the possibility to measure and quantify metabolic information and physiological processes with inherent co-registration of its anatomical context at high resolution. Modern CT and proton MRI

achieve a spatial resolution on the micron scale and are therefore already useful for tumor localization, delineation, and characterization of size, morphology and structure.[9] In contrast, the resolutions of PET and SPECT are relatively low due to intrinsic physical limitations, but they are powerful for metabolic imaging with highest specificity and sensitivity.[23, 41]

During the last two decades, several hybrid imaging machines have been developed for clinical oncology. Hybrid ultrasound imaging such as ultrasound/CT/MRI for the visualization of tumor vascularization and angiogenesis is an emerging field[42], which however will not be discussed in this work. A brief overview of SPECT/CT and PET/CT is given as follows. However, the main focus will be hybrid PET/MR, because the key study of this thesis was performed on such a state-of-the art clinical system (**chapter 4**).

1.4.1 SPECT/CT and PET/CT

SPECT/CT and PET/CT were the first commercially available hybrid systems that were introduced at the beginning of this millennium.[20] At first, both modalities were arranged in a tandem and patients had to be moved between the two scanners, which implied problems for an accurate co-registration of the images. Today, the techniques are available within one system, which eliminates registration problems and allows for the sequential acquisition of anatomical and metabolic information.

In oncology, SPECT/CT is widely used to detect cancers and metastases of the skeleton and in particular to differentiate neoplastic alterations from trauma and infections with higher accuracy than with SPECT only. Commonly used tracers are radioiodine and ^{123}I- or ^{131}I-metaiodo benzyl guanithidine (MIBG) for the detection, staging and restaging of thyroid and neural crest tumors and metastases, respectively.[40] The combination of both techniques has reduced both, the false-positive and false-negative rate of lymph node biopsy in breast cancer patients.[40] Another striking example of SPECT/CT superiority over the stand-alone methods has been shown for diagnosis, treatment planning and prognosis of prostate cancers using ^{111}In-Capromab.[24]

Robustness, steady hardware development and the discovery of a variety of PET tracers has significantly contributed to establish PET/CT in the clinic. Today, the hybrid modality allows a high throughput and an increased accuracy of about 10 - 15% compared to the stand-alone techniques for cancers of the head, neck, thyroid, lung, breast oesophagus, colorectum, lymph nodes, and many more.[43] Therefore, it is the current “work-horse in clinical routine for diagnosis, staging,…[restaging] and outcome prediction of cancer patients allowing for a patient specific treatment planning”.[44] The glucose analogue ^{18}F-FDG is still the most applied and best studied PET tracer that is

useful for at least one application for every tumor entity even though it was established almost half a century ago.[40, 45] However, radiochemistry progressively develops sophisticated molecules with high specificity, which is believed to improve every stage of patient care aiming at an accurate diagnosis and a tailored treatment planning with PET/CT.

1.4.2 PET/MR

Magnetic resonance imaging has an excellent soft-tissue contrast, does not apply additional ionizing radiation to patients and allows for the characterization of tumor biology with diffusion-weighted imaging, dynamic contrast enhanced (DCE) imaging and MRSI.[46-49] It is therefore not surprising that medical engineers steadily focused[50] on combining PET and MR to finally release the first commercial sequential and simultaneous systems less than a decade ago.[47] Sequential PET/MR and PET/CT-MR scanners did not require huge technical modifications and allow for the combination of CT attenuation correction for PET with high-end coincidence-timing resolution (time-of-flight-PET). However, exact temporal co-registration of anatomical, functional and metabolic images is not possible and acquisition requires longer times than the simultaneous solution.

One major achievement for the invention of true hybrid PET/MR was the usage of MR compatible shielded electronic components and the replacement of classical photomultiplier tube detectors by non-magnetic semiconducting avalanche photodiodes or silicon photomultipliers. In addition, strong magnetic fields and the small MR bore size did not allow rotating PET sources for attenuation correction. Therefore several MR approaches using template-, atlas- or sequence-based corrections have been developed and it has been shown that a tracer quantification comparable to PET/CT is feasible for most tissues and organs “except for the lung, subcutaneous fat and the blood pool.”[51] However, the clinical value of PET/MR is only given, if it provides unique features or information complementary to other modalities that improve patient care and outcome. This is in particular important, because PET/MR is fairly expensive and requires both radiology and nuclear medicine expertise for an accurate image interpretation. The superiority of PET/MR over PET/CT has therefore been analyzed since the first PET/MR has been commercialized and this is still ongoing research.[25, 46, 47]

Indeed and with regards to oncology, a number of studies showed that the combined modality improves the sensitivity for lesion detection in brain, bone, breast, cervix, liver, kidney and ovaries as well as a better lesion delineation in the bone and soft-tissues (except lung).[25, 52] Rosenkrantz et al.[25] and Fraum et al.[52] reviewed that multiparametric PET/MR can be used for an accurate identification of biopsy targets in

glioma patients and post-operative differentiation of recurrent tumors from radiation necrosis. For breast cancer, initial staging is typically performed by sequential PET/CT and MRI where the radiation dose can be significantly reduced using PET/MR (up to 54 – 81% without the use of whole-body CT).[52] In fact, this is also beneficial for vulnerable patients like children or pregnant women.

Whole-body imaging is important to detect nodal or distant metastases. Comparative PET/CT and PET/MR studies on breast cancer patients showed equivalent detection sensitivity of metastases in most organs. However, PET/MR was superior for detection of secondary lesions in brain and liver.[53]

The possibility to combine PET and anatomical imaging with contrast-enhanced MRI and diffusion-weighted imaging holds promise for an individual treatment planning. The combined assessment of FDG uptake and tumor cellularity has, for instance, proven higher accuracy to detect early treatment response compared to stand-alone measurements of breast tumors.[25] Another example where PET/MR could prove high oncologic value is prostate cancer. In the clinic, MRI is routinely used for diagnosis, localization and multimodal assessment of tumor grade due to the excellent soft-tissue contrast. FDG-PET is not very sensitive to malign prostate lesions, but ^{11}C-choline performs well for diagnosis of localized cancers and was recently FDA-approved for clinical use with PET.[54] Other studies with ^{18}F-fluorcholine showed that tracer uptake and simultaneously acquired tumor cellularity were significantly different for benign and malign lesions.[25] In addition, ^{68}Ga-PSMA holds great promise to be translated into the clinic to be used for an improved handling of prostate cancer patients.

Simultaneous PET/MR combining hyperpolarized ^{13}C-metabolic imaging and PET with cellular and anatomic context is one of the most recent cutting edge hybrid techniques that facilitates new insights into tumor biology.[55, 56] This thesis demonstrates the value of the simultaneous acquisition of FDG-PET, diffusion-weighted imaging and metabolic imaging using hyperpolarized ^{13}C-pyruvate. The following chapters will describe the biological relevance of combined FDG-PET, hyperpolarized pyruvate imaging and in addition pH *in vivo* mapping with regards to tumor biology, namely the Warburg effect.

2. FDG-PET, HP Pyruvate MRSI and HP pH Imaging

Main cellular hallmarks of cancers are an extensive growth, cell proliferation, metastasis and survival. For this purpose, tumors have an increased need for anabolic precursor molecules and a ready availability of energy sources such as adenosine triphosphate (ATP).

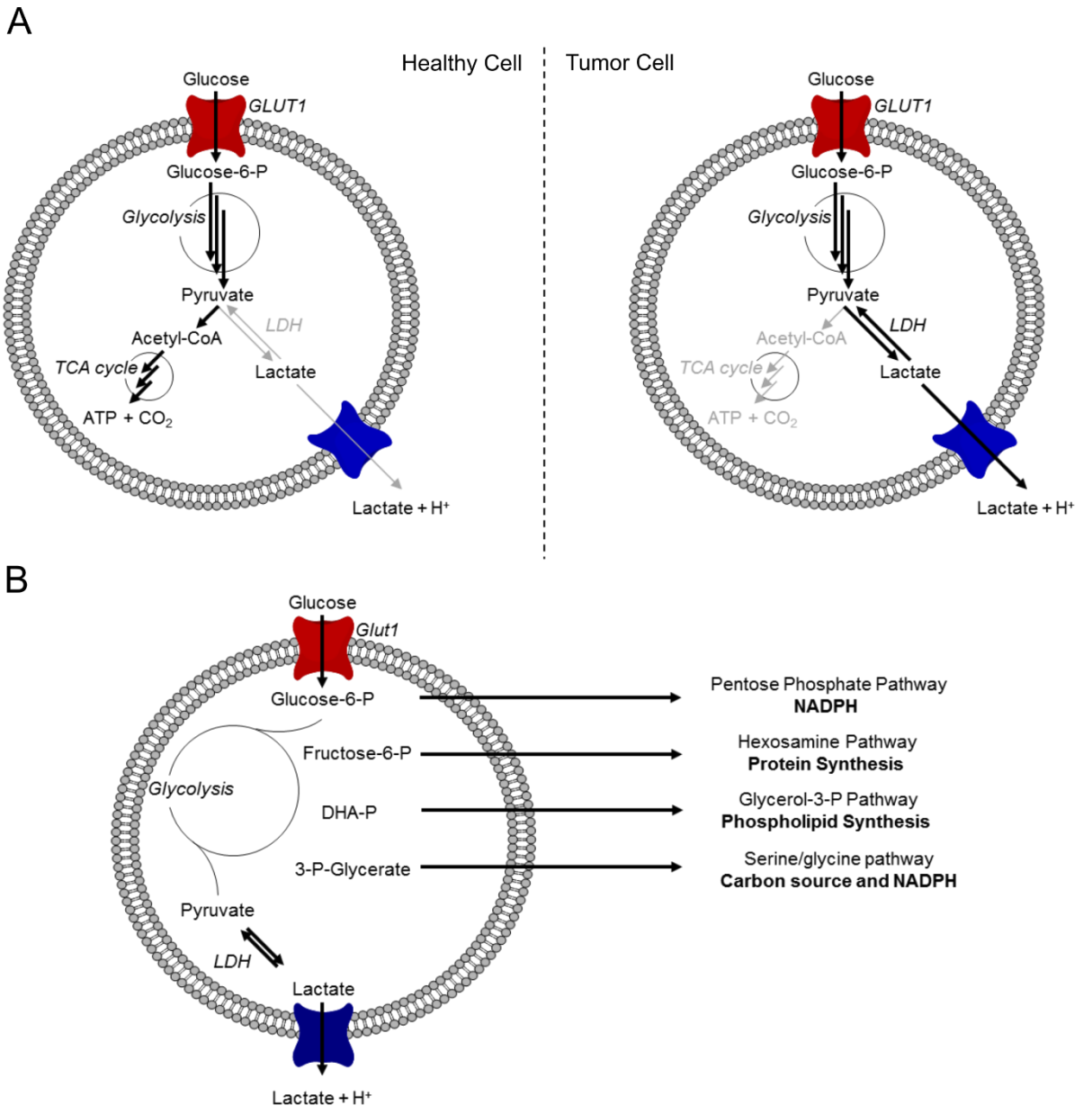

Figure 2.1. The Warburg effect and related anabolic shunts. (A) Tumor cells take up high levels of glucose compared to normal cells, which is facilitated by overexpression and upregulation of GLUT1 transporters. Even under normoxic conditions, glucose is not oxidized in the tricarboxylic acid cycle (TCA) of mitochondria via pyruvate and acetyl-coenzyme A (Acetyl-CoA) to adenosine triphosphate (ATP) and carbon dioxide (CO_2). It is rather reduced by lactate dehydrogenase (LDH) A to lactate. Lactate is finally exported to the extracellular space, leading to an acidification of the tumor microenvironment. **(B)** Tumors can shunt the excess of glucose into different other pathways to fulfill their anabolic needs. Key branching points of glycolysis are glucose-/ and fructose-6-phosphate, dihydroxyacetone phosphate (DHA-P) and 3-phosphoglycerate (3-P-glycerate).

More than a century ago, Otto Warburg discovered that malignant tissues take up high levels of glucose and produce an increased amount of lactate. At that time, he believed that this was due to a defect of mitochondria[57, 58], but his assumption was proven wrong in several upcoming studies.[59, 60] Compared to normal cells, tumors consume high levels of glucose that are rather reduced to lactate even under normoxic conditions than processed by oxidative phosphorylation even if mitochondria are fully functional.

Increased glucose uptake and reduction of pyruvate is facilitated by overexpression and upregulation of key glycolytic enzymes such as glucose transporters (GLUT1) and lactate dehydrogenase (LDH) A.[61] This metabolic adaption has been termed the Warburg effect or aerobic glycolysis and it is considered as a main metabolic hallmark of tumors (**Figure 2.1A**). Malignant cells benefit from the Warburg effect, which is apparent at closer examination of the glycolysis and its related pathways.

The generation of cytosolic ATP through aerobic glycolysis is about 10 - 100 times faster than mitochondrial oxidation of glucose,[62] which provides a quick fuel for cell growth and proliferation. In addition, the increased glucose consumption can be used as a source for anabolic processes if oxidative phosphorylation is circumvented on the one hand. On the other hand, aerobic glycolysis is used to produce the reduction equivalents NADH and NADPH, which can be limiting factors for proliferating cells. **Figure 2.1B** shows main checkpoints of glycolysis that support the synthesis of DNA, lipids, proteins and NADPH. Glucose-6-phosphate (G6P) can be shuttled through the pentose phosphate pathway (PPP) yielding the DNA sugar precursor ribose-6-phosphate and NADPH. The latter molecule drives anabolic reductions like during synthesis of palmitic acid. One step further downstream of G6P, fructose-6-phosphate may be used for the hexamine synthesis, which together with glutamine yields glucosamine-6-phosphate and finally N-acetylglucosamine (GlcNAc). GlcNAc is an important key metabolite for the glycosylation of extracellular proteins. The biosynthesis of phospholipids, which are the most important structural components of cellular membranes, can be fuelled by dihydroxyacetone phosphate. Finally, 3-phoshoglycerate can be shunted from glycolysis to generate the carbon donor molecules serine and glycine. In addition, this pathway also generates NADPH. A comprehensive overview of these glucose shunts is, for instance, given by van der Heiden et al.[63], Hsu et al.[64] and Pavlova et al.[65]

In order to facilitate such complex metabolic adaptions, transporters and enzymes that are involved in the respective pathways are either overexpressed or misregulated by oncogenes or tumor suppressors such as Ras (rat sarcoma)[66] or p53.[67]

Increased glucose uptake and aerobic glycolysis produce an excess of lactate that is co-exported with protons to the extracellular space. This leads to an acidification of the tumor microenvironment and generates a hostile milieu for surrounding healthy cells allowing tumors to grow and metastasize. In addition, an acidic environment serves as

a protection barrier against immune cells and facilitates tumor survival.[68, 69] Finally it has been shown that the pH is critical for cancer treatment efficacy as many chemotherapeutic agents are sensitive to pH.[70]

Overall, the non-invasive and quantitative assessment of the Warburg effect has several applications such as diagnosis, staging, treatment planning, outcome prediction and disease follow-up. As shown in **Figure 2.2**, an augmented glucose uptake of tumors can be addressed by FDG-PET.[71] FDG is a glucose analogue that bears the ^{18}F-radionuclide at position two.[72] During the first steps of internalization, FDG behaves similar to glucose until it is phosphorylated by hexokinase. The phosphorylated version is not recognized by subsequent glycolytic enzymes and the molecule gets trapped, leading to an accumulation of FDG-6-P that is quantifiable with PET.[73-75]

Downstream of glycolysis, a high LDH activity, i.e. an increased reduction of pyruvate to lactate can be addressed with magnetic resonance spectroscopic imaging (MRSI) using hyperpolarized [1-^{13}C]pyruvate.[76, 77] The molecule is readily internalized by malignant tissues and its conversion can be followed in real-time allowing for the quantification of the kinetic rate constant of LDH. Finally, lactate acidification of the tumor microenvironment can be measured with hyperpolarized MRSI of pH sensor molecules such as [1,5-^{13}C]zymonic acid (ZA) - the dehydrated dimer of pyruvate.[78]

The aim of this work is the non-invasive assessment of the three presented key metabolic steps that characterize the Warburg effect, namely: 1. augmented glucose uptake, 2. augmented pyruvate-to-lactate reduction and 3. acidification of the extracellular space.

After discussion of the theoretical background of PET, MRI and MRSI in the upcoming **chapter 3**, peer reviewed publications will be presented (**chapters 4 – 7**). **Chapter 4** shows that a simultaneous quantification of metabolic processes in their anatomical context is feasible for a pre-clinical model of breast cancer in rats on a clinical PET/MR scanner. In **chapter 5**, a review on pH imaging using hyperpolarized molecules will be given. **Chapter 6** shows that deuterium enrichment of ^{13}C-labelled zymonic acid is a feasible concept to prolong the hyperpolarized signal lifetime and thus enhances the sensitivity of pH imaging *in vitro* and *in vivo*. Finally, a systematic study exploring amino acids and their derivatives for potential new pH probes is presented in **chapter 7**.

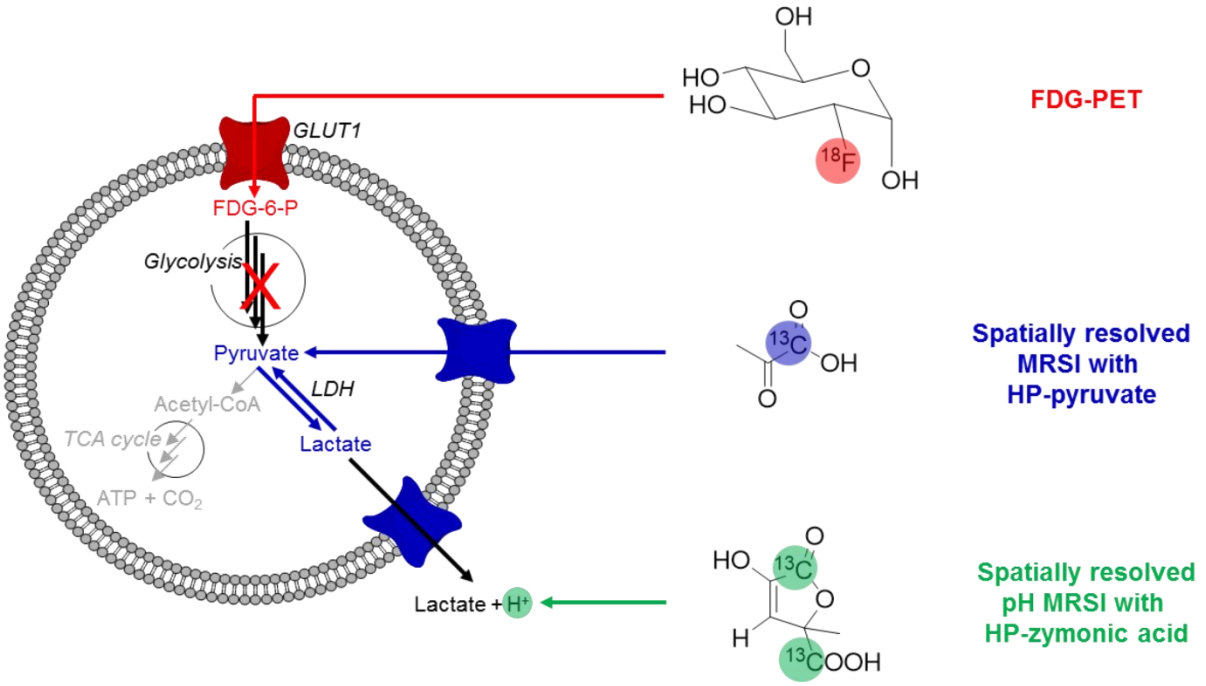

Figure 2.2. Non-invasive imaging strategies for the quantitative assessment of the Warburg effect. Tumors have an increased energy demand and take up high levels of glucose. ^{18}F-FDG is a positron emitting analogue of glucose with similar behaviour during the first steps of internalization. However, once taken up, FDG is phosphorylated by hexokinase and gets trapped, because downstream glycolytic enzymes do not recognize the phosphorylated version. Thus FDG accumulates and can be quantified with PET, which allows for the assessment of augmented glucose uptake (red). Pyruvate-to-lactate reduction catalysed by LDH is observable in many tumors even in presence of sufficient oxygen. The kinetic rate constant of LDH can be quantified by non-invasive imaging of hyperpolarized [1-^{13}C]pyruvate, which is rapidly converted to lactate *in vivo* (blue). Due to the Warburg effect, an excess of lactate is produced and exported to the extracellular space. This leads to an acidification of the tumor microenvironment, which can be measure non-invasively by ^{13}C-labelled pH sensor molecules such as zymonic acid – the dimer of pyruvate (green).

3. Principles of PET, MR and MRSI

3.1. PET

3.1.1 Radionuclides

Positron emission tomography is a nuclear medicine imaging technique for the metabolic imaging and quantification of physiological parameters *in vivo*.[79] It relies on positron emitting nuclei such as ^{11}C and ^{18}F that are generated by a cyclotron or in case of ^{68}Ga by a generator. After production, radioactive nuclei are incorporated into tracers that are either metabolized, or bind to markers and surface structures of malignant tissues with high specificity. The radionuclide continuously undergoes a radioactive decay, which is governed by the nucleus half-life. Typical half-lives of clinical relevant radionuclides and examples for their usage in oncology can be found in **Table 3.1**.[22, 23, 80] Note that most of the knowledge of the following PET theory chapter was adapted from “Principles and Practice of PET/CT”.[81]

Table 3.1: Positron emitting radionuclides, half-lives, examples of tracers and oncologic applications.

Isotope	Half-live (min)	Tracer	Target
^{11}C	20.3	Choline	Lipid metabolism[80]
		Acetate	Lipid and energy metabolism[82]
^{13}N	9.98	Ammonia	Perfusion and glutamine synthesis[83]
^{15}O	2.03	Water	Perfusion[84, 85]
^{18}F	109.8	FDG	Glucose uptake[81]
		F-DOPA	Dopamine synthesis[80]
		FLT	DNA synthesis[75]
^{68}Ga	68.0	PSMA-ligand	PSMA expression[86]

Abbreviations: FDG: [2-^{18}F]fluordesoxyglucose; F-DOPA: 6-Fluoro-[^{18}F]-L-3,4-dihydroxyphenylalanine; FLT: 3'[^{18}F]fluorothymidine; PSMA: Prostate-specific membrane antigen.

3.1.2 Image Acquisition

The radioactive decay of a PET tracer generates a positron that leaves its origin with a certain kinetic energy. While travelling rather short distances, it loses most of its energy and interacts with an electron. This causes an annihilation event that sends out two γ-rays with an energy of 511 keV at nearly 180° to each other. Classical PET systems contain arrays of inorganic scintillator crystals like lutetium-orthosilicate (LSO) that produce light beams excited by radioactivity.[79] The resulting photons are

converted to electric signals by photomultiplier tubes (PMT), which are, however, magnetic field sensitive. Hybrid PET/MR scanners detect photons either by MR compatible silicon photomultipliers (SiPM) or avalanche photodiodes (APD) with MR-shielded electronics. The PET/MR used in this thesis detects coincidence with detector rings consisting of 56 blocks of 8x8 arrays of 4x4x20 mm^3 LSO crystals that are linked to 3x3 APDs each (**Figure 3.1A**). To finally increase the field of view, several rings of such blocks are aligned next to each other (8 in the underlying case).[87, 88]
Any photon pair that leaves the patient as true coincidence defines a line of response (LOR), whereas the sum or integral of events registered by opposing detectors respectively define a spatial column, which is called the volume of response (VOR, **Figure 3.1B**). Furthermore, 2D and 3D acquisition mode can be differentiated (**Figure 3.1C**). In 2D mode, only coincidences within the same detector ring are measured, whereas events for planes connecting different detector rings are counted in 3D mode. Note that 2D mode is normally not used anymore, because it has a lower sensitivity than 3D mode.

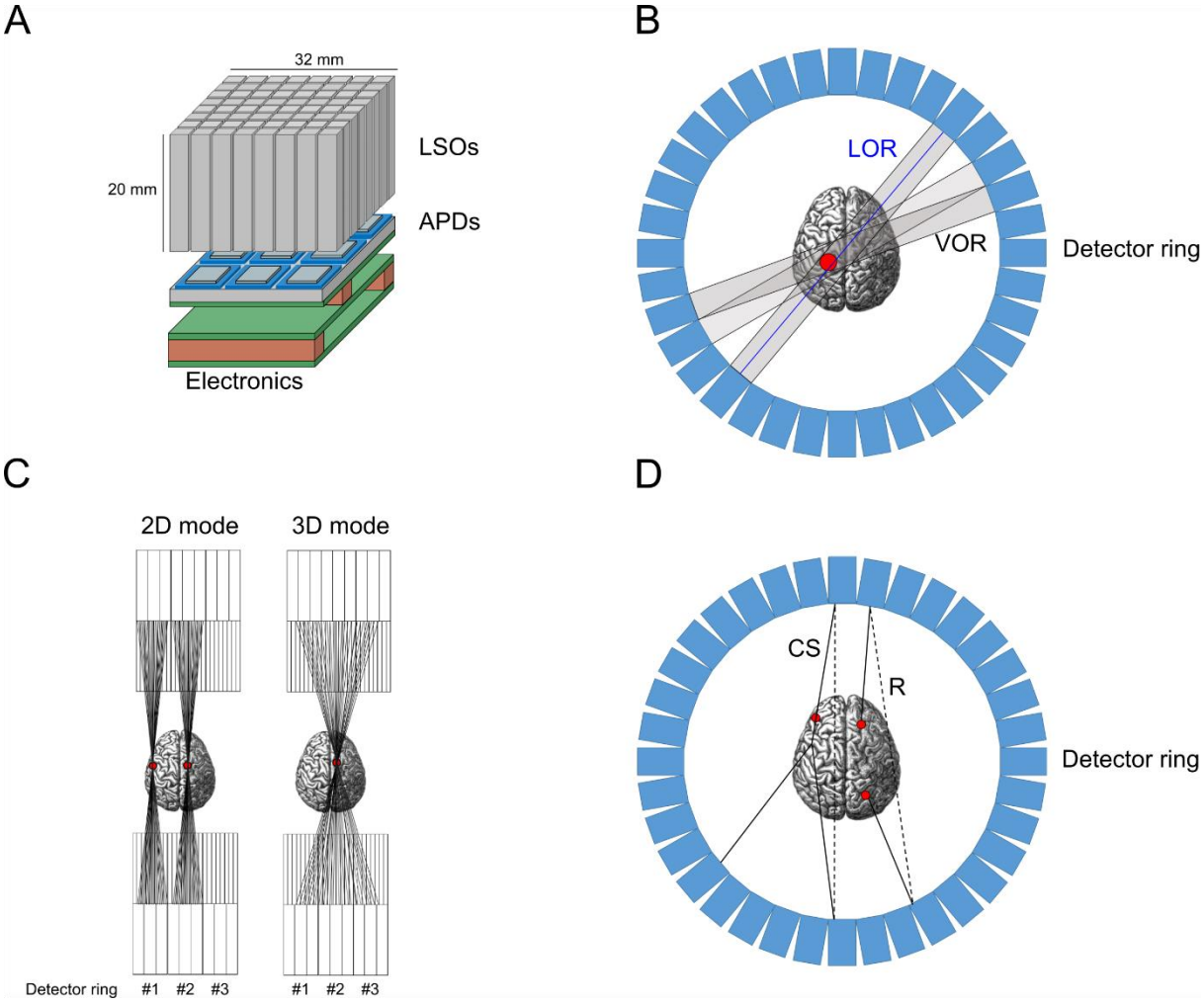

Figure 3.1: PET instrumentation. (A) Schematic detector module of PET/MR used in this work. The size of a single crystal is 4x4x20 mm^3 and crystals are arranged in an array of 8x8. Conversion of light to electrical current within the magnetic field is facilitated by 3x3 APDs. Electronics are shielded. **(B)** Schematic detection of an annihilation event (red) with detectors circumventing the FOV of the PET/MR

scanner. Detector pairs registering two photons at the same time define a volume of response (VOR) in which the annihilation must have occurred (gray columns). Coinciding photons define a line of response (LOR, blue). **(C)** Principle of 2D and 3D PET acquisition mode. In 2D mode, only events within one detector ring are registered. In 3D LORs that combine different detector rings are registered in addition. **(D)** Background noise is the sum of Compton scattering (CS) and random (R) events. The images were designed according to reference [81]. (Copyright information: The brain image is license free and part of the public domain).

3.1.3 Data Corrections

The *in vivo* quantification of PET tracers requires some essential data corrections that are system- and subject-related. The most obvious correction that needs to be applied is the correction of the radioactive decay. However, this can easily be performed if the initial dose and the half-life are known.

With regards to the hardware, detector responses, detector dead times, and random coincidences need to be taken into account, which is normally part of the vendor's software package. First, detectors do not respond uniformly to radiation events, which is a matter of slightly non-uniform fabrication and different geometric arrangement of the opposing detectors. During the time a detector is processing a coincidence, it cannot process additional events, which leads to a so-called dead-time loss. It scales linearly for rather low activities and non-linearly when very high doses are measured. Besides, random background events can cause false positive reads of γ-rays that originate inside or outside the field of view (**Figure 3.1D**).

Compton scattering (CS) is a usual event that occurs within the subject. Its probability scales with the subject size and a significant amount of coincidences up to 50% is lost. Correction of CS is not within the scope of this work, but there is a vast number of works that for instance used different energy windows or analytical approaches based on Monte-Carlo calculations to address this problem.[89] Inter-crystal scattering (ISC) also contributes to a loss of true events, but it is usually discarded as it can be differentiated from other events. Nevertheless, correction for ISC could significantly enhance the image signal-to-noise ratio and it is therefore a focus of current research.

One very important correction that has to be performed is photon attenuation correction. Attenuation happens within the body and increases exponentially with the body size, i. e. the distance a photon travelled through attenuating tissue.[81] This leads to a loss of true incidences, which degrades the image quality, increases noise and introduces a bias for the quantification of tracer uptake. In general there are two basic ways to quantify attenuation. The first method is pre-correction of emission data with attenuation correction factors (ACF) that are different for several tissues such as brain, bone or lung. The second method is the forward projection of an attenuation

map, also called μ-map, which basically represents the spatial distribution of attenuation factors.
Classically, PET transmission scans with rotating positron emitting sources such as ^{68}Ge, ^{68}Ga, ^{124}Cu or γ-ray sources like ^{137}Cs were performed before the actual examination to calculate μ-maps. With the invention of PET/CT (and SPECT/CT), μ-maps were determined from the attenuation of the CT x-rays. Indeed, there are differences in the energies of PET (511 keV) and CT (60-140 keV) attenuation scans, but scaling factors derived from piece-wise linear calibration curves are available.
A smaller bore size and magnetic field incompatibility do not allow rotating PET sources or integration of a CT into a PET/MR. Therefore, MR-based attenuation is needed, which comes along with the advantage of radiation reduction. Even though the MR signal is not related to the tissue density, a variety of attenuation correction approaches based on templates, atlas segmentation or MR segmentation have been developed and the topic is still ongoing research.[90] Template-based attenuation correction uses averaged PET μ-maps from transmission scans and co-registered MR templates. Patient-specific MR images are transformed to match the MR templates yielding correlation matrices that are used for the adaption of the PET templates to the corresponding patient data. Atlas correction uses CT attenuation information that are matched to patient-specific MR images creating a synthetic CT μ-map that is finally non-linearly adjusted to the patient's PET. More sophisticated methods use additional anatomical information and relative positions of different tissues for correction.[90]
MR-based attenuation uses standard T_1 or ultrashort echo time (UTE) sequences to derive μ-maps. T_1-weighted imaging (see **chapter 3.2.3**) is able to segment most soft tissues but cannot distinguish between air and bone. However, this is problematic, because these two tissues have opposite, respectively low and high, attenuation factors. In contrast, UTE sequences were specifically designed to visualize short spin-spin relaxation time (T_2) regions and allow for the differentiation between bone and air. Current research is focusing on the improvement of UTE acquisition at two or more echo times to respectively visualize bone and additional Dixon fat-water separation.[90]

3.1.4 PET Resolution

The spatial resolution of PET is defined by a couple of physical constraints. First, the crystal dimension is the most dominant factor as it determines the size of the coincidence column. Therefore, developers steadily minimized scintillator crystals that today reach sizes of below 1.0x1.0x15 mm^3 in pre-clinical PET cameras.[91-94] Next, positrons leave the tracer with a certain energy and capture electrons with non-zero kinetic energy. On the one hand, this means that the position of the annihilation

process rather than the tracer position is localized. To give an example, the average distance between the two locations is less than a millimetre for ^{18}F-fluorine. On the other hand, the residual momentum of the positron causes a non-linearity between the emitting photons, which leads to a Gaussian distribution of detected events and finally to an image blurring. In fact, this effect is stronger for bigger bore diameters.
Additional factors that impact the resolution of PET are related to decoding, penetration and sampling. Decoding errors arise from the block structures of the detectors that combine multiple crystals with one diode or PMT. For such arrays, an exact back-calculation of the photon's location of entry into the crystal might be imperfect. In addition, a photon could penetrate through the actual crystal of coincidence and therefore be registered by a neighbouring one (ISC). Last, there is a defined number of LORs depending on the crystal number and size. Some pixels in the field of view are therefore transected by a larger number of LORs than others.
Overall and as a general rule of thumb, the measured object should be greater than three times the spatial resolution to be accurately reconstructed with PET.[95]

3.1.5 Image Reconstruction

3-dimensional PET information is reconstructed as a stack of thin 2D cross-sectional slices that are derived from annihilation events originating from positrons emitted by a tracer. Data can be recorded as event histograms - also called sinograms - or as projections. Another approach appends data to a list of coincidences with temporal information measured in the so called list-mode. Later, this allows for the reconstruction of images for a specific time frame of a defined length.
In general, PET data reconstructed by analytical filtered-back projection (FBP) or statistical iterative methods such as maximum likelihood expectation maximization (MLEM) or paring ordered subset (OS) reconstruction with expectation maximization (OSEM).
For every 2D plane, the sum of all coincidences within a VOR can be expressed as a function $f(x, y)$ of the Cartesian coordinates x, y with the centre of the gantry being the origin and the rotation angle Φ. The measured PET data $p(x',\Phi)$ are given by

$$p(x', \Phi) = \int f(x, y) dy' \quad (3.1),$$

where x' and y' are the Cartesian coordinates rotated by the angle Φ and where each volume defined by (x',Φ) corresponds to a specific column defined by an opposing detector pair. A projection is defined as the assembly of parallel projection rays corresponding to one specific rotation angle (**Figure 3.2A**). The sum of all projections is finally proportional to the total radioactivity in the object given as (**Figure 3.2B**):

$$\sum_{x'} p(x', \Phi) = \iint f(x, y) dx dy \quad for\ all\ \Phi \qquad (3.2)$$

The graphical illustration of the rotation angle against x' is called a sinogram, because the projection of any point source yields a sine wave (**Figure 3.2C**).

Filtered back projection applies filtering and back-projection on the data to finally obtain the actual PET image. Basically, back-projection is the opposite operation of forward-projection, which is done by the scanner during regular acquisition mode storing data as projections.

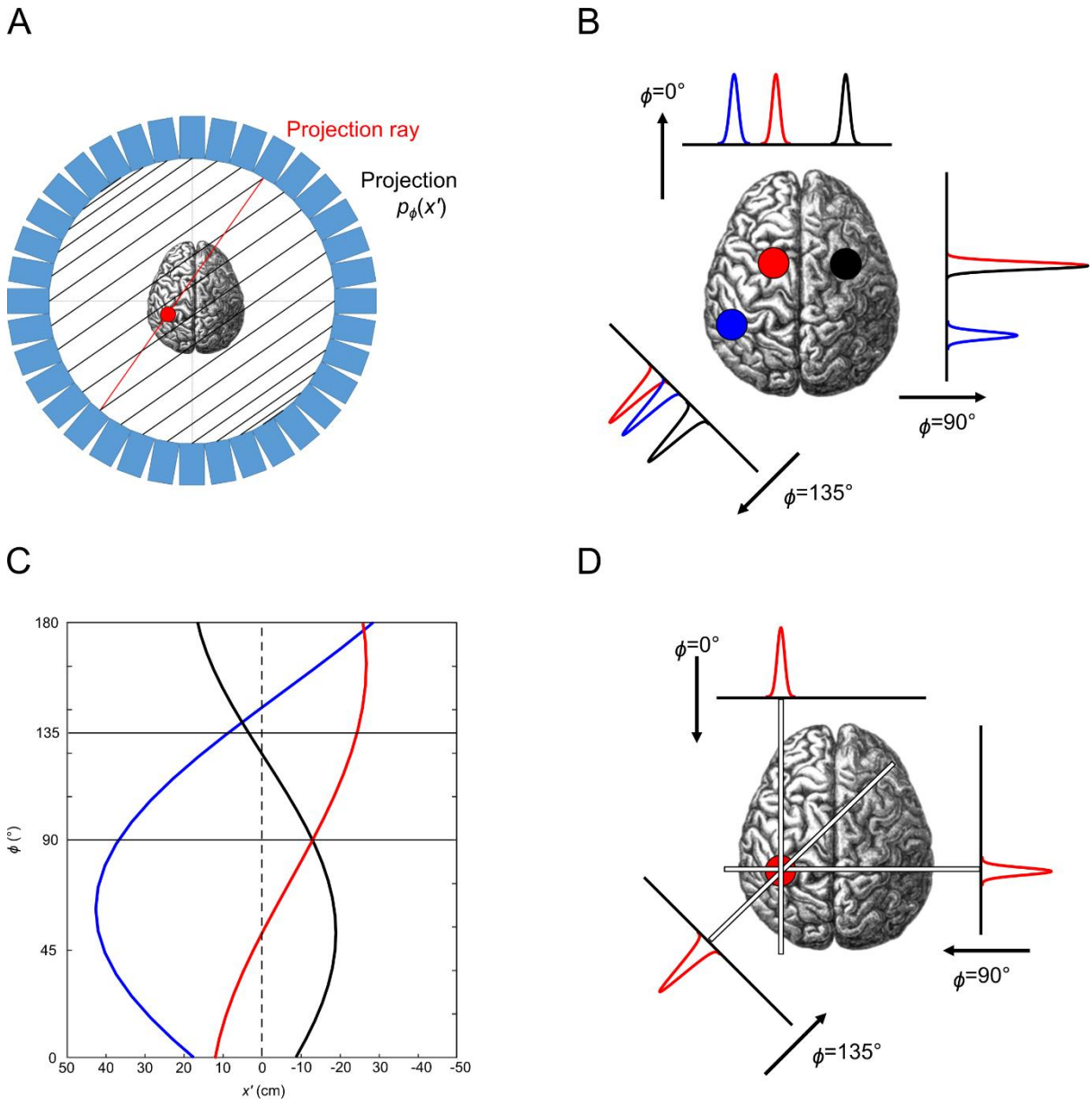

Figure 3.2. PET image projection and back-projection. (A) Projections for a 2D slice through a human brain showing one projection ray (red) and the projection for a given angle Φ. **(B)** shows three two-dimensional projections for an object containing three radioactivity sources with equal radioactivity for three different angles. A full projection contains all angles from 0° to 180°. **(C)** The sinogram projection is the plot of all projection rays $p(x', \Phi)$ or line integrals for a given distance to the gantry center with a defined angle. **(D)** Two dimensional back-projection of an object containing a single radioactive source,

whereas each projection is related to a peak originating from the amount of measured counts. Back-projection without a filter leads to a continuous line in the image, which causes to star-shape artefacts. The images were designed according to reference [81]. (Copyright information: The brain image is license free and part of the public domain).

However, back-projection of data does not yield the actual image, but rather a star-like image as indicated for a point source in **Figure 3.2D**. In order to obtain the true image, filtering is necessary. This is basically done by Fourier transformation of projection data into the frequency space, multiplication with certain frequency space filters to increase actual signals and decrease noise. Finally, inverse Fourier transform and back-projection ($b(x,y)$) yields the image.

$$b(x,y) = \int_0^{2\pi} p(x', \Phi) d\Phi \quad (3.3)$$

A major challenge of FBP is the fact that data are not noise free. In the frequency space, noise has a uniform frequency distribution, while real incidence data tend to decline at higher frequencies. A good number of filter functions (ramp filter, Butterworth, Hamming) have therefore been considered. Although they are still not ideal for an optimal noise suppression, they are reasonably accurate for images of high signal-to-noise ratio (SNR).

Iterative methods require higher computational effort as they initially estimate images from projections. They compare forward projections to the actual data and then refine the estimates by optimization of an objective function. In mathematical terms, this requires the determination of a model describing the data, an operation that allows the objective quantification of the similarity of estimated and projected data and an algorithm that determines the next refined image.

The general model of iterative methods relates the projections *p* to the values of all image voxels *f* by a forward projection or transition matrix *A*. *A* thereby contains the probabilities of an annihilation event in a voxel *i* detected by a projection ray *j*.

$$p = A \cdot f \quad (3.4)$$

Including *a priori* constraints like non-negativity of data or object boundaries from CT or MR images, the algorithm tries to successively maximize the objective function while having a criterion for stopping the iteration. A commonly used algorithm is the so called maximum-likelihood expectation-maximization (MLEM), “which…maximize[s] the logarithm of the Poisson-likelihood.”[81] However, in practice, the logarithm of the likelihood function is maximized for computational reasons. The image is finally calculated as follows:

$$f_i^{k+1} = \frac{f_i^k}{\sum_{j=1}^{m} A_{ij}} \sum_{j=1}^{m} \left[A_{ij} \frac{p_j}{\sum_{j=1}^{n} A_{i'j} f_i^k} \right] \quad (3.5),$$

with f^k and f^{k+1} being the image estimated from iteration k and k+1 and A_{ij} being the forward projection for mapping f into p.
The computational load of this algorithm is about double the amount as for FBP, but can considerably be reduced by grouping projection data into several subsets and application of EM. In theory, if each subset would consist of one projection ray, OSEM would be as fast as MLEM. However, it has been shown that reconstruction of images from subsets of randomly distributed rays will yield a similar or even better image quality at lower computational cost. One problem of OSEM is that the algorithm does not converge to the maximum likelihood. This has been tried to overcome with more sophisticated objective functions, which however won´t be within the scope of this thesis.

3.1.6 Tracer Quantification

If all data corrections are performed accurately and images have been reconstructed correctly, the tracer concentration at a given space and time can be quantified by two different approaches.
The semi-quantitative method relates the activity ($c(t)$) of a defined voxel in a static image at a defined time point t to the administered dose and the body-weight of the subject. This yields a unitless parameter, which is called the standard uptake value (*SUV*). For a defined region-of-interest (*ROI*), one can additionally differentiate the maximum measurable *SUV* (SUV_{max}) and the mean of all *SUVs* (SUV_{mean}). The mean is frequently calculated from *SUVs* within a ROI that are greater than a defined percentage of SUV_{max}.

$$SUV = \frac{c(t) \cdot weight}{dose} \quad (3.6)$$

In the clinic, *SUVs* are normally determined in static late frame images, where tracer accumulation is expected to reach a plateau. The tracer is therefore administered outside the scanner and measured later at a defined time-point thus allowing higher throughput. *SUVs* are highly relevant in the clinical routine, as they provide diagnostic information, facilitate staging, treatment response monitoring and a comparison of different patients.
However, the tracer distribution changes with time and the knowledge of its temporal behaviour *in vivo* could yield important biological information such as “blood flow, glucose metabolism, protein synthesis, neurotransmitter levels, enzyme activity and receptor binding site densities.”[81] It is therefore worth to acquire dynamic PET data in clinical and pre-clinical studies.
The analytical process that calculates true quantitative measures is called compartmental modeling. It assumes a finite number of compartments that might

actually be physically separated or that describe different physical or chemical states. The time-dependent interchange of a tracer between the compartments is expressed by kinetic rate constants and can be described by first-order differential equations.
For instance, the dynamic uptake of ^{18}F-FDG by tumors from the blood stream can be described with compartmental modeling. As this is part of this work, crucial steps of the process and ways to solve the underlying differential equations will be explained quickly and on the basis of FDG.

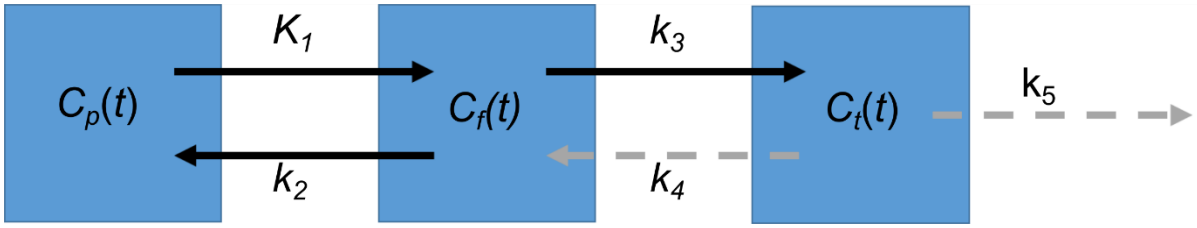

Figure 3.3. Two-tissue compartment model of ^{18}F-FDG uptake. FDG ($C_p(t)$) is taken up from the blood stream by GLUT1 transporters, which is determined by the uptake constant K_1. The reversible reaction is given by k_2. In the cytosol, free FDG ($C_f(t)$) is trapped by phosphorylation through hexokinase (rate constant k_3), and does not react further ($k_5 = 0$). The de-phoshorylation of FDG-phosphate is very slow (low k_4). The image was designed according to reference [81].

The pathway that processes FDG has been described in **chapter 2**. The underlying compartmental model is a two-tissue model that contains three compartments (**Figure 3.3**): The first one is the blood containing FDG, the second is the intracellular space containing free FDG and the third one is trapped FDG that has been phosphorylated by hexokinase. The rate constants K_1 and k_2 describe the for- and backward transport of FDG over the cell membrane by GLUT1 transporters, whereas k_3 describes the phosphorylation reaction. k_4 and k_5, that describe the dephosphorylation and further catabolism through glycolysis are respectively slow or not possible and can therefore be ignored.
Thus, the net consumption rate of FDG thus amounts to K_i

$$K_i = \frac{K_1 k_3}{k_2 + k_3} \quad (3.7),$$

and the metabolic rate consumption of glucose is given by

$$MRGlu = \frac{c_{glc}}{LC} \cdot \frac{K_1 k_3}{k_2 + k_3} \quad (3.8),$$

with c_{glc} being the glucose plasma concentration and LC being the lumped constant that accounts for differences between FDG and glucose uptake.
In theory, one could fit the time-dependent tracer concentration measured in a PET image to the underlying differential equations. However, Patlak et al. demonstrated that linearized multiple time graphical analysis (MTGA) of the blood time activity curve

(input function) and region/lesion-of-interest time activity curve can be used to quantify K_i and thus *MRGlu*.[96]
MTGA assumes that FDG is in reversible exchange with the plasma, which means that there is a constant ratio of tracer plasma and tracer tumor concentration. This is the case shortly after FDG injection where the input function peak has already been observed and the tracer is slowly washed out of the blood stream. The irreversible trapping of FDG in the tumor is then solely affecting the distribution volume of the tracer. In case of equilibrium, it can finally be shown that the graphical operation described by **equation 3.9** becomes linear allowing the determination of the net influx rate or the composite rate constant of FDG (K_i) by linear regression.

$$\frac{c_{tissue}(t)}{c_{plasma}(t)} = K_i \frac{\int_0^\tau c_{plasma}(\tau)d\tau}{c_{plasma}(t)} + V \quad (3.9),$$

with t being the time after tracer injection, $c_{tissue}(t)$ being the FDG activity concentration in the tumor, $c_{plasma}(t)$ being the FDG activity concentration in blood vessel, ${}_0\int^\tau c_{plasma}(\tau)d\tau$ being the integral of FDG concentration in the blood vessel, K_i being the composite rate constant ($K_1*k_3/(k_2+k_3)$) and V being the distribution volume of the tracer in the blood.
For more details on Patlak plotting and analysis, the reader is referred to chapter **4.6.2** (**Figure S4.2** and **S4.3**).

3.2. MRI

Magnetic resonance imaging is based on the fundamentals of nuclear magnetic resonance, which exploits the behaviour of NMR-active nuclei in a strong external magnetic field. NMR was developed in the mid of the 20th century by Edward M. Purcell[97] and Felix Bloch.[98] It took another 20 years to spatially resolve resonance signals using variable field gradients which was proposed by Paul C. Lauterbur.[99] In the following years, Peter Mansfield improved image reconstruction and introduced data acquisition with fast echo planar imaging.[100] Jürgen Hennig et al.[101] and Axel Haase et al.[102] further developed sequences for fast image acquisition, which are nowadays still used to generate high throughput with high spatial resolution in the clinic.
MRI has become a powerful technique to study small molecules, biomolecules, tissues, organs and malignancies *in vivo* without invading the system. It is therefore not surprising that Purcell, Bloch, Mansfield and Lauterbur received the Nobel Price for their outstanding scientific contributions. If not cited otherwise, most of the following information was derived from NMR and MRI textbooks.[103-105]

3.2.1 Principles of NMR

NMR exploits the spin of NMR-active nuclei. In contrast to classical mechanics, the spin *S* is quantized and can adopt discrete values according to

$$S = \frac{h}{2\pi} \cdot \sqrt{I(I+1)} \quad (3.10),$$

with *h* being the Planck's constant and *I* the quantum number that can adopt integer of half-integer numbers. The spin vector is defined by the amplitude given in **equation 3.10** and the direction S_z

$$S_z = \left(\frac{h}{2\pi}\right) m \quad (3.11),$$

with *m* being the magnetic quantum number that can have 2*I*+1 values. The spin quantum number of the nucleons and electrons is ½. In contrast, the spin of nuclei can be zero, half-integer or integer depending on the atomic mass and charge number as shown in **Table 3.2**.

Table 3.2: General rules for determination of spin quantum numbers and examples of nuclei typically used in NMR (except *I* = 0).

Mass number	Number of Protons	Number of Neutrons	I	Example
			1/2	^{1}H, ^{13}C, ^{15}N, ^{19}F, ^{31}P, ^{129}Xe
Odd (o)	e / o	o / e	3/2	^{11}B, ^{23}Na, ^{39}K
			5/2	^{17}O
Even (e)	o	o	1	^{2}H, ^{6}Li, ^{14}N
Even (e)	e	e	0	^{12}C, ^{16}O, ^{32}S

Nuclei with a spin quantum number of zero are not NMR-active and do not produce a measurable signal. Analog to classical mechanics, NMR-active nuclei have a magnetic moment *μ*, which is quantized and proportional to the spin *S* with the gyromagnetic ratio *γ* being the constant of proportionality. The magnetic moment along the z-axis is given by **equation 3.12**.

$$\mu_z = \gamma S_z = \gamma \left(\frac{h}{2\pi}\right) m \quad (3.12)$$

In an external magnetic field B_0 with orientation in z direction, NMR-active nuclei acquire discrete and quantized energy levels,

$$E = -\mu_z B_0 = -\gamma \left(\frac{h}{2\pi}\right) m B_0 \quad (3.13),$$

whereas two energy levels with the energy difference *ΔE* can be observed for spin-½, which is also called Zeeman splitting (**Figure 3.4A**).

$$\Delta E = \gamma \left(\frac{h}{2\pi}\right) B_0 \quad (3.14)$$

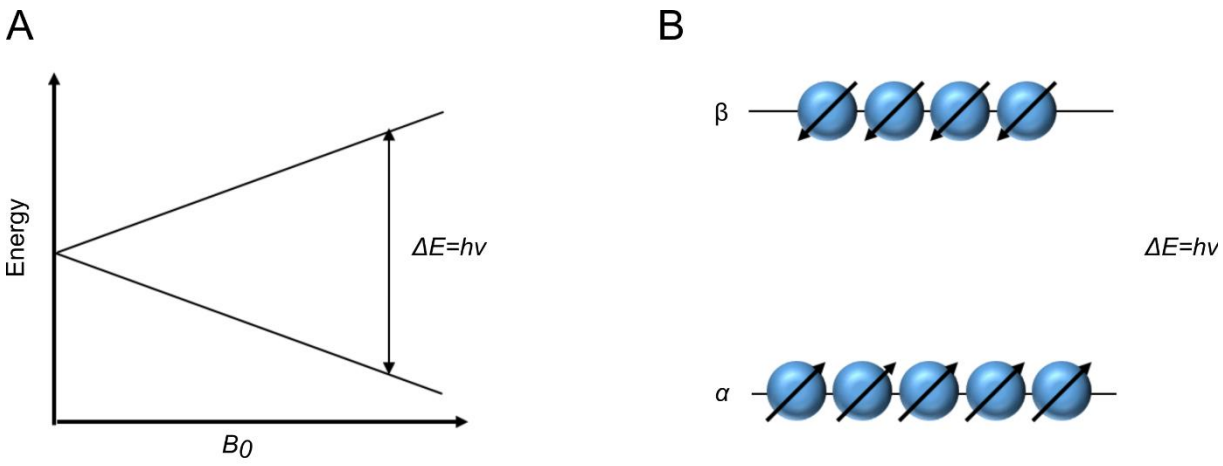

Figure 3.4. Principles of NMR. (A) Zeeman splitting of spin-½ nuclei. **(B)** Schematic thermal Boltzmann equilibrium of spin-½ nuclei facing an external magnetic field.

Transitions between the spin states can be induced by absorption or emission of photons with energies equal to *ΔE*, which is achieved by applying an oscillating magnetic field perpendicular to μ_z with a distinct frequency ν_o also called Larmor frequency.

$$\nu_0 = \left(\frac{\gamma}{2\pi}\right) B_0 = \frac{\omega_0}{2\pi} \quad (3.15),$$

In a macroscopic sample, more than one spin is prevalent and spins distribute randomly (different phases) on the surface of two cones thereby precessing about z-axis and at a defined angle *Φ*. However, there is a small difference in the population of the spins of lower and higher energy, i.e. of spins that are aligned parallel (α-state) and antiparallel (β-state) to the external magnetic field. The distribution follows the Boltzmann equation

$$\frac{n_\alpha}{n_\beta} = e^{\frac{\Delta E}{kT}} = e^{\frac{h\nu_0}{kT}} \quad (3.16),$$

with n_α and n_β respectively being the number of spins in the α-state and the β-state, *k* being the Boltzman constant and *T* the temperature.
The NMR signal is proportional to this population difference, which is fairly small at physiological temperatures (*T* = 37 °C) and clinical magnetic field strength (B_0 = 3 T). For one million atoms, (n_α-n_β) is only 10 spins, which equals 0.001%. This makes NMR a rather insensitive spectroscopic technique compared to others with higher energy differences.

The net observable macroscopic magnetization (M_0) is finally the sum of the individual magnetic moments, which cancel out in the xy plane, but have a small excess in the z-plane.

$$M_0 = n_\alpha {\mu_z}^\alpha + n_\beta {\mu_z}^\beta = \gamma \left(\frac{h}{4\pi}\right)\left(n_\alpha - n_\beta\right) \quad (3.17)$$

Finally, the Taylor series approximation with n being the sum of n_α and n_β

$$n_\alpha - n_\beta \approx \left(\frac{nh\nu_0}{2kT}\right) \quad (3.18)$$

gives

$$M_0 = \left(\frac{\gamma h}{2\pi}\right)^2 \left(\frac{nB_0}{4kT}\right) \quad (3.19).$$

From **equation 3.19**, it is readily understood why NMR scientists seek to use high γ-nuclei (^{1}H) and high magnetic field strength.

In order to generate an NMR signal, an oscillating magnetic field B_1 (or radiofrequency pulse in the MHz range) at the Larmor frequency must be applied perpendicular to B_0. Depending on the length and amplitude of the pulse, the magnetization vector is tipped into the transverse plane (M_{xy}) and precesses around B_0 resulting in a spiral motion on the surface of a sphere. Furthermore, the spins distribute equally parallel and antiparallel to B_0 and acquire the same phase, called phase coherence.

The rotation of the transverse magnetization at the Larmor frequency finally induces an electromotive force (emf) that is recorded and amplified by the receiver coil. However, once the radiofrequency (RF) pulse is turned off, spins return to their initial state, which is called relaxation. This process can be described with Bloch equations, which consider the time dependent change of the macroscopic magnetizations in x,y and z direction. The underlying models are exponential decay curves with characteristic decay times:

$$\frac{dM_z(t)}{dt} = -\frac{M_z(t) - M_0}{T_1} \quad (3.20),$$

$$\frac{dM_x(t)}{dt} = -\frac{M_X(t)}{T_2} \quad (3.21),$$

$$\frac{dM_y(t)}{dt} = -\frac{M_y(t)}{T_2} \quad (3.22),$$

with dM_z(t)/dt, dM_x(t)/dt and dM_y(t)/dt being the derivatives of the magnetizations in z, x and y direction to time t. dM_z(t) dM_x(t) and dM_y(t) are the magnetizations at time t, and T_1 and T_2 are the spin-lattice and spin-spin relaxation times, respectively.

Equation 3.20 describes the spin-lattice relaxation time T_1. Thermal motion causes interactions of molecules accompanied by energy transfer of nuclei to their environment or lattice. The T_1 relaxation is most effective if molecular motions or interactions occur at the Larmor frequency.

Equations 3.21 and **3.22** describe the magnetization decay due to the so-called spin-spin relaxation T_2. It can be considered as phase coherence loss of the individual spins that experience slightly different magnetic fields and therefore precess at different Larmor frequencies. This results in a different phase evolution in the transverse plane over time. In addition to local field fluctuations, the inhomogeneities of the static magnetic field can further accelerate dephasing. Therefore, T_2^* is observed in an NMR experiment, which is the sum of the inverse "intrinsic T_2 relaxation and … macroscopic and microscopic magnetic field"[103] fluctuations (T_{2i}).

$$\frac{1}{T_2^*} = \frac{1}{T_2} + \frac{1}{T_{2i}} \quad (3.23)$$

Taking relaxation into account, the detectable NMR signal in the xy plane can be described by the following equation after RF excitation was shut off.

$$M_{xy}(t) = M_{xy}(0)e^{-\frac{t}{T_2^*}} \quad (3.24)$$

Bearing in mind that the net magnetization is still rotating while relaxing, **equation 3.24** can be expressed as two damped periodic functions (sine and cosine), which define the so called free induction decay (FID)

$$M_x(t) = M_0\, cos((\omega_0 - \omega)\, t + \Phi))e^{-\frac{t}{T_2^*}} \quad (3.25),$$

$$M_y(t) = M_0\, sin((\omega_0 - \omega)\, t + \Phi))e^{-\frac{t}{T_2^*}} \quad (3.26),$$

with Φ being the phase at t = 0. M_x and M_y respectively are defined as real and imaginary FID, ω_0-ω is the reduced precessional frequency if the B_1-field is chosen to be the reference frequency of the so-called rotating frame.

The FID is a time dimension signal and in theory contains all information about the spin ensembles contributing to the observable magnetization. However, if two or more damped periodic curves overlap, it is hard to extract all required information, which is why the FID is finally Fourier transformed. This mathematical operation decodes a frequency domain signal $F(\omega)$ for each decay curve. The graphical expression of $F(\omega)$ is a Lorentzian line shape with a defined frequency on the x-axis and the intensity that is proportional to the initial magnetization M_z on the y-axis.

$$F(\omega) = \int_{-\infty}^{+\infty} f(t) e^{-i\omega t} dt \quad (3.27)$$

At last, the chemical shift δ is defined as the frequency of the Lorentzian peak of a defined signal referenced to the frequency of a reference substance ($\omega_{ref.}$, usually tetramethylsilane for ^{1}H and ^{13}C-NMR). Further it is usually given in parts per million (ppm), which is given as follows:

$$\delta = \frac{\omega - \omega_{ref.}}{\omega_{ref.}} \quad (3.28)$$

The Larmor frequency of an NMR-active nucleus is not only determined by the gyromagnetic ratio and the external magnetic field, but also by slight differences in the molecular environment even within a molecule. This is especially interesting, because the chemical shift can be used to identify different metabolites with NMR.

3.2.2 Spatially-Resolved NMR

The essential ingredient of MRI are linear field gradients (G) that can be applied along the x, y and z axis. To achieve spatial resolution, MRI makes use of the resonance condition ($\omega_0 = \gamma B_0$). However, instead of exploiting spectral resolution as shown for NMR, a linear gradient varies the amplitude of the static magnetic field yielding position (r) dependent Larmor frequencies.

$$\omega(r) = \gamma B(r) + \gamma r G \quad (3.29)$$

Furthermore, this facilitates to selectively excite a slice (e.g. z) perpendicular to the gradient (**Figure 3.5A**). The spatial information of the other two dimensions (e.g. x and y) is normally obtained by frequency and phase encoding for instance by a spin echo sequence given in **Figure 3.5B**. The slice is selected with a narrow-band 90° RF pulse (z-direction) and magnetization starts decaying with T_2^* after the RF has been shut off

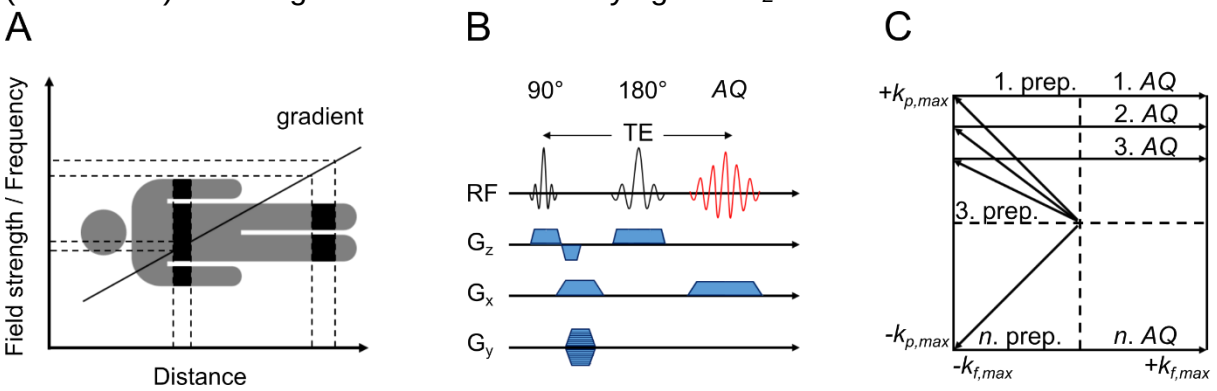

Figure 3.5. Principles of spatially encoded nuclear magnetic resonance. (A) Slice selection is performed by narrow band excitation in presence of gradients. **(B)** Typical MRI acquisition scheme

based on spin echoes. **(C)** *k*-space sampling of the spin echo sequence. Abbreviations: *AQ*: acquisition; *TE*: echo time; RF: radiofrequency; prep.: preparation. The image was designed according to reference [103]. (Copyright information: The human shape is license free and part of the public domain).

(t = 0 s). After phase evolution for ½ *TE* (echo time), a 180° (in x-direction) pulse is applied, which rotates the spins about the x-axis. This allows the spins to refocus to their initial position (t = 0 s) after further ½ *TE*. The spin echo train is a typical operation in NMR and MRI to cancel out B_0-inhomogeneities.

After one *TE*, the spins are phase coherent and an echo with a position dependent frequency can be recorded giving the first transversal dimension (e.g. x-direction). The second transversal dimension is obtained by a number of experiments of variable gradient strengths from $+G_{phase}(max)$ to $-G_{phase}(max)$. For each defined gradient strength, the spins will acquire a position-dependent phase (e.g. y-direction).

In order to finally obtain an image from frequency and phase information, it is necessary to introduce the *k*-space formalism. The observable signal of a transverse slice in presence of time-dependent field gradients ($G(t)$) can be described by the following equation (ignoring T_2*-relaxation).

$$s(t) = \iiint \rho(r,\omega) e^{+i(\omega+\gamma G r)t} d^2 r d\omega \quad (3.30),$$

with $\rho(r,\omega)$ being the spin density and with $\omega = 2\pi\nu$ the reciprocal space vector being

$$k(t) = \frac{\gamma}{2\pi} \int_0^t G(t')dt' \quad (3.31)$$

equation 3.30 simplifies to the **equation 3.32**.

$$s(k,t) = \iiint \rho(r,\nu) e^{i2\pi(\nu t + kr)} d^2 r d\nu \quad (3.32)$$

Thus, the spectral density $\rho(r,\nu)$ and the signal $s(k,t)$ represent a Fourier transform pair. **Figure 3.5C** shows the acquisition of spatial frequencies by the spin echo sequence in **Figure 3.5B**. After excitation k_f and k_p are zero. In the first experiment $G_y(max)$ is applied moving k_p to $+k_{p,max}$. The dephasing gradient in the frequency encoding direction (G_x) yields $-k_{f,max}$. At this point, the frequencies are prepared in *k*-space. The re-phasing grading during acquisition linearly increases k_{freq} and fills the first line of *k*-space with data points. Successive decrease of G_y, while repeating this procedure will create the full *k*-space image. Finally, the obtained signal $s(k,t)$ which can be converted to the desired spectral density $\rho(r,\nu)$ (the actual image) by Fourier transformation as given in **equation 3.33**.

$$p(r,\nu) = \iiint s(k,t) e^{-i2\pi(\nu t + kr)} d^2 k dt \quad (3.33)$$

3.2.3 Image Contrast

Bulk water faces different environments in the human body, which can be exploited to create image contrast. However, even though water is highly abundant *in vivo*, proton MRI is fairly insensitive and requires multiple acquisitions. The time between two acquisitions is the repetition time (*TR*), and the usage of variable *TR* and *TE* can be used to weigh images by T_1, T_2 or the proton density.

Once excited, it takes about five T_1 for the z magnetization to be recovered. If *TR* is chosen rather short ($TR < 5T_1$ and short *TE*), T_1-weighted images are obtained, because the magnetization of spins with a long T_1 might not be recovered compared to those with short T_1.

The transversal magnetization (or the FID) decays with T_2^*, which is generally shorter than T_1. No big differences between signals of variable T_2 are observable after a short echo time. However, if spins are allowed to relax during a long *TE* (and long *TR*), some spins might already be relaxed, while others are not. This operation yields T_2-weighted images, which are frequently acquired in the clinic to localize and delineate tumors. Finally, proton density-weighted images exploit both, a long TR and a short TE to use as much magnetization as possible to generate an image.[106]

3.2.4 DWI

The cell density of healthy and malignant tissues can be studied with diffusion-weighted imaging, because it measures the mobility of water which is generally restricted by membranes *in vivo*. A quantifiable parameter is the so-called apparent diffusion coefficient (*ADC*), which is small for cancerous tissues with a high cell density compared to healthy tissues.[107] DWI is therefore not only useful for tumor diagnosis and staging, but also to follow changing cellularity with tumor growth and measure the response to treatment, because the *ADC* changes with tumor grade or when membranes are disrupted after therapy.[108, 109]

Most DWI acquisition schemes are based on the spin echo sequence that uses pulsed gradients combined with an echo planar imaging readout (SE-EPI, **Figure 3.6A**).

In general, every gradient (G_D) induces a phase shift of precessing spins that can be reversed by refocusing pulses. Particles that are not moving during that procedure, will appear with a net phase shift of zero while those which undergo diffusion driven motion will have acquired a net phase shift. This leads to a loss of phase coherence and attenuation of the observed signal within a voxel thus creating diffusion-weighted contrast.

In vivo, the motion of spins is generally restricted and their net displacement per time is therefore smaller than for freely diffusing spins. Overall, a higher degree of restriction caused by increasing cellularity will thus yield a smaller quantifiable apparent diffusion

coefficient. Quantification of the *ADC* can be performed with the Stejskal-Tanner sequence.[110] It records several images with variable degrees of diffusion-weighting by increasing the time *Δ* between the phase inducing and refocusing pulse. In that case, *Δ* is also termed *b*-value or diffusion-weighting factor. Plotting the signal intensity of a voxel or a region-of-interest against the *b*-value yields an exponentially decaying curve that can be fitted with the Skejskal-Tanner equation

$$S = S_0 \cdot e^{(-b \cdot ADC)} \quad (3.34),$$

with *S* being the signal intensity for a given *b*-value and S_0 the signal intensity without diffusion-weighting.

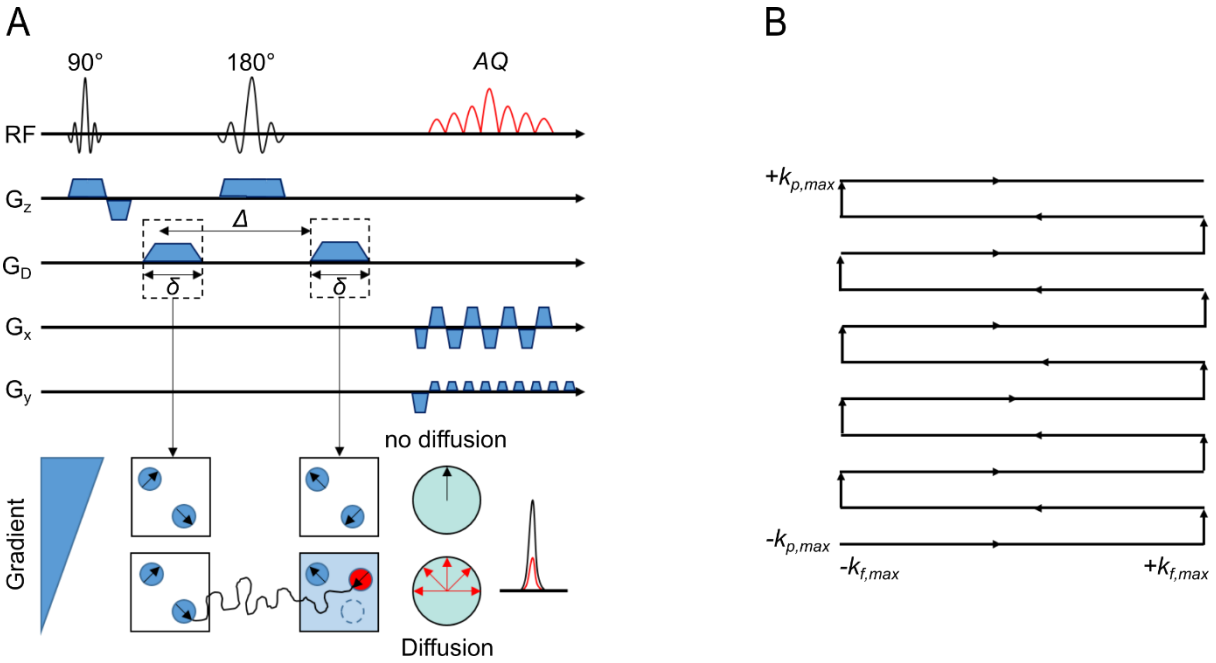

Figure 3.6. Spin-echo echo planar imaging sequence (SE-EPI) and EPI *k*-space readout. (A) Diffusion-weighted imaging based on the spin echo sequence is achieved by the use of diffusion gradients (G_D) of defined strength, length *δ* and temporal distance *Δ* (upper image). The first diffusion gradient creates a distinct phase (lower image), which defines the initial position of the spins. The second pulse refocuses the initial phase. However, in case of diffusion to a different position along the gradient field (gradient) during *Δ*, refocusing is imperfect, which causes a macroscopic dephasing and a decrease in the signal intensity. **(B)** Echo planar imaging is a fast imaging technique that samples the *k*-space in a "zig-zag" shape. The first negative G_x phase in A) moves the *k*-space to $-k_{f,max}/-k_{p,max}$. The following alternation of the G_x gradients will sweep the *k*-space from $-k_{f,max}$ to $+k_{f,max}$. The y-direction of *k*-space is sampled by the small G_y blips, which progressively increase k_p. **Figure 3.6A** was created according to reference [111].

3.2.5 Dissolution DNP and Hyperpolarized MRSI

The sensitivity of NMR is rather low as it is governed by the Boltzmann equilibrium (**equation 3.19**) that can also be expressed by the thermal polarization level ($P_{thermal}$).

$P_{thermal}$ is defined by the population difference of spins aligned parallel and antiparallel to the external magnetic field B_0 divided by the sum of all spins.

$$P_{thermal} = \frac{n_\alpha - n_\beta}{n_\alpha + n_\beta} = \tanh\left(\frac{\hbar\gamma B_0}{2kT}\right) \quad (3.35)$$

At clinical field strength (3 T) and physiological temperature, the surplus of spins in the n_α state is rather small and the thermal polarization for prominent spin-½ nuclei like ^{1}H, ^{13}C and ^{15}N is just 0.001%, 0.0002% and 0.0001%, respectively (**Figure 3.7**).

To overcome these sensitivity limitations, basically four different hyperpolarization methods have been developed in the past: 1. brute force, 2. spin exchange optical pumping (SEOP), 3. parahydrogen induced polarization (PHIP) and 4. dissolution dynamic nuclear polarization (DNP).

The brute force method exposes a nucleus of interest to a high magnetic field and low temperatures. This yields hyperpolarization, which can be maintained and measured if the sample is rapidly brought to physiological temperature.[112] “Spin exchange optical pumping (SEOP) is a frequently used method to enhance the signal of noble gases (e.g. ^{129}Xe). In short, circularly polarized laser light is used to selectively excite a D1 transition of an alkali metal vapor (e.g. rubidium).…Spin exchange through collisions of the noble gas atoms with the polarized alkali metal atoms [finally] transfers the electron-polarization to the… gas nuclei.”[113]

PHIP exploits the so called scalar state of parahydrogen that can be converted to polarization in NMR-active nuclei.[114] The transfer process occurs either by chemical addition of parahydrogen to unsaturated precursor molecules[115, 116] or by reversible exchange.[117-119] Both approaches require a catalyst that binds the substrate and parahydrogen.

Today, the most effective hyperpolarization method for spin-½ nuclei (except noble gases) remains DNP. It exploits the fact that electron polarization approximates 100% at very low temperatures below 1 K and high external magnetic field strength above 3 T. For an efficient hyperpolarization, a mixture of a probe that exhibits spin-½ nuclei and a free stable radical such as tempol or trityl are prepared at a ratio of about 100/1 to 1000/1. The mixture needs to form a so-called glass at low temperatures which requires the solubility of the probe (and the radical) in common glassing agents. These are dimethylacetamide, dimethylsulfoxide, glycerol, or mixtures of them with water or D_2O.[120] Pure water is a bad glassing agent, because it forms crystals in the frozen state, which scatter the microwave photons that trigger the polarization transfer from the electrons to the nuclei (**Figure 3.7A**). Polarization takes about 30 minutes to two hours.

Once the polarization has reached saturation, the frozen solution is rapidly dissolved by a pressurized and heated buffered liquid. The final solution contains the hyperpolarized probe at a concentration of about 50 mM to 100 mM and physiological

pH. Recently, DNP polarizers for sterile use intent operating at good manufacturing practice (GMP) have been commercialized for clinical applications. These filter out the radical during the dissolution process.[37]

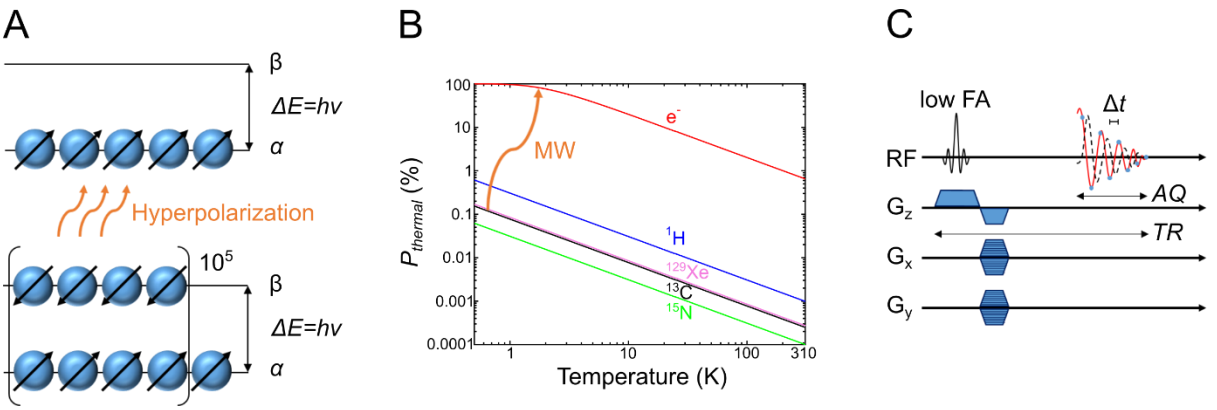

Figure 3.7. Basic principle of hyperpolarization and chemical shift imaging sequence (CSI). (A) The population difference of spin-½ nuclei in an external magnetic field (see also **Figure 3.4B**) is rather low. Hyperpolarization changes the thermal equilibrium, which yields a higher population of the α-state. **(B)** The thermal polarization level of protons, ^{13}C, ^{15}N and ^{129}Xe at B_0 = 3 T is relatively low for a temperature range from 0.5 K to 310 K. In contrast, the electron polarization approximates 100% at low temperatures below 1 K. Dissolution dynamic nuclear polarization exploits the high electron polarization and transfers it to spin-½ nuclei by continuous microwave (MW) irradiation at low temperatures. Commercially available pre-clinical (Hypersense, Oxford Instruments, Abingdom, United Kingdom) and clinical polarizers (SPINlab, GE Healthcare, Boston, MA, USA) operate at an external magnetic field of 3.35 T and 5 T, respectively. **(C)** Chemical shift imaging (CSI) uses two phase gradients (G_x and G_y) to encode the position of spins in x- and y-direction after a slice selection (G_z). For hyperpolarized signal acquisition, only a small portion of the magnetization is excited with a radiofrequency pulse (RF) with a rather low flip angle (*FA* = 5° - 20°). A flip angle of 90° would use all hyperpolarized magnetization for one single acquisition point in *k*-space, which would not yield an image. The repetition time (*TR*) is the time from excitation until the end of the acquisition of the FID. The time required for recording the FID is the acquisition time AQ. 1/Δ*t* is the sampling rate and should be at least two times the desired spectral width to accurately recover the NMR signals (Nyquist theorem).

With DNP, signal enhancements of four to five orders of magnitude are possible,[121] which allow metabolic imaging with spatial and temporal resolution and without radiation exposure. The hyperpolarized polarization level (P_{hyper}) is thereby defined as

$$P_{hyper} = \frac{S_{hyper}}{S_{thermal}} P_{thermal} = \varepsilon \cdot P_{thermal} \quad (3.36),$$

with S_{hyper} being the hyperpolarized signal, $S_{thermal}$ the observed thermal signal at a defined field strength and temperature and ε being the signal enhancement.
Common hyperpolarized probes are generally enriched with the stable isotope ^{13}C, because it has a fairly high gyromagnetic ratio and is NMR-active compared to carbon-12. Furthermore, carbon is a basic building block of metabolites and thus highly

abundant *in vivo*. However, the main pitfall of hyperpolarized imaging is the fact that the signal decays with T_1 in the liquid state, which is in the order of a few tens of seconds. This limits the time available for an experiment, i.e. the dissolution process, the transfer to the MRI system, the injection into an organism and signal acquisition after distribution in the body. As a rule of thumb, an experiment should therefore be performed within three times T_1.

As T_1 is most critical for the hyperpolarized signal, several strategies have been proposed for prolongation.[120] On the one hand, the usage of probes with carbonyl or tertiary ^{13}C nuclei is beneficial, because T_1 loss is mainly governed by dipolar couplings of carbon nuclei with directly attached protons that have a high γ. Another strategy to prolong T_1 of a hyperpolarized probe is the replacement of stably attached protons with deuterons, which have similar biochemical properties, but a 6.5 fold smaller gyromagnetic ratio. **Chapter 6** demonstrates that deuterium enrichment of ^{13}C-labelled zymonic acid prolongs the T_1 and thus enables sensitivity enhanced pH imaging *in vitro* and *in vivo*.[122] Further strategies are reviewed in **Chapter 5**.[113]

Acquisition of hyperpolarized probes with spatial and temporal resolution should be rather fast. Furthermore, spectral information should be encoded in the images, because hyperpolarized probes are generally metabolized to other molecules that exhibit a different chemical shift (**chapter 4**)[44] In addition, several pH sensors such as zymonic acid (**chapter 6**)[78, 122] or amino acid derivatives (**chapter 7**)[123] exhibit a pH dependent chemical shift.[113] Chemical shift imaging (CSI) is the most straightforward and robust way to acquire the signal of hyperpolarized probes. The acquisition scheme for CSI is given in **Figure 3.7C**. After slice selective excitation along the z-direction, each point in *k*-space is selected by phase encoding gradients in x and y direction where the FID is recorded for each voxel. Even though the sequence is robust and delivers spectral, spatial and temporal information, the sampling rate is rather low and it requires one excitation with a defined flip angle for each point in *k*-space. This consumes quite a large amount of hyperpolarization making CSI a fairly ineffective sequence. Therefore, a number of new approaches and acquisition schemes such as undersampled *k*-space acquisition, IDEAL spiral CSI[124] spectral-spatial echo planar imaging (EPI)[125], echo planar spectroscopic imaging (EPSI)[126] or multi-echo balanced steady state free precession (me-bSSFP)[127] have been proposed recently. However, discussion of these are beyond the scope of this thesis.

The gold-standard probe for hyperpolarized imaging is [1-^{13}C]pyruvate, because it polarizes to high levels, has a fairly long T_1 and is the nexus of the metabolic network downstream of glycolysis. As discussed in **chapter 2**, many tumors follow the Warburg effect and reduce glucose to lactate even under normoxic conditions. Numerous studies have shown that imaging of hyperpolarized pyruvate is beneficial for tumor diagnosis, staging, re-staging, response to treatment monitoring and outcome

prediction. Therefore, pyruvate holds promise to be translated into the clinic, which is revealed by the fact that *in vivo* studies in humans are already conducted.[128]
Once injected, [1-^{13}C]pyruvate is readily internalized by most tumors and converted to [1-^{13}C]lactate catalysed by lactate dehydrogenase A. For both, pyruvate and lactate, a single ^{13}C-resonance can be measured, which can be used to quantify the kinetic rate constant k_{pl} of LDH. In some cases, even the decarboxylation product bicarbonate or the transamination product alanine can be observed *in vivo*. Another resonance that will always accompany the signal of hyperpolarized pyruvate is pyruvate hydrate, which forms in aqueous solution dependent on the pH. Several approaches for the quantification of k_{pl} have been proposed. However, the most robust starts with the acquisition of a whole time course of pyruvate-to-lactate exchange. It is governed, by the delivery of pyruvate into the tumor and conversion of lactate. This yields a rising signal of pyruvate, which is followed by a slightly delayed rise of the lactate signal. Both curves soon have a turning point and then follow an exponential decay according to T_1 (see **chapter 4**). Mathematically, the temporal evolution of pyruvate and lactate can be described with the following two-site-exchange models.

$$\frac{dM_{lac}(t)}{dt} = +k_{pl} \cdot M_{pyr}(t) - k_{lp} \cdot M_{lac}(t) - \rho_{lac}(M_{lac}(t) - \lim_{t\to\infty} M_{lac}(t)) \qquad (3.37),$$

$$\frac{dM_{pyr}(t)}{dt} = -k_{pl} \cdot M_{pyr}(t) + k_{lp} \cdot M_{lac(t)} - \rho_{pyr}(M_{pyr}(t) - \lim_{t\to\infty} M_{pyr}(t)) \qquad (3.38),$$

where "M_{lac} and M_{pyr} are the lactate and pyruvate z-magnetizations, k_{pl} and k_{lp} are the apparent rate constants for the pyruvate-to-lactate exchange and the reverse reaction. ρ_{pyr} and ρ_{lac} are the effective decay rates of the pyruvate and the lactate signal including T_1-relaxation and radiofrequency (RF) excitation. If the thermal signals at the limits at infinite time are neglected, the contributions from backward conversions, RF excitation and T_1 relaxation can be merged into effective relaxation rates $T_{1pyr,eff.}$ and $T_{1lac,eff.}$."[44]
According to Day et al., pyruvate and lactate data can be fitted to piecewise exponential equations yielding k_{pl}.[77] Finally, a rather simple approach was proposed by Hill et al.[129] It simply calculates the ratio of the sum of the lactate signals over time divided by the sum of the pyruvate signals over time yielding the *AUC* ratio value, which is proportional to k_{pl}.
A more detailed explanation of imaging of hyperpolarized pyruvate and signal quantification is given in the following **chapter 4**. The theory of pH *in vivo* imaging will not be discussed here, because the method is comprehensively reviewed in **chapter 5** and explained again in **chapter 6** and **chapter 7**.

4. Simultaneous Characterization of Tumor Cellularity and the Warburg Effect with PET, MRI and Hyperpolarized ^{13}C-MRSI

Christian Hundshammer, Miriam Braeuer, Christoph A. Müller, Adam E. Hansen, Mathias Schillmaier, Stephan Düwel, Benedikt Feuerecker, Steffen J. Glaser, Axel Haase, Wilko Weichert, Katja Steiger, Jorge Cabello, Franz Schilling, Jan-Bernd Hövener, Andreas Kjær, Stephan G. Nekolla and Markus Schwaiger

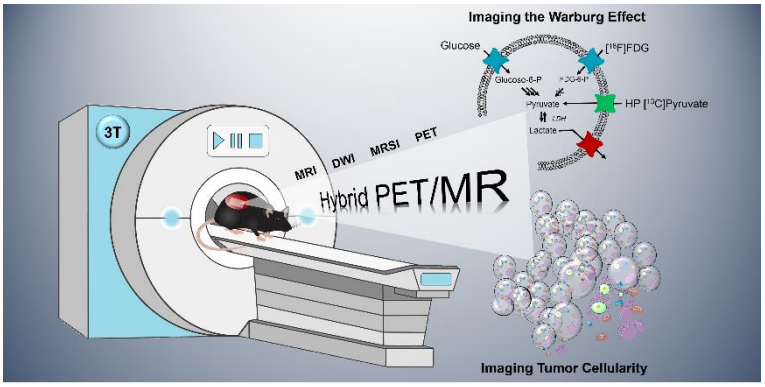

Summary

Modern oncology aims at patient-specific therapy approaches, which triggered the development of biomedical imaging techniques to synergistically address tumor biology at the cellular and molecular level. PET/MR is a new hybrid modality that allows acquisition of high-resolution anatomic images and quantification of functional and metabolic information at the same time. Key steps of the Warburg effect - one of the hallmarks of tumors - can be measured non-invasively with this emerging technique. The aim of this study was to quantify and compare simultaneously imaged augmented glucose uptake and LDH activity in a subcutaneous breast cancer model in rats (MAT-B-III) and to study the effect of varying tumor cellularity on image-derived metabolic information.

Methods: For this purpose, we established and validated a multimodal imaging workflow for a clinical PET/MR system including proton magnetic resonance (MR) imaging to acquire accurate morphologic information and diffusion-weighted imaging (DWI) to address tumor cellularity. Metabolic data were measured with dynamic ^{18}F-FDG-PET and hyperpolarized (HP) ^{13}C-pyruvate MR spectroscopic imaging (MRSI). We applied our workflow in a longitudinal study and analyzed the effect of growth dependent variations of cellular density on glycolytic parameters.

Results: Tumors of similar cellularity with similar apparent diffusion coefficients (*ADC*) showed a significant positive correlation of FDG uptake and pyruvate-to-lactate exchange. Longitudinal DWI data indicated a decreasing tumor cellularity with tumor growth, while *ADC*s exhibited a significant inverse correlation with PET standard uptake values (*SUV*). Similar but not significant trends were observed with HP ^{13}C-MRSI, but we found that partial volume effects and point spread function artifacts are major confounders for the quantification of ^{13}C-data when the spatial resolution is limited and major blood vessels are close to the tumor. Nevertheless, analysis of longitudinal data with varying tumor cellularity further detected a positive correlation between quantitative PET and ^{13}C-data.

Conclusions: Our workflow allows the quantification of simultaneously acquired PET, MRSI and DWI data in rodents on a clinical PET/MR scanner. The correlations and findings suggest that a major portion of consumed glucose is metabolized by aerobic glycolysis in the investigated tumor model. Furthermore, we conclude that variations in cell density affect PET and ^{13}C-data in a similar manner and correlations of longitudinal metabolic data appear to reflect both, biochemical processes and tumor cellularity.

4.1 Introduction

The new paradigm in oncology is to tailor therapies for patient-specific phenotypes, which triggered the invention of powerful hybrid imaging modalities that address tumor biology in greater depth. PET/CT (positron emission tomography/computed tomography) has become commercially available at the beginning of this century and is currently the work-horse in clinical routine for diagnosis, staging, monitoring of response to treatment and outcome prediction of cancer patients. During the last decade, PET/MR has been introduced as a promising new hybrid modality that is potentially superior to PET/CT[25]. This is mainly because MR has an excellent soft-tissue contrast that is not available with CT and delivers accurate high-resolution anatomical images close to CT resolution and without additional radiation exposure. Furthermore, it allows quantitative functional imaging (fMRI), diffusion-weighted imaging (DWI) and metabolic imaging with hyperpolarized ^{13}C-labelled metabolites[46-49].

One of the main hallmarks of tumors that can be addressed non-invasively with metabolic imaging is the Warburg effect.[58, 67] Solid tumors consume abnormally high levels of glucose and catabolize it through inefficient glycolysis, which is an ubiquitous feature of tumors that malignant cells benefit from, e.g., through fast energy production.[130] Pyruvate is the final product of glycolysis and the nexus of the entire metabolic network. Even under normoxic conditions, it is mainly reduced to lactate by fermentation rather than oxidized.[35, 63, 76, 77, 131]

2-deoxy-2-[^{18}]fluoro-D-glucose (FDG) is an established clinical PET tracer that can be used for qualitative and quantitative characterization of tissues with high energy demands.[74, 75] Like glucose, it is taken up from the blood stream by glucose transporters and phosphorylated by hexokinase once it is internalized. FDG is finally trapped and accumulates in the cytosol because it is not amenable to the subsequent glycolytic enzymes.[72] Currently, FDG-PET is an established method for staging in clinical oncology and it is widely used on PET/CT scanners that deliver anatomical localization at the same time.[132] However, it requires complementary approaches to better characterize malignant tissues, because FDG uptake is an indirect measure of the Warburg effect. Furthermore, it cannot discriminate between tumors and tissues that consume high amounts of glucose on a regular basis like in the brain, heart or during inflammatory processes.[35, 133]

Magnetic resonance spectroscopic imaging (MRSI) has classically been used to study biochemical processes non-invasively, although it suffers from a low sensitivity and requires long scan times.[134] The invention of hyperpolarization (HP) techniques has shifted these limits, allowing signal enhancements of ^{13}C-labelled metabolites by more than five orders of magnitude.[121] However, hyperpolarized signals decay with the spin-lattice relaxation time (T_1) which is on the order of a few tens of seconds, limiting

the time available for signal acquisition and requiring fast signal acquisition. Furthermore, supra-physiologic concentrations of ^{13}C-metabolites are administered to achieve analyzable *in vivo* spectra in pre-clinical and clinical[128] studies. In fact, this could potentially bias the quantification of metabolic parameters, but Serrao et al. have recently shown that exchange rates are not significantly altered by high metabolite concentrations in the blood stream.[135]

Hyperpolarized [1-^{13}C]pyruvate (pyruvate) is most often used *in vivo*, because of its key role in glucose metabolism, its fast metabolic conversion to lactate, its high achievable polarization level and a relatively long T_1.[77] Tumors readily internalize and metabolize pyruvate to lactate by lactate dehydrogenase (LDH-A). The expression of LDH-A is upregulated in many tumors, which results in an increased pyruvate-to-lactate conversion[61] that can be quantified with MRSI.[136]

So far, only a few sites worldwide attempted to assess the flux of glucose through the glycolytic pathway either sequentially or simultaneously with FDG-PET and pyruvate imaging (HyperPET[55, 56, 137, 138]). Witney et al. demonstrated a late treatment effect[139] and Menzel et al.[140] showed a qualitative correlation between both imaging modalities. Ravoori et al. recently detected an early treatment response with pyruvate that was not observed with PET/CT.[141] However, these studies indicate that sequential imaging of FDG uptake and pyruvate-to-lactate conversion with different modalities might not be ideal, because the metabolic status of an organism could change drastically during transport of animals, if the delay between the experiments is too long, or if anesthesia is interrupted.

Precise temporal and spatial correlation of complementary PET and MR data can inherently be achieved with PET/MR. However, it is a relatively expensive modality and not a standard technique in pre-clinical and clinical research. Although it has been shown that co-registration of sequentially acquired PET and MR images is feasible, for instance in brain[142], PET/MR is particularly useful for regions of low CT contrast. In addition, the ability to perform diffusion-weighted imaging could benefit data interpretation as variations of the cell density might lead to apparently decreased tracer uptake or conversion, affecting quantification of PET and MRSI data.[107]

In this study, we established and validated a workflow at a clinical whole-body PET/MR for the multiparametric characterization of the glycolytic flux in a pre-clinical MAT-B-III breast cancer model. We analyzed the *in vivo* correlation of FDG uptake with pyruvate-to-lactate conversion and performed a longitudinal study with a group of tumor-bearing rats to study the effect of changing tumor cellularity on metabolic PET and MRSI data.

4.2 Methods

Chemicals

All chemicals were used as purchased without further purification. Cell culture media (RPMI-1640 and Mc Coy's) were obtained from ThermoFisher Scientific (Waltham, MA, USA) and medium supplies (fetal calf serum, penicillin/streptomycin mixture) from Biochrom/Merck (Berlin, Germany). [1-^{13}C]pyruvate, OX063 ((tris(8-carboxy-2,2,6,6-tetra-(hydroxyethyl)-benzo-[1,2-4,5]-bis-(1,3)-dithiole-4-yl)-methyl sodium salt) and gadolinium chelate (Dotarem) for hyperpolarization were respectively obtained from Cambridge Isotope Laboratories (Tewksbury, MA, USA), Oxford Instruments (Abingdon, United Kingdom) and Guerbet Laboratories Ltd. (Villepinte, France). Isoflurane was purchased from CP-Pharma (Burgdorf, Germany). Pentobarbital (Narcoren) was purchased from Merial (Lyon, France). Chemicals for the dynamic nuclear polarization (DNP) dissolution buffer were obtained from Sigma Aldrich (St. Louis, MO, USA). FDG was synthesized on site using a standard technique modified from the synthesis reported by Hamacher et al.[143] and with chemicals purchased from Sigma Aldrich (St. Louis, MO, USA).

Tumor model

Animal experiments were approved by the local governmental committee for animal protection and welfare (Tierschutzbehörde, Regierung von Oberbayern).
Subcutaneous tumors were induced at the right flank of eleven female Fischer344 rats (age = six weeks, average weight = 146 ± 10 g; Charles River, Wilmington, MA, USA) by implantation of 1×10^6 MAT-B-III 13762 breast cancer cells derived from mammary adenocarcinoma (ATCC, Manassas, VI, USA). For this purpose, cells were cultivated in RPMI-1640 medium supplied with 10% fetal calf serum, 1% penicillin and 1% streptomycin and re-suspended in 200 µL Mc Coy's 5A medium for implantation. A tumor growth curve can be found in **Figure S4.1**.

Study population

For quantitative validation of FDG uptake measured in a clinical PET/MR scanner, three animals were imaged eight days after tumor implantation in a small-animal PET/CT scanner (Inveon, Siemens Healthcare, Erlangen, Germany) after two hours of fasting. Approximately ten hours later, the same animals were imaged again after two hours of fasting in a clinical 3 T PET/MR scanner (Biograph mMR, Siemens Healthcare, Erlangen, Germany). Furthermore, eight animals were measured in the clinical PET/MR scanner eight, ten and thirteen days after tumor implantation in a

longitudinal study (fed ad libitum). One hyperpolarized [1-^{13}C]pyruvate measurement was excluded from analysis because of respiratory problems during tracer injection, one PET scan failed (see workflow) and one animal was sacrificed on day ten, because it met a study abortion criterion. In total, ten comparable FDG-PET, HP [1-^{13}C]pyruvate and DWI measurements for day eight, eight for day ten and six for day thirteen were used for analysis and clustered into three groups of similar *ADC* values.

PET/MR workflow

For PET/MR scans, animals under anesthesia (1 - 3% isoflurane) were placed right lateral and head first with the tumor in the middle of the isocenter of the magnet and on top of the center of a flexible ^{1}H/^{13}C dual-tuned transmit-receive surface coil (Rapid Biomedical, Rimpar, Germany). PET scans were started with tail-vein injection of FDG.

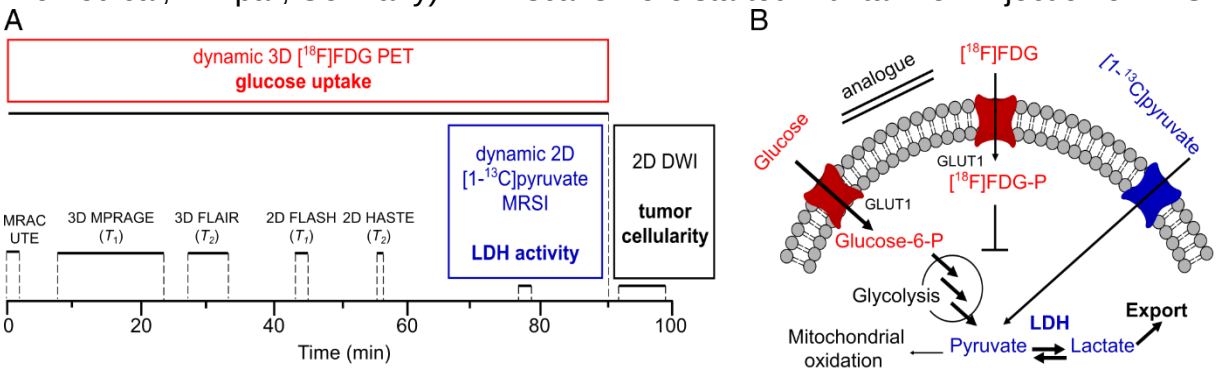

Figure 4.1. Multimodal imaging workflow (A) and addressed metabolic pathways (B). Dynamic 90 min PET acquisition was started with tail-vein injection of ^{18}F-FDG. Simultaneously, magnetic resonance-based attenuation correction ultra-short echo time (MRAC UTE), 3D and 2D T_1- and T_2-weighted proton MRI for determination of tumor localization and slice positioning of ^{13}C and DWI acquisition were performed. Dynamic ^{13}C-MRSI was measured after injection of HP pyruvate at the end of the PET scan (70 - 90 min after FDG injection). DWI was performed after PET acquisition. Metabolic parameters (glucose uptake and LDH activity) and structural parameters (tumor cellularity) that were addressed with PET, MRSI and DWI are given in bold. Acquisition times are indicated with black solid lines. Acquisition parameters for proton MRI can be found in the supplement (**Table S4.1**). Metabolic pathways (B) that were addressed with FDG-PET and ^{13}C-MRSI are colored in red and blue, respectively. Note that arrows with bigger fonts indicate an increased metabolic flux as observable for various tumors.

During PET acquisition (**Figure 4.1A**), a magnetic resonance-based attenuation correction ultra-short echo time (MRAC UTE), a 3D T_1 magnetization-prepared rapid acquisition gradient echo (MPRAGE), a 3D T_2-weighted fluid-attenuated inversion recovery (FLAIR), an axial 2D T_1-weighted (FLASH) and an axial 2D T_2-weighted half Fourier acquisition single shot turbo spin echo (HASTE) sequence were acquired. Metabolic imaging using pyruvate was performed at the end of the PET scan (~70-90 min after PET start) using an axial 2D chemical shift imaging sequence (CSI). For diffusion-weighted imaging, a 2D axial spin-echo, echo-planar imaging (EPI) sequence

was applied. DWI was started after the PET scan was finished, because the sequence attempted to move the slice position in the isocenter of the bed, which interfered with PET acquisition. All 2D sequences were positioned in the same axial center of the tumors. Acquisition parameters of the proton MRI sequences are summarized in the supplement (**Table S4.1**). During PET/MR acquisition, blood oxygenation (Expression MR Patient Monitor, Invivo, Gainesville, FL, USA) and breathing rate (ECG Trigger Unit, Rapid Biomedical, Rimpar, Germany) were continuously monitored. With exception of one animal that stopped breathing (for about 60 s and then resumed breathing) after injection of pyruvate, breathing (50 ± 13 min^{-1}) and blood oxygen saturation (93 ± 6%) did not show any abnormalities during all performed experiments. Blood glucose (c_{Glc}) and blood lactate (c_{lac}) were determined before each measurement (Accutrend Plus, Roche, Basel, Switzerland). The average time of animals under anesthesia was 155 ± 27 min.

Tumor region-of-interest (ROI) definition

Quantification of metabolic and cellular parameters was performed for whole tumor ROIs. Detailed information will be given in the respective image analysis chapters. The threshold for the region grower for PET analysis was chosen to cover the whole tumor in three dimensions including areas of lower FDG uptake. The acquisition slices of ^{13}C-images were oriented in the axial direction with the slices being in the middle of the tumors and having a slice thickness of 13 mm to cover the tumor in the axial direction. ROIs for ^{13}C-analysis were defined for the whole tumor in T_2-weighted images overlaid on ^{13}C-images. For diffusion-weighted imaging, three images (per *b*-value) with a slice thickness of 3 mm and a distance of 2 mm (total volume: 13 mm) between the slices were acquired to cover the same tumor volume as was measured with ^{13}C-CSI. For histology, four slices per tumor were analyzed with a total distance of 7 - 10 mm between the two slice pairs.

PET/CT acquisition and reconstruction

FDG-PET scans in the small-animal PET/CT were started with a tail-vein injection of FDG (11.5 ± 0.6 MBq). Three-dimensional PET data were acquired in list mode for 60 min followed by a CT-acquisition (low dose, 120 projections, 200 ms exposure time, 80 kVp (peak kilovoltage) x-ray voltage, 500 µA anode current at 220° rotation). Images were reconstructed in 12×10 s, 6×30 s, and 11×300 s frames using an ordered-subsets expectation-maximization 3D algorithm with 2 iterations and 16 subsets, followed by 18 maximum-a-posteriori iterations (recommended parameters from manufacturer), without attenuation or scatter correction. The final image matrix was 128×128 pixels, 159 axial slices and a pixel size of 0.77×0.77×0.80 mm^3. The CT images were

reconstructed with a modified Feldkamp algorithm yielding image matrices of 256×256 pixels, 384 axial slices and a pixel size of 0.17×0.17×0.17 mm^3.

PET/MR acquisition and reconstruction

3D FDG-PET data were acquired in list mode for 90 min after tail-vein injection of FDG (10.5 ± 2.1 MBq). Images were reconstructed with the same framing as described for PET/CT, using a fully iterative 3D OSEM (ordered subset expectation maximization) algorithm (3 iterations and 21 subsets as recommended by the manufacturer) with an ultra-short echo time magnetic resonance imaging-based attenuation correction (MRAC UTE). The final PET image matrix contained 344×344 pixels, 127 axial slices, and a voxel size of 1.04×1.04×2.03 mm^3 resulting in a FOV of 359×359×258 mm^3.

PET image analysis

PET analysis was performed in Matlab (The MathWorks, Natick, MA, USA). Tumor ROIs were semi-automatically segmented using a region grower algorithm with the initial seed manually selected. We calculated the standard uptake value (*SUV*) in the tumor ROI by normalizing the mean activity concentration in the ROI by the injected dose and the animal weight. All voxels, in which we measured an FDG activity greater than half of the maximum *SUV* (SUV_{max}) were appended to the ROI by the region grower (SUV_{mean}, with $SUV > 0.5 \times SUV_{max}$). The threshold was chosen in order to cover the whole tumor including areas of lower FDG uptake. All *SUV* were measured on a 5 min frame 47 min post injection.

In addition, we calculated the total volume of voxels with $SUV_{mean} > 0.5 \times SUV_{max}$ which is defined as the tumor metabolic volume (*TMW*). The product of the SUV_{mean} and the *TMW* is the total lesion glycolysis (*TLG*). Both *TMW* and *TLG* are a measure of the metabolic burden [144, 145].

For PET Patlak [96] analysis, image-derived input functions (IDIFs) were segmented semi-automatically with a threshold of $0.7 \times SUV_{max}$ in the inferior vena cava in coronal images obtained from PET/CT and PET/MR. The average ROI size was 21 ± 10 mm^3. Tumor time-activity curves were fitted to a Patlak kinetic model (fit intervals: 10 min to 40 min) yielding the composite rate constant K_i ($K_1 \times k_3/(k_2+k_3)$), with k_1 being the primary tracer uptake rate from blood to free tracer in tissue, k_2 the tissue clearance rate and k_3 the rate of exchange between free and trapped tracer in tissue. The rate of tumor glucose uptake (*MRGlu*) was calculated as $K_i \times (c_{Glc}/LC)$, with *LC* being the lumped constant equaling 0.60[140] For PET/MR longitudinal data, K_i and *MRGlu* values were divided by a correction factor f = 2.7 that was obtained from the comparison of PET/CT and PET/MR data. More detailed information for Patlak analysis can be found in the supplement (**Chapter S4.6.2, Figures S4.2** and **S4.3**).

Hyperpolarization of pyruvate

For the HP process, 14 M [1-^{13}C]pyruvate (36.7 ± 1.9 mg) supplemented with 15 mM OX063 trityl radical and 1 mM Dotarem were polarized with a HyperSense (Oxford Instruments, Abingdon, United Kingdom) for ~30 min at 1.2 K using a microwave frequency of 94.155 GHz and 100 mW power. The sample was dissolved in a solution pressurized to 10 bar and heated to 180 °C containing 4.5 ± 0.3 mL 100 mM phosphate buffered saline (PBS) supplemented with 100 mM sodium hydroxide (NaOH) and 0.1 g/L sodium ethylenediaminetetraacetic acid (EDTA). Finally, the solution for injection contained an average pyruvate concentration of 90.3 ± 3.9 mM at pH 7.6 ± 0.2. The polarization level was about 38% (measured at B_0 = 1 T, Spinsolve Carbon, Magritek, Aachen, Germany).[123] The hyperpolarized solution was rapidly transferred to the clinical PET/MR scanner and injected 21.7 ± 2.1 s after dissolution.

^{13}C-MRSI

The excitation profile of the ^{1}H/^{13}C surface coil was measured as shown in **Figure S4.4**. Prior to the *in vivo* experiments, the ^{13}C-resonance frequency was determined and a calibration of the B_1-field was performed using a 5 mL model solution containing 2.2 M [1-^{13}C]lactate (lactate), 5 mM Dotarem and 0.1% sodium azide. The ^{13}C-transmit frequency was set to the center between lactate and pyruvate. CSI was started at the same time as the injection of 1.0 ± 0.1 mL of hyperpolarized pyruvate and injection took 18.0 ± 5.1 s.

A slice-selective, 2D phase-encoded CSI sequence was applied with the following parameters: 3 kHz spectral bandwidth; 512 acquisition points; 5.9 Hz spectral resolution; 8×8 matrix size; 13 mm slice thickness; 8 cm FOV; 15° flip angle; 200 ms repetition time; 29 excitations; 5.8 s scan time per slice; 20 consecutive measurements/scan; 118 s total acquisition time, 10×10×13 mm^3 nominal voxel size. The *k*-space was sampled in elliptic order from the center on outwards.

For qualitative comparison of PET and ^{13}C-images, a CSI image with a separate animal that was not used for quantitative analysis was measured using a matrix size of 16×16 and nominal resolution of 0.5×0.5×13 mm^3. Number of excitations and scan time were 128 and 28 s respectively. All other acquisition parameters were not changed.

^{13}C-Image analysis

Images were reconstructed as described previously (Matlab, The MathWorks, Natick, MA, USA).[126] The data were zero-filled by a factor of four in both *k*-space space dimensions and by a factor of two in the temporal dimension prior to Fourier

transformation. In the spectrum of each voxel and for each time step, the resonances of lactate and pyruvate were quantified by integration.
The mean of the integrals of the pyruvate and the lactate signals were determined for whole tumor ROIs. The ROIs were defined from axial T_2-weighted images overlaid on the ^{13}C-images. Mean signals were then fitted with a two-site-exchange model as follows:[77]

$$\frac{dM_{lac}(t)}{dt} = +k_{pl} \cdot M_{pyr}(t) - k_{lp} \cdot M_{lac}(t) - \rho_{lac}(M_{lac}(t) - \lim_{t\to\infty} M_{lac}(t)) \quad (4.1),$$

$$\frac{dM_{pyr}(t)}{dt} = -k_{pl} \cdot M_{pyr}(t) + k_{lp} \cdot M_{lac(t)} - \rho_{pyr}(M_{pyr}(t) - \lim_{t\to\infty} M_{pyr}(t)) \quad (4.2).$$

M_{lac} and M_{pyr} are the lactate and pyruvate z magnetizations, k_{pl} and k_{lp} are the apparent rate constants for the pyruvate-to-lactate exchange and the reverse reaction. ρ_{pyr} and ρ_{lac} are the effective decay rates of the pyruvate and the lactate signal including T_1 relaxation and radiofrequency (RF) excitation. If the thermal signals at the limits against infinity are neglected, the contributions from backward conversions, RF excitation and T_1-relaxation can be merged into effective relaxation rates $T_{1pyr,eff.}$ and $T_{1lac,eff.}$. Pyruvate data were fitted piecewise according to **equation 4.3**:

$$M_{pyr}(t) = \begin{cases} \frac{r_{inj.}}{T_{1pyr,eff}}(1 - e^{-T_{1pyr,eff}\cdot(t-t_{arr.})} & t_{arr} \le t \le t_{max,pyr} - 5.9s \\ M_{pyr,max}\, e^{-T_{1pyr,eff}\cdot(t-(t_{max,pyr}+5.9s))} & t \ge t_{max,pyr} + 5.9s \end{cases} \quad (4.3),$$

where $r_{inj.}$ is the rate of injection, $t_{arr.}$ is the time of substrate arrival and $t_{max,pyr}$ is the time at the observed maximum of pyruvate.
We found that fitting of the lactate signal with the following differential equation was more reliable than using the input function parameters obtained by the pyruvate fit. This was mainly due to the fact that the sampling rate of ^{13}C-data was not high enough to accurately determine the actual $t_{max,pyr}$. For discrete values, the simplified differential **equation 4.4** can be expressed as matrix equation for k_{pl} and $T_{1lac,eff.}$

$$\frac{dM_{lac}}{dt} = k_{pl} \cdot M_{pyr} - T_{1lac,eff.} \cdot M_{lac}(t) \quad (4.4)$$

and solved using the Moore-Penrose pseudoinverse.
Furthermore we calculated the kinetic value from the area under the curves (*AUC* ratios) according to the model-free approach of Hill et al.[129] in **equation 4.5**:

$$AUC\ ratios = \frac{\sum_{n=1}^{20} \overline{I(lactate_{tumor})}}{\sum_{n=1}^{20} \overline{I(pyruvate_{tumor})}} \quad (4.5),$$

with $I(lactate)_{tumor}$ and $I(pyruvate)_{tumor}$ being the summed mean lactate and pyruvate nuclear magnetic resonance (NMR) integrals observed in the same tumor ROIs as mentioned above.

Additionally to analysis of tumor ROIs, we analyzed mean pyruvate and lactate integrals measured in the whole axial CSI slice, which is similar to a slice-selective excitation approach yielding $k_{pl,\mathrm{slice}}$ and *AUC* ratios$_{\mathrm{slice}}$. This avoids errors of manual ROI determination but instead includes pyruvate and lactate signals from regions outside of the tumor.

Diffusion-weighted image analysis

We performed experiments with an ice-water phantom[146] to show reproducibility and validation for *ADC* quantification. Detailed information is given in the **Supplement S4.6.2** (**Figure S4.5**). *In vitro* and *in vivo* tumor apparent diffusion coefficients (*ADC*) were calculated from the image intensities (*S*) according to the Stejskal-Tanner **equation 4.6**[147]:

$$S = S_0 e^{(-b \cdot ADC)} \quad (4.6),$$

with S_0 being the image signal intensity without diffusion-weighting and *b* being the diffusion-weighting factor.
Calculations were performed using least squares fitting and calculations resulted in pixelwise *ADC*-maps (MATLAB, MathWorks, Natik, MA, USA). The *ADC* values were obtained at first by averaging the signal intensities in the manually segmented ROI and subsequently calculating the *ADC* value. The workflow was performed for three slices per animal to cover the whole tumor in the axial direction. Finally, a weighted mean of three slice-specific *ADC* values per animal was determined.[108, 109] A representative series of T_2-weighted images, diffusion-weighted images and *ADC* fits are shown in the supplement (**Figure S4.5**).

Histology

Seven animals from terminal experiments were sacrificed with an excess of pentobarbital (n = 1 and n = 6, respectively, ten and thirteen days after tumor implantation). One animal was left out for analysis, because the PET scan failed as described in the workflow chapter. Tumors and adjacent tissue were removed, marked according to their spatial orientation and divided in two halves that were subsequently fixed in 10% neutral-buffered formalin solution for 48 h, dehydrated under standard conditions (Leica ASP300S, Wetzlar, Germany) and embedded in paraffin. Each half was flattened and from each half two 2 um-thin sections, separated by 200 µm and with a distance of 7 - 10 mm to the slices from the other tumor half (distance of the outer slices) were prepared with a rotary microtome (HM355S, ThermoFisher Scientific, Waltham, MA, USA), collected and subjected to histological analysis.

Hematoxylin-Eosin (H.-E.) staining was performed on deparaffinized sections with Eosin and Mayer's Haemalaun according to a standard protocol.
The percentage as well as the pattern of necrosis (i.e., large central necrosis vs. multifocal small areas of necrosis) covering the tumor area were evaluated by two experienced pathologists. Representative H.-E. stained images are given in the supplement (**Figure S4.6**). Percentages of necrosis are given as mean (± standard deviation) values calculated for all slices (**Figure S4.7**).

Measurement of distance between tumor and blood vessel

The distance between the vena cava and the center of mass of the tumors ($d_{t\text{-}v}$) was defined in T_2-weighted images (RadiAnt Dicom Viewer, Medixant, Poznan, Poland).

Statistical analysis

All data are represented as mean values and standard deviations (*std*). Correlations for all quantitative parameters were calculated with a two-sided *t*-test yielding the Pearson product-moment coefficient (*R*) using GraphPad Prism (GraphPad Software, Inc., La Jolla, CA, USA). Longitudinal data were analyzed with an unpaired two-sided *t*-test. Values of < 0.3, 0.3 - 0.5 and 0.5 - 1.0 were considered as weak, moderate and strong correlations, respectively, according to the guidelines of Cohen[148] and as reported earlier.[149] The statistical significance levels are indicated by asterisks, *p < 0.05, **p < 0.01, ***p < 0.001, ****p < 0.0001.

4.3 Results

Validation of FDG uptake measured at a human PET/MR compared to a small-animal PET/CT

Tumor-time activity curves measured with pre-clinical PET/CT and clinical PET/MR are displayed in **Figure 4.2A-B**. The SUV_{max} were 7.4 ± 1.2 and 7.5 ± 0.7 and the SUV_{mean} were 4.9 ± 0.5 and 4.8 ± 0.6 for the PET/CT and PET/MR respectively, showing no significant difference (t = 47 min, **Figure 4.2C**). For kinetic analysis of FDG uptake, image-derived input functions (IDIFs) could reproducibly be measured in the inferior vena cava (see supplement, **Figure S4.2** [150]) rather than in the aorta where the IDIF was not quantifiable.[151] However, the area under the curve values of IDIFs (**Figure S4.3**) were smaller for IDIF measurements at the PET/MR (**Figure 4.2E**) compared to the PET/CT (**Figure 4.2D**). This caused an overestimation of PET/MR K_i values by a factor of f = 2.7 (**Figure 4.2F**).

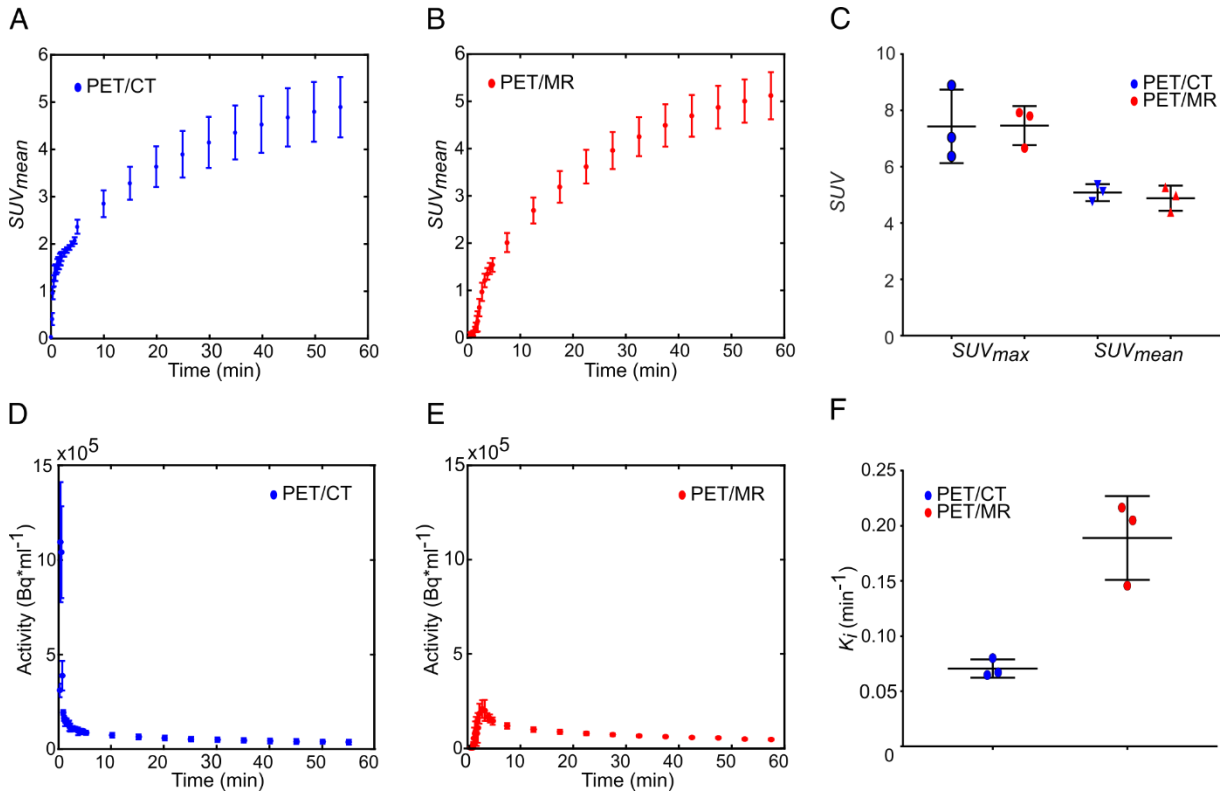

Figure 4.2. Comparison of the FDG uptake and Patlak analysis of subcutaneous MAT-B-III tumors measured with a pre-clinical PET/CT and a clinical PET/MR scanner. FDG uptake curves of subcutaneous tumors obtained from the **(A)** PET/CT (blue) and the **(B)** PET/MR (red). **(C)** The comparison of SUV_{max} and SUV_{mean} does not show a significant difference between the two systems. **(D-E)** are image-derived input functions (IDIFs) used for Patlak analysis measured in the inferior vena cava for PET/CT and the PET/MR images, respectively. **(F)** shows that the K_i values obtained from PET/MR measurements are overestimated by a factor of 2.7 compared to values obtained with the PET/CT. Note that equal thresholds for the region grower algorithm were used to obtain quantitative PET/CT and PET/MR data (tumor: 0.5×SUV_{max}, input function: 0.7×SUV_{max}).

Metabolic mapping of hyperpolarized pyruvate

HP pyruvate was readily observed in the vena cava in the first CSI images (t = 5.9 s) after tail-vein injection. Lactate was observed in the subsequent data sets. The maximum signals of pyruvate and lactate in the tumor were observed at 22 ± 4 s and 27 ± 4 s, respectively, after the start of the acquisition. Representative metabolic images of pyruvate and lactate at time t = 23.6 s from a dynamic time course are displayed in **Figure 4.3A** and **Figure 4.3D**, respectively. The signal of pyruvate was about five-fold higher in the vena cava than in the tumor and about ten-fold higher than the maximum lactate signal. Effective relaxation rates of pyruvate and lactate in tumor ROIs were $T_{1pyr,eff.}$ = 14.6 ± 2.0 s and $T_{1lac,eff.}$ = 9.8 ± 2.5 s (n = 24). Hyperpolarized lactate was mainly visible in tissues around the vena cava and the tumor. *AUC* ratios and k_{pl} indicated a higher LDH activity in the tumors (*AUC* ratios = 0.28 ± 0.06, k_{pl} =

0.029 ± 0.009 s^{-1}) than in tissues surrounding the vena cava (*AUC* ratios = 0.10 ± 0.01, k_{pl} = 0.015 ± 0.004 s^{-1}). The time course of pyruvate and lactate signals of a representative tumor and a non-tumor voxel are shown in **Figure 4.3B** and **Figure 4.3E**. Respective plots of the integrals of the dynamic NMR series are given in **Figure 4.3C** and **Figure 4.3F**. Tumor *AUC* ratios and k_{pl} values showed a strong positive correlation (R = 0.62, p = 0.0012), as reported in the literature.[129]

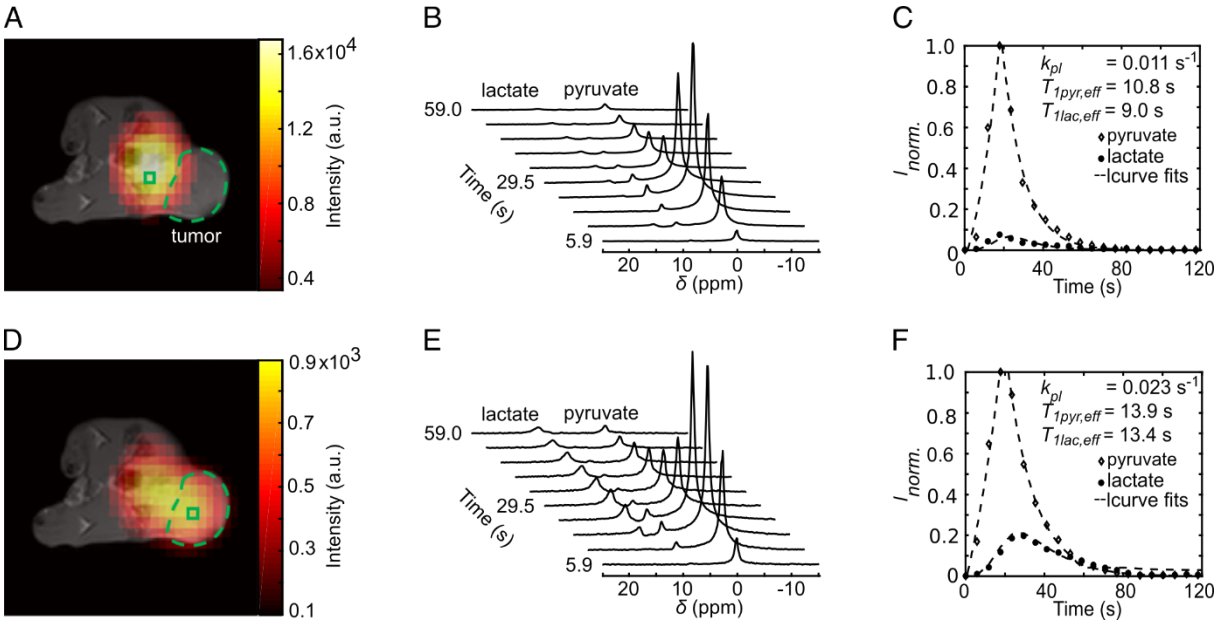

Figure 4.3. Dynamic metabolic mapping of the LDH activity of subcutaneous MAT-B-III tumors using hyperpolarized pyruvate. (A) Static image of hyperpolarized pyruvate at pyruvate maximum in tissues surrounding the vena cava overlaid on an axial T_1-weighted image. A non-tumor voxel is indicated with the green box, the tumor is delineated with the green dashed line. **(B)** Stacked plot of the first ten dynamic ^{13}C-spectra of a non-tumor voxel from (A). **(C)** Dynamic series of pyruvate and lactate NMR signal integrals from (B) and normalized to the maximum integral of pyruvate ($I_{norm.}$). Curve fits are given with dashed lines. **(D)** Static image of hyperpolarized lactate at lactate maximum overlaid on an axial T_1-weighted image. **(E)** Stacked plot of the first ten NMR spectra from a representative tumor voxel (green box in (D)). **(F)** Dynamic series of pyruvate and lactate NMR signal integrals of the tumor ROI and normalized to the maximum integral of pyruvate. Curve fits are given with dashed lines. Note that the pyruvate signal was about a factor of ten higher than that of lactate.

We observed that partial volumes and point spread function[152] artifacts caused by both a high pyruvate blood signal and a low spatial resolution of ^{13}C-images influenced the tumor k_{pl} and *AUC*, especially in cases where the tumor was close to the vessel. A positive correlation between the tumor k_{pl} and *AUC* ratios with the distance of the tumor ($d_{t\text{-}v}$) to the blood vessel illustrates this effect (R = 0.66, p = 0.0004 and R = 0.60, p = 0.0020, respectively, **Figure 4.4A-B**).

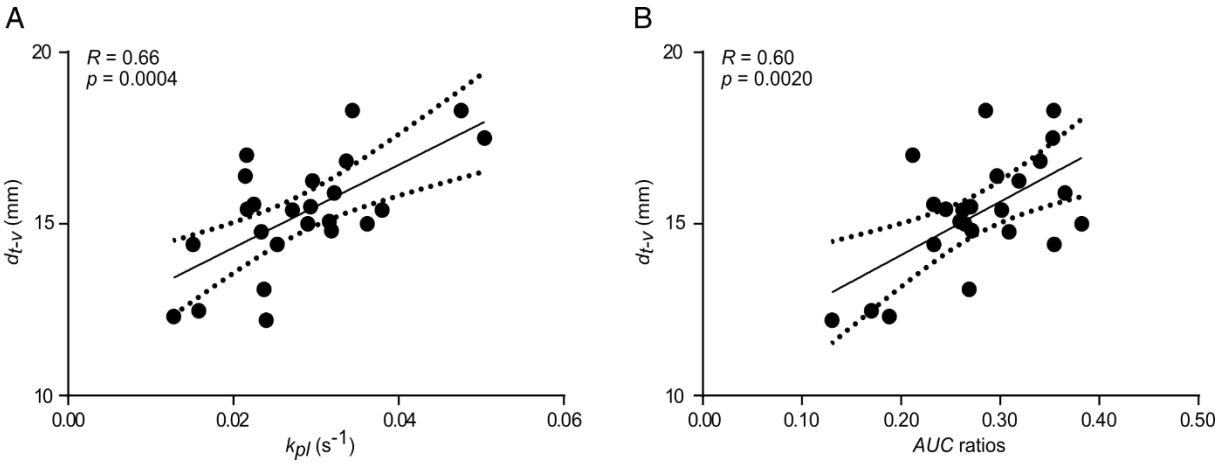

Figure 4.4. Correlation between k_{pl} (A) and *AUC* ratios (B) with distance between the major blood vessel and the center of MAT-B-III tumors ($d_{t\text{-}v}$). Best fit (solid line) and 95% confidence bands (dashed lines).

Qualitative comparison of PET and HP-MRSI

Our PET/MR setup enabled the acquisition of three-dimensional T_1- and T_2-weighted proton images of whole animals (except the head) with a resolution below one cubic millimeter (**Table S4.1**). This allowed an accurate tumor delineation in the axial direction, which facilitated the positioning of 2D proton images that were used for anatomical referencing of MRSI and DWI. Quantification of pyruvate-to-lactate exchange was based on tumor ROI definition on ^{13}C-images overlaid with 2D T_2-weighted proton images. Two- and three-dimensional T_1-weighted proton images were used for visualization of inherently co-registered PET or MRSI data as shown in **Figure 4.5**.

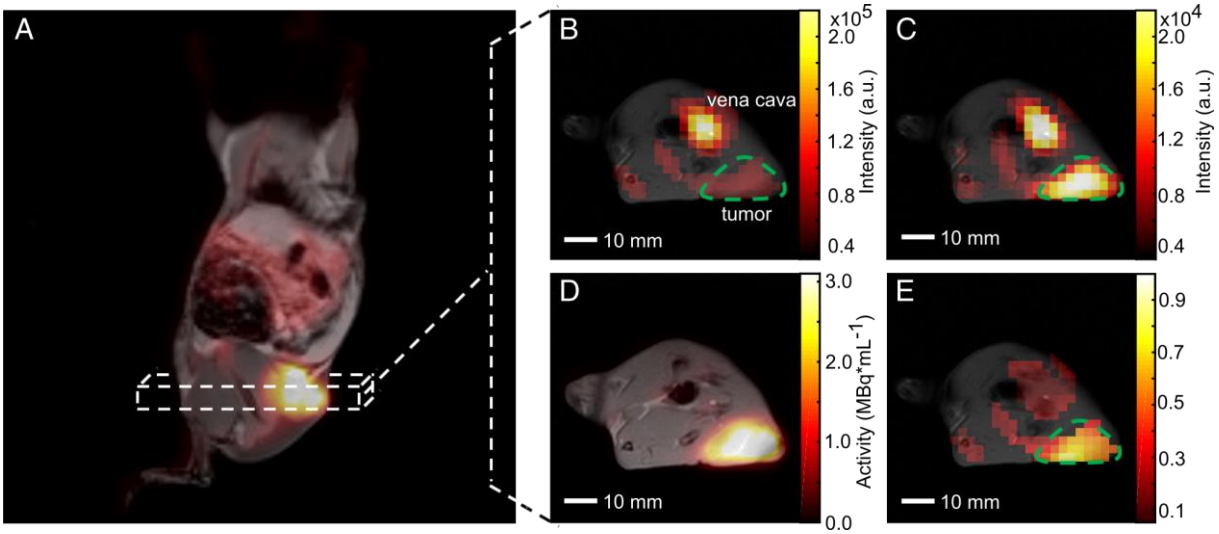

Figure 4.5. Qualitative comparison of simultaneously imaged FDG uptake and pyruvate-to-lactate exchange in MAT-B-III tumor-bearing rats. (A) Coronal slice of a late frame PET image overlaid on the respective slices of an MPRAGE image. Static axial images of pyruvate **(B)**, lactate **(C)** and FDG **(D)** in the same orientation. **(E)** is the ratio of (C) and (B) showing a higher lactate to pyruvate

ratio in the tumor than observed in the surrounding tissue, which correlates well with the high FDG uptake shown in (D). Note that for CSI images, only pixels with a signal > 20% of the maximum signal of hyperpolarized pyruvate and lactate are displayed, respectively. Note further that the pyruvate signal is about a factor of ten higher than the lactate signal and that the nominal resolution of ^{13}C-images was two-fold higher than the resolution used for quantitative analysis.

A coronal (from 3D T_1-weighted images) and an axial static late frame FDG image (t = 55 min) show high FDG uptake in tumors (**Figure 4.5A** and **Figure 4.5D**). Representative static metabolic images of hyperpolarized pyruvate and lactate are displayed in **Figure 4.5B** and **Figure 4.5C** revealing pyruvate uptake and conversion to lactate in the same region as given in **Figure 4.5D**. **Figure 4.5E** displays the ratio of lactate-to-pyruvate and indicates a high pyruvate-to-lactate exchange in the tumor region, which qualitatively correlates well with a high FDG uptake (**Figure 4.5D**).

Quantitative comparison of PET, DWI and HP MRSI data

We measured 24 multimodal longitudinal PET/MR data sets to investigate the correlation between FDG uptake and pyruvate-to-lactate exchange and the effect of tumor cellularity on metabolic data. However, it has to be noted again that ROIs for PET, DWI and MRSI analysis did not exactly correlate in space, as mentioned in the methods.

ADC values significantly increased with tumor growth (**Figure S4.8A**) due to increasing necrosis. This was verified by histological analysis (**Figure S4.7**) that showed a positive but not significant correlation between *ADC* and percentage of necrosis for the terminal samples (R = 0.46, p = 0.2150, n = 7).

Metabolic data showed a negative correlation with increasing necrosis without significance (SUV_{mean}: R = -0.46, p = 0.2960, K_i: R = -0.68, p = 0.0916), whereas only a very weak trend was observable for ^{13}C-data (k_{pl}: R = -0.23, p = 0.6147). Comprehensive plots are shown in **Figure S4.7**. Note, that only small amounts of granulation tissue in the necrotic parts and immune cell infiltration were observed.

Based on these observations, we clustered quantitative ^{13}C- and PET data into three groups of low, medium and high *ADC* values: $(0.57 \pm 0.04)\times10^{-3}$ mm^{2}s^{-1}, $(0.85 \pm 0.09)\times10^{-3}$ mm^{2}s^{-1} and $(1.22 \pm 0.10)\times10^{-3}$ mm^{2}s^{-1} (with n = 13, n = 7 and n = 4, respectively). We then analyzed the correlation of quantitative PET and ^{13}C-data of the low *ADC* group in order to exclude partial volume effects that affect metabolic data caused by a varying tumor cellularity (**Figure 4.6**).

Tumor k_{pl} exhibited a significant positive correlation with SUV_{mean} (R = 0.59, p = 0.0352, **Figure 4.6A**) and K_i (R = 0.57, p = 0.0399, **Figure 4.6C**). A similar but not significant trend was observed with SUV_{max} (R = 0.51, p = 0.0761, **Figure 4.6B**) and no correlation was seen with *MRGlu* (R = 0.05, p = 0.8636, **Figure 4.6D**). Tumor *AUC* ratios significantly correlated with SUV_{mean} (R = 0.59, p = 0.0326, **Figure 4.6E**), SUV_{max} (R =

0.55, p = 0.0498, **Figure 4.6F**) and K_i (R = 0.68, p = 0.0103, **Figure 4.6G**), but not with *MRGlu* (R = 0.36, p = 0.2245, **Figure 4.6H**). Slice-selective k_{pl} and *AUC* ratios, excluding errors from manual tumor ROI definition, also showed a positive correlation

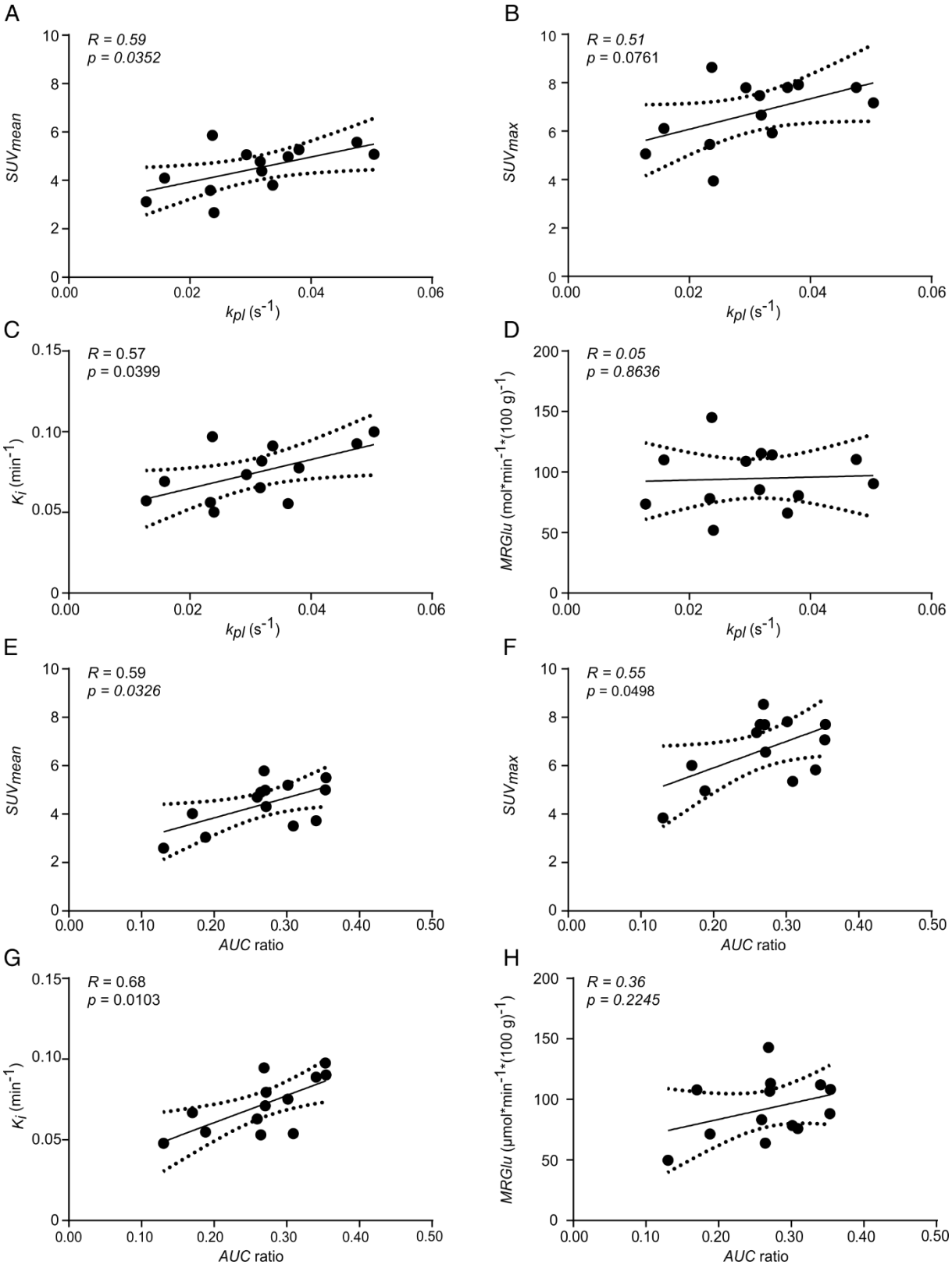

Figure 4.6. Correlation plots of FDG uptake and hyperpolarized pyruvate CSI data of tumors with similar *ADC* values. Correlation of k_{pl} with **(A)** SUV_{mean}, **(B)** SUV_{max}, **(C)** K_i and **(D)** *MRGlu*. Correlation of *AUC* ratios with **(E)** SUV_{mean}, **(F)** SUV_{max}, **(G)** K_i and **(H)** *MRGlu*. Best fit (solid line) and 95%

confidence bands (dashed lines). The mean *ADC* of analyzed tumors was (0.57 ± 0.04)×10^{-3} mm^{2}s^{-1} (*n* = 13).

with quantitative PET data: $k_{pl,\ slice}$ with SUV_{mean}: R = 0.56, p = 0.0481 and with K_i: R = 0.65, p = 0.0158; *AUC* ratios$_{slice}$ with K_i: R = 0.70, p = 0.0079 and with *MRGlu*: R = 0.81, p = 0.0008. A comprehensive correlation matrix for tumors with a similar *ADC* can be found in the supplement (**Table S4.2**). Longitudinal PET data showed a significant inverse correlation with *ADC*, while a similar but not significant trend was observed for k_{pl}. No correlation or trend was observed between *AUC* ratios and *ADC*. Representative correlation plots of SUV_{mean} and k_{pl} with *ADC* are given in **Figure 4.7**.

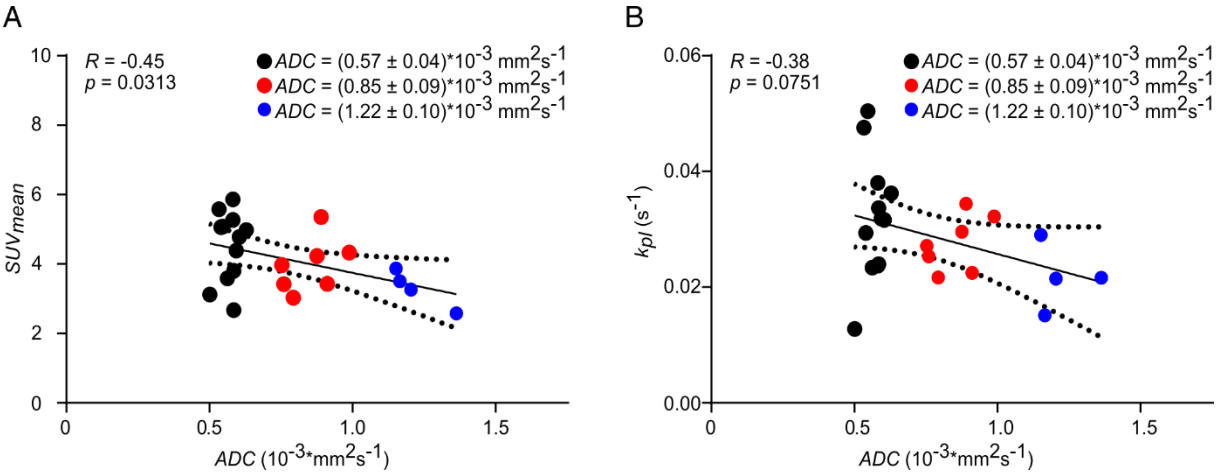

Figure 4.7. Correlation of SUV_{mean} (A) and k_{pl} (B) with *ADC*. Longitudinal data were clustered into three groups (black, red, blue) of different *ADC* values to analyze the effect of tumor cellularity on metabolic data. Best fit (solid line) and 95% confidence bands (dashed lines).

A comprehensive matrix of Pearson correlation coefficients for longitudinal data can be found in **Table 4.1**, excluding slice-selective-like ^{13}C-data analysis (see **Table S4.3**).

Overall, k_{pl} (**Figure S4.8C**) and PET uptake (SUV_{mean}, SUV_{max}, K_i and *MRGlu*) apparently decreased (**Figure S4.8D-G**) for bigger tumors. With tumor growth, the tumor metabolic volumes (*TMW*, **Figure S4.8H**) and the total lesion glycolysis (*TLG*, **Figure S4.8I**) increased and showed a strong correlation with *ADC* values (R = 0.81, p < 0.0001; R = 0.73, p < 0.0001, respectively, **Table 4.1**) and with the blood lactate concentration (R = 0.60, p = 0.0020; R = 0.51, p = 0.0118, respectively; **Table 4.1** and **Figure S4.8J**). In addition, we detected an inverse correlation of PET SUV_{mean}/SUV_{max} and k_{pl} with blood lactate concentration (R = -0.52, p = 0.0099; R = -048, p = 0.0172; R = -0.44, p = 0.0314; **Table 4.1**), which increases for animals with bigger tumors. Blood glucose levels slightly decreased but without significance (**Figure S4.8K**). *AUC* ratios did not change significantly and solely correlated with SUV_{mean} (R = 0.41, p = 0.0484). Similar but not significant trends were observed for their correlations with SUV_{max}, K_i and *MRGlu* (R = 0.37, p = 0.0728; R = 0.37, p = 0.0747; R = 0.25, p = 0.2374). For k_{pl}, we observed significant positive correlations with tumor SUV_{mean}

/SUV_{max} (R = 0.67, p = 0.0004; R = 0.61, p = 0.0014) and K_i (R = 0.65, p = 0.0006), which was not detected for *MRGlu* (R = 0.34, p = 0.1081).

Table 4.1. Pearson correlation coefficients for ^{18}F-FDG PET, [1-^{13}C]pyruvate CSI, DWI.

	SUV_{mean}	SUV_{max}	K_i	*MRGlu*	k_{pl}	*AUC rat*	$d_{t\text{-}v}$	*TMW*	*TLG*	*ADC*	c_{lac}	c_{glc}
SUV_{mean}	1											
SUV_{max}	0.99****	1										
K_i	0.68***	0.60**	1									
MRGlu	0.65***	0.58**	0.94****	1								
k_{pl}	0.67***	0.61**	0.65***	0.34$^{n.s.}$	1							
AUC rat	0.41*	0.37$^{n.s.}$	0.37$^{n.s.}$	0.25$^{n.s.}$	0.62**	1						
$d_{t\text{-}v}$	0.25$^{n.s.}$	0.19$^{n.s.}$	0.45$^{*.}$	-0.07$^{\cdot n.s.}$	0.66***	0.60**	1					
TMW	-0.49*	-0.49*	-0.37$^{n.s}$	-0.34$^{n.s.}$	-0.33$^{n.s.}$	0.21$^{n.s.}$	0.22$^{n.s.}$	1				
TLG	-0.29$^{n.s.}$	-0.29$^{n.s.}$	-0.27$^{n.s.}$	-0.24$^{n.s.}$	-0.21$^{n.s.}$	0.38$^{n.s.}$	0.26$^{n.s.}$	0.95****	1			
ADC	-0.45*	-0.46*	-0.36$^{n.s}$	-0.37$^{n.s.}$	-0.38$^{n.s.}$	0.03$^{n.s.}$	0.38$^{n.s.}$	0.81****	0.73****	1		
c_{lac}	-0.52**	-0.48*	-0.30$^{n.s.}$	-0.19$^{n.s.}$	-0.44*	-0.13$^{n.s.}$	0.08$^{n.s.}$	0.60**	0.51*	0.35$^{n.s.}$	1	
c_{glc}	0.14$^{n.s}$	0.13$^{n.s.}$	0.17$^{n.s.}$	0.49**	-0.17$^{n.s.}$	0.11$^{n.s.}$	-0.20$^{n.s.}$	0.02$^{n.s.}$	0.06$^{n.s.}$	-0.11$^{n.s.}$	0.17$^{n.s.}$	1

*p < 0.05, **p < 0.01, ***p < 0.001, ****p < 0.0001

ADC: apparent diffusion coefficient; *AUC* rat: *AUC* ratios; c_{glc},: blood glucose concentration; c_{lac}: blood lactate concentration; $d_{t\text{-}v}$: distance of tumor to central blood vessel; K_i: composite rate constant; k_{pl}: pyruvate-to-lactate exchange rate; *MRGlu*: metabolic rate of glucose utilization; n.s.: not significant; SUV_{max}: maximum standard uptake value; SUV_{mean}: mean standard uptake value; *TLG*: total lesion glycolysis, *TMW*: tumor metabolic volume.

4.4 Discussion

We established and validated a multimodal imaging workflow on a whole-body PET/MR scanner to characterize the Warburg effect in a pre-clinical tumor model in rats. Using this workflow, we addressed the glycolytic flux in tumors and analyzed the effect of tumor growth on longitudinal metabolic data. Our setup enables the acquisition of high-resolution anatomical images and the quantification of physiological and biochemical data with PET, MRSI and DWI in one scan session. Furthermore, it has potential for translation to large animal models[55, 56, 138] and into the clinic, where it could prove the oncological value of hybrid PET/MR.

FDG is an important tracer for diagnosis, staging and response to treatment monitoring of malignant tissues.[132] Comparative measurements with the gold-standard for pre-clinical imaging (PET/CT) showed that tumor *SUV*s (tumor size: > 500 mm^3) can be measured reliably using a clinical system that has an isotropic spatial resolution of 4.3 mm.[153] However, quantification of FDG uptake could be biased due to false-positive results of glycolytic granulation tissue and infiltrating immune cells[154] Histological analyzes detected only a low proportion of fibroangioblastic granulation tissue consistent with a mesenchymal reaction to tumor implantation, whereas no distinct

differences between animals were noticed. Furthermore, only scarce immune cell infiltration (mainly consisting of lymphocytes) surrounding the tumor tissue was observed and only single immune cells were present within the neoplasia (**Figure S4.6**).

In small structures like the inferior vena cava (~3 mm diameter for rats[155]), the activity recovery is biased due to partial volume effects, which leads to an overestimation of the composite rate constant (K_i). The spatial resolution of the PET/CT (< 1.5 mm[93]) is about a factor of three higher than that of the PET/MR, allowing a better quantification of the input function and correction of the PET/MR data. However, for future studies we seek to approximate this correction factor more accurately either by measurements with dynamic contrast-enhanced (DCE) MRI[156] or by invasive arterial blood sampling.[157] Nevertheless, it should be noted that input functions could reproducibly be measured (**Figure S4.2**) in the inferior vena cava[150, 151] with a clinical PET/MR, enabling a quantification of tumor glucose consumption (*MRGlu*) even though values are biased.

Chemical shift imaging (CSI) is a reliable sequence to acquire spatially resolved spectroscopic data *in vivo*. However, CSI requires a single excitation for the acquisition of each position in the *k*-space for spatial information, and thus results in relatively long scan times and an ineffective use of HP magnetization. Nevertheless, we were able to perform time-resolved CSI measurements with a matrix size of 10×10×13 mm^3 and obtained time courses of pyruvate-to-lactate exchange that allowed a quantification of *in vivo* rate constants of LDH. However, due to the low image resolution, we defined whole tumor ROIs including necrotic areas for analysis. This caused partial volume effects likely yielding smaller apparent rate constants (k_{pl} and *AUC*). In addition, quantitative LDH measures (**Figure 4.4**) were further underestimated due to partial volumes and point spread function artifacts,[152] in particular for the pyruvate signal in the vena cava, likewise caused by the low image resolution. Methods to partially compensate for such artifacts would for instance be the inclusion of an arterial[158] or image-derived input function for pyruvate. However, we found that due to the low data sampling rate, the latter approach was not as reliable as solving the differential equation (**equation 4.4**) with the pseudoinverse of the matrix equation. At this point it should also be noted that a lower sensitivity of the ^{13}C-coil further away from its surface probably also impeded optimal quantification (**Figure S4.4**). In future, implementation of fast state-of-the-art imaging sequences like IDEAL spiral CSI [124], spectral-spatial EPI [125] or echo planar spectroscopic imaging (EPSI) [126] could be used to increase spatial resolution, which will improve the quantification of *in vivo* ^{13}C-data.

In the past, several studies sequentially measured FDG uptake and pyruvate-to-lactate exchange on consecutive days.[139] Menzel et al. noticed that longer delays between experiments might change the glucose metabolism, obscuring the biological significance of metabolic information.[140] Simultaneously acquired FDG-PET and

HP-pyruvate MRSI data for tumors with similar cell density herein demonstrated a positive qualitative (**Figure 4.5**) and quantitative (**Figure 4.6**) correlation between FDG uptake and LDH activity. However, metabolic images from different acquisitions were not precisely matched in space and correlations of quantitative data are probably still biased. In the future, this could be improved by an analysis of ROIs that are identical in space and dimension. Furthermore, provided that the spatial resolution of MRSI could be improved, inclusion of a voxel-wise[56] or histogram-based analysis could be beneficial to address tumor heterogeneity in greater depth[109]

Our workflow included diffusion-weighted imaging to address changes of tumor cellularity with tumor growth, because variations of tissue density and "tissue organization and extracellular space tortuosity"[109] can affect image-derived FDG uptake and pyruvate-to-lactate conversion. DWI is an emerging technique in oncology for diagnosis, monitoring and outcome prediction of malignancies. However, the diffusion encoding is inherently sensitive to motion and the imaging readout based on single-shot echo planar imaging (EPI) is prone to image distortions, as partially observed in our study (**Figure S4.5**). This could lead to quantification errors. We therefore performed comparative measurements with standardized phantoms, which revealed a good reproducibility of *ADC* measurements between different systems, yielding values in agreement with the literature (**Supplement S.4.6.2, S4.5**).

As *ADC*s significantly changed with tumor growth, we clustered longitudinal data in three groups of low, medium and high *ADC*. By minimizing the influence of variations in cell density on metabolic data, the correlation of FDG uptake (SUV_{mean} and K_i) and pyruvate-to-lactate exchange indicates that a major portion of consumed glucose is reduced via pyruvate to lactate for the low *ADC* group. Tumors use oxidative glycolysis to generate fast energy from glucose and fulfill their anabolic needs [35]. The excessive lactate production is crucial for invasion and immune evasion of tumors, facilitating their survival and metastasis [159]. A quantitative measure of the lactate production in tumors (k_{pl} or *AUC* ratios) is therefore valuable information that is complementary to FDG-PET and will potentially allow a more precise and patient-specific phenotyping.

Our setup enables the simultaneous quantification of FDG uptake, LDH activity and tumor cellularity to analyze the impact of tumor tissue density on metabolic data. In fact, negative correlations of longitudinal PET and DWI (**Table 4.1** and **Figure 4.7**) data showed that the measured FDG concentration (e.g., SUV_{mean} or K_i vs. *ADC*) decreases with decreasing tumor cellularity (**Figure S4.8**). This was validated by histology (**Figure S4.7**) and is in agreement with the literature [107, 160-162]. Similar effects were observed with ^{13}C-data (k_{pl}), but we assume that a rather imprecise quantification caused by a limited spatial resolution of our ^{13}C image obscured the significance. In addition, k_{pl} values appeared to reflect longitudinal averaging effects better than *AUC* ratios, where no trend was observed for the correlation with *ADC*.

With tumor growth, the overall tumor cellularity decreased while the absolute number of active tumor cells increased. This was indicated by increasing *TMW* and a strong positive correlation of the respective parameters (*ADC* and *TMW*). Thus, the absolute amount of FDG uptake (*TLG*) and lactate production in tumors both increased, which led to a progressive lactate acidification of animals. This was reflected by an increasing blood lactate concentration (c_{lac}) for animals with bigger tumors and its strong positive correlation with *TMW* and *TLG* [163].
Finally, longitudinal PET and ^{13}C-data also showed a positive correlation (k_{pl} with SUV_{mean}/SUV_{max} and K_i, *AUC* ratios with SUV_{mean}). Taking the results of the low *ADC* group and the correlations of the longitudinal data with *ADC* into account, we conclusively assume that this correlation is a combined effect of the Warburg effect and partial volume effects.
The simultaneous acquisition of high-resolution anatomical images, DWI, PET and hyperpolarized MRSI data is now possible with hybrid PET/MR in a clinical environment [55, 56, 138]. Better acquisition schemes for fMRI and MRSI and the growing number of approved PET tracers and hyperpolarized probes will further help to characterize tumor biology in greater depth.

4.5 Conclusion

We established and validated a multimodal imaging workflow for a clinical PET/MR scanner to simultaneously quantify glucose uptake, LDH activity and cell density in rodents with PET, hyperpolarized MRSI and DWI. Despite resolution limitations of dynamic ^{13}C-data, we demonstrated a good correspondence between high glucose uptake and elevated LDH activity in tumors of similar cellularity. This indicates that a major portion of glucose is reduced to lactate in the analyzed tumor model. Longitudinal DWI data showed a decrease in cell density during tumor growth, which affected the quantification of both, PET and MRSI data.
Our workflow includes a multiparametric and non-invasive tumor characterization that can possibly be applied to larger animal models with potential for clinical applications paving the way for tailored and patient-specific therapy approaches.

4.6 Supplementary Information

4.6.1 Supplementary Tables

Table S4.1. Acquisition parameters of ^{1}H-MRI sequences.

	Dim.	slice thickn. / mm	FOV / mm^2	*TR* / ms	*TE* / ms	Matrix	nom. resol. / mm^3	avg.	Slices / slab	AQ time
MRAC UTE	3	1.6	300×300	11.94	0.07	-	4.1	-	192	2min 2s
T_1 MPRAGE	3	1	250×211	1120	3.02	256×256	0.8	4	60	16 min
T_2 FLAIR	3	1	250×211	5000	91	256×256	0.8	2.7	60	6min 4s
T_1 Flash	2	3	160×160	250	2.48	320×320	0.75	2	-	2min 9s
T_2 HASTE	2	3	160×160	1600	93	256×256	1.2	20	-	1min 33s
Diffusion[a]	2	3	70×70	4000	71	48×48	6.4	8	-	6min 55s

[a]b-values: 10, 150, 300, 500, 700 s*mm^{-2}

AQ time: acquisition time; avg.: averages; Dim.: Dimensions; FLAIR: fluid-attenuated inversion recovery; FLASH: fast low-angle shot; FOV: field of view; HASTE: half Fourier acquisition single shot turbo spin echo; MRAC: magnetic resonance-based attenuation correction; MPRAGE: magnetization prepared rapid acquisition gradient echo; nom. resol.: nominal resolution; T_1: spin lattice relaxation time; T_2: spin spin relaxation time; *TE*: echo time; thickn.: thickness; *TR*: repetition time; UTE: ultra-short echo time.

Table S4.2. Pearson correlation coefficients for ^{18}F-FDG PET, [1-^{13}C]pyruvate CSI, DWI of tumors with similar cellularity (*ADC* of (0.57±0.04)*10^{-3} mm^{2}s^{-1}).

	SUV_{mean}	SUV_{max}	K_i	*MRGlu*	k_{pl}	$k_{pl,\ slice}$	*AUC ratio*	*AUC ratio*$_{slice}$
SUV_{mean}	1							
SUV_{max}	0.98****	1						
K_i	0.65*	0.56*	1					
MRGlu	0.56*	0.53$^{n.s.}$	0.76**	1				
k_{pl}	0.59*	0.51$^{n.s.}$	0.57*	0.05$^{n.s.}$	1			
$k_{pl,\ slice}$	0.56*	0.46$^{n.s.}$	0.65*	0.26$^{n.s.}$	0.70**	1		
AUC ratio	0.59*	0.55*·	0.68*	0.36$^{n.s.}$	0.77**	0.74**	1	
AUC ratio$_{slice}$	0.47$^{n.s.}$	0.45$^{n.s}$	0.70**	0.81***	0.26$^{n.s.}$	0.34$^{n.s.}$	0.59*	1

*p < 0.05, **p < 0.01, ***p < 0.001, ****p < 0.0001.

AUC ratio: areas under the curve ratio from tumor region-of-interest ^{13}C-analysis; *AUC* ratio$_{slice}$: areas under the curve ratio from slice-selective like ^{13}C-analysis; K_i: composite rate constant; k_{pl}: pyruvate-to-lactate exchange rate; $k_{pl,\ slice}$: pyruvate-to-lactate exchange rate *from slice-selective like analysis; MRGlu*: metabolic rate of glucose utilization; n.s.: not significant; SUV_{max}: maximum standard uptake value; SUV_{mean}: mean standard uptake value.

Table S4.3. Pearson correlation coefficients for of ^{13}C-data from slice selective like analysis correlated with longitudinal PET and MRI data.

	SUV_{mean}	SUV_{max}	K_i	*MRGlu*	$k_{pl,\ slice}$	AUC_{slice}	$d_{t\text{-}v}$	*TMV*	*TLG*	*ADC*	c_{lac}	c_{glc}
SUV_{mean}	1											
SUV_{max}	0.99****	1										
K_i	0.68***	0.60**	1									
MRGlu	0.65***	0.58**	0.94****	1								
$k_{pl,\ slice}$	0.39$^{n.s.}$	0.34$^{n.s.}$	0.41*	0.14$^{n.s.}$	1							
AUC_{slice}	0.28$^{n.s.}$	0.23$^{n.s.}$	0.31$^{n.s.}$	0.43*	0.29$^{n.s.}$	1						
$d_{t\text{-}v}$	0.25$^{n.s.}$	0.19$^{n.s.}$	0.45$^{*.}$	-0.07$^{n.s.}$	0.59**	0.23$^{n.s.}$	1					
TMV	-0.49*	-0.49*	-0.37$^{n.s}$	-0.34$^{n.s.}$	0.06$^{n.s.}$	0.23$^{n.s.}$	0.22$^{n.s.}$	1				
TLG	-0.29$^{n.s.}$	-0.29$^{n.s.}$	-0.27$^{n.s.}$	-0.24$^{n.s.}$	0.12$^{n.s.}$	0.33$^{n.s.}$	0.26$^{n.s.}$	0.95****	1			
ADC	-0.45*	-0.46*	-0.36$^{n.s}$	-0.37$^{n.s.}$	0.15$^{n.s.}$	0.35$^{n.s.}$	0.38$^{n.s.}$	0.81****	0.73***	1		
c_{lac}	-0.52**	-0.48*	-0.30$^{n.s.}$	-0.19$^{n.s.}$	0.04$^{n.s.}$	-0,05$^{n.s.}$	0.08$^{n.s.}$	0.60**	0.51*	0.35$^{n.s.}$	1	
c_{glc}	0.14$^{n.s}$	0.13$^{n.s.}$	0.17$^{n.s.}$	0.49**	-0,09$^{n.s.}$	0.41*	-0.20$^{n.s.}$	0.02$^{n.s.}$	0.06$^{n.s}$	-0.11$^{n.s.}$	0.17$^{n.s.}$	1

*p < 0.05, **p < 0.01, ***p < 0.001, ****p < 0.0001.

ADC: apparent diffusion coefficient; *AUC* rat: areas under the curve ratio from tumor region-of-interest ^{13}C-analysis; c_{glc},: blood glucose concentration; c_{lac}: blood lactate concentration; $d_{t\text{-}v}$: distance of tumor to central blood vessel; K_i: composite rate constant*;* $k_{pl\ slice}$: pyruvate-to-lactate exchange rate from slice-selective like analysis; *MRGlu*: metabolic rate of glucose utilization; n.s.: not significant; SUV_{max}: maximum standard uptake value; SUV_{mean}: mean standard uptake value; *TLG*: total lesion glycolysis, *TMW*: tumor metabolic volume.

4.6.2 Supplementary Figures

Tumor growth curve

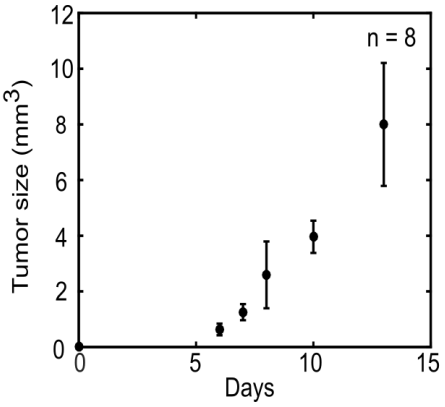

Figure S4.1. Tumor growth curves of subcutaneous MAT-B-III tumors (n=8).

^{18}F-FDG PET, input functions and tumor uptake curves

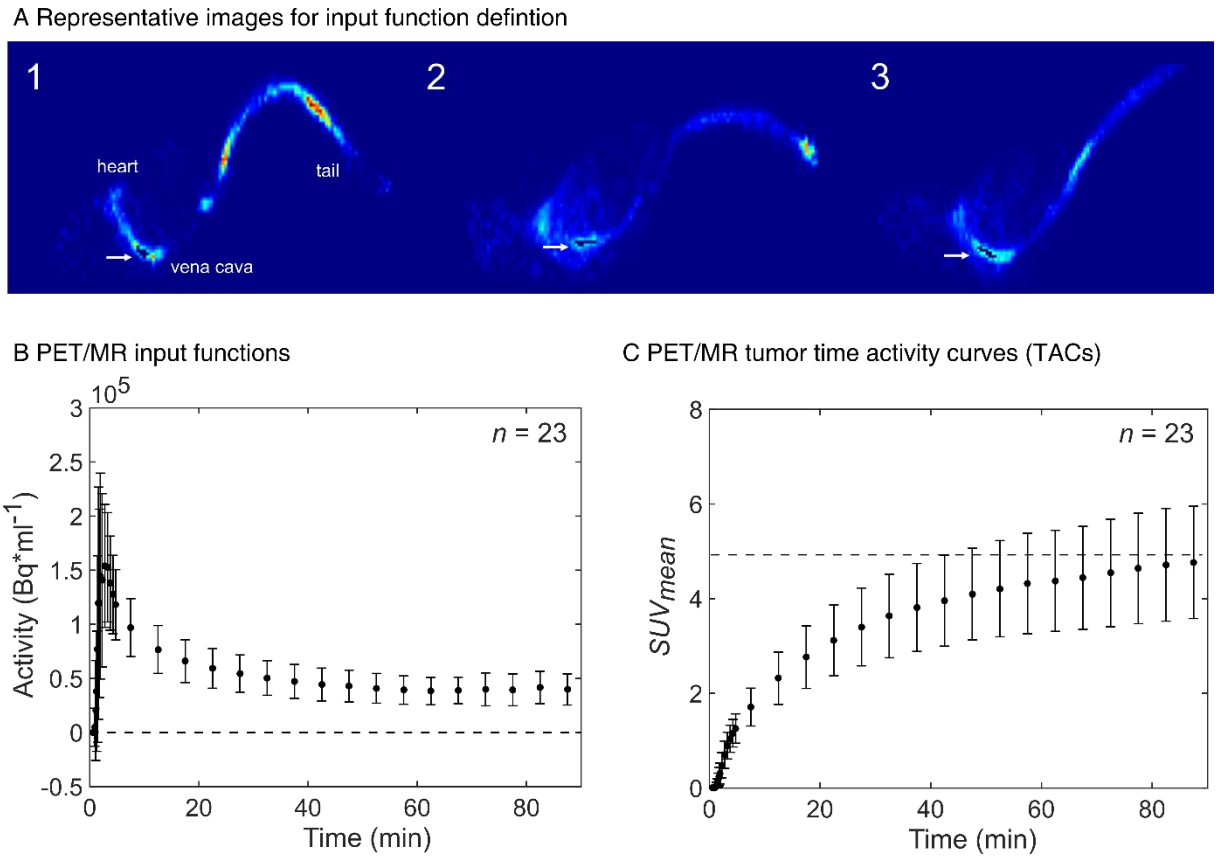

Figure S4.2. PET/MR input functions and time activity curves of tumors. **(A)** shows three representative coronal images where image derived input functions were segmented semi-automatically. **(B)** shows the mean ± *std* of all image derived input functions except for one animal. An explanation for excluding the animal is given in **Figure S4.3C4**. **(C)** is the mean ± *std* of all tumor time

activity curves corrected by the respective animal weights and injected doses. The measurement of the same animal as mentioned in (B) was excluded.

Image derived input functions (IDIFs) were segmented in the inferior vena cava[150] for kinetic Patlak[72, 96] analysis of the glucose utilization of subcutaneous MAT-B-III tumors. Three exemplary coronal images showing the segmented IDIF ROIs are displayed in **Figure S4.2A**. Except for one measurement, the mean ± *std* of all measured IDIFs and tumor time activity curves are displayed in **Figure S4.2B** and **C**, respectively. An explanation for excluding one measurement is given in the next chapter.

[^{18}F]FDG PET, Patlak analysis

The kinetic Patlak analysis was performed according to **equation S4.1** [72, 96]

$$\frac{c_{tissue}(t)}{c_{plasma}(t)} = K\frac{\int_0^\tau c_{plasma}(\tau)d\tau}{c_{plasma}(t)} + V \quad (S4.1)$$

with t being the time after tracer injection, $c_{tissue}(t)$ being the FDG activity concentration in the tumor, $c_{plasma}(t)$ being the FDG activity concentration in the vena cava (IDIF), $_0\int^T c_{plasma}(\tau)d\tau$ being the integral of FDG concentration in the vena cava (IDIF), K_i being the composite rate constant ($K_1 \times k_3/(k_2+k_3)$) and V being the FDG distribution volume in the vena cava (IDIF).

A comparison of [^{18}F]FDG tumor uptake curves measured for three animals at a small animal PET/CT scanner and at a clinical PET/MR scanner showed no significant differences. However, the K_i value was by a factor of f = 2.7 higher for PET/MR data compared to PET/CT data. A reduced resolution of the PET/MR leads to an underestimation of $_0\int^T c_{plasma}(\tau)d\tau$ determining higher K_i values (**Figure S4.3A** and **B**). All PET/MR K_i values (and *MRGlu*) obtained in the longitudinal study were finally corrected by the factor *f*.

Figure S4.3C1 and **C2** show representative Patlak plots. In some few animals, we noticed that the injection of pyruvate slightly disturbed FDG uptake as shown in (**Figure S4.3C3**) indicated with a black arrow. We assume that this was due to temporary FDG clearance in the blood stream surrounding the tumor. For one animal, 49.5% FDG resided in the tail vein at first injection but was added to the blood system at pyruvate injection (**Figure S4.3C4**, indicated with a black arrow). However, the linearity of the Patlak plot in the defined fit range (10 min to 40 min) was still given as this analysis is not dependent on the amount of injected FDG. For an accurate SUV_{mean} and SUV_{max} analysis, the tumor time activity curves of the “first” and the “second” FDG injection were fitted to an exponential function ($y = a \times (1\text{-}e^{(-b \times t)})$ and plateau values were

extracted. The actual dose of the first injection was calculated according to the ratio of these plateau values.

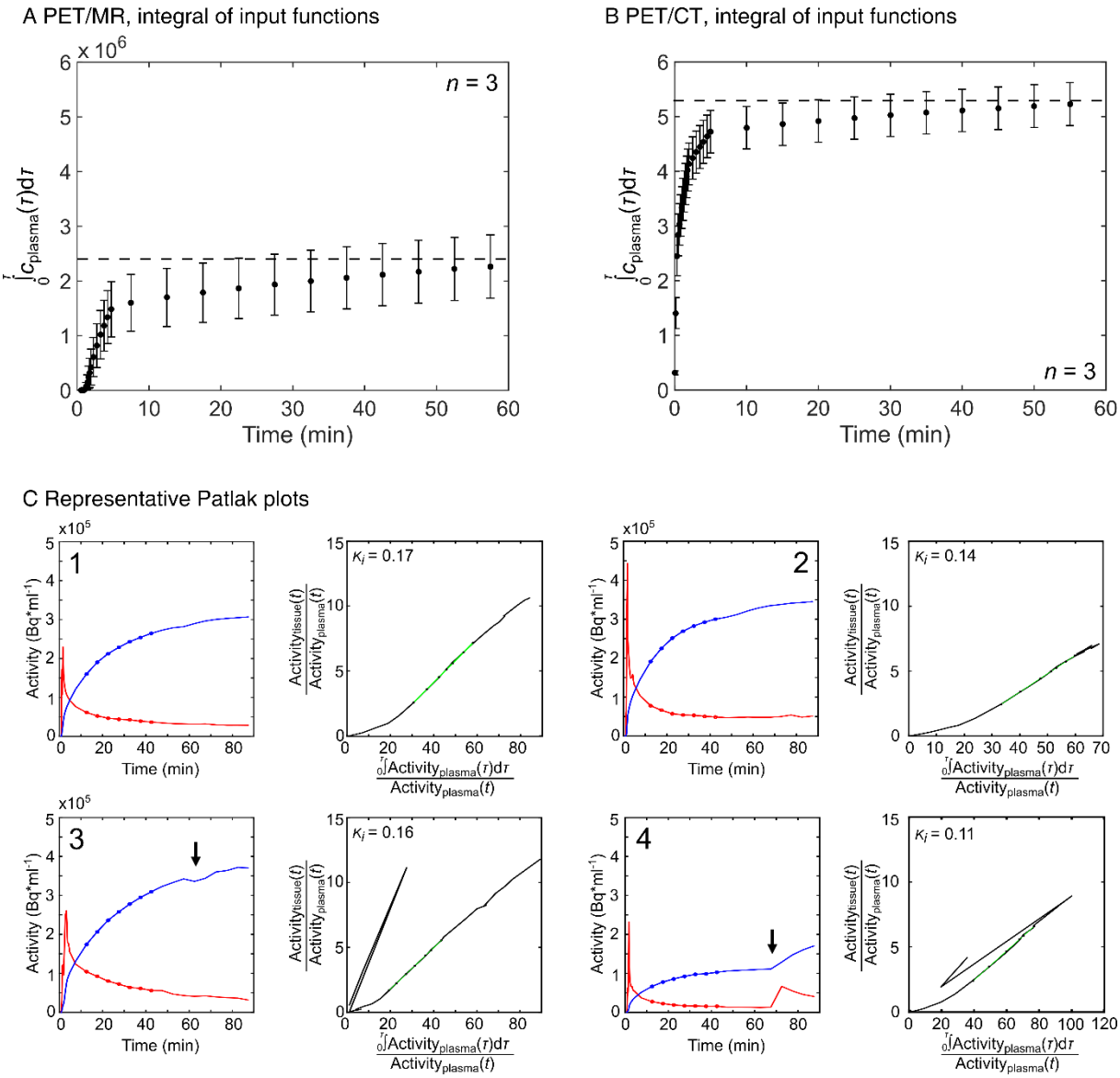

Figure S4.3. Input function integrals of PET/CT and PET/MR and PET/MR Patlak analysis. **(A)** and **(B)** compare the integrals of the image derived input functions segmented in the vena cava inferior of three animals measured with a delay of about ten hours respectively at the PET/MR and the PET/CT. **(C)** displays four individual image derived input functions and tumor uptake curves in one plot (C1-4). The respective Patlak plots are given to the right of the uptake curves. C1, C2 show good linearity in the chosen time range of 10 - 40 minutes (green line). In few animals, we observed slight disturbance of tumor FDG uptake at ^{13}C-pyruvate injection (C3, black arrow). For one animal, a major portion of FDG resided in the tail vein at injection but was co-injected at ^{13}C-pyruvate injection (C4). The actual amount of injected FDG was corrected to accurately determine SUV_{mean} and $\underline{SUV_{max}}$. Note that the K_i values displayed in the plot C1-4 have not been corrected by f = 2.7.

^{13}C-B_1 calibration and field profile of a ^{1}H/^{13}C surface coil

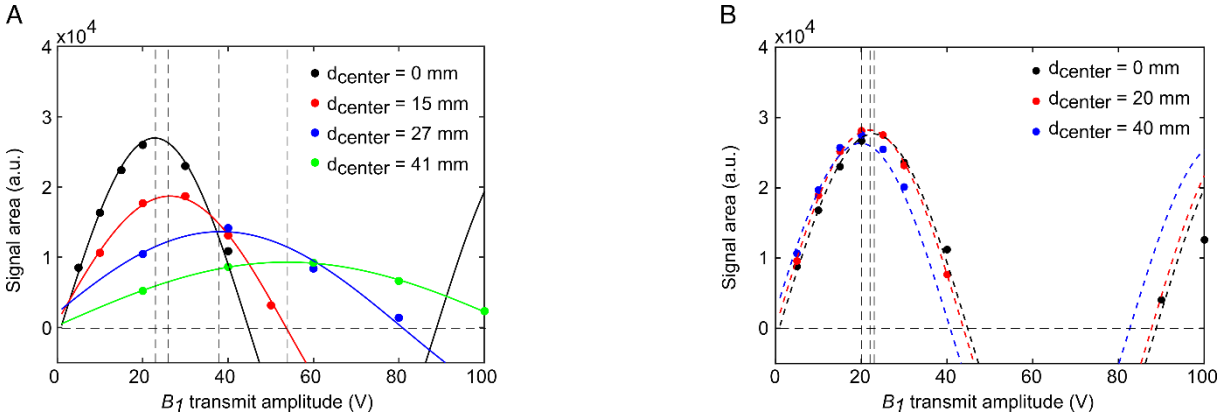

Figure S4.4. ^{13}C MR signal (dots) and fit (line) of 8 M ^{13}C-urea model solution in a 5 mL glass vial measured as function of transmitter voltage in vertical (A) and horizontal (B) distance to the ^{1}H/^{13}C surface transmit-receive coil. (A) At 35 mm vertical distance, the maximum signal amplitude was decreased by 50% compared to the maximum signal when the phantom was directly placed on the surface of the coil (black). (B) No relevant difference of the MR signal was observed when the position of the model solution was moved by 0 - 40 mm in horizontal direction (zero vertical direction). These results indicate that the excitation of the CSI sequences is constant in horizontal direction but varies significantly in vertical direction over the examined animals. Tumors were therefore placed directly onto the surface coil (animal position: head first, right lateral) minimizing quantification errors due to B_1-inhomogeneity in vertical direction.

Diffusion-weighted imaging

Reproducibility and validation experiments

We used an ice-water phantom to validate quantitative DWI measurements and verify reproducibility. The phantom consisted of two plastic tubes with the space between the inner and the outer tube being filled with frozen water.[146] The inner tube was filled with water that was kept at a temperature of 0 °C. The setup provides the chance to measure *ADC* values at a constant temperature over a reasonable period of time.
Diffusion-weighted imaging was performed on the clinical 3 T PET/MR scanner (mMR biograph, Siemens, Erlangen, Germany) and on a 7 T pre-clinical scanner (Avance III, Bruker BioSpin, Billerica, MA, USA). Acquisition parameters at the clinical system were: *TE*/*TR* 74/6000 ms, b-values 10, 150, 300, 500, 700 s/mm², matrix 48×48, FOV 58×58 mm, slice thickness 3 mm, averages 8. Acquisition parameters at the pre-clinical system were: *TE*/*TR* 17/1500 ms, b-values 18, 158, 308, 508, 708 s/mm², matrix 128×128, FOV 40×40 mm, slice thickness 2 mm, averages 3. For the clinical and pre-clinical systems we respectively obtained *ADC* values of 1.105×10^{-3} mm²/s (95% confidence interval: $1.102 – 1.109\times10^{-3}$ mm²/s) and 1.117×10^{-3} mm²/s (95% confidence interval: $1.107 – 1.126\times10^{-3}$ mm²/s), which are in agreement with literature values $1.099\times10^{-3} – 1.138$ mm²/s (for T = 0 - 1 °C).[164]

Exemplary T_2-weighted, diffusion-weighted images and ADC plots

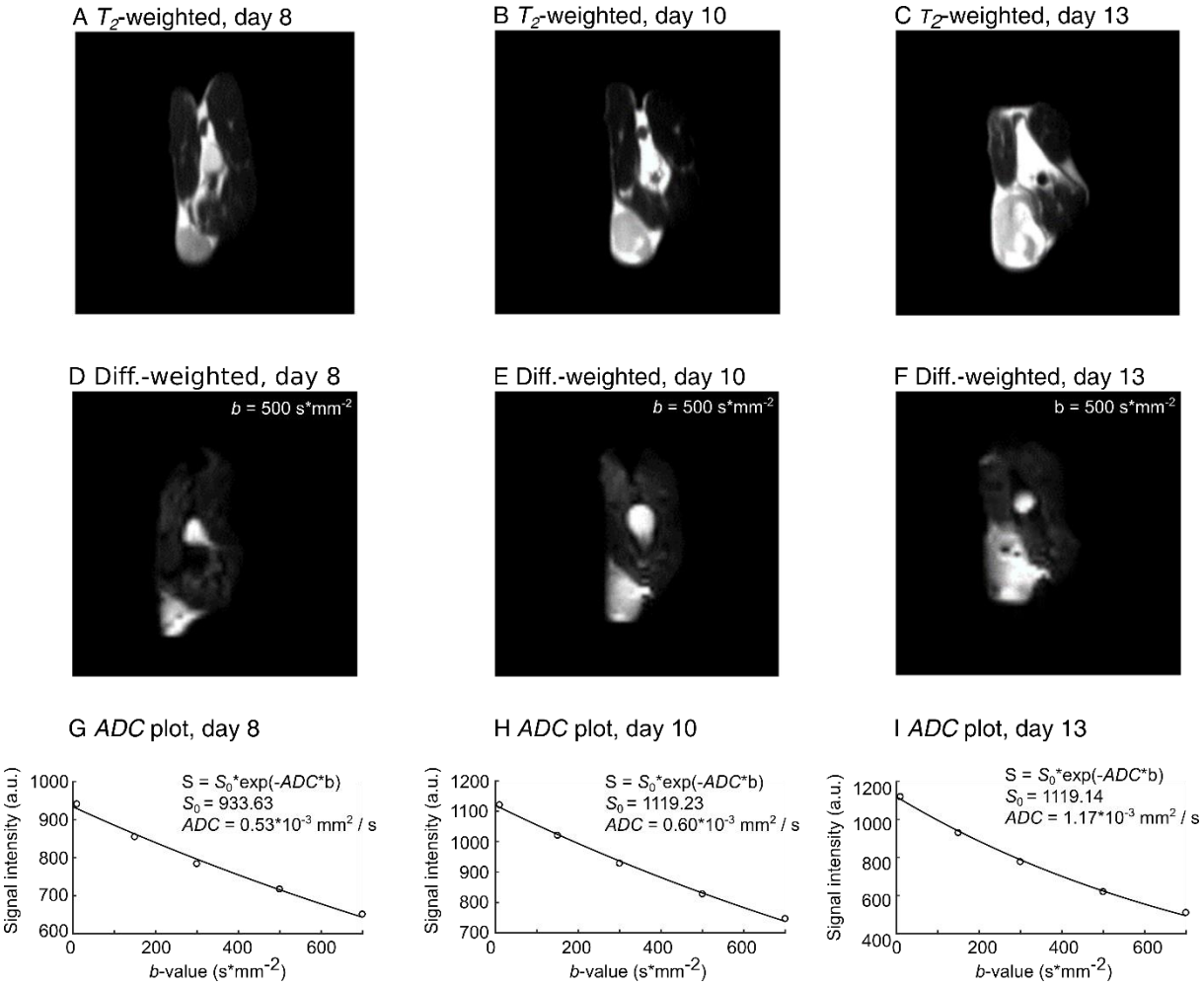

Figure S4.5. Exemplary T_2-weighted images, diffusion-weighted images and *ADC* fits. (A-C) T_2-weighted images of an animal measured on day eight, ten and thirteen, respectively. **(D-F)** Representative diffusion-weighted images acquired for the same animal as in (A-C) for *b*-value = 500 s×mm^{-2}. **(G-I)** Respective *ADC* fits for whole tumor ROIs.

Histology

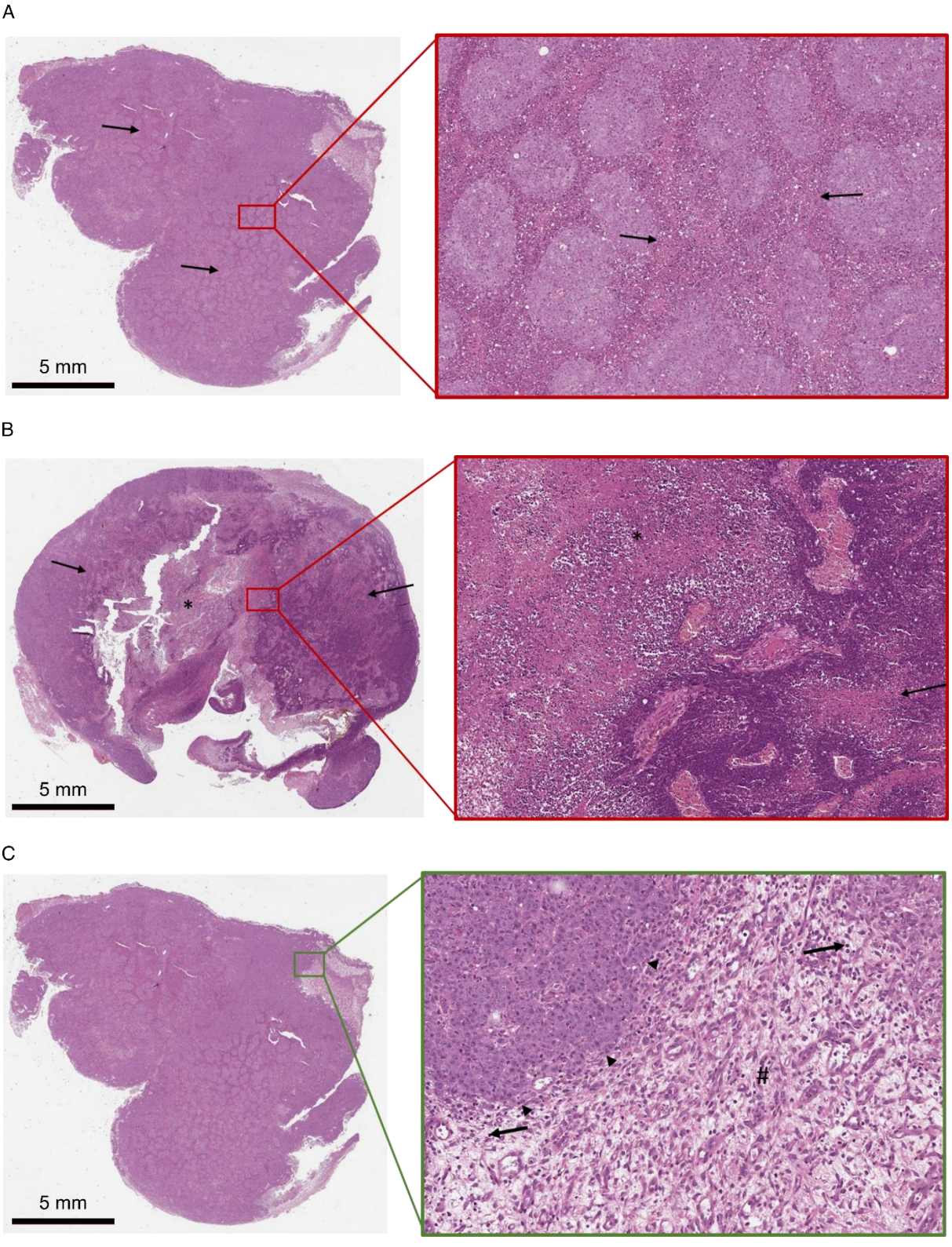

Figure S4.6. Representative Hematoxylin-Eosin (H.-E.) stained histological tumor slices. (A) tumor slice with a total 15% of tumor area covered by necrosis. The multifocal necrotic parts of the tumors (arrows) in two of the cases did not merge to a large central necrotic area. (H.-E. staining, overview (left), original magnification 100 × (right)). **(B)** tumor slice with a total 35% of tumor area covered by necrosis. The multifocal necrotic parts of the tumors (arrows) in the majority of cases was

confluent in a larger central necrosis (*). (H.-E. staining, overview (left), original magnification 100 × (right)). **(C)** example of fibroangioblastic granulation tissue (#) and slight infiltration (lymphocytes, arrows) in tumor (arrowheads) periphery. (H.-E. staining, overview (left), original magnification 200 × (right)).

Correlation plots of %-necrosis with DWI, PET and MRSI data

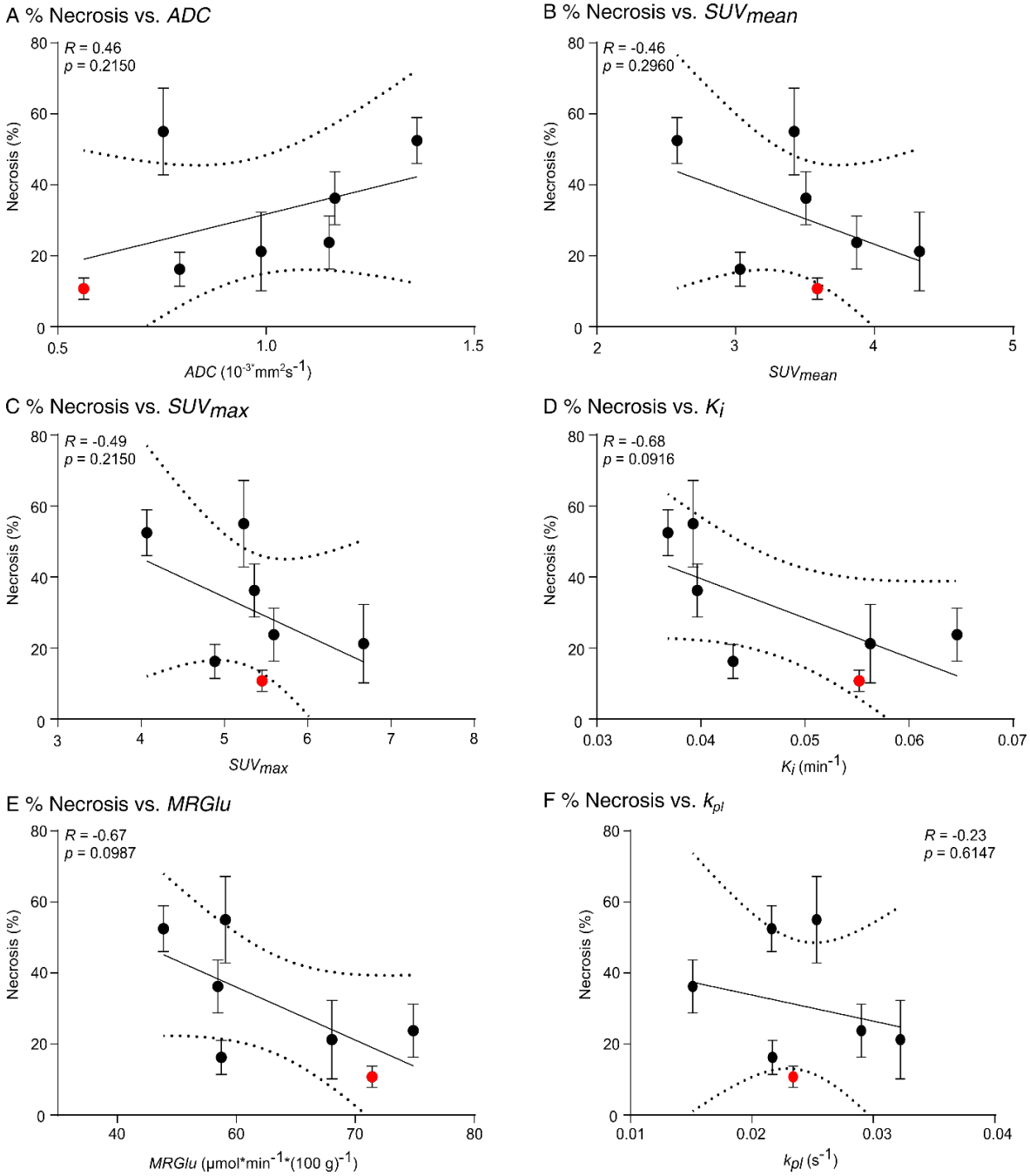

Figure S4.7. Correlation plots of necrosis and DWI, PET, MRSI data. Correlation of%-necrosis ± standard deviation with **(A)** *ADC*, **(B)** SUV_{mean}, **(C)** SUV_{max}, **(D)** K_i, **(E)** *MRGlu* and **(F)** k_{pl}. Data from the animal sacrificed on day ten are marked in red. Best fit (solid line) and 95% confidence bands (dashed lines). Correlation coefficients for %-necrosis and *AUC* ratios were: R = -0.21, p = 0.6506.

For validation of signal averaging effects with progressive necrosis in growing tumors, quantitative parameters obtained from DWI, PET and MRSI from n = 7 (out of eight) terminal measurements were correlated with the percentage of necrosis in histological tumor slices stained with H.-E. One animal was left out for analysis, because the PET scan failed as described in the materials and methods chapter in the main manuscript. One animal was sacrificed on day ten, six on day thirteen. Necrosis was estimated for four slices per tumor and the given value is the mean (± standard deviation) for the respective four slices. Overall, the following trend is observed: progressive or bigger tumors showed a higher percentage of necrosis (%-Nec), which was measured by DWI with increasing *ADC* values. %-Nec and *ADC* exhibited a positive correlation (**Figure S4.7A**). This led to partial volume artifacts for metabolic data shown by negative correlations with %-Nec (**Figure S4.7B-E**). However, correlations were not significant, which was probably due to the small group size and the low spatial correlation of histological slices and MRI/PET/MRSI regions of interest. Note, that only a very weak trend is shown for ^{13}C-MRSI data (**Figure S4.7F**).

Quantitative longitudinal data for three groups of similar tumor cellularity each

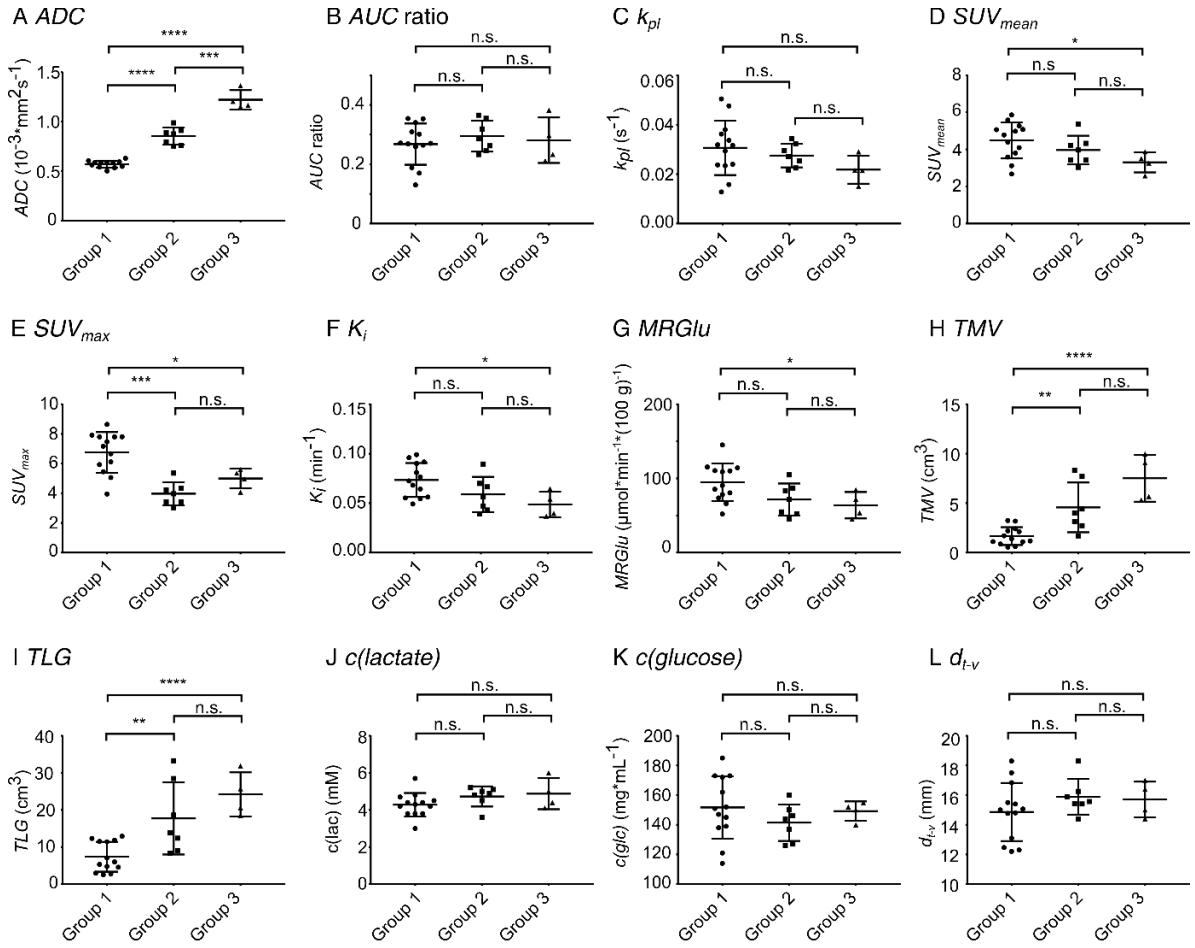

Figure S4.8. Overview of all multimodal semi-/quantitative longitudinal data measured for animals clustered into three groups of different tumor cellularity (*ADC* values) measured with DWI. (A) *ADC*, **(B)** *AUC* ratios from ^{13}C-MRSI, **(C)** k_{pl} from ^{13}C-MRSI, **(D)** SUV_{mean} from FDG-PET, **(E)** SUV_{max} from FDG-PET, **(F)** K_i from FDG-PET, **(G)** *MRGlu* from FDG-PET, **(H)** tumor metabolic volume (*TMV*), **(I)** total lesion glycolysis (*TLG*), **(J)** blood lactate concentration, **(K)** blood glucose concentration, **(L)** distance of tumor to central blood vessel.

5. Imaging of Extracellular pH Using Hyperpolarized Molecules

Christian Hundshammer, Stephan Düwel and Franz Schilling

This chapter is an amended version of [113].

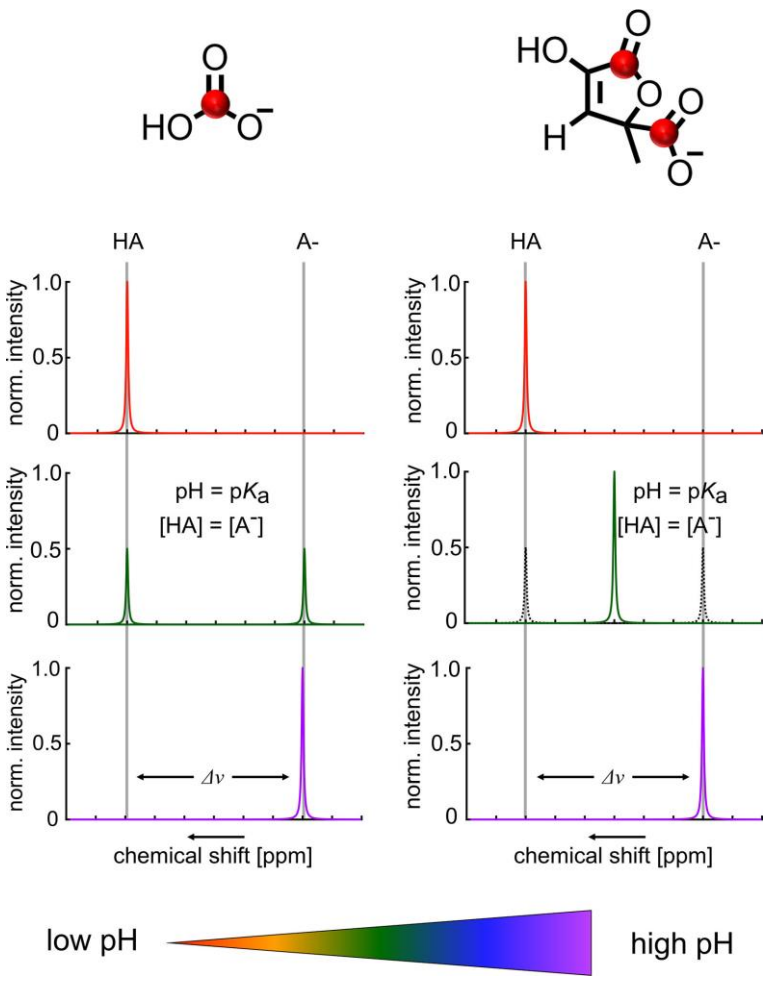

Summary

Many diseases can overrule natural pH regulatory mechanisms and alter the extracellular pH (pH_e). A non-invasive method that resolves pH_e *in vivo* with high spatial and temporal resolution could therefore improve diagnosis and monitoring of diseases, contributing to the concept of precision medicine. During the last decades, several techniques have been proposed to image pH_e non-invasively. The majority of these methods relies on magnetic resonance because of its good spatial resolution, high penetration depth, non-ionizing radiation and excellent complimentary soft tissue contrast. Dissolution dynamic nuclear polarization (DNP) is an emerging concept to enhance NMR signals by more than four orders of magnitude, making it possible to observe *in vivo* metabolic processes in real-time. Here, we summarize and review recent developments in pH_e imaging techniques based on hyperpolarization methods and give an overview of recently discovered hyperpolarized pH sensor molecules that have been applied *in vitro* and *in vivo*.

5.1 Introduction

Pathologies such as infections, inflammation, ischemia, renal failure, pulmonary disease or cancer are characterized by abnormal metabolism, which can disturb pH regulatory mechanisms and lead to changes of the extracellular pH (pH_e).[29, 165, 166] Because pH_e can be critical for disease progression[167] and drug efficiency[168], imaging of pH_e could prove valuable for diagnosis, drug development, treatment selection and response to treatment monitoring,[29, 169, 170] thereby contributing to the concept of precision medicine.[171, 172] However, currently no method for imaging of pH_e is available in the clinic. To this day, a multitude of approaches and modalities have been proposed to map pH_e non-invasively *in vivo*. Positron emission tomography (PET) tracers like ^{11}C-labelled dimethyloxazolidine-2,4-dione (DMO)[173], $^{11}CO_2$[174] and ^{18}F-FDG glycosylamines[175] show a pH-dependent tracer distribution. The pH low insertion peptide (pHLIP), conjugated with ^{18}F[176], ^{64}Cu[177] or ^{99}Tc[178], inserts into cell membranes in regions of acidic pH_e.

Optical methods exploit the fluorescence signal of a tracer and measure pH_e either based on a ratiometric approach (fluorescence ratio imaging microscopy, FRIM), or relying on a pH-dependent fluorescence lifetime (fluorescence lifetime imaging microscopy, FLIM).[179] The versatile chemical structure of many fluorescence biosensors facilitates coupling to molecules that target specific disease markers. pH-sensitive dyes were recently attached to pHLIP and used for tumor pH_e imaging in mice.[180, 181] Although fluorescence based pH_e imaging has a tissue penetration depth of only a few millimeters,[182] it offers excellent spatial and temporal resolution. Such penetration depth limitations of optical imaging can be partially overcome by using optoacoustic techniques for which a pH-sensitive albumin-based probe has recently been introduced.[183]

High penetration depth, excellent soft tissue contrast and good spatial resolution is possible by magnetic resonance imaging (MRI). Standard proton MRI can be combined with imaging of pH_e by utilizing exogenous molecules with pH_e dependent relaxivities or exchange properties. For instance, gadolinium (Gd)-loaded single-[184, 185] or poly-[186] ion complexes show altered hydrogen bonding or water accessibility at increased proton concentrations, directly affecting the longitudinal spin lattice relaxation constant (T_1) of water. For an absolute pH_e determination, the *in vivo* concentration of these complexes needs to be determined, which was achieved by subsequent or simultaneous injection of pH-sensitive and pH insensitive Gd-complexes[187]. Frullano et al. developed a bimodal agent that measures pH by MRI and, at the same time, agent concentration by PET.[188]

Exogenous paramagnetic and diamagnetic complexes with dissociable protons have been designed to image pH_e *in vivo* based on chemical exchange saturation transfer (CEST) and have been termed PARACEST and DIACEST, respectively. In CEST

approaches, the resonance signal of bound protons is selectively saturated by a radiofrequency pulse leading to a decrease of the bulk magnetic resonance (MR) signal because of exchange between the bound and the bulk water pool. pH can then be determined from a calibration curve relating pH to the CEST contrast, e.g. an acidic pH relates to a slower exchange compared to the exchange at physiological pH.[189, 190]

Several chelators loaded with paramagnetic lanthanides[191-193] as well as diamagnetic molecules that possess amide or hydroxyl groups[194, 195] have been suggested as pH-sensitive PARACEST or DIACEST agents, respectively. Three FDA approved CT/X-ray contrast agents, whose pH-sensitivity was recently investigated, are the DIACEST molecules iobitridol[196], iopamidol[197, 198], and iopromide[199, 200] (acidoCEST).

Chemical shift based sensors with pH-sensitive resonance signals of alternative nuclei, such as ^{1}H, ^{19}F and ^{31}P, have been developed to estimate pH_e *in vivo* using magnetic resonance spectroscopy (MRS). The two membrane-impermeable and non-toxic imidazole derivatives IEPA[201] and ISUCA[202] contain pH-sensitive protons which show a change in chemical shift as a function of pH. Fluorinated derivatives of vitamin B6[203] accumulate in the intra- and extracellular space and the respective pH values can be obtained from differences in chemical shift with respect to a chemical shift standard. 3-aminopropylphosphonate (3-APP)[204] has been widely used to measure pH_e *in vivo* in animal models and as a gold standard to validate new pH_e sensors (e.g. ZK-150471[205]). Nevertheless, these MRS-based ^{1}H, ^{19}F and ^{31}P pH_e sensors suffer from the intrinsic low sensitivity of NMR for the detection of molecules at low concentration. Therefore, their application for imaging of pH_e *in vivo* remains challenging.

In addition, a variety of biocompatible nanoparticles, nanogels and quantum dots using a multitude of modalities have been presented for pH imaging.[206, 207] They can be designed both to target disease specific surface structures and to detect pH.[208, 209] One approach, for example, uses magnetic discs spaced by swellable hydrogels that change their shape with pH, thus generating detectable pH-dependent magnetic fields.[210] Recently, the first multifunctional theranostic pH sensor for bimodal pH imaging and photodynamic therapy was developed.[211]

5.2 Hyperpolarized pH Sensor Molecules

Hyperpolarization is an effective approach to increase NMR signal amplitudes by up to five orders of magnitude[121] and to overcome the sensitivity limitations of traditional magnetic resonance spectroscopic imaging (MRSI). To this day, several

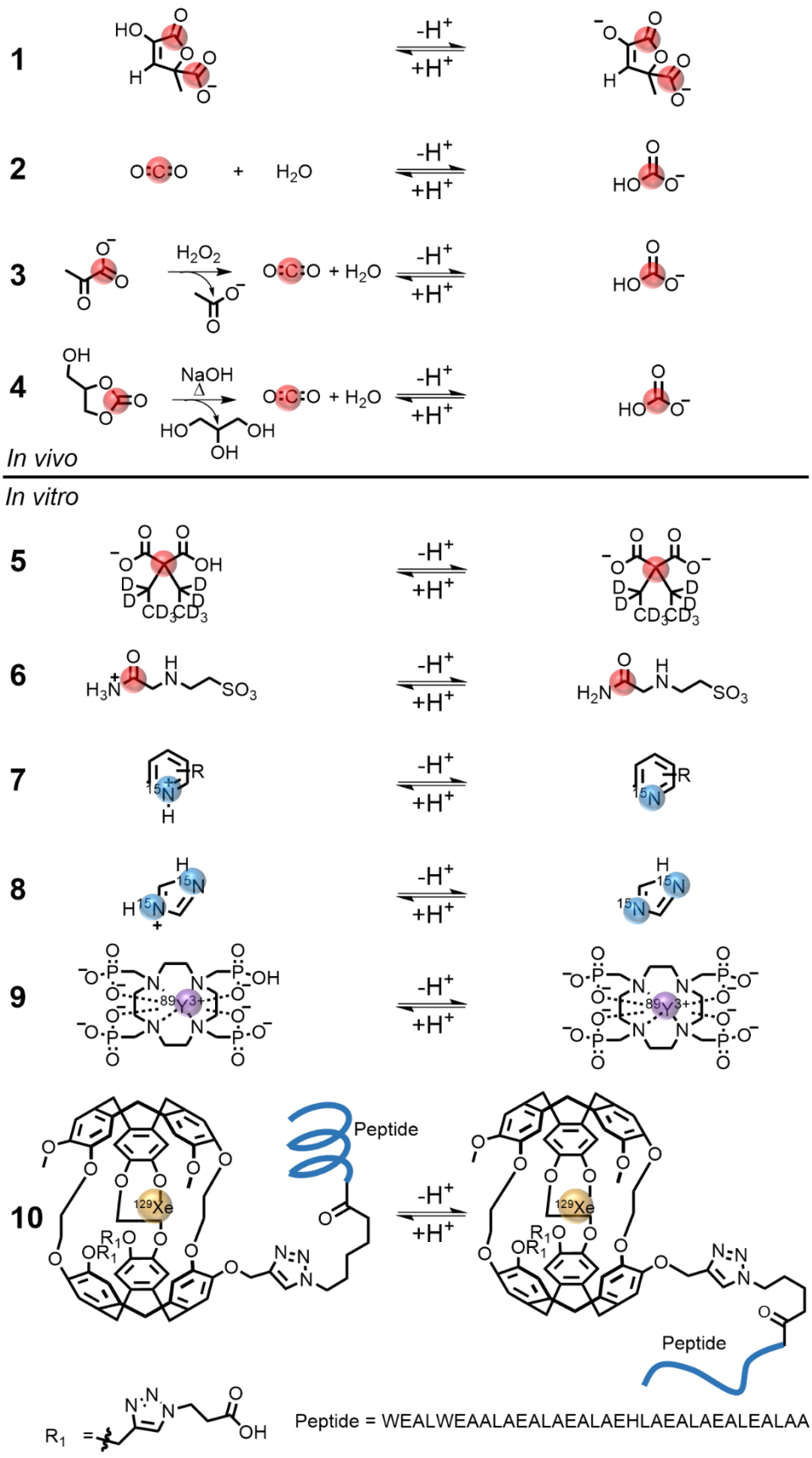

Figure 5.1: Hyperpolarized pH sensor molecules. Overview of pH-sensitive molecules labelled with ^{13}C, ^{15}N, ^{89}Y and ^{129}Xe (red, blue, violet, yellow, respectively) which have successfully been hyperpolarized. References and NMR properties of the molecules can be found in **Table 5.1**.

hyperpolarized molecules belonging to different molecular classes that are sensitive to pH at physiological and pathological pH values (pH 6.4 - pH 7.4) have been presented. These molecules are summarized in **Figure 5.1**. Their NMR properties as well as the respective references are given in **Table 5.1**.^{13}C-labelled [1,5-$^{13}C_2$]zymonic acid[78] (1) and ^{13}C-bicarbonate[166, 212] (2) are the only two molecules that have been applied to image pH_e in pre-clinical studies *in vivo*. Hyperpolarized ^{13}C-bicarbonate was presented in 2008 as the first hyperpolarized pH_e imaging sensor. In the following years, molecules such as [1-^{13}C]pyruvate[213, 214] (3) and ^{13}C-1,2-glycerol carbonate[215] (GLC, 4) were Investigated to be used as precursors of bicarbonate. Zymonic acid was recently presented as a novel pH_e sensor. It is a cyclic dimer of pyruvate, non-toxic, most likely accumulates in the vascular and extracellular space, and allows pH_e determination based on the pH-dependent chemical shifts of its two ^{13}C atoms with respect to a chemical shift reference. ^{13}C-labelled dicarboxylic acids[216] and molecules of the Good's buffers family[217] have been shown to be pH-sensitive *in vitro*. [2-^{13}C]diethylmalonic acid (5) and [1-^{13}C]N-(2-acetamido)-2-aminoethanesulfonic acid (ACES, 6) were used to generate pH images of buffered phantoms in MRI scanners. pH-sensitive hyperpolarized molecules that bear heteronuclei other than ^{13}C are ^{15}N-labelled pyridine derivatives[218] (7) and ^{15}N-imidazole[119] (8). Furthermore, the two chelators 1,4,7,10-tetraazacyclododecane-1,4,7,10-tetramethylene-phosphonic acid[219] (DOTP, 9) and a modified cryptophane cage[220] (10) have been loaded with hyperpolarized ^{89}Y and ^{129}Xe, respectively.

5.3 Hyperpolarization of pH Sensor Molecules

So far, three hyperpolarization techniques have been applied to increase the NMR signal intensity of molecules that are pH sensitive in the physiologically and pathologically relevant range: 1) spin exchange optical pumping (SEOP), 2) signal amplification by reversible exchange in shield enables alignment transfer to heteronuclei (SABRE-SHEATH) and 3) dissolution dynamic nuclear polarization (DNP).

SEOP is a polarization method that can be applied to noble gasses. First, circularly polarized laser light is used to selectively excite a D1 transition of an alkali metal vapor (e.g. rubidium). Then, spin exchange through collisions of the noble gas atoms with the polarized alkali metal atoms transfers the electron-polarization to the noble gas nuclei.[221] Hyperpolarized ^{129}Xe bound to a cryptophane cage which is coated with carboxylic acids shows a pH-dependent chemical shift at pH 3.5 - 5.[222] Similar properties at physiological pH were reported by Riggle et al. who have synthesized the xenoncryptophane pH sensor complex (10) that inserts into membranes of cancer cells at acidic pH.[220] SABRE transfers the polarization of parahydrogen via an activated

catalyst (iridium) to the compound of interest.[223] As this transfer is most efficient at a magnetic field strength smaller than that of the Earth's magnetic field, the apparatus is "shielded" by µ-tesla metals (SABRE-SHEATH).[118]

Table 5.1: Hyperpolarized *in vitro* pH_e and *in vivo* pH_e sensors.

pH sensor or precursor	Index	Nucleus	Reference	γ [MHz·T^{-1}]	Relative sensitivity (to ^{1}H) [%]	T_1 [s]	pK_a	δ_{min} [ppm]	δ_{max} [ppm]	$\Delta\delta$ [ppm]
Zymonic acid	**1**	^{13}C	[78]	10.71	1.59	51 ± 4 (3 T)	6.90	174.0 178.1	179.2 180.6	5.2 2.5
Bicarbonate	**2**	^{13}C	[166]	10.71	1.59	50 ± 3 (3 T)	6.17	Ratiometric approach		
Pyruvate as bicarbonate precursor	**3**	^{13}C	[213, 214]	10.71	1.59	67 ± 3 (3 T)	6.17	Ratiometric approach		
GLC as bicarbonate precursor	**4**	^{13}C	[215]	10.71	1.59	64 ± 6 (11.7 T)	6.17	Ratiometric approach		
Diethylmalonic acid	**5**	^{13}C	[216]	10.71	1.59	84 ± 1 (3 T)	7.39	60.1	63.4	3.3
ACES	**6**	^{13}C	[217]	10.71	1.59	25 (3 T)	6.58	170.5	178.9	8.4
Pyridine derivatives	**7**	^{15}N	[218]	4.31	0.10	31 ± 2 (9.4 T)	6.60	202	292	90
Imidazole	**8**	^{15}N	[119]	4.31	0.10	86 ± 2 (9.4 T)	6.95	174	205	31
Y-DOTP	**9**	^{89}Y	[219]	-2.09	0.012	123 ± 10 (9.4 T)	7.64	140	150	10
Xenon-cryptophane pH sensor	**10**	^{129}Xe	[220]	-11.77	1.62	64.8 ± 1.2 (11.7 T)	≈ 6	64.2	67.6	3.4

A major limitation of SABRE is the need of transient metal binding to the target compound, which restricts its application to a few molecule classes. Nevertheless, the method was already used to enhance the NMR signal of several ^{15}N-heterocycles like imidazole (8).[117, 119] Although direct parahydrogen induced polarization (PHIP) [115, 116] was not yet used for hyperpolarization of molecules that are pH-sensitive in the physiologically and pathologically relevant range, it might be possible to find an unsaturated precursor molecule, that, after addition of parahydrogen, yields a pH-sensitive molecule relevant for *in vivo* applications.[224, 225] Both SABRE and PHIP do not require the use of expensive cryogens and could offer a low-cost approach to generate hyperpolarized pH-sensitive molecules.

DNP is by far the most applied hyperpolarization technique for *in vivo* imaging and is already used in clinical studies.[128] Pre-clinical (HyperSense, Oxford Instruments)

and clinical (SPINlab, GE Healthcare) polarizers are commercially available and can increase the NMR sensitivity of several nuclei such as ^{13}C, ^{15}N or ^{89}Y by up to five orders of magnitude.[121] During DNP, polarization from electrons provided by free stable radicals (most commonly the trityl radical OX063) that exhibit ~95% electron polarization at a temperature of ~1.2 K and a magnetic field strength of 3.35 T (HyperSense) is transferred to the nucleus of interest in a frozen solid state. Clinical and several home-built polarizers operate at a higher magnetic field strength (up to 7.0 T) and are able to achieve more than 2-fold higher polarization levels than at 3.35 T.[226-230] After a sufficient polarization build up (usually ~0.5 - 2 h), the compound is dissolved by a pressurized, heated and pH buffered solution. The SPINlab hyperpolarizer is designed to filter potentially toxic radicals and includes a quality control mechanism to ensure that only physiologically tolerable solutions are injected. Further approaches to remove the radicals used during hyperpolarization exploit the low solubility of modified BDPA[231], organosilica[232] or agarose[233] bound radicals in aqueous solution, or the usage of immiscible mixtures of organic and aqueous solvent vapors that dissolve the radical and the hyperpolarized compound separately.[234] A radical free hyperpolarization technique relying on UV light induced polarization was recently proposed.[235] So far, ^{89}Y-DOTP (9), ^{15}N-pyridine derivatives (7), members of the Good's buffers family (6) and ^{13}C-dicarboxylic acids (5) have been polarized with DNP to sense pH changes *in vitro*. The only hyperpolarized molecules that have successfully been used to image pH_e *in vivo* are ^{13}C-bicarbonate (either hyperpolarized directly (2) or derived from ^{13}C-labelled and hyperpolarized precursor molecules (3, 4)) and ^{13}C-zymonic acid (1).

5.4 NMR-Mechanisms of pH-Sensitivity

The acid dissociation constant (pK_a) determines the center of the range of pH-sensitivity of an NMR-active nucleus. It is derived from the chemical equilibrium of two species - the acid (HA) and its conjugate base (A^-) - that are in pH-dependent exchange with the exchange rate *k*. If *k* is much smaller than the difference ($\Delta\nu$) in NMR resonance frequencies (in Hz) of HA and A^- ($k << \Delta\nu$), the two species are in slow exchange and two distinct peaks are observed (**Figure 5.2**). In this case, the pH can be determined by a ratiometric approach from either the signal amplitudes or integrals (I, **equation 5.1**). A prominent example is the equilibrium of bicarbonate (HCO_3^-) and carbon dioxide (CO_2), which has a moderate exchange rate of 0.1 Hz and a relatively large chemical shift difference of 35 ppm (≈ 1.1 kHz at 3 T).[166]

$$pH(\delta) = pK_a \pm log_{10}\left(\frac{I(A^-)}{I(HA)}\right) \quad (5.1)$$

If the two species are in fast exchange, i.e. if k is much larger than $\Delta\nu$ ($k >> \Delta\nu$), only a single peak will appear in the NMR spectrum. The observed chemical shift (δ) is the mean of the chemical shifts of HA and A^- weighted by the signal integrals. A modified

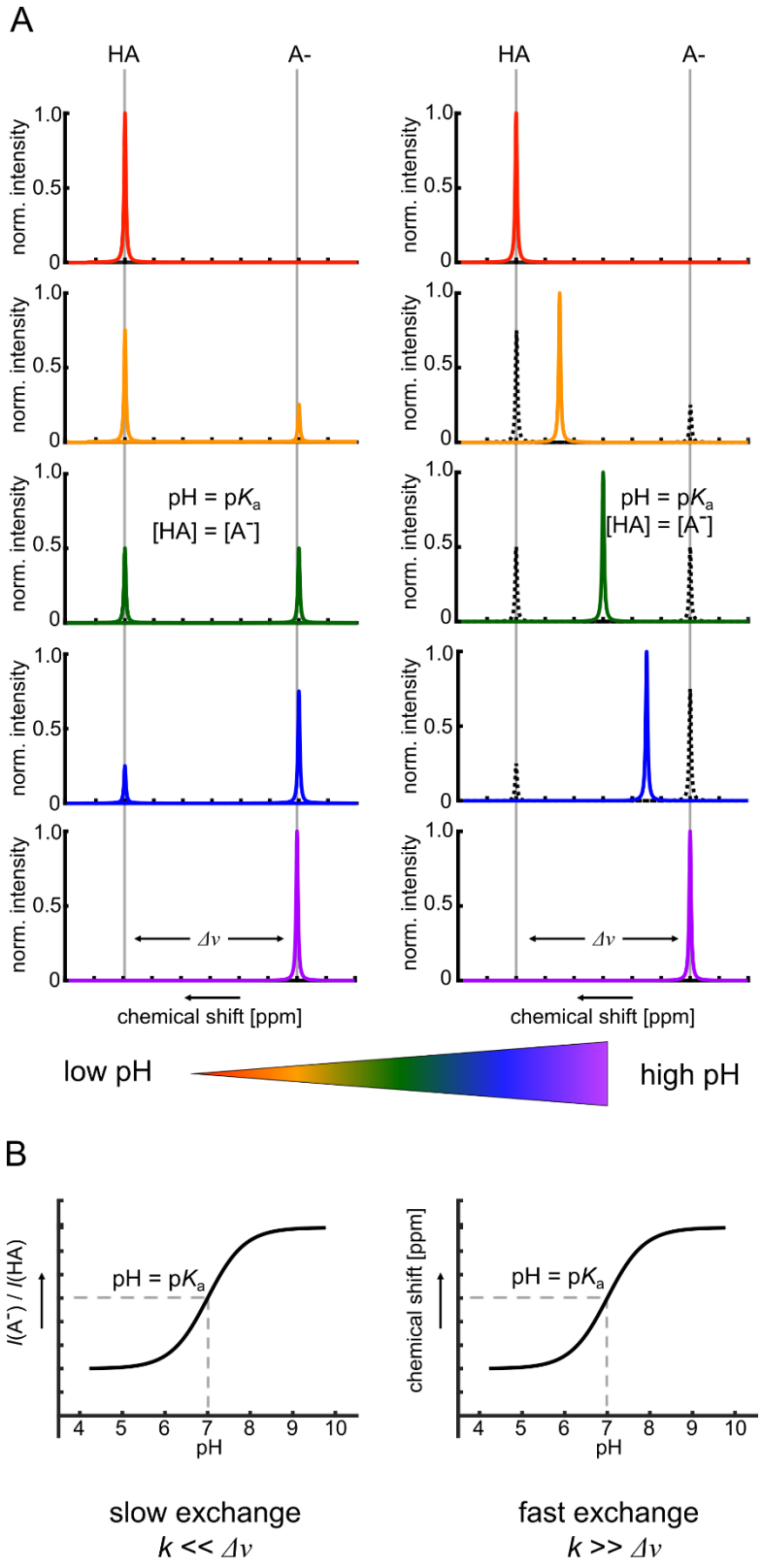

Figure 5.2. pH-dependent fast and slow chemical exchange of molecules with NMR resonance signals. (A) In slow exchange ($k << \Delta\nu$), two resonance signals at a distinct chemical shift are observed. Their signal amplitudes or integrals change with respect to pH (left column). A single resonance signal

shifts with respect to pH when HA and A^- are in fast exchange ($k >> \Delta\nu$). The theoretically observable fractions of HA and A^- are indicated in dashed lines (right column). **(B)** A modified Henderson-Hasselbalch equation allows the pH calculation from resonance signals that are in slow (**equation 5.1**) or fast (**equation 5.2**) exchange.

Henderson-Hasselbalch equation can be used to determine the pH from the observed chemical shift with the sign of the second summand being positive for downfield shifts and negative for upfield shifts with increasing pH values (**equation 5.2**). δ_{min} and δ_{max} are the lower and upper limits of the observed chemical shift and correspond to the chemical shift of the fully protonated and deprotonated form of the molecule or vice versa.

$$pH(\delta) = pK_a \pm log_{10}\left(\frac{\delta - \delta_{min}}{\delta_{max} - \delta}\right) \quad (5.2)$$

With the exception of bicarbonate (2, 3, 4) and the xenon-cryptophane pH sensor (10), all hyperpolarized nuclei in the molecules shown in **Figure 5.1** are in fast exchange. Their chemical shift differences range from 3 ppm to 100 ppm, which equals $\nu = 10^2$ - 10^3 Hz at 3 T. Exchange rates of hydroxyl and amino protons are on the order of 10^3 - 10^4 Hz.[236] In the case of the cryptophane-bound ^{129}Xe (10), its chemical shift is affected by a combination of pH-dependent peptide conformational changes and membrane insertion.

In vivo exchange rates of the mentioned pH sensors are dependent on several factors like proton diffusion, temperature and the pH itself. This could lead to a so-called intermediate exchange regime ($k \approx \Delta\nu$) for which the proton exchange rate is approximately equal to the frequency separation. The resulting resonance signal is characterized by a broad linewidth which is unfavorable for an accurate pH determination. Measuring at a different external magnetic field strength (ideally at a clinically relevant field strength) might be a possible solution to circumvent this problem.

5.5 Sensitivity, Signal Lifetime, pH-Sensitivity and Biocompatibility of pH Sensor Molecules

The pH biosensors shown in **Figure 5.1** bear different isotopically enriched (>99%) spin-½ nuclei (X). Their NMR sensitivity at thermal equilibrium with respect to hydrogen is defined by the gyromagnetic ratio $\gamma(X)^3/\ \gamma(^1H)^3$.[105] Hyperpolarization increases the NMR sensitivity, which can be quantified by the polarization enhancement or the polarization level. The polarization enhancement (ε) is the ratio of the hyperpolarized signal (S_{hyper}) to the thermal signal ($S_{thermal}$) measured under the same experimental conditions. The polarization level (P_{hyper}) can be determined by multiplying the thermal polarization level $P_{thermal}$ with ε (**equation 5.3**):[237]

$$P_{hyper} = \frac{S_{hyper}}{S_{thermal}} \cdot tanh\frac{\gamma(X)\hbar B_0}{2kT} = \varepsilon \cdot P_{thermal} \quad (5.3),$$

with $\hbar$ being the reduced Planck constant and k the Boltzmann constant. The relative sensitivities of ^{13}C and ^{129}Xe nuclei are similar to each other while the ones of ^{15}N and ^{89}Y nuclei are more than 10 - fold or 100 - fold smaller, respectively. Achievable polarization levels for ^{13}C, ^{129}Xe, ^{15}N, and ^{89}Y are 15 - 70%, 1 - 64%[238], 2 - 10% and 1 - 8%, respectively. To our best knowledge, ^{15}N and ^{89}Y nuclei have only been polarized using pre-clinical polarizers and their polarization levels can probably be enhanced by a factor of two if high-field polarization techniques are used.

For *in vivo* applications, hyperpolarized substances need to be transported from the polarizer to the scanner and prepared for injection. After administration, further time is required for the molecules to circulate in the blood and accumulate in the region of interest before signal acquisition is possible. Although these procedures can be accelerated and standardized, a high initial polarization level and a long spin lattice relaxation time (T_1, both *in vitro* and *in vivo*) are critical for hyperpolarized experiments. Hyperpolarized signals decay with the spin lattice relaxation time (T_1), which is mainly governed by dipolar coupling with neighboring protons. Dipolar coupling scales with γ^2 and the distance between the interacting nuclei (d^6). Heteronuclei with directly attached protons have a relative short T_1, which for instance makes ^{13}C-carbonyls favorable for hyperpolarization. If the molecule of interest is not symmetric, chemical shift anisotropy effects scaling with B_0^2 need to be taken into account as well.[120] In case dipolar coupling between high-γ nuclei (^1H) and heteronuclei is inevitable, deuterium enrichment is a feasible strategy to prolong T_1, which was demonstrated for hyperpolarized molecules, such as choline[239], glucose[240] and pyruvate[241]. So far, pH-sensitive dicarboxylic acids[216], e.g. (5), have been deuterated and thus exhibit long T_1 values of > 1 min even at high field strength (B_0 = 11 T).[216] The same strategy should be beneficial for hyperpolarized ACES (6) and zymonic acid (1), which contain replaceable protons as well.[78, 217]

Radical removal after dissolution is not only important to guarantee physiologically tolerable solutions for injections, but also to reduce paramagnetic relaxation between the pH sensor and the radical in solution. Techniques for radical filtering or radical free polarization for DNP were summarized in **chapter 5.3**.

In special cases where isotopically enriched nuclei of interest are directly attached to spin-1 nuclei (i.e. ^{13}C, ^{14}N), isotope exchange (i.e. ^{14}N vs. ^{15}N) is a feasible way to avoid fast scalar coupling relaxation to quadrupolar nuclei at Earth's magnetic field (i.e. ACES, 6). Alternatively, magnetic transfer lines[242] as well as hand-held permanent magnets[243] or specifically designed electromagnetic transport boxes[244] have been proposed to reduce this unfavorable relaxation process during transport of the samples and to increase T_1.[245]

Ji et al. showed that metabolites (or pH sensors) can be trapped in microparticles that physically separate them from paramagnetic polarization agents, which allows long time storage (up to 16 h) and facilitates a convenient transport of the hyperpolarized substances even to a remote MR scanner.[246] SAMBADENA (Synthesis Amid the Magnet Bore, A Dramatically Enhanced Nuclear Alignment) – a recent polarization approach based on PHIP – constantly produces the hyperpolarized substance directly in the MR scanner and avoids polarization losses during transport.[247]

Chemistry-based approaches to increase the polarization level and T_1 use well polarizable precursor molecules that yield the desired hyperpolarized pH sensor molecule at high concentrations after chemical decomposition. The most commonly used molecule used for hyperpolarization, [1-^{13}C]pyruvate, yields ^{13}C-bicarbonate in presence of hydrogen peroxide (3).[213, 214] Korenchan et al. have recently presented ^{13}C-enriched carbonates which decompose to sodium bicarbonate and biologically tolerable side products (4).[215] These precursors have up to three-fold longer T_1 times than bicarbonate, which saves magnetization during transport and sample preparation.[166, 248]

Another elegant approach to prolong hyperpolarized signal lifetime exploits the phenomenon of so-called long-lived states, which are prevalent in molecules bearing a pair of magnetically equivalent spin-½ nuclei.[249-251] They form either a triplet or singlet nuclear spin state, with the lifetime of the singlet state being potentially much longer than T_1, since it is not affected by dipolar relaxation mechanisms. Although long-lived states cannot be directly observed by NMR, magnetization can be transferred from the triplet to the singlet state for storage and later on be recovered for the experiment by chemical reactions[252], specific pulse sequences[253-255] or at low µ-tesla magnetic fields.[256, 257] This concept has not yet been applied to pH-sensitive molecules, but it was already used *in vivo*[256] and could potentially increase the available signal intensity of hyperpolarized pH imaging molecules as well.

Although the signal enhancement is highest for ^{13}C-nuclei, their T_1 is shorter compared to ^{15}N and ^{89}Y. The T_1 of ^{129}Xe is in a similar range as the one of ^{13}C. Nonetheless, DNP polarization techniques combined with efficient transportation and fast acquisition techniques (see **chapter 5.7**) allow for the acquisition of a pH image within a few seconds.

In general, the highest pH-sensitivity of a pH biosensor is around its pK_a. For ratiometric approaches, an accurate pH determination requires a high SNR, which minimizes potential errors of the quantification of the signal amplitudes (or integrals). Hyperpolarized bicarbonate (2) was the first and so far only ratiometric sensor applied both *in vitro* and *in vivo*.[166] A main drawback of the molecule is its short T_1 (*in vivo* ~10 s at both 3 T and 9.4 T[166, 248]) and a small SNR of $^{13}CO_2$ at physiological pH due to the low pK_a.[248, 258]

The pH sensitivity of chemical shift based sensors is given by Δδ, the difference of the maximum and minimum observed chemical shift. The bigger Δδ, the higher the pH-sensitivity of the sensor. **Table 5.1** gives an overview of the pH-sensitivity of chemical shift based sensors. Proton binding and dissociation at the nitrogen of ^{15}N-heterocycles changes the chemical environment of the NMR-active nucleus leading to the largest chemical shift changes, compared to ^{89}Y-DOTP (9), ^{129}Xe cryptophane (10) and ^{13}C-labelled pH biosensors (1, 5, 6). However, the suggested ^{15}N-labelled pH sensors (7, 8) are likely to be toxic and would therefore not be transferable to the clinic. DOTP (9) forms high affinity complexes with yttrium[259] and has a relatively large Δδ of ~10 ppm, but toxicity and low sensitivity of ^{89}Y also preclude this sensor from *in vivo* use. The xenon-cryptophane sensor (10) and ^{13}C-labelled chemical shift pH sensors (1, 5, 6) have a similar pH sensitivity, ranging from Δδ ≈ 2.5 ppm to Δδ ≈ 8 ppm, and cryptophanes have also already been shown to be non-toxic when applied in cell experiments.[260-262] The pH determination using the ^{129}Xe sensor in HYPER-CEST experiments allows a targeted detection of aberrant pH at picomolar concentrations *in vitro*. The two advantages of the chemical shift based ^{13}C pH sensors (1, 5) are a high polarization level and – except for ACES (6) – a long T_1. For diethylmalonic acid (5), the toxicopathological profile needs to be evaluated for *in vivo* compatibility. Zymonic acid (1) is used as a food additive and flavouring agent[263] and does not show toxicity against cells and rodents.[78] The molecule is synthesized from [1-^{13}C]pyruvate and exhibits two pH-sensitive carbon atoms. It is the first hyperpolarized chemical shift based pH sensor that was successfully applied *in vivo* (see **chapter 5.8**).

5.6 Screening Strategies for New Hyperpolarizeable ^{13}C pH_e Biosensors

Hyperpolarized ^{13}C pH sensors need to have an exchangeable proton, e.g. in a carboxylic acid-, stable enol- or amine-group, that is close to a ^{13}C nucleus with long T_1. For *in vivo* use, the pK_a of this proton should be between 6.4 < pK_a < 7.6 in order to detect aberrant changes compared to the physiological pH_e.[217-219]

Small molecules are in general favorable, as they are easy to synthesize and to label and since they tend to have a long T_1, which decreases as a function of the molecule size and correlation time (τ_c). Because dipolar coupling with high-γ spin-½ nuclei determine the magnetization loss and T_1 shortening to a major extent, systems without directly neighboring protons to the hyperpolarized nucleus are favorable. Fortunately, most pH-sensitive functional groups like carbonyls and carboxylic acids are devoid of directly attached protons. For an efficient hyperpolarization based on DNP, the molecule should be self-glassing or soluble at high concentrations (> 4 M) in common glassing agents such as dimethyl-sulfoxide, glycerol or N,N-dimethylacetamide.[120]

Furthermore, non-toxicity and sufficient chemical stability during the dissolution process and in aqueous solution is necessary.

Before being applied *in vivo*, the pH-sensitivity (pK_a) of potential pH sensor candidates should be proven to be independent of the following five parameters: 1) sensor concentration, 2) temperature, 3) ionic strength, 4) bivalent metal ions[217] and 5) proteins. This is because sensor concentration, temperature and ionic strength may vary slightly in different tissues, and because bivalent metal ions and proteins are present *in vivo*. Both ions and proteins can complex or unspecifically bind to the sensor molecule, which potentially alters the pH-sensitive mechanism and might lead to an erroneous pH determination.[78]

5.7 MR Acquisition Strategies for Hyperpolarized pH-Sensitive Nuclei

The requirements for MRI sequences with regard to spectral resolution depend on the underlying mechanism of the pH sensor molecule: For molecules in the slow exchange regime, such as ^{13}C-bicarbonate (2, 3, 4), two distinct NMR resonances need to be detected, whereas for molecules in the fast exchange regime, such as zymonic acid (1), one varying, pH-dependent chemical shift of a pH-sensitive nucleus with respect to a reference peak needs to be resolved.

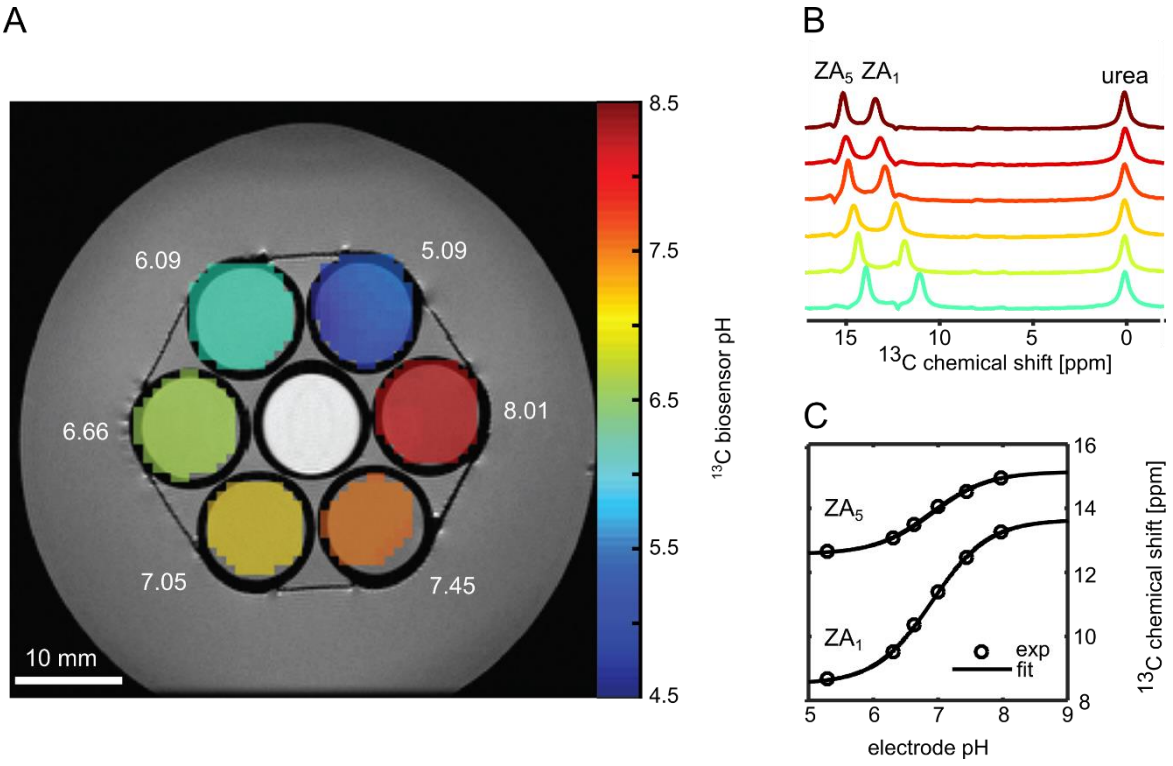

Figure 5.3. *In vitro* pH measurement using a CSI sequence and hyperpolarized zymonic acid (ZA) as a pH sensor. (A) pH images (colored scale) in an axial slice overlaid on proton images (grayscale). The electrode pH values are shown in white. ZA and urea were simultaneously hyperpolarized and injected into six buffer phantoms prepared at different pH values. **(B)** Spectra of hyperpolarized ZA and

urea in buffer phantoms at different pH values. The pH-sensitivity in the physiological range leads to a change of the chemical shifts of the two ^{13}C-labelled carbon positions with respect to the pH insensitive ^{13}C-urea peak as a function of pH. **(C)** A modified Henderson-Hasselbalch equation fitted to the data from (B) results in a calibration curve with a direct dependence between chemical shift and pH. **Figure 5.3** was adapted from Ref. [78].

The most straightforward method for spatial imaging of pH using hyperpolarized compounds either in fast or slow exchange is a 2D chemical shift imaging (CSI) sequence,[126, 264] as shown in **Figure 5.3** in an *in vitro* phantom experiment. CSI has been applied with different gradient encoding strategies such as Cartesian, spiral, or radial readouts and can be combined with variable flip angle schemes to increase the encoding efficiency.[265] A strategy to speed up the inherently slow phase-encoded CSI sequence is the use of an echo-planar spectroscopic imaging (EPSI) readout, which allows to acquire spectroscopic images within a couple of seconds.[126, 266] EPSI increases the gradient hardware and magnetic field homogeneity requirements but reduces the time needed to acquire an image, thereby improving SNR and real resolution.[126]

For the case of ^{13}C-bicarbonate (2, 3, 4), three alternative acquisition schemes were applied for pH imaging: first, a Dixon-type IDEAL spiral CSI[124, 248], second a gradient-echo sequence which utilized a resulting spatial shift in the frequency encoding direction between the bicarbonate and CO_2 resonances for separation of the respective signals[214] and third, a 3D double spin-echo pulse sequence with a flyback echo-planar readout trajectory[267]. However, for pH sensors in the slow exchange regime in general, the large decrease of one of the two signals at pH values far from the pK_a remains a challenge, because the increased noise of the smaller of the two resonances is problematic for the determination of a signal ratio.[248]

For pH sensors in the fast exchange regime, a larger change in chemical shift as a function of pH allows for a higher accuracy of the pH measurement but also comes with drawbacks: RF excitation pulses need to cover a larger bandwidth, which is challenging for the RF pulse design. If resonances are spread out further, chemical shift displacement artifacts impede accurate slice selective excitation of all pH-sensitive resonances. These limitations could pose a challenge for ^{15}N-labeled probes based on pyridine derivatives (7) and imidazole (8) that have been reported to show pH-dependent changes of chemical shifts of more than 80 ppm.[119, 218]

5.8 *In Vivo* pH_e Imaging with Hyperpolarized ^{13}C-Nuclei

So far, hyperpolarized ^{13}C-bicarbonate (2, 3, 4) and [1,5-$^{13}C_2$]zymonic acid (1) have been used to image pH_e *in vivo* in pre-clinical studies.

Brindle et al. pioneered the field of hyperpolarized pH imaging by introducing ^{13}C-bicarbonate as the first hyperpolarized *in vivo* pH_e imaging sensor. They demonstrated

the feasibility of hyperpolarized ^{13}C pH imaging by probing the acidic tumor microenvironment of EL4 lymphoma (**Figure 5.4**).

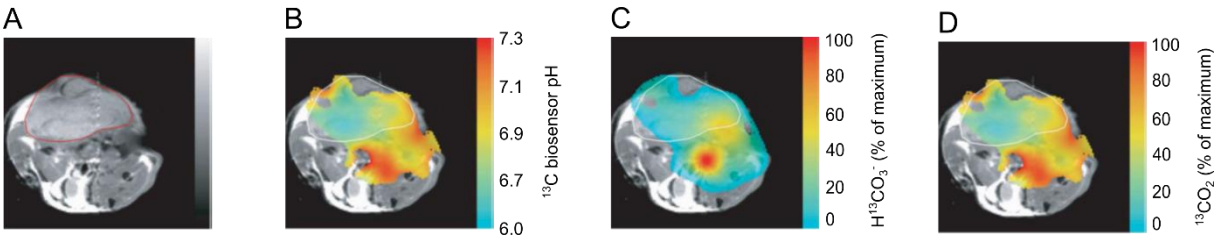

Figure 5.4. *In vivo* pH_e imaging with hyperpolarized ^{13}C-labelled bicarbonate. (A) Axial proton image of a mouse bearing a subcutaneous EL4 tumor. **(B)** pH_e image calculated from the ratio of the intensity images of bicarbonate in **(C)** and carbon dioxide in **(D)**. The tumor is outlined in red, in (B-D) in white. Adapted and with permission from [166].

Upon treatment with bicarbonate and ammonium chloride, bicarbonate showed pH_e alterations, which were confirmed by spectroscopic ^{31}P pH_e measurements with 3-APP.[3] Other studies detected an acidic tumor microenvironment in transgenic adenocarcinoma of mouse prostate (TRAMP).[215, 267] Scholz et al. induced an acute inflammation with Concavalin A and measured an acidic pH 7.0 compared to systemic blood pH 7.4.[248]

Zymonic acid is a cyclic dimer of pyruvic acid and can be synthesized in one step and in reasonable quantities. Physiological parameters that could influence the pH_e sensitivity do not affect its pK_a (see **chapter 5.6**). Düwel et al. co-polarized ZA with ^{13}C-urea to back-calculate the *in vivo* pH_e from a calibration curve (**Figure 5.3**). Zymonic acid was demonstrated to image the pH_e of three kidney compartments indicating the renal blood filtration process (**Figure 5.5**). Furthermore, an acidification of the tumor microenvironment of subcutaneous mammary adenocarcinoma (MAT-B-III) was imaged and confirmed with 3-APP and invasive measurements with an optical electrode. Both bicarbonate (2) and zymonic acid (1) have advantages and disadvantages. Bicarbonate has a relatively short T_1 and CO_2 freely diffuses through membranes. The measured pH is therefore a mean of the extra- and intracellular pH although the value seems to be rather weighted towards the extracellular fraction.[212] In disease states, carbonic anhydrase, which speeds up the process of reaching a steady state in the bicarbonate/CO_2 equilibrium, could partially be inhibited, which could impair the accuracy of the measurement. Nonetheless, the use of highly polarizable precursors makes this endogenous compound promising for further *in vivo* applications.

Zymonic acid has a longer T_1 *in vivo* than bicarbonate and distributes in vascular and extravascular (interstitial/extracellular) compartments. The signal stemming from the vascular compartment after intravenous injection of zymonic acid is dominant because of the large blood pool. The detection of other compartments is challenging because it requires a sufficient chemical shift separation compared to the signal in blood and a sufficient signal-to-noise ratio. However, it has been demonstrated both in tumor and

kidney that the interstitial/extracellular pH_e can be detected simultaneously together with the vascular pH within the same voxels, rendering this molecule interesting for further *in vivo* applications.[78]

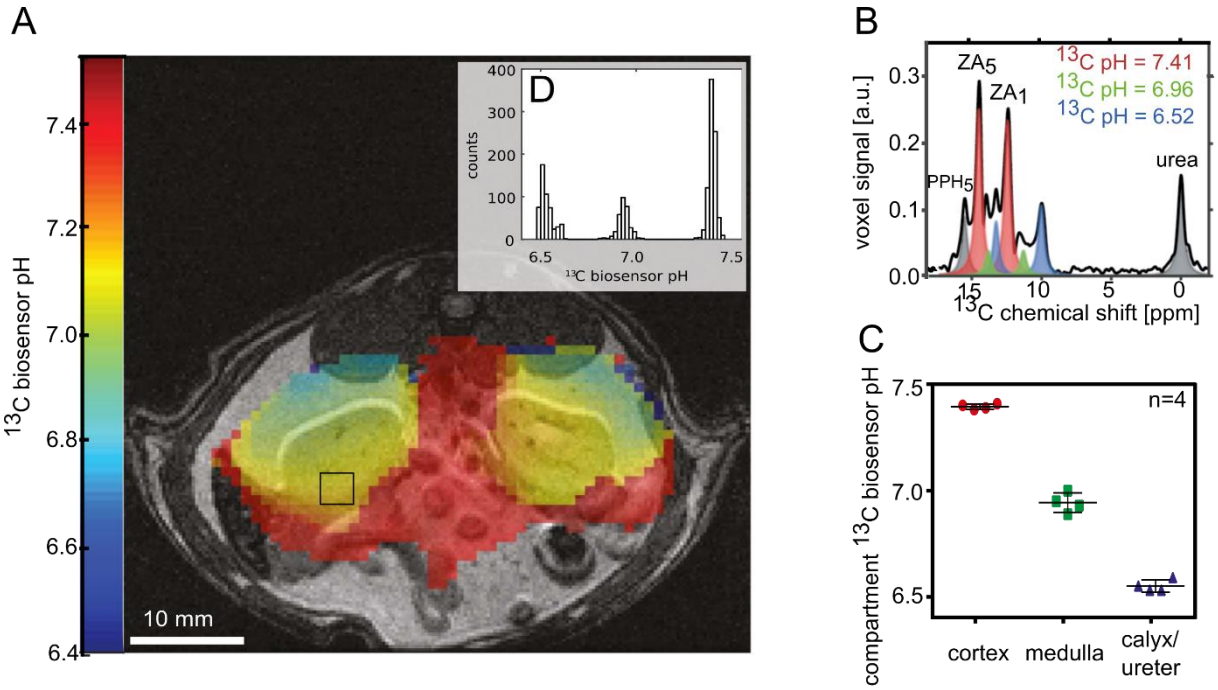

Figure 5.5. ***In vivo*** **kidney pH_e imaging with hyperpolarized zymonic acid. (A)** Mean pH_e image of a kidney from a hyperpolarized ^{13}C measurement using zymonic acid (colored scale) in an axial slice overlayed on an anatomical proton image (greyscale). Mean pH_e values are lower in the kidneys than in the surrounding tissue. A voxel **(B)** contains up to three pairs of zymonic acid resonance signals (colored in red, green and blue). The pH_e values indicate the renal filtration process of the blood (**C**, data points of four animals given as mean ± standard deviation) and cluster into three groups (**D**, data from a representative animal). **Figure 5.5** was adapted from Ref. [78].

5.9 Conclusion

Many efforts have been undertaken to develop imaging methods for quantitative, non-invasive pH_e imaging. However, so far, none of these techniques has been applicable in the clinic. In patients, local deviations from the systemic pH are often caused by pathologies, such as cancer, inflammation, infection, ischemia, renal failure or pulmonary disease, making pH a potentially useful clinical imaging biomarker.

During the last decade, several hyperpolarized pH_e sensor molecules using various polarization techniques have been developed (**Figure 5.1** and **Table 5.1**). The underlying mechanism of pH-sensitivity for all of these techniques is a pK_a-dependent protonation or deprotonation in the vicinity of the hyperpolarized nucleus. This leads to a pH-dependent chemical shift for nuclei in fast exchange and to a change in the signal ratio for nuclei in slow exchange. Efficient, robust and fast pH imaging approaches for hyperpolarized nuclei are available. In addition, prolongation of T_1 by deuteration or

long-lived spin states could be exploited in the future as a strategy to enhance NMR-sensitivity.

Two hyperpolarized pH_e sensors have so far been applied *in vivo*: hyperpolarized ^{13}C-bicarbonate and [1,5-$^{13}C_2$]zymonic acid. Using both sensors, it was possible to measure extracellular tissue acidification in tumors. Bicarbonate was used to detect a decrease in pH in acute inflammation and zymonic acid resolved three different pH compartments within the same renal voxel, where the ability to resolve more than one pH compartment per voxel is a unique feature of fast exchanging pH-sensitive molecules. Therefore, both ^{13}C-bicarbonate and zymonic acid have demonstrated promising results for pH_e imaging in pre-clinical animal models. Besides increasing NMR-sensitivity and spatial resolution of the imaging approaches, future work needs to evaluate the benefit of pH imaging techniques for specific diagnosis and monitoring of disease as well as for specific selection and prediction of therapies. Since intravenous injections of both bicarbonate and zymonic acid have shown no toxic side-effects and since hyperpolarized pyruvate is already being used in clinical studies, the translation of hyperpolarized pH_e sensors to the clinic seems promising.

6. Deuteration of Hyperpolarized ^{13}C-labeled Zymonic Acid Enables Sensitivity-Enhanced Dynamic MRI of pH

Christian Hundshammer, Stephan Düwel, Simone S. Köcher, Malte Gersch, Benedikt Feuerecker, Christoph Scheurer, Axel Haase, Steffen J. Glaser, Markus Schwaiger and Franz Schilling

This chapter is an amended version of [122].

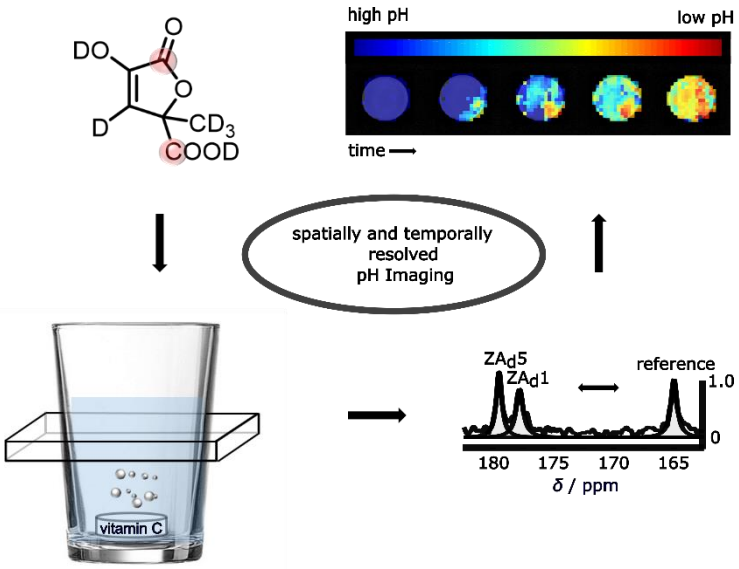

Summary

Aberrant pH is characteristic of many pathologies such as ischemia, inflammation or cancer. Therefore, a non-invasive and spatially resolved pH determination is valuable for disease diagnosis, characterization of response to treatment and the design of pH-sensitive drug delivery systems. We recently introduced hyperpolarized [1,5-$^{13}C_2$]zymonic acid (ZA) as a novel MRI probe of extracellular pH utilizing dissolution dynamic polarization (DNP) for a more than 10,000-fold signal enhancement of the MRI signal. Here we present a strategy to enhance the sensitivity of this approach by deuteration of ZA yielding [1,5-$^{13}C_2$, 3,6,6,6-D_4]zymonic acid (ZA_d), which prolongs the liquid state spin lattice relaxation time (T_1) by up to 39% *in vitro*. Measurements with ZA and ZA_d on subcutaneous MAT-B-III adenocarcinoma in rats show that deuteration increases the signal to noise ratio (SNR) by up to 46% *in vivo*. Furthermore, we demonstrate proof of concept for real-time imaging of dynamic pH changes *in vitro* using ZA_d, potentially allowing for the characterization of rapid acidification/basification processes *in vivo*.

6.1 Introduction

Complex buffer systems maintain a constant extracellular pH (pH_e) of 7.35 – 7.45 which is necessary for cellular and sub-cellular functions in healthy tissues. Diseases like ischemia, inflammation, and tumors can overcome these regulatory mechanisms and locally alter pH[29], which is critical for disease evolution and drug efficacy[268]. The knowledge of local pH is therefore beneficial for the diagnosis of pathologies and for the design of targeted drug delivery platforms, which release therapeutics in acidic environments.[70, 269] In addition, imaging of pH could assist in monitoring and individualization of treatments, thereby contributing to the concept of personalized medicine.[189]

Several approaches for non-invasive pH imaging *in vivo* have been proposed, including optical fluorescence[180, 206, 270] and positron emission tomography (PET).[175, 271] Because of its good spatial resolution, high penetration depth and the use of non-ionizing radiation, the majority of pH imaging methods are based on magnetic resonance (MR). They exploit pH-dependent relaxivity and chemical exchange saturation transfer (CEST) properties of exogenous[272, 273] and endogenous[33] molecules or rely on pH-sensitive nuclear magnetic resonance (NMR) signals.[179, 189]

Dynamic nuclear polarization (DNP) is an effective method to increase the NMR signal up to more than four orders of magnitude, which drastically reduces scan times and enables magnetic resonance spectroscopic imaging (MRSI) of metabolites at micromolar concentrations. The development of DNP triggered the search for *in vivo* sensors bearing different hyperpolarizable heteronuclei that are sensitive to pH.[113] Most of them were used to investigate the acidification of the tumor micro-environment, caused by the Warburg effect, hypoxia and low perfusion.[166, 216, 218] However, even though hyperpolarization creates a large signal enhancement, the signal irreversibly decays after dissolution with the longitudinal relaxation time (T_1), reducing the time available for data acquisition to a few tens of seconds. The impact of this limitation of DNP-based sensors - which also affects the pH-sensors ^{13}C-bicarbonate[248] and Good's buffers[217] - can be reduced by designing long-lived precursor molecules[215] or by deuterium enrichment. We recently discovered hyperpolarized [1,5-$^{13}C_2$]zymonic acid (ZA), which exhibits pH-sensitive chemical shifts, a high polarization level (22 ± 2%) and a long T_1 *in vivo* (17 ± 2 s at 7 T) and *in vitro* (51 ± 4 s at 3 T).[78] The molecule has been able to spatially resolve the pH_e of three renal compartments and an acidic microenvironment of mammary adenocarcinoma.[78] Herein, we show that deuteration of ZA further enhances the sensitivity of pH imaging *in vivo* and even enables time-resolved pH imaging on a timescale of seconds.

6.2 Results and Discussion

The relaxation constants of carbon nuclei are mainly governed by dipolar couplings,[120] which scale with the gyromagnetic ratio (γ). Replacement of adjacent protons is an effective way to prolong the T_1 of carbon nuclei because the γ of deuterium (^{2}H) is ≈ 6.5 fold smaller than the one of hydrogen.[239, 240] ZA is a cyclic condensation product of pyruvic acid. It bears three methyl protons and one enol proton (H_3), all of which can be substituted with ^{2}H. To synthesize deuterated ZA, we deuterated ^{13}C-pyruvate by exchanging its protons with ^{2}H at pH > 10[241, 274], which formed deuterated parapyruvate if incubated for two days. Final removal of D_2O yielded zymonic acid with > 99% deuterium enrichment at position six and ≈ 88% at position three (**Figure S6.1**).

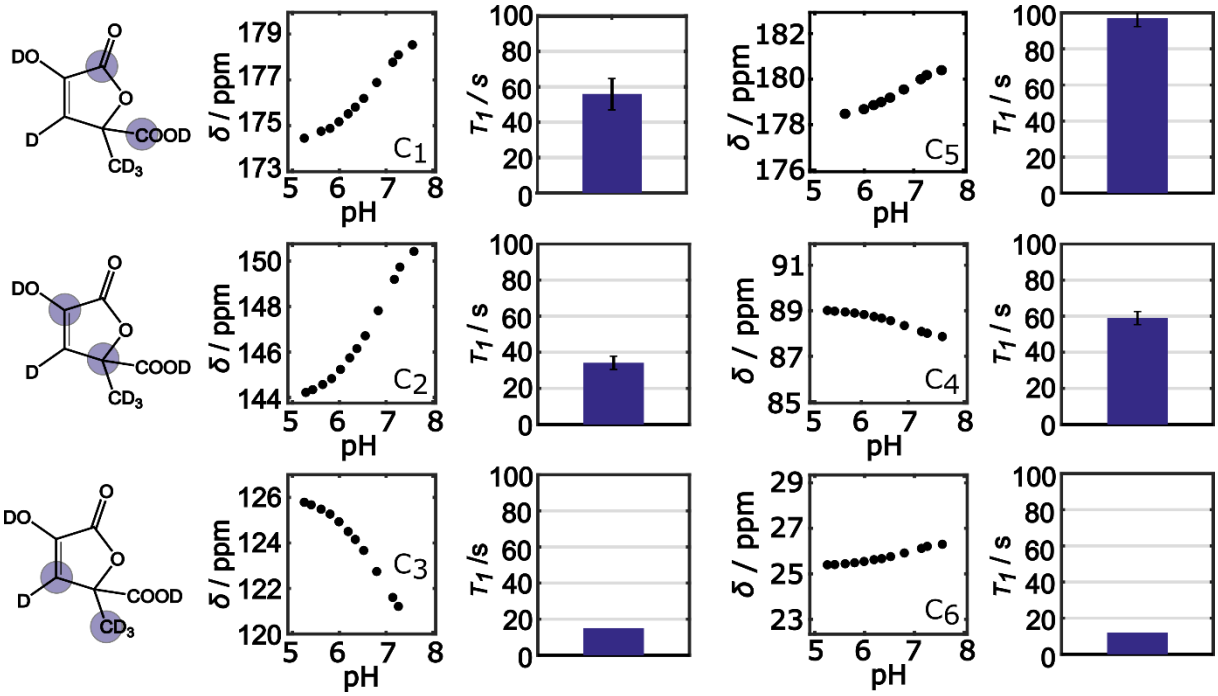

Figure 6.1: T_1 values and pH-dependent chemical shifts of the carbon atoms of ZA_d. Closer proximity to the pH-sensitive hydroxyl group (respectively -OD group) results in a larger pH-dependent change in chemical shift, but decreases T_1 mainly due to dipolar couplings with exchangeable protons. The best trade-off between pH sensitivity and T_1 is observed for carbon atom C_1. (carbon atoms C_1, C_2, C_4 and C_5: n = 3; carbon atoms C_3 and C_6: n = 1 for T_1 measurements; values are given as mean ± *std*; experiments where performed at 1T in D_2O). Note that titration experiments where performed in aqueous solution containing 10% D_2O.

Ab initio calculations of the ^{13}C chemical shieldings of ZA confirm that the enol form is the prevalent structure in aqueous solution and that dissociation of the hydroxyl proton causes significant ^{13}C chemical shift changes. By including interactions of ZA with solvent water molecules explicitly, the trends of the pH induced chemical shift differences could be reproduced quantitatively in silico (see **supplement M6.4**).

Table 6.1. *In vitro* T_1 values (B_0 = 1 T and 3 T) of ZA and ZA_d.

B_0 [T]	T_1 [s]	T_1 [s]	T_1 gain [%]	T_1 [s]	T_1 [s]	T_1 gain [%]
	C_1(ZA)	C_1(ZA_d)	C_1	C_5(ZA)	C_5(ZA_d)	C_5
1	44 ± 6	56 ± 9	27	70 ± 5	97 ± 5	39
3	43 ± 5[a]	49 ± 8	14	51 ± 4[a]	71 ± 3	39

[a] Data from Düwel et al.[78]

Closer proximity of a ^{13}C nucleus to the pH-sensitive hydroxyl group of ZA results in a stronger sensitivity of its chemical shift (δ) with pH, but at the same time shortens its T_1, which is mainly attributed to dipolar couplings of carbons with exchangeable protons (or deuterons). This dependency was analyzed using selectively labeled [1,5-$^{13}C_2$, 3,6,6,6-D_4]ZA, [2,4-$^{13}C_2$, 3,6,6,6-D_4]ZA and [3,6-$^{13}C_2$, 3,6,6,6-D_4]ZA. T_1 values of all carbon atoms of ZA_d (B_0 = 1 T) compared to the respective pH sensitivities of their chemical shifts are summarized in **Figure 6.1**. The best trade-off between pH sensitivity and T_1 is observed for C_1 ($\delta \approx$ 2.3 ppm at pH 6.4 - 7.4, T_1 = 56 ± 9 s, n = 3, with n being the number of measurements). If [1-^{13}C]pyruvate is used for synthesis, C_5 is also labeled with ^{13}C. Its resonance signal shifts ≈ 1.2 ppm between pH 6.4 - 7.4 and it exhibits the longest T_1 = 97 ± 5 s (n = 3) of all of ZA's carbon atoms (**Table 6.1**). Deuteration increases the T_1 values by 27% (C_1) and 39% (C_5) at 1 T (in D_2O, n = 3) compared to undeuterated zymonic acid.

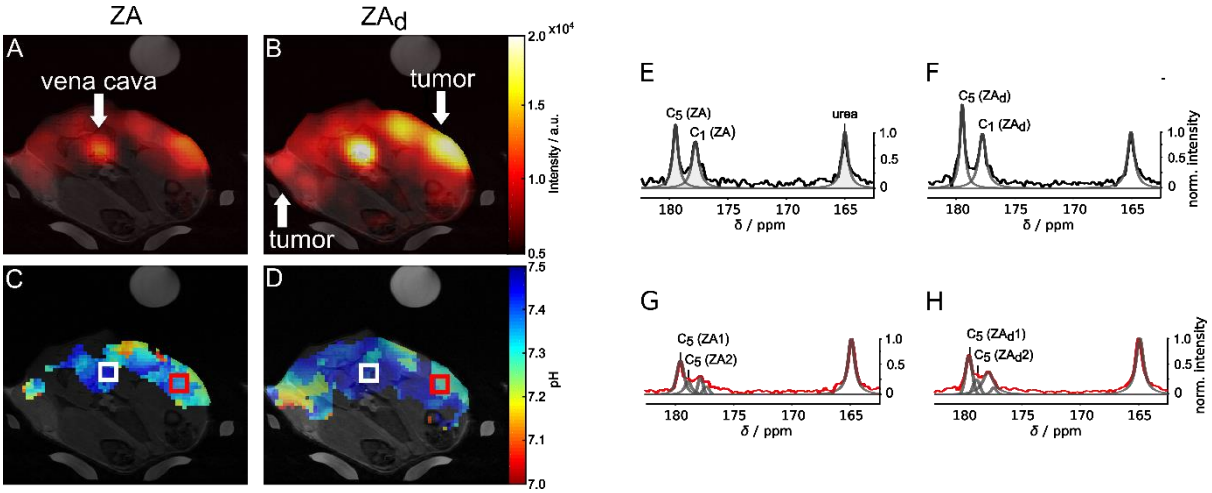

Figure 6.2: *In vivo* SNR comparison of ZA and ZA_d. ZA intensity images acquired from axial slices after tail-vein injection of ZA **(A)** and ZA_d **(B)** overlaid on anatomical T_1-weighted ^1H images. The images are masked to the ^1H images of the animal. (**C** and **D**) pH images calculated from the chemical shift differences of C_5 and urea, weighted by the respective signal intensities, show an acidification of the tumor environment. Only signals greater than 30% of the maximum intensity of (B) are displayed for both (A) and (B). (**E** and **F**) ZA and ZA_d spectra of a representative voxel of the vena cava (black squares), indicating the physiological blood pH. (**G** and **H)** Representative spectra of a tumor voxel (red squares) show two pairs of ZA or ZA_d, which indicate a vascular tumor pH ~ 7.5 and an acidic extracellular pH ≈ 7.1 when compared to the vena cava spectra which show only one ZA or ZA_d peak

pair corresponding to the blood pH ≈ 7.5. Spectra are normalized to the intensity of the urea signal (set to 1).

At clinical field strength (B_0 = 3 T, buffered aqueous solution, n = 3), the T_1 increase is 14% (C_1) and 39% (C_5). The different T_1 gains due to deuteration of C_1 at different field strengths indicate that its T_1 is stronger affected by chemical shift anisotropy[275] effects than the T_1 of C_5. T_1 decay curves can be found in **Figure S6.2-4**.

In vivo, we compared successive static measurements of ZA and ZA_d in rats bearing subcutaneous MAT-B-III tumors in a 7 T small animal MRI system (**Figure 6.2**). In both cases, the same amounts of pH sensor and urea (c_{final} = 50 mM and 75 mM, respectively) were polarized to saturation and the time between dissolution and data acquisition was kept equal for each set of experiments (**Table M6.2**). An accumulation of ZA and ZA_d in well perfused tumors and a noticeable amount of signal from the blood pool of the vena cava is visible in the signal intensity maps (**Figure 6.2A** and **B**). Both images were scaled to the same maximum intensity revealing an SNR gain by deuteration which amounts to 43 ± 16% and 46 ± 4% for C_1 and C_5, respectively (n = 3). We observed two peak pairs of zymonic acid in the malignant regions, which we assigned to the vascular and the interstitial/extracellular tumor pH compartments.[78] In order to visualize the acidification of the tumor environment compared to the vena cava, we calculated pH images from the chemical shift difference between the C_5 and urea peaks weighted by their respective signal intensities (**Figure 6.2C** and **D**). Both ZA and ZA_d indicate an acidification of the tumor environment. However, the higher signal amplitudes of ZA_d allow to image pH_e also in low-perfused tumor regions (**Figure S6.5**). Representative spectra of vascular vena cava voxels (**Figure 6.2E** and **F**) show one peak pair of ZA corresponding to a pH 7.53 ± 0.08 (mean ± *std*, calculated from vena cava regions of interest (ROI), n = 3 animals). Spectra of tumor voxels (**Figure 6.2G** and **H**) display two peak pairs of ZA indicating the pH of the vasculature in the tumor 7.58 ± 0.01 (entire tumor ROI, mean ± *std*, n = 3 animals) and the extracellular tumor pH 7.10 ± 0.05 (entire tumor ROI, mean ± *std*, n = 3 animals).

Longer lifetime of hyperpolarized magnetization of ZA_d can be utilized to monitor dynamic pH changes. *In vivo*, this could potentially be used to study fast acidification/basification processes either induced by treatments or upon metabolic changes, e.g. during exercise. For an *in vitro* proof of concept experiment, we added powdered vitamin C stepwise (60 mg, 30 mg, and 2 x 20 mg) to a Tris-buffered solution containing co-polarized ZA_d and urea. We then acquired a time-resolved series of pH images at a clinical 3 T MRI scanner (**Figure 6.3A** and **B**). The first image (t = 6 s) represents the pH of the solution in absence of vitamin C. After each addition of vitamin C, the solution was mixed gently and pH changes were dynamically observed for more than one minute. During the acquisition of the last four images, no further vitamin C was added. The initial pH measured by our sensor was pH 7.58 ± 0.02 (mean ± std). Spectra, summed over the same ROI of each timestep, can be found in **Figure S6.6.**

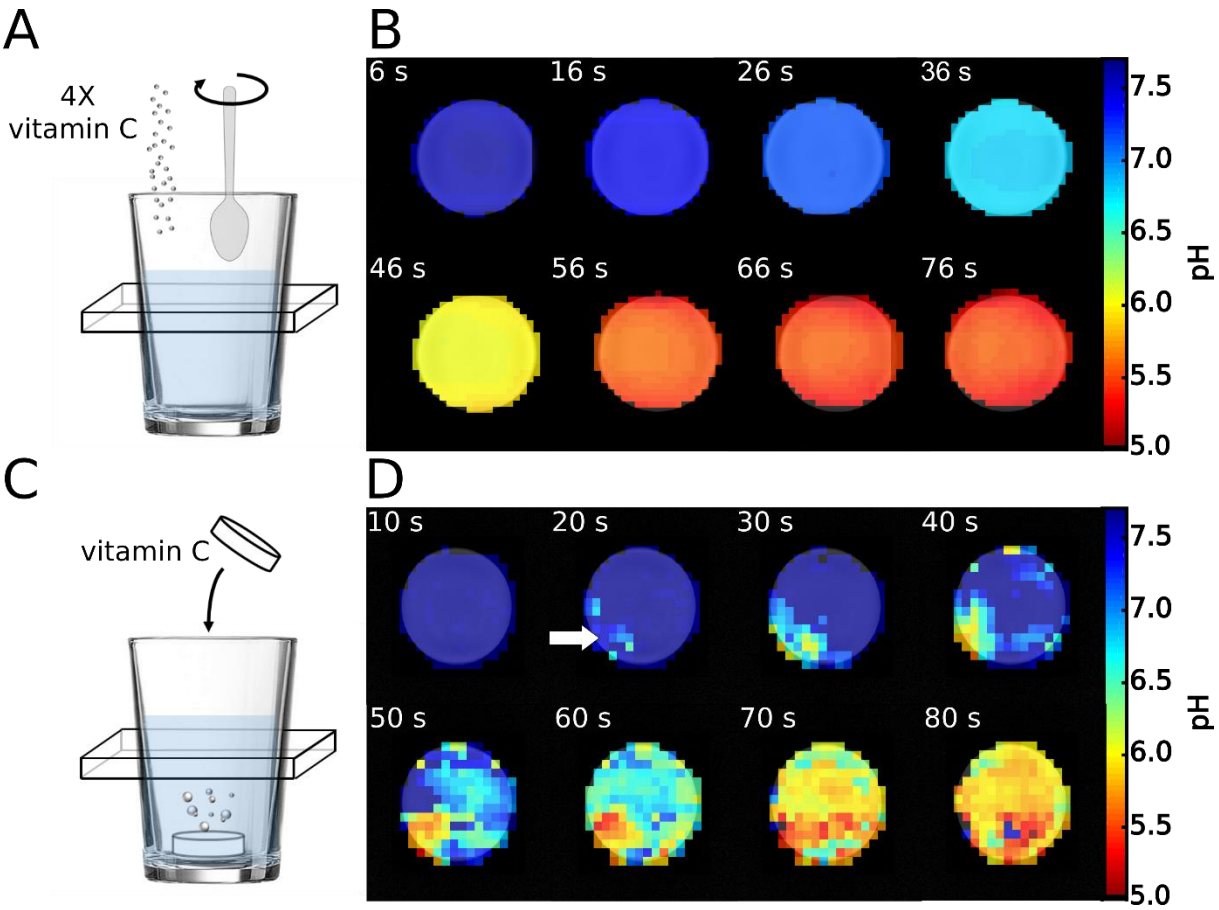

Figure 6.3: Spatially resolved imaging of temporal pH changes. (A and **C)** Experimental setups. **(B)** Time-resolved pH images of a reaction vessel filled with 72 mL of 80 mM Tris at pH ~ 7.7 and 3 mL co-polarized ZA_d (c_{final} = 2 mM) and urea (c_{final} = 3 mM). After addition of distinct amounts of powdered vitamin C during each of the first four acquisition pauses of 10 s, the solution was mixed gently with a plastic spatula. The pH images of (A) were calculated from the chemical shift difference between $C_1(ZA_d)/C_5(ZA_d)$ and urea on a voxel-by-voxel basis (see Methods). **(D)** Time-resolved pH images show localized dynamic pH changes after a dissolvable vitamin C tablet was added to the reaction vessel (white arrow) once the first pH image was recorded. Only carbon signal intensities greater than 20% of the maximum signal intensity are displayed for both (B) and (D).

Both resonance signals C_1 and C_5 of ZA_d shift up-field with respect to urea and with respect to decreasing pH, giving a final pH of 5.4 ± 0.2 (mean ± std).

Finally, we imaged a dynamic pH change caused by dissolution of a dissolvable vitamin C tablet (**Figure 6.3 C** and **D**). The first pH image shows a homogenous pH distribution of pH 7.61 ± 0.02 (mean ± *std*). Once added to the solution, the vitamin C tablet gradually dissolved and released bicarbonate, CO_2, citric and ascorbic acid. This caused a local drop in pH already observable in the second image. Interestingly, we detected two distinct ZA_d peak pairs corresponding to a pH ≈ 7.5 – 7.7 and a pH ≈ 5.0 - 5.7 in the spectra of most voxels (**Figure S6.7**). This observation can be explained by the relatively large slice thickness (13 mm), which covers a volume with an inhomogeneous pH distribution reaching from acidic regions around the bottom of the reaction vessel, where the vitamin C tablet is located, to regions with a neutral pH at

the top. We calculated mean pH images of the two different pH values, weighted by their respective signal intensities. Intensity and weighted pH images of each timestep are shown in **Figure S6.8**. The progressive dissolution of vitamin C led to a dynamic mixing of the solution, which decreased the pH over time.

6.3 Conclusion

[1,5-$^{13}C_2$]zymonic acid was the first hyperpolarized chemical shift based pH biosensor successfully applied pre-clinically *in vivo*.[78] Our work demonstrates an efficient way to deuterate ZA which notably prolongs T_1 at clinical field strength and thus increases its NMR-sensitivity *in vivo.* The application of ZA_d allows a better accuracy in spatially resolving pH, which could contribute to an improved diagnosis and characterization of diseases. This method for pH imaging could even be further simplified by selective labeling of ZA_d at position C_1 or C_5 only, thereby reducing the number of resonance signals to be analyzed.

Here, we presented the first spatially resolved MRSI measurements of a dynamic pH change sensed by a hyperpolarized and chemical shift based molecule on a timescale of seconds. *In vivo*, this could help to detect immediate changes of the extracellular pH_e, e.g. in cases where pH changes are caused by enzymatic reactions[212], in alkaline treatments of acute metabolic acidosis[276] and in exercised muscle.[277] In addition, time-resolved spatial mapping of pH could verify targeted drug delivery for localized acidification or basification.

6.4 Supplementary Information

6.4.1 Supplementary Figures

^{1}H and ^{13}C NMR measurements of zymonic acid (ZA) and deuterated zymonic acid (ZA_d) (natural abundance ^{13}C)

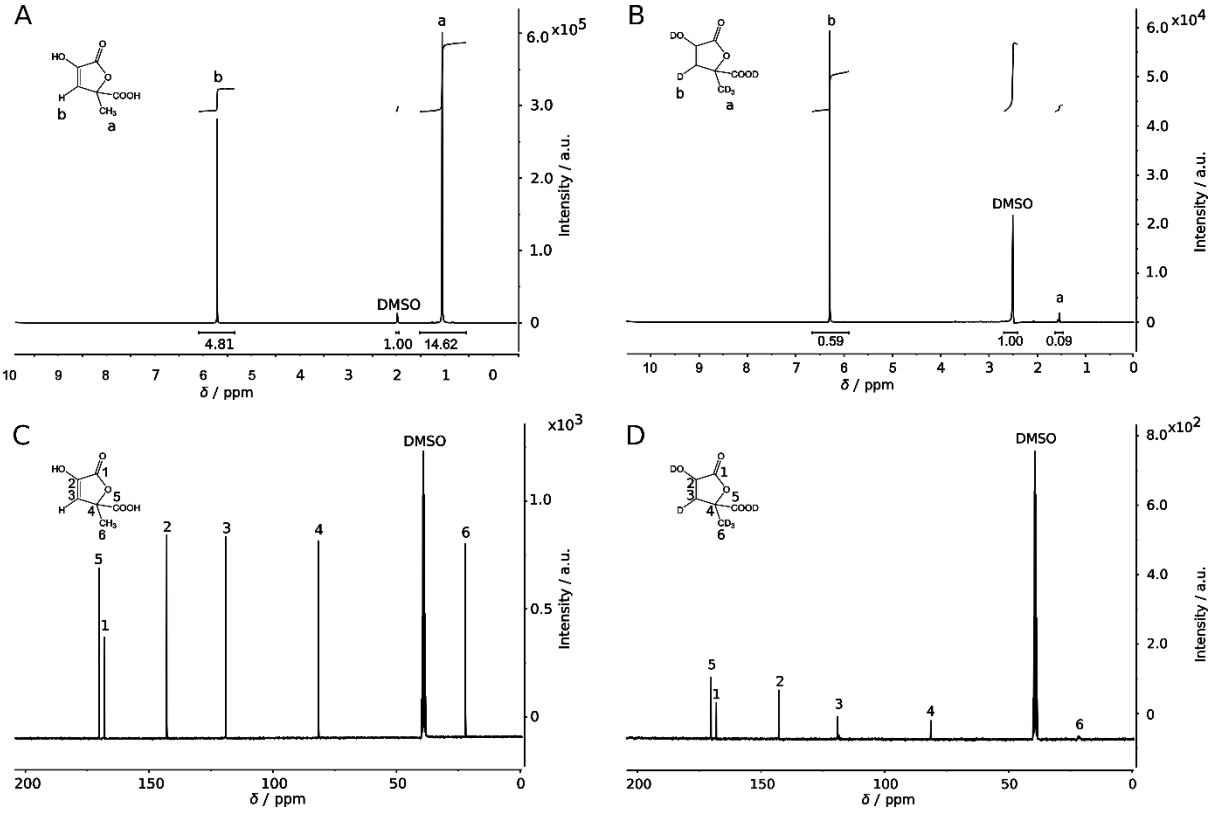

Figure S6.1: ^{1}H and ^{13}C measurements of zymonic acid and [3,6,6,6-D_4]zymonic acid. **(A)** and **(B)** show proton NMR spectra of 0.5 M ZA and ZA_d dissolved in DMSO-d_6, respectively (measured at 300 MHz). Traces of DMSO were used as internal standard to estimate the degree of deuterium enrichment of ZA_d, which is > 99% for position a and ≈ 88% for position b. Figure **(C)** and **(D)** show the respective carbon spectra of ZA and ZA_d. Note that magnetization transfer for ^{13}C signal enhancement is smaller for deuterium enriched zymonic acid, which leads to smaller carbon signal intensities, with respect to DMSO (NOE-enhanced decoupled ^{13}C measurements). Note further that ZA and ZA_d were purified with a H_2O/acetonitrile and a D_2O/acetonitrile gradient (**chapter M6.2**), which labeled the exchangeable protons with H and D respectively.

T_1-measurements of deuterated zymonic acid (ZA_d) at B_0 = 1 T in D_2O

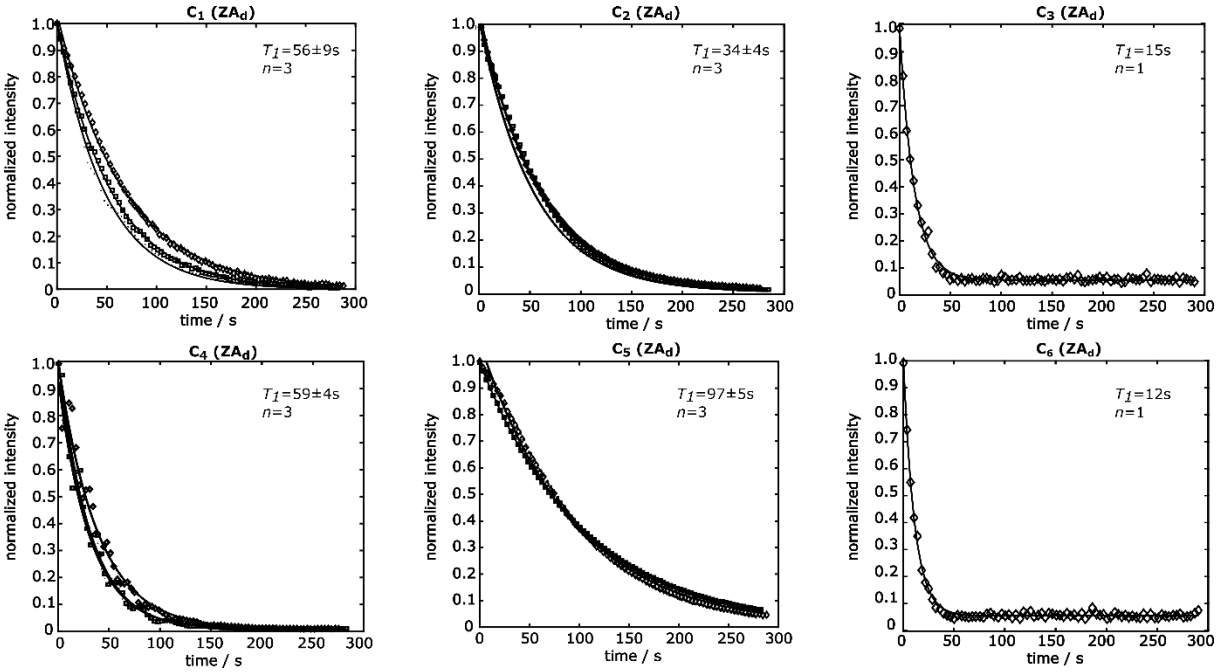

Figure S6.2: T_1 decay curves of ^{13}C atoms of [1,5-$^{13}C_2$-3,6,6,6-D_4]zymonic acid, [2,4-$^{13}C_2$-3,6,6,6-D_4]zymonic acid and [3,6-$^{13}C_2$-3,6,6,6-D_4]zymonic acid at B_0 = 1 T in D_2O. T_1 measurements and data analysis were performed according to **chapter M6.5**. Since the T_1 of C_3 and C_6 is relatively short and [3,6-$^{13}C_2$-3,6,6,6-D_4]zymonic acid is therefore not useful for pH imaging, we acquired this T_1 only once (n = 1).

T_1-measurements of undeuterated zymonic acid (ZA) at B_0 = 1 T in D_2O

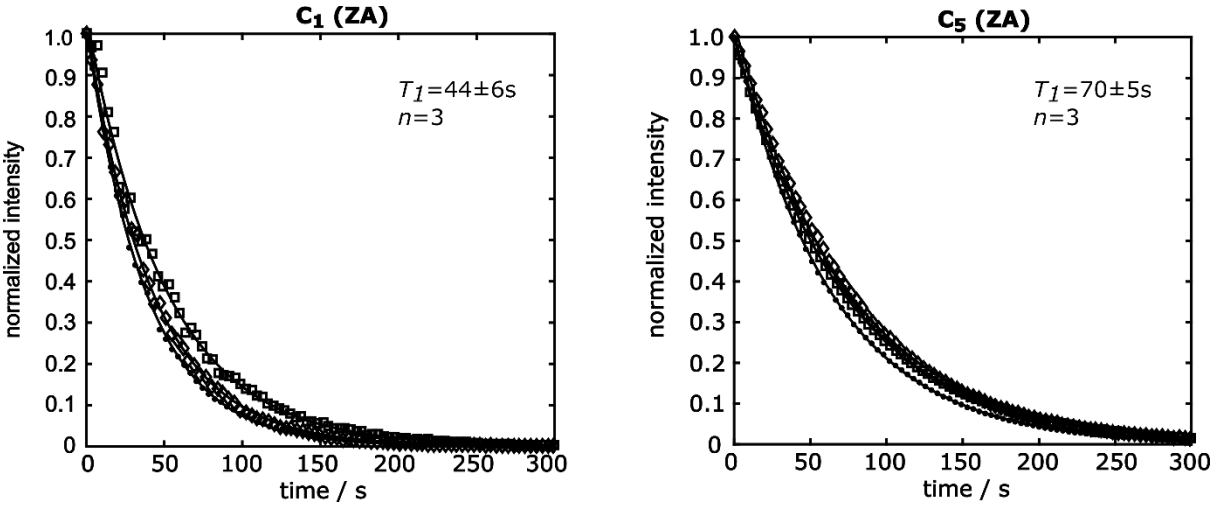

Figure S6.3: T_1 decay curves of ^{13}C atoms of [1,5-$^{13}C_2$]zymonic acid at B_0 = 1 T in D_2O. T_1 measurements and data analysis were performed according to **chapter M6.5**.

T_1-measurements of deuterated zymonic acid (ZA_d) at B_0 = 3 T in 80 mM Tris buffered aqueous solution

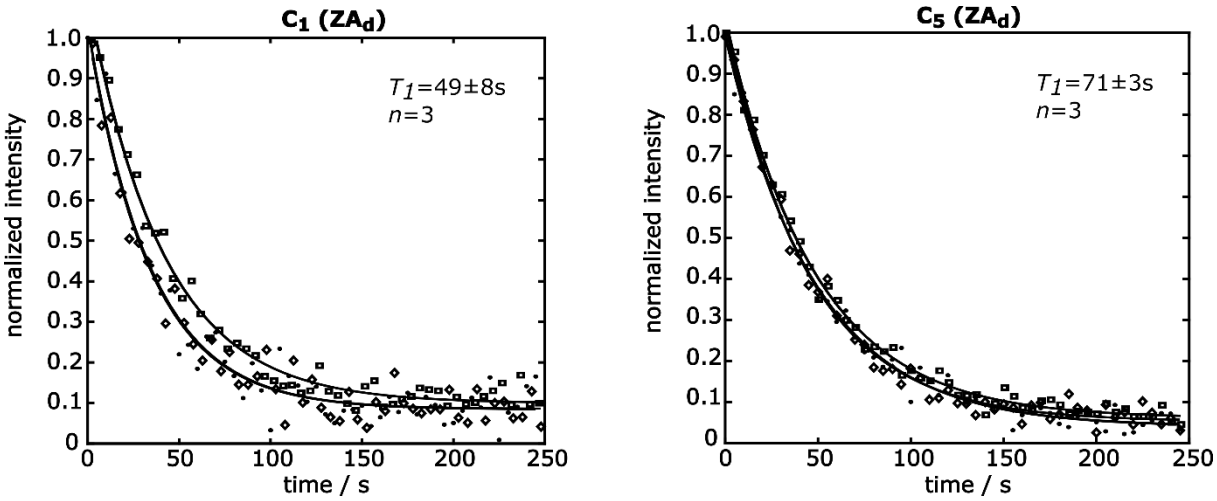

Figure S6.4: T_1 decay curves of carbon atom C_1 and C_5 of [3,6,6,6-D_4]zymonic acid at B_0 = 3 T in 80 mM Tris buffered aqueous solution. T_1 measurements and data analysis were performed according to **chapter M6.5**. Note that these data were obtained with hyperpolarized natural abundance ^{13}C [3,6,6,6-D_4]zymonic acid. Comparable T_1 values of non-deuterated zymonic acid were published previously.[78]

In vivo pH imaging of subcutaneous MAT-B-III tumors

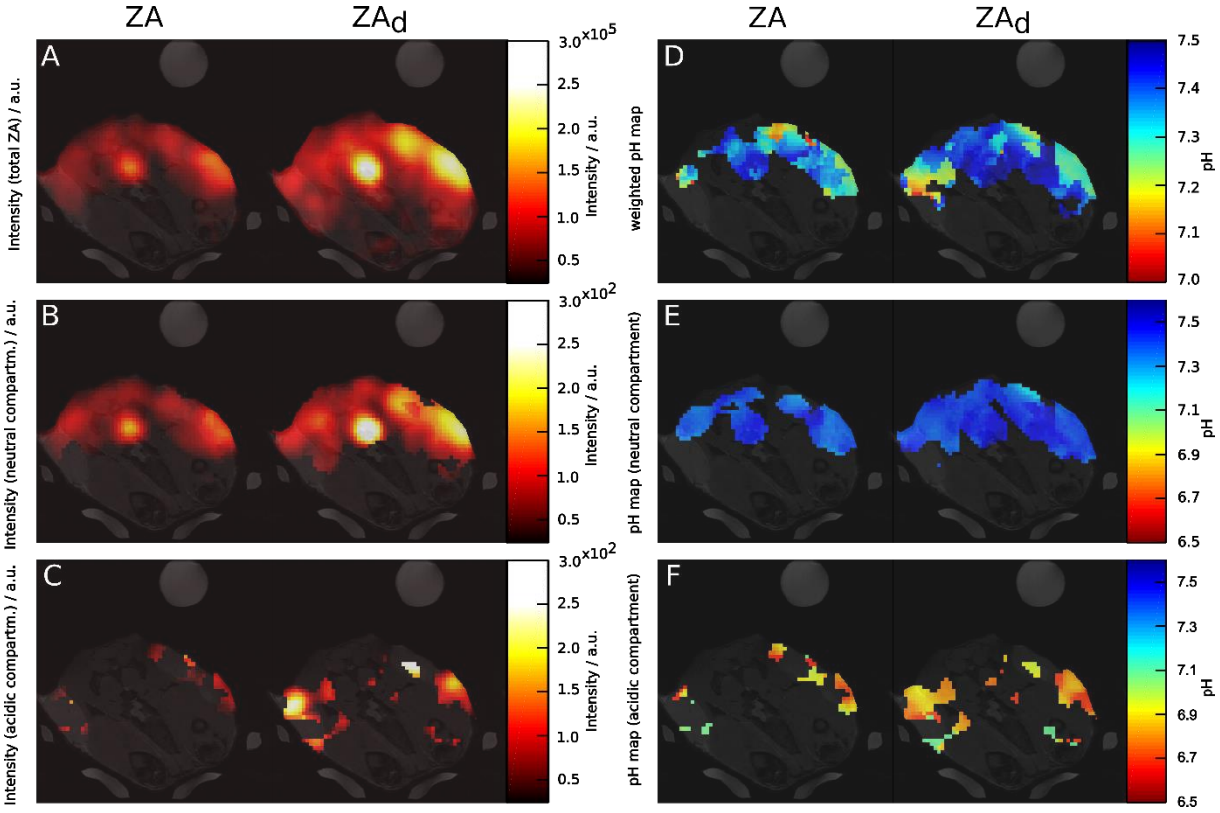

Figure S6.5: Comparative *in vivo* ZA and ZA_d signal intensity images and pH images of axial slices of rats bearing subcutaneous MAT-B-III tumors. **(A)** Signal distribution of ZA and ZA_d in the animals. Zymonic acid accumulates in well perfused tumors and a noticeable amount of zymonic acid is visible in the blood pool. **(B)** and **(C)** signal amplitudes of the fitted peaks of C_5 of ZA, corresponding to the neutral vascular pH and the acidic extracellular tumor pH, respectively. **(D)** Weighted pH images, calculated according to **M6.7** (only signals greater than 30% of the ZA_d maximum intensity are displayed). **(E)** and **(F)** pH images of observable neutral vascular and acidic tumor pH values, respectively (for ZA, only signals greater than 25% and for ZA_d only signals greater than 20% of the ZA_d maximum intensity are displayed). All images were masked according to the anatomical proton images for better visualization.

NMR spectra of *in vitro* pH imaging of a pH change caused by a stepwise addition of vitamin C

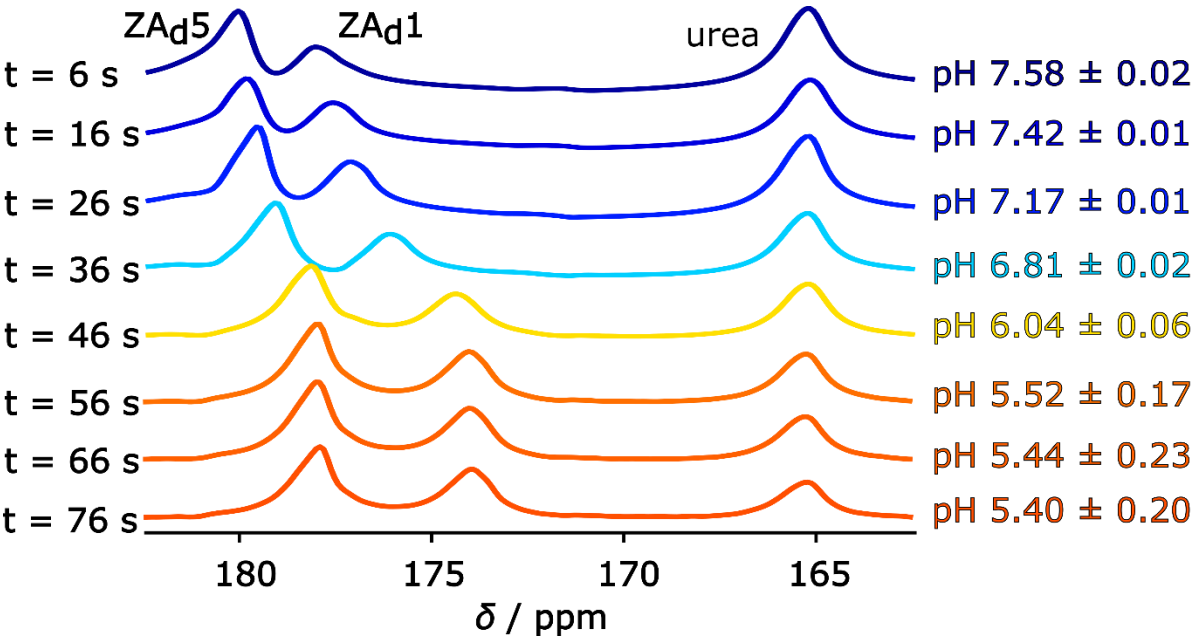

Figure 6.6: Summed NMR spectra of pH images of a pH change caused by a stepwise addition of vitamin C to a Tris buffered aqueous solution. The summed spectra of each respective timestep of all voxels with ZA_d signals greater than 30% of the maximum carbon intensity are displayed. The respective pH values (mean ± *std*) were calculated according to **M6.8**.

In vitro pH imaging of a dynamic pH change caused by vitamin C dissolution: Spectra from representative voxels

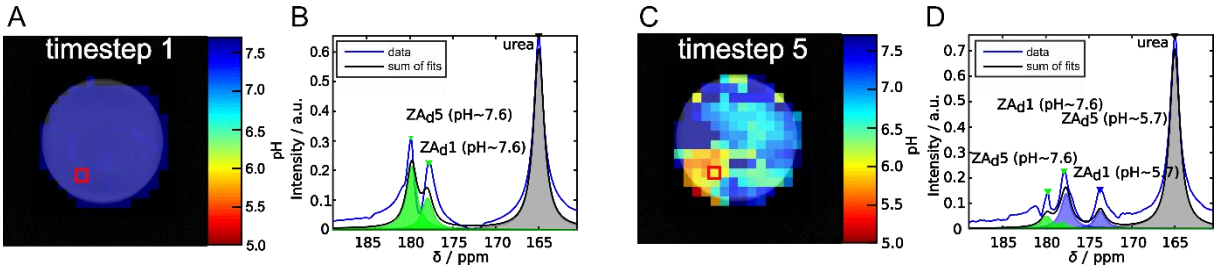

Figure S6.7: Representative fitted spectra of co-polarized ZA_d and urea of a vitamin C tablet dissolved in 80 mM Tris buffered aqueous solution of initial pH ~ 7.7. **(A)** At time *t* = 10 s after adding the vitamin C tablet to the solution, the first image is acquired. **(B)** A representative voxel spectrum from (A) shows one peak pair of zymonic acid and one urea resonance signal. The calculated pH from the chemical shift differences is pH ≈ 7.6. **(C)** At time *t* = 50 s, the fifth image is acquired. **(D)** A representative voxel spectrum from (C) shows two distinct peak pairs of zymonic acid and one urea resonance signal. The green peak pair corresponds to a pH ≈ 7.6, the blue to a pH ≈ 5.7.

In vitro pH imaging of a dynamic pH change caused by vitamin C dissolution: Intensity and pH Images

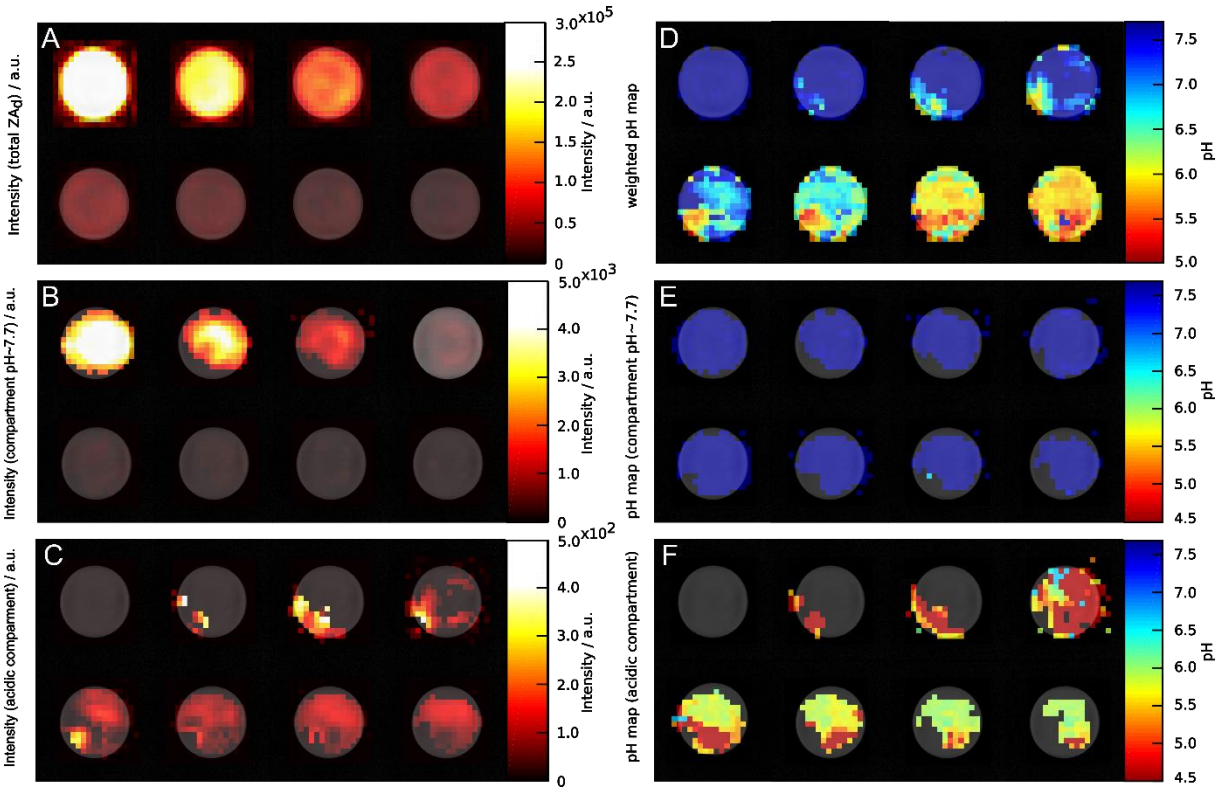

Figure S6.8: Slices of ZA$_d$ intensity images and pH images of a vitamin C tablet dissolved in 80 mM Tris buffered aqueous solution of initial pH ≈ 7.7. (A) Total signal intensity of ZA$_d$ in the phantoms. **(B)** and **(C)** Intensity of the fitted C_5 peaks of ZA$_d$ corresponding to the initial pH ≈ 7.7 of the Tris solution and corresponding to the pH ≈ 5.0 - 5.7 of the part of the solution already acidified by dissolution of the vitamin C tablet, respectively. **(D)** Mean pH, weighted as described in **M6.7** by the signal intensities shown in (B) and (C), from **(E)** the detected pH value of the initial Tris solution and from **(F)** the detected pH value of the solution acidified by dissolution of the vitamin C tablet. In all images, only signals greater than 20% of the respective maximum ZA$_d$ intensity are displayed for clarity.

6.4.2 Material and Methods

M6.1 Chemicals

Isotope-enriched chemicals were purchased from Sigma-Aldrich (USA) or provided by Cambridge Isotope Laboratories, Inc. (USA). All other chemicals were purchased from Sigma-Aldrich (USA).

M6.2 Synthesis of zymonic acid, [3,6,6,6-D_4]zymonic acid, [1,5-$^{13}C_2$]zymonic acid (ZA), [1,5-$^{13}C_2$-3,6,6,6-D_4]zymonic acid (ZA_d),[2,4-$^{13}C_2$-3,6,6,6-D_4]zymonic acid, [3,6-$^{13}C_2$-3,6,6,6-D_4]zymonic acid and [$^{13}C_6$-3,6,6,6-D_4]zymonic acid

ZA was synthesized according to Düwel et al.[78] For deuterium enrichment, pyruvic free acid or sodium pyruvate were diluted in D_2O at a final concentration of 0.1 - 0.2 M. The pH was adjusted to pH ≈ 12 with NaOD and the solution was left standing for two days. After acidification with DCl (pH ≈ 1), D_2O was removed using a freeze dryer (alpha 2-4 LD plus, Christ, UK). Zymonic acid raw product was diluted in acetone and NaCl was filtered off before it was purified by reversed phase high pressure liquid chromatography using a C18 column (HPLC system: Prominence, Shimadzu (Japan), column: Nucleodur® C_{18}, (Macherey Nagel, Germany), gradient: linear gradient, 2-20% acetonitrile, buffer A: 0.1% TFA in water, buffer B: 0.1% TFA in acetonitrile) and freeze-dried *in vacuo* (alpha 2-4 LD plus, Christ, UK). The experimental yield of ZA_d was approximately 37%. [1-^{13}C]pyruvate, [2-^{13}C]pyruvate and [3-^{13}C]pyruvate were used for selective labelling of zymonic acid at position C_1 and C_5, C_2 and C_4 and C_3 and C_6, respectively. For ^{13}C-labelling of all carbon positions, [1,2,3-$^{13}C_3$]pyruvate was used as starting compound.

M6.3 NMR measurements

Proton and carbon NMR spectra were acquired on either a 300 MHz or 600 MHz NMR spectrometer (Avance III, Bruker BioSpin, Germany). For the determination of pH-dependent chemical shifts, [U-$^{13}C_6$]zymonic acid dissolved in 90% H_2O and 10% D_2O and adjusted with 1 M HCl and 1 M NaOH to distinct pH values. Because ZA contains exchangeable protons and is unstable in aqueous solution (half-life ≈ 2.5 h), it was dissolved in dimethyl sulfoxide-d_6 (DMSO-d_6) to estimate the deuterium enrichment from NMR signal integrals, using DMSO traces as quantitative reference (MestReNova 10.0, Mestrelab Research, Spain).

M6.4 Theoretical calculation of the ZA structure in aqueous solution and its pH-dependent chemical shift mechanism

Computational details

The proton and carbon chemical shieldings were calculated with GAUSSIAN09.[278] In order to describe the pH dependency of the chemical shift, the singly (ZA^-, pK_a = 2.35) and doubly (ZA^{2-}, pK_a = 6.95) deprotonated zymonic acid were considered, which correspond to the limiting cases of pH 5.2 and pH 9.5.

The initial structures were constructed with Avogadro[279] and the MMFF94 force field.[280-284] The pre-optimization step was conducted on the level of Hartree-Fock (HF) with the 6-31++G(d) basis set.[285] Based on the pre-optimized structures, the geometry was further refined by geometry optimizations on the level of density functional theory (DFT) with the B3LYP exchange-correlation functional[286-289] using the larger, triple-zeta basis sets TZVP[290] and aug-cc-pVTZ.[291] The choice of diffuse basis functions was necessary to describe the high polarizability of the delocalized electron density in the ZA anions. The inclusion of polarization functions improved the description of directional bonding as well as hydrogen bonds. The solvent effects of zymonic acid in water were taken into account implicitly by the polarizable continuum model (PCM)[292] to generate the solvent reaction field. The tight convergence criterion was used. Based on the optimized geometries, the chemical shieldings were calculated with B3LYP and TZVP as well as the aug-cc-pVTZ basis sets. Again, water as solvent was described by PCM. NMR properties were computed with the gauge including atomic orbitals (GIAO) method.[293, 294]

For the singly deprotonated zymonic acid ZA^-, four different configurations were considered: the keto configuration, the hydrated configuration, and the enol configuration with and without a hydrogen bond between the C_2-OH and the C_1=O group. In order to improve the accuracy of the theoretical predictions, explicit solvent molecules were included in the calculation. Up to two water molecules were positioned at the most polar groups (positions of deprotonation) of the optimized ZA^- and $ZA2^-$ molecules, either the C_2-OH (or C_2-O-, respectively) or the C_5OO- group. The computational effort of the geometry optimizations was reduced by reducing the level of theory to Hartree-Fock using the 6-31++G(d,p) basis set. Additionally, in this step, the coordinates of the entire molecule were fixed, with exception of the degrees of freedom of the groups interacting with the water molecules. For water added to the (deprotonated) hydroxyl group, the bond lengths and angles of the oxygen and hydrogen atoms on the C_2 and neighboring C_1 were unrestricted. Analogously, all degrees of freedom of the oxygen atoms on the C_5 remained unrestricted when water was added to the carboxylate group. Naturally, the explicit solvent molecules were not restricted during the geometry optimization. Different equilibrium structures, some of

which were forming rings, were found. The combined effect of hydration of both the C_2 and C_5 positions was studied by adding water molecules to both the C_2 and C_5 positions. Initial structures were generated by combining the optimized coordinates of the separately optimized C_2 and C_5 water regions. The geometry was relaxed with Hartree-Fock using the 6-31++G(d) basis set. The geometry was restricted with exception of the functional groups at the C_1, C_2 and C_5 positions as described above. The effect of the solvent reservoir was taken into account by the PCM method.

Discussion

The calculations for the enol configuration of ZA^- showed good agreement with the experimental values with a root mean square error (rmse) of about 4.6 ppm. In contrast, the keto and enol configurations were excluded by high rmse values in the order of 35 ppm, which were mainly based on large deviations of the ^{13}C chemical shifts of the C_2 and C_3 atoms.

The advantages of ZA as MRI biomarker of extracellular pH are based on the pH dependency of the carbon chemical shifts. The computed chemical shielding differences between the ZA^- and ZA^{2-} anions without explicit water molecules reproduced the trends of up- and downfield shift (**Table M6.1 and Figure M6.4**). However, the magnitudes of the shift differences were considerably overestimated by a factor of 2 to 3, especially for C_2 and C_3 (rmse = 7.1 ppm). The consistency with the experiment benefitted from including explicit water molecules on the polar groups of ZA. The experimental pH-induced shift differences were reproduced with an rmse of about 4.0 ppm.

Table M6.1: Summary of the pH-induced carbon and proton chemical shift differences (δ_{pH} = 9.5 – δ_{pH} = 5.2) of ZA. The experimental results are compared to the calculated shift differences for the isolated anionic molecules (with PCM) and the ZA anions with explicit water molecules on the C_2 and C_5 positions.

	δ (H_{methyl}) [ppm]	δ (C_6H_3) [ppm]	δ (C_1) [ppm]	δ (C_2) [ppm]	δ (C_3) [ppm]	δ (C_4) [ppm]	δ (C_5) [ppm]	δ (C_6) [ppm]	rmse [ppm]
Experiment (Δ pH)	-0.1	-0.7	4.8	7.4	-6.0	-1.4	2.3	1.1	-
ZA^- vs ZA^{2-}	-0.2	-1.3	10.1	15.1	-21.1	-3.4	7.2	2.9	7.1
With explicit H_2O	-0.2	-1.1	9.2	11.2	-15.6	-2.3	3.5	2.8	4.0

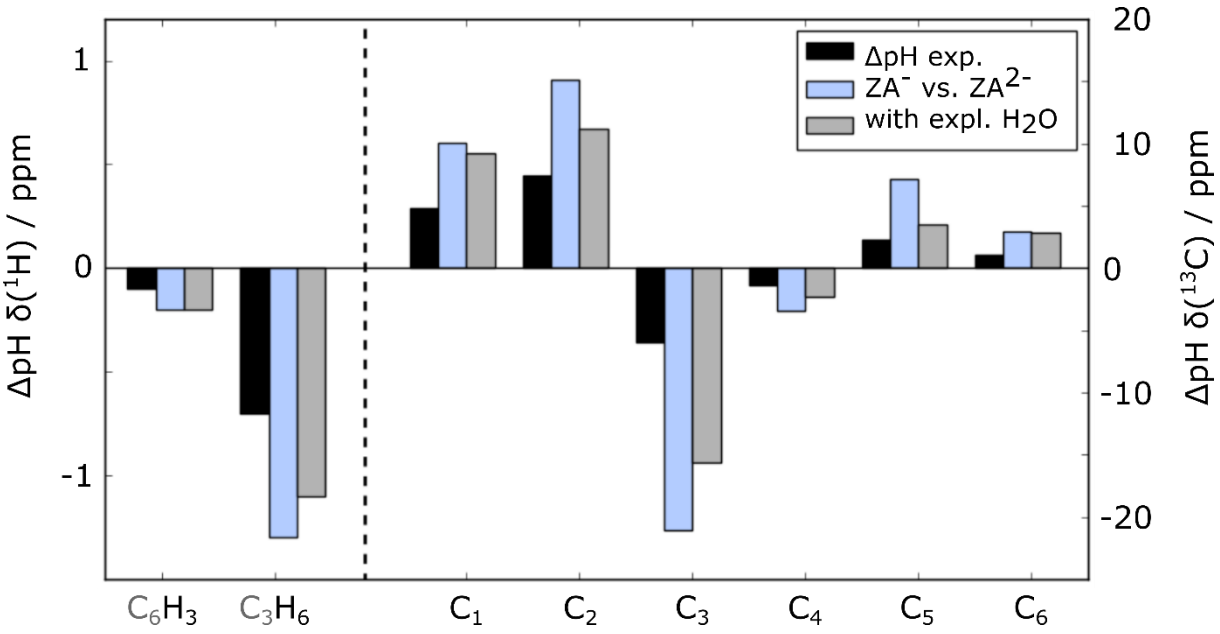

Figure M6.4: Comparison of the calculated pH-induced chemical shift differences to the experimental values. On the left side of the vertical dashed line, the pH-induced proton chemical shift differences are depicted (left ordinate axis), whereas the right side illustrates the ^{13}C-chemical shift differences (right ordinate axis). The black bars denote the experimental values. The simulated pH-induced chemical shift differences of the ZA anions with and without explicit water molecules are given in light blue and gray, respectively.

M6.5 Dissolution dynamic nuclear polarization (DNP) and T_1 measurements

4 M ZA or ZA_d and 15 mM of free radical (OX063, Oxford Instruments, UK) were dissolved in dry DMSO and added to a standard DNP sample cup. For *in vivo* experiments, the ZA solution was frozen in liquid nitrogen and covered by another frozen layer of 30 µL 10 M ^{13}C urea containing 30 mM of free radical and 1.5 mM of gadolinium chelate (Dotarem, Guerbet, France). The polarization was performed in a DNP polarizer (Hypersense, Oxford Instruments, Abingdon, UK) using the microwave source at 94.175 GHz for 1.5 - 2 hours. The sample was dissolved in a pressurized (10 bar) and heated (180 °C) solution of 4 mL D_2O or 80 mM Tris in H_2O, which were adjusted with NaOH to reach a final pH ≈ 6.6 - 7.4. For T_1 measurements at 1 T, the final concentrations of ZA and ZA_d were approximately 25 mM. For T_1 measurements at 3 T and *in vivo* measurements at 7 T, the final ZA and ZA_d concentrations were approximately 50 mM. If urea was co-polarized, its final concentration was 75 mM. ^{13}C T_1 measurements were performed on a 1 T NMR spectrometer (Spinsolve Carbon, Magritek, Aachen, Germany) with ^{13}C-enriched ZA and ZA_d in 5 mm standard NMR tubes. T_1 measurements at a clinical 3 T PET/MR mMR Biograph (Siemens, Germany) were performed with hyperpolarized deuterated ^{13}C-natural abundance zymonic acid in 5 mL syringes using a pulse-and-acquire free induction decay (FID) sequence and a ^{1}H/^{13}C dual-tuned transmit/receive surface flex coil (RAPID Biomedical, Germany).

The center frequency and flip angle were determined using 5 mL phantom containing 8 M ^{13}C urea with 5 mM Dotarem (Guerbet, Villepinte, France) and 0.1% sodium azide. Acquisition parameters at 1 T were 10° flip angle and 3 s repetition time (TR), at 3 T 15° flip angle and 5 s TR. The acquired FIDs were Fourier transformed using MestReNova 10.0 (Mestrelab Research, Santiago De Compostela, Spain). T_1 decay curves were flip angle corrected and fitted by a three parameter mono-exponential decay curve.

M6.6 Animal handling and tumor implantation

Animal experiments were approved by the local governmental committee for animal protection and welfare (Tierschutzbehörde, Regierung von Oberbayern). MAT-B-III cells (13762 MAT-B-III, ATCC, USA) were cultivated in RPMI-1640 medium (+10% FKS, 1% PenStrep) and re-suspended in McCoy's 5A medium for implantation in three female Fischer 344 rats (Charles River, Wilmington, MA, USA, average weight 226 ± 5 g, left and right flank, subcutaneously, 1 x 10^6 cells / 200 µL). Animals were imaged nine days after cell implantation. Catheters were placed before rats were put in the MR scanner and tail vein injections were performed at a dose of 5 mL / kg and a rate of 0.17 mL / s. Anaesthesia was performed with 2 - 4% isoflurane inhalation gas. Rat body temperature was maintained with a water heated pad. During experiments, heart and breathing rates were monitored (ECG Trigger Unit, Rapid Biomedical, Rimpar, Germany).

M6.7 Imaging procedures

In Vivo pH Imaging and Data Post-Processing

In vivo imaging experiments were performed on a 7 T small animal MR scanner (GE / Agilent, Santa Clara, CA, USA).

Table M 6.2: Polarized amounts of ZA, ZA_d and urea and times from dissolution of hyperpolarized substances to measurement.

	ZA measurement			ZA_d measurement		
	m (ZA) [mg])	M (urea) [mg]	*t* (diss. to meas.) [s]	*m* (ZA_d) [mg]	M (urea) [mg]	*t* (diss. to meas.) [s]
Animal 1	24.06	25.20	40	24.04	25.20	41
Animal 2	24.06	25.20	33	24.04	25.20	33
Animal 3	24.04	25.20	41	24.05	25.18	42

Two subsequent tail vein injections of hyperpolarized ZA and ZA_d into the same animal were performed within ≈ 2.5 h delay between the measurements (n = 3). Equal amounts of ZA and ZA_d, both together with urea, were polarized until the solid-state polarization reached saturation (≈ 2.5 h), and the time between dissolution and start of the measurements were, although different from animal to animal, the same for each set of experiments of ZA and ZA_d (see **Table M 6.2**). The center of the imaged slice was positioned on the center of the subcutaneous MAT-B-III tumors. A 72 mm dual tuned $^{1}H/^{13}C$ birdcage coil was used for signal transmission in combination with a two-channel flexible coil ^{13}C receive-array (Rapid Biomedical, Rimpar, Germany). The surface coil was positioned directly on the tumors. Proton images were recorded with a fast spin echo (FSE) sequence (slice thickness 1 mm, field of view 6 cm, image matrix 256 x 256, repetition time 2.6 s, effective echo time 20 ms, number of averages 2). *In vivo* experiments were performed using a free induction decay chemical shift imaging (FIDCSI) sequence. Images were reconstructed with Matlab (MathWorks, Natick, MA, USA) as described previously[126], with *k*-space being sampled in centric order from the center on outwards. ^{13}C imaging parameters were: 5 kHz spectral bandwidth, 512 sampling points, 9.8 Hz spectral resolution, 16 x 16 nominal matrix size, 5 mm slice thickness, 6 cm field of view, 4° flip angle, 118 ms repetition time, 208 excitations, 25 s total scan time. A 10 Hz Gaussian filter was applied along the readout dimension and the data was zero-filled by a factor of four in the two spatial dimensions as well as in the spectral dimension before fast Fourier transforms (FFTs) were applied along all three dimensions.

Stepwise and dynamic *in vitro* pH imaging and data post-processing

A stepwise addition of vitamin C to a 80 mM Tris buffered aqueous solution was performed at a 3 T PET/MR mMR Biograph (Siemens Healthineers, Erlangen, Germany) using a $^{1}H/^{13}C$ dual-tuned transmit/receive surface flex coil (Rapid Biomedical, Rimpar, Germany). Proton sequences were recorded using a T_1-weighted fast low angle shot (FLASH) sequence (3 mm slice thickness, 16 cm x 16 cm field of view, 320 x 320 image matrix, 0.25 s repetition time, 2.5 ms effective echo time, number of averages 2). Imaging was performed with a free induction decay chemical shift imaging (FIDCSI) sequence using an elliptical *k*-space readout beginning from the center outwards. Imaging parameters were: 3 kHz spectral bandwidth, 512 points sampled, 9.8 Hz spectral resolution (bandwidth divided by sampled points), 8 x 8 nominal matrix size, 13 mm slice thickness, 8 cm field of view, 15° flip angle, 200 ms repetition time, 29 excitations, 5.8 s total scan time, 10 s pause after each imaging experiments for addition of vitamin C and mixing. The first portion of 60 mg vitamin C to 72 mL 80 mM Tris containing 3 mL hyperpolarized ZA_d (final concentration c_{final} = 2 mM) and urea (c_{final} = 3 mM) was added after the first pH image was recorded. During

the next three pauses, 30 mg, 20 mg, and again 20 mg vitamin C were added. Thus, four portions of vitamin C (m_{total} = 130 mg) were added to achieve a pH decrease. Image post-processing and reconstruction was performed in Matlab (MathWorks, Natick, MA, USA). The data was zero-filled by a factor of four in the two spatial dimensions before fast Fourier transformation was applied in the spatial and spectral dimensions. 20 Hz line broadening was applied to NMR spectra, multiplying the free induction decay (FID) with an exponential function.

In order to observe a dynamic pH change, 200 mg of a dissolvable vitamin C tablet was added to 72 mL 80 mM Tris containing 3 mL hyperpolarized ZA_d (c_{final} = 2 mM) and urea (c_{final} = 3 mM) after the first image was recorded. Imaging parameters were: 13 mm slice thickness, 8 cm x 8 cm field of view, 10 x 10 nominal matrix, 15° flip angle, 200 ms repetition time, 49 excitations, 9.8 s acquisition time per image. No pause was implemented between each image acquisition. Data were zero-filled by a factor of 1.6 in the two spatial dimensions before fast Fourier transformation was applied. 5 Hz line broadening was applied to the NMR spectra of the first four images, 10 Hz for image five and six and 20 Hz for image seven and eight, accounting for the decrease in SNR over time.

M6.8 Image analysis

In vivo signal to noise ratio (SNR) evaluation of ZA and ZA_d

For SNR comparison, spectra of all tumor pixels were extracted using Matlab (MathWorks, Natick, MA USA) and imported into MestReNova 10.0 (Mestrelab Research, Santiago de Compostela, Spain). Automatic phasing was performed before the SNR was calculated using the SNR Peak Calculator. The SNR gain due to deuterium enrichment is given in percent and is the ratio of the mean SNR calculated for all ZA_d peaks (either C_1 or C_5) divided by the mean SNR calculated for all respective ZA peaks (either C_1 or C_5, respectively) (**equation M6.1**).

$$SNR\ gain = \frac{\overline{SNR\ (ZA_d)}}{\overline{SNR\ (ZA)}} \quad \text{(M6.1)}$$

Back-calculation of pH values and images

Back-calculation of pH values and images was carried out in Matlab (MathWorks, Natick, MA, USA) on a voxel-by-voxel basis. The resonance signal of urea was used as internal chemical shift reference (δ = 0 ppm). Magnitude signal peaks of zymonic acid were detected and fitted to a sum of Lorentzian functions based on their chemical shift. The linewidth for all peaks in each voxel was determined from the urea signal in

the respective voxel. The chemical shifts of C_1 and C_5 of ZA and ZA_d can be described as a function of pH by two scaled logistic functions

$$\delta_{1/5}(pH) = \delta_{1/5,acid} + \frac{(\delta_{1/5,base} - \delta_{1/5,acid})}{(1 + 10^{pK_a - pH})} \quad \text{(M 6.2)},$$

with the five parameters[78]

- $\delta_{1,acid}$ = 8.52 ppm the limiting acid (minimum) ^{13}C chemical shift of C_1 of the protonated form of ZA/ZA_d,
- $\delta_{1,base}$ = 13.65 ppm the limiting base (maximum) ^{13}C chemical shift of C_1 of the deprotonated form of ZA/ZA_d,
- $\delta_{5,acid}$ = 12.57 ppm the limiting acid (minimum) ^{13}C chemical shift of C_5 of the protonated form of ZA/ZA_d,
- $\delta_{5,base}$ = 15.14 ppm the limiting base (maximum) ^{13}C chemical shift of C_5 of the deprotonated form of ZA/ZA_d,
- and pK_a = 6.90 the acid dissociation constant for the hydrogroup of ZA/ZA_d.

In vivo

Peak fitting was performed by iteratively varying peak positions and amplitudes for all detectable peaks in the acquired spectra. As the C_1 peak of the more acidic tumor compartment was not detectable *in vivo*, probably due to the lower SNR as compared to the *in vitro* data, due to the shorter T_1 of the C_1 position compared to the C_5 position and due to the relatively small size of the tumor compartment compared to the vasculature, the two pH values (pH_1 and pH_2) for the two compartments were calculated based on the chemical shifts of the two C_5 resonances of ZA/ZA_d, using **equation M6.2**. Mean pH images were calculated from the fitted pH values (pH_1 and pH_2) of the two C_5 peaks weighted by the respective fitted peak intensities (I_1 and I_2) of the two C_5 peaks according to **equation M6.3**

$$pH_{weighted} = \frac{pH_1 \cdot I_1 + pH_2 \cdot I_2}{I_1 + I_2} \quad \text{(M6.3)}$$

In vitro

During the dynamic pH measurement with the vitamin C tablet, we observed two peak pairs of ZA_d within most of the voxels, corresponding to a pH ≈ 7.5 – 7.7 for the first and a pH ≈ 5.0 - 5.7 for the second peak pair (see **Figure S.6**). The C_1 peak of ZA_d with pH ≈ 7.5 - 7.7 overlapped with the C_5 peak of ZA_d with pH ≈ 5.7, whereas the C_5 peak of ZA_d with pH ≈ 7.5 - 7.7 and the C_1 peak of ZA_d with pH ≈ 5.7 were easily separable. We therefore implemented an algorithm to first identify the latter two peaks,

which are better to separate. In case both peaks were detected (C_5 with pH ≈ 7.5 - 7.7 and C_1 with pH ≈ 5.7), their pH values were back-calculated using **equation M6.2**. From these pH values, the expected peak positions of the other two (overlapping) peaks were calculated and the positions and signal intensities of the two now complete peak pairs were fitted simultaneously by varying the two pH values and peak pair intensities assuming a signal intensity ratio of C_5:C_1 = 2:1. This ratio was estimated from the first image, where only one peak pair was present and where we could thus clearly identify both the C_1 and C_5 peak corresponding to a pH ≈ 7.5 - 7.7 (**Figure S6.7 B**). Mean pH images were then calculated from the two fitted pH values (pH_1 and pH_2), weighted by the two-fitted peak pair intensities (I_1 and I_2) according to **equation M6.3** and as shown in **Figure S6.7**.

7. Hyperpolarized Amino Acid Derivatives as Multivalent Magnetic Resonance pH Sensor Molecules

Christian Hundshammer, Stephan Düwel, David Ruseckas, Geoffrey Topping, Piotr Dzien, Christoph Müller, Benedikt Feuerecker, Jan-Bernd Hövener, Axel Haase, Markus Schwaiger, Steffen J. Glaser and Franz Schilling

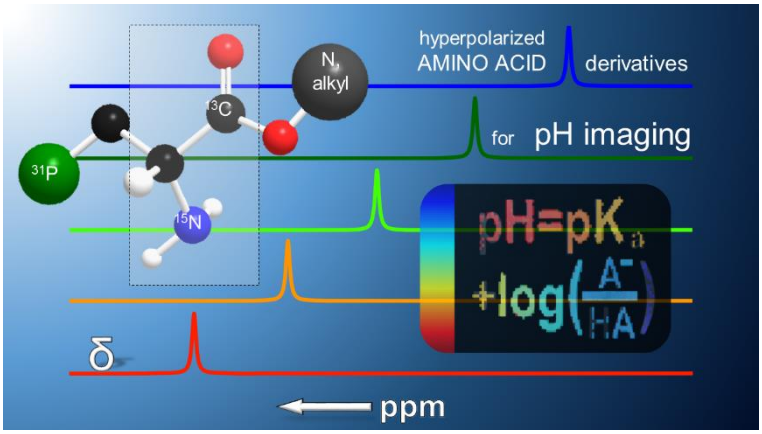

Summary

pH is a tightly regulated physiological parameter that is often altered in diseased states like cancer. The development of biosensors that can be used to non-invasively image pH with hyperpolarized (HP) magnetic resonance spectroscopic imaging has therefore recently gained tremendous interest. However, most of the known HP-sensors have only individually and not comprehensively been analyzed for their biocompatibility, their pH sensitivity under physiological conditions, and the effects of chemical derivatization on their logarithmic acid dissociation constant (pK_a). Proteinogenic amino acids are biocompatible, can be hyperpolarized and have at least two pH sensitive moieties. However, they do not exhibit a pH sensitivity in the physiologically relevant pH range. Here, we developed a systematic approach to tailor the pK_a of molecules using modifications of carbon chain length and derivatization rendering these molecules interesting for pH biosensing. Notably, we identified several derivatives such as [1-^{13}C]serine amide and [1-^{13}C]-2,3-diaminopropionic acid as novel pH sensors. They bear several spin-½ nuclei (^{13}C, ^{15}N, ^{31}P) with high sensitivity up to 4.8 ppm/pH and we show that ^{13}C spins can be hyperpolarized with dissolution dynamic polarization (DNP). Our findings elucidate the molecular mechanisms of chemical shift pH sensors that might help to design tailored probes for specific pH *in vivo* imaging applications.

7.1 Introduction

The pH is an important physiological parameter that is tightly regulated in living organisms by intrinsic buffer systems. Several diseases such as inflammation, ischemia and cancer are associated with metabolic changes affecting the extracellular tissue pH.[28, 29, 165, 166, 295, 296] Biocompatible sensor molecules that can be used to non-invasively measure pH *in vitro* and *in vivo* are therefore highly valuable to study disease induced metabolic changes. In the clinic, measuring pH would be helpful for diagnosis of malignant tissues, monitor response to treatment, and tailor therapies to patient-specific phenotypes.[170-172]

In the past, several pH-sensitive small molecules and nanoparticles for positron - tomography, fluorescence, and optoacoustics have been proposed.[206] In contrast to these methods, magnetic resonance imaging (MRI) approaches do not rely on ionizing radiation, offer a high penetration depth and excellent soft tissue contrast, and allow fast acquisition of high-resolution anatomical images at the same time. Saturation transfer between bulk water and exchangeable protons of molecules with pH-dependent exchange rates[297] or relaxivities of lanthanide complexes can be used for pH imaging.[113] Additionally, thermally polarized signals of molecules bearing pH sensitive ^{1}H, ^{19}F[203] and ^{31}P[204] nuclei can be exploited for *in vivo* pH measurements. IEPA ((+/−)2-imidazole-1-yl-3-ethoxycarbonylpropionic acid)[201, 298] and ISUCA ([(+/−)2-(imidazol-1-yl)succinic acid])[202] were applied for proton pH imaging in pre-clinical studies, while histidine was able to measure pH with spatial localization in human brain after oral loading of the amino acid.[299]

During the last two decades, efficient hyperpolarization (HP) techniques such as spin exchange optical pumping (SEOP)[221], parahydrogen induced polarization (PHIP)[115, 116, 223] and dissolution dynamic nuclear polarization (DNP) have been developed to increase the thermal NMR signal by more than five orders of magnitude and to overcome signal limitations of classical NMR and MRSI (magnetic resonance spectroscopic imaging).[121] pH-sensitive molecules with spin-½ nuclei (^{13}C[166, 215-217], ^{15}N[119, 218], ^{31}P[300], ^{89}Y[219] and ^{129}Xe [220, 222]) have been polarized with these methods and were applied *in vitro*, while only ^{13}C-labelled sensors have been used *in vivo* so far.[78, 113, 166] ^{13}C-nuclei can be polarized to high levels of above 70%, they have a fairly high gyromagnetic ratio and a relatively long T_1 especially for carbonyls, quaternary or deuterated carbons.[120] Nevertheless, almost all of the presented molecules were only characterized individually and a generally applicable strategy for the design of biocompatible magnetic resonance pH sensors is needed.

Proteinogenic amino acids are essential for living organisms. They are used as precursors for neurotransmitters, nucleotides, co-factors, and proteins and are crucial metabolic carriers or serve as energy sources in phases of low nutrient supply. In this work, we systematically analyzed the effects of derivatization on the pK_a of natural

amino acids. We characterized the NMR pH sensitivity of several spin-½ nuclei with high natural abundance (^{31}P) or that can be isotopically enriched (^{13}C, ^{15}N) in amino acid derivatives. Furthermore, we investigated the potential of HP using dissolution dynamic nuclear polarization (DNP) for the most interesting candidates to ultimately obtain novel *in vivo* pH biosensors.

7.2 Materials and Methods

Chemicals

Non-labelled and labelled chemicals were purchased from Sigma Aldrich (St. Louis, MI, USA) and Cambridge Isotope laboratories (Andover, MA, USA), respectively.

Synthesis of ^{15}N-labelled 2,3-diamino propionic acid (DAP)

Synthesis of DAP was performed as described previously.[301, 302] [1,4-$^{13}C_2$]aspartic acid or [1,4-$^{13}C_2$-2-^{15}N]aspartic acid (1 equivalent) were dissolved in fuming sulfuric acid (30%) under ice-bath cooling followed by addition of dry chloroform. Sodium azide (2 equivalents) was then added in small portions under reflux for 5 h. After that, the mixture was brought to room temperature and stirred for another 2 h under reflux. After ice-bath-cooling, the chloroform layer was removed, and ice was added to dissolve the paste-like residue. The solution was passed through a DOWEX-column (H^+-form, 100–200 mesh) that was washed with 0.5 N HCl followed by washing with water to neutrality. Elution of the raw product was performed with 4 N NH_3 in MeOH. ninhydrin-positive fractions were pooled and concentrated by rotary evaporation. The final addition of 6 N HCl precipitated diaminopropionic acid hydrochloride at pH ~ 2.
The raw product was filtered, washed with methanol and acetone and recrystallized twice in methanol yielding white crystalline [1-^{13}C, 2-^{15}N]2,3-diaminopropionic acid hydrochloride (^{13}C-^{15}N-DAP or [1-^{13}C, 2,3-$^{15}N_2$]2,3-diaminopropionic acid hydrochloride (^{13}C-$^{15}N_2$-DAP). The experimental yield for both was about 40%.

Synthesis of serine ethyl and propyl ester

Thionyl chloride (1 equivalent, 36 mmol) was added slowly to dry absolute ethanol or propanol (47 mL and 13 mL) cooled to 0 °C. After the addition of serine (1 equivalent, 10 mmol) and removal from the ice-bath, the mixture was stirred for another two minutes before slowly being heated to reflux temperature, dissolving serine. After stirring for ten minutes, the mixture was cooled to 0 °C, followed by the addition of dry tert-butylether (150 mL) leading to crystallization of serine ethylester crystals. The crystals were filtered and washed with tert-butylether, yielding serine ethylester in form

of white crystals (experimental yield: 49% and 16% for serine ethyl and propyl ester, respectively).

NMR measurements

Carbon NMR spectra were acquired either on a 300 MHz or 600 MHz NMR spectrometer (Avance III, Bruker BioSpin, Billerica, MA, USA) in 5 mm NMR tubes and at 25 °C if not stated differently. Carbon spectra were measured using ^{1}H-decoupling, phosphorus and nitrogen without decoupling. For the determination of the pH-dependent chemical shifts, amino acids and ^{13}C-urea were dissolved in 1 M KCl in 90% H_2O/10% D_2O and adjusted with 10 M HCl and 10 M KOH to the desired pH values measured with a standard glass electrode (pH meter: ProLab 4000, SI Analytics or Lab850, Schott, pH electrode: N6000A, Weilheim, Germany). If not stated differently, final concentrations of non-labelled and labelled compounds were 250 mM and 2.5 mM, respectively.
For analysis of the temperature dependency, solutions were measured at 25 °C, 37 °C and 50 °C controlled by an air heating within the NMR spectrometer. DAP and serine amide (SA) concentrations were varied for analysis of the dependency of the sensor concentration on the chemical shift (100 mM, 250 mM, 500 mM). In cases where effects of the ionic strength on the NMR sensitivity was tested, respective amounts of KCl were added, taking the sensor concentration into account. Then, 0.4 and 2.0 equivalents (for SA, 0.4 and 2.5 equivalents for DAP) of $CaCl_2$ were added to solutions containing 250 mM of amino acid to test for potential interaction or complexation of SA/DAP with bivalent metal ions. Chemical shift sensitivity in presence of proteins was tested with increasing bovine serum albumin (BSA) concentrations (0, 50, 75, 100 and 210 g/L) at fixed pH values (pH 6.6, 7.0, and 7.4), which were adjusted after each addition of BSA.
Carbon and nitrogen NMR spectra of 300 mM solutions of ^{13}C-^{15}N-DAP and ^{13}C-$^{15}N_2$-DAP, carbon spectra of a 100 mM solution of ^{13}C-SA, and phosphorus spectra of a 300 mM solution of P-Ser were acquired on a 300 MHz spectrometer (all in solutions of 90% H_2O/10% D_2O). [^{13}C]urea was added to the solutions as internal chemical shift reference for ^{13}C-measurements.

Analysis of NMR titration curves

NMR spectra were analyzed with MestReNova 10.0 (Mestrelab Research, Santiago de Compostela, Spain). 5 Hz line broadening using an exponential filter was applied to all NMR spectra. The resonance signal of urea was set to 165 ppm and used as an internal reference for carbon spectra. Nitrogen and phosphorus spectra were referenced to the respective spectrometer frequencies.

The pH-dependent chemical shifts were fitted to the following **equation 7.1**[303]:

$$\delta_{obs} = \frac{\delta_{min} + \sum_{i=1}^{n} \delta_{max,i}\ 10^{\left(\sum_{j=n-i+1}^{n} pK_{a,j}\right)-ipH}}{1 + \sum_{i=1}^{n} 10^{\left(\sum_{l=n-i+1}^{n} pK_{a,l}\right)-ipH}} \quad (7.1).$$

δ_{obs} is the measured chemical shift, δ_{min} the lowest observable chemical shift, n is the number of proton exchange sites, δ_{max} is the highest observable chemical shift for the respective deprotonated species, pK_a is the logarithmic acid dissociation constant of the respective nucleus, and the pH value was measured with a glass electrode. The pH sensitivity $\Delta\delta$ [ppm] is given as the chemical shift difference between pH 6.4 and pH 7.6 calculated from fit curves.

WST-1 cytotoxicity tests

T-cell murine lymphoma (EL4)-derived cells were cultivated in RPMI 1640 medium (high glucose, ATCC, Manassas, VA, USA). Increasing amounts of serine amide hydrochloride or 2,3-diaminopropionic acid hydrochloride from stock solutions in PBS, pH 7.1 and 10 µL dimethyl sulfoxide (DMSO) were added to 10 mL culture medium containing 5.5 − 6.1 × 10^5 cells (final amino acid concentrations: 0, 1.25, 2.5, 5, 10, and 20 mM). As positive control, 10 µL of 15 mM etoposide solution in DMSO was added to a separate 10 mL cell culture. Flasks were incubated for 22 h at 37 °C and 5% CO_2. Cell media were then changed, and a 100 µL sample of each culture was taken for a water-soluble tetrazolium 1 (WST-1) assay. Each 100 µL cell culture sample was incubated with 10 µL of the WST-1 reagent for 2 h at 37 °C and 5% CO_2, after which the optical absorbance at 450 nm was measured using an Infinite 200 PRO (Tecan, Männedorf, Switzerland) absorbance microplate reader. The WST1 assay was carried out three times for each condition.

^{13}C-hyperpolarization and T_1 measurements

Table 7.1. Sample preparation scheme for hyperpolarization.

Compound	*c* (OX063) [mM]	*c* (Dota) [mM]	Solvent	c_{final} [M]	*v* [GHz]
SA	24	3	60% 10 M NaOH, 40% H_2O	6	94.165
DAP	26	7	90%10 M NaOH, 10% glyc	7	94.155
PA	16	1	self-glassing	14	94.172

Abbreviations: OX063, trityl radical, Oxford Instruments (Abingdon, UK); Dota, Dotarem gadolinium chelate, Guerbet (Villepinte, France); glyc: glycerol.

[1-^{13}C]serine amide hydrochloride (SA), [1-^{13}C]2,3-diaminopropionic acid hydrochloride (DAP) and pyruvate (PA) were prepared for polarization (1–3 h, Hypersense, Oxford Instruments, Abingdon, UK) according to **Table 7.1**. Solid build up

curves were normalized to the respective ^{13}C-molar amount (molar solid build up in units per mole; u.*mol^{-1}) and fitted to an exponential function (**equation 7.2**).

$$P_{molar\ solid\ build\ up}(t) = P_{solid\ state,max} \cdot \left(1 - e^{\left(t \cdot T^{-1}\right)}\right) \cdot n \quad (7.2),$$

with $P_{\text{molar solid build up}}(t)$ being the solid state polarization at time t, $P_{\text{solid state,max}}$ being the maximum achievable solid state polarization, T being the solid state build up constant and n being the molar amount of the respective polarized molecule.

The samples were dissolved in pressurized (10 bar) and heated (180 °C) 80 mM Tris (Tris(hydroxymethyl)-aminomethan) buffered solution, which was adjusted with KOH or HCl to reach distinct pH values. Final concentrations of SA, DAP and PA were: 28.5 ± < 0.1 mM (pH 5.3 ± 0.8, n = 3), 20.9 ± 1.7 mM (pH 5.8 ± 0.4, n = 3), and 103.3 ± <0.1 mM (pH 7.2 ± 0.2, n = 3). For SA and DAP, ~100 mM vitamin C were added to the dissolution buffer to quench the free radical and also decreased the pH of the solution to acidic pH. ^{13}C T_1 measurements of hyperpolarized substances were performed in 5 mm standard NMR tubes on a 1 T NMR spectrometer (Spinsolve Carbon, Magritek, Aachen, Germany) using the following acquisition parameters: 4° flip angle and 3 s repetition time (TR) for PA; 1° flip angle, TR = 3 s or 20° flip angle TR = 5 s for SA and DAP. A 25 Hz line broadening using an exponential filter was applied to all NMR spectra of hyperpolarized compounds. Hyperpolarized signals ($S_{\text{hyper,obs.}}$) at time point t were flip angle corrected according to **equation 7.3**.

$$S_{hyper,corr.}(t) = \frac{S_{hyper,obs.}}{cos(\alpha)^{n-1}} \quad (7.3),$$

with $S_{\text{hyper,corr.}}(t)$ being the flip angle corrected hyperpolarized signal at time t, α the nominal flip angle, and n the indexed number of each individual experiment. Flip angle corrected T_1 decay curves were fitted to a monoexponential decay curve (**equation 7.4**) and interpolated to the time-point of dissolution (S_{hyper} (t = 0)).

$$S_{hyper,corr.}(t) = S_{hyper}(t = 0) \cdot e^{-t \cdot T_1^{-1}} \quad (7.4),$$

with T_1 being the spin lattice relaxation time.

Hyperpolarized signal enhancements (ε) and liquid state polarization levels (P_{hyper}) were calculated using **equation 7.5**.

$$P_{hyper} = \frac{S_{hyper}(t = 0) \cdot sin(\alpha)}{S_{thermal} \cdot sin(90°)} \cdot tanh\left(\frac{\gamma \hbar B_0}{2 k_B T}\right) = \varepsilon \cdot P_{thermal} \quad (7.5),$$

with γ being the gyromagnetic ratio of carbon, $\hbar$ the reduced Planck constant, k the Boltzmann constant, and T = 300.15 K (constant spectrometer temperature). $S_{thermal}$ is the thermal signal of a 10 M ^{13}C-urea solution acquired at the same spectrometer with a single shot (flip angle 90°) and corrected for the concentration of the respective hyperpolarized molecule as given in **equation 7.6**.

$$S_{thermal} = \frac{signal_{10Murea,90°} \cdot c(HP\ molecule)}{10\ mol \cdot L^{-1}} \quad (7.6)$$

Thermal phantom imaging and back-calculation of pH maps

Custom-made 3D-printed phantoms with letter-shaped compartments were used to acquire spatially resolved pH maps (coronal orientation) from the thermal signals of 250 mM ^{13}C-SA (phantom 1: “TUM MRI”) and ^{13}C-DAP (phantom 2: “pH = pK_a + log(A^-/HA)”) in 100 mM citric acid/200 mM disodium phosphate buffer (universal buffer) supplied with 250 mM ^{13}C-urea as internal reference and 2 mM gadolinium chelate (Dotarem, Guerbet, Villepinte, France). Distinct pH values were adjusted with 10 M KOH or 12 M HCl.

MR images were acquired with a 7 T magnet operating with Bruker AVANCE III HD electronics (Bruker Biospin, Billerica, MA, USA). A dual-tuned ^{1}H/^{13}C volume coil (RAPID Biomedical, Rimpar, Germany) with inner diameter 31 mm was used for radiofrequency (RF) transmission and signal reception. Proton localization images were acquired with a fast low angle shot (FLASH) sequence using the following acquisition parameters: repetition time 150 ms, echo time 3.1 ms, flip angle 15°, matrix size 380 × 260 (phantom 1), 420 × 260 (phantom 2), field of view (FOV) 38 mm × 26 mm (phantom 1) or 42 mm × 26 mm (phantom 2), slice thickness 5 mm (phantom 1) or 3mm (phantom 2), four averages, total scan time 2 min 36 s, receiver bandwidth 100 kHz and excitation bandwidth 12 kHz. ^{13}C spectroscopic images were acquired with a 2D phase-encoded chemical shift imaging sequence (CSI), with repetition time 300 ms, nominal flip angle 30°, matrix size 72 × 52, (phantom 1) and 84 × 52 (phantom 2), field of view and slice thickness matching the proton localization images, 12 (phantom 1) or 14 (phantom 2) averages for each of six (phantom 1) or four (phantom 2) repetitions, total scan time 23 h 43 min (phantom 1) or 20 h 23 min (phantom 2), receiver bandwidth 4 kHz, 256 points acquired per phase-encode, spectral resolution 7.8 Hz, excitation bandwidth 12 kHz. Automated iterative linear shimming on the proton signal was run prior to proton acquisition. Reference power was determined automatically for protons by the scanner and used a predetermined value for ^{13}C-based on separate phantom measurements. ^{13}C-images were reconstructed in Matlab (Mathworks, Natick, MA, USA). In the spectral dimension, 15 Hz line broadening was applied before Fourier transformation.

NMR signals were summed over all repetitions. For each voxel, the maximum intensity of each peak was determined automatically with Matlab (Mathworks, Natick, MA, USA) and the respective peak frequencies were used to determine the chemical shift difference between the resonance signal of urea set to 165 ppm and the respective sensor signal. The pH maps were back-calculated (numerical for DAP and analytical

for SA) using the mean pK_a and chemical shift values obtained from the three respective pH titration curves of DAP and SA at different temperatures acquired with NMR spectrometers and with the fit parameters in **Table 7.2**.

Table 7.2. Fit parameters for back-calculation of pH maps for ^{13}C-SA and ^{13}C-DAP.

Sensor	pK_{a1}	pK_{a2}	δ_{min}	δ_{max1}	δ_{max2}
^{13}C-SA	7.35	-	172.44	180.67	-
^{13}C-DAP	6.95	9.65	173.28	179.00	183.7

7.3 Results

Amino acids bear carbonyl carbons with a relatively long T_1. They are amenable for hyperpolarization[304-306] and exhibit a pH-dependent chemical shift around the pK_a of their pH sensitive moieties (**Figures 7.1** and **S7.1**): the amino group (pK_a < 9), the carboxylic acid group (pK_a < 3), and in some cases a side chain group that has a pK_a close to physiological pH like histidine (pK_{a2} = 6) and cysteine (pK_{a2} = 8.1).

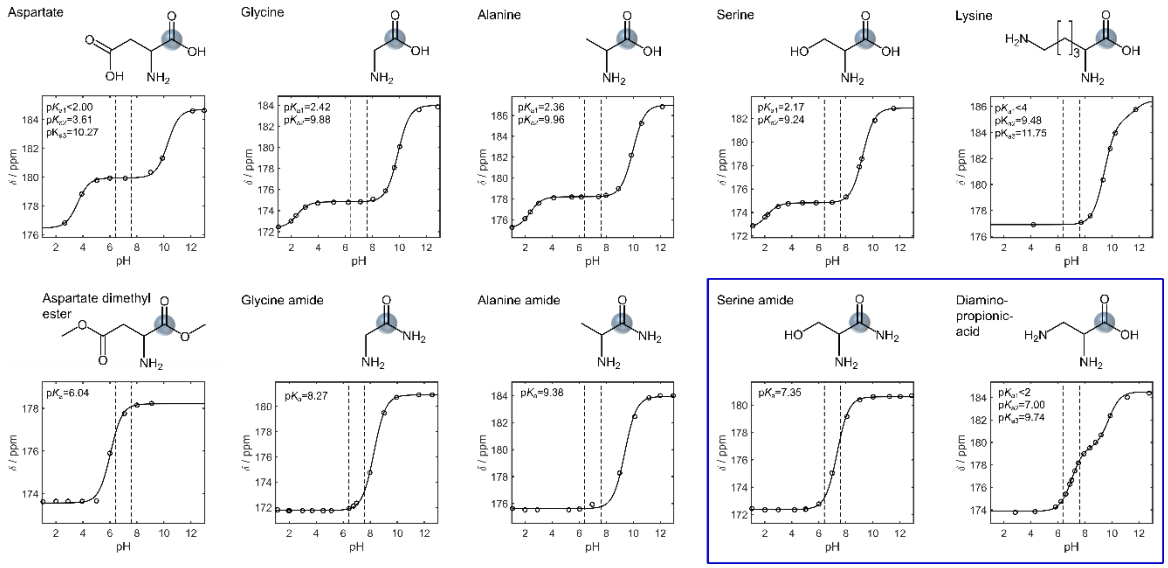

Figure 7.1. pH-dependent chemical shift of carbonyl ^{13}C-atoms of representative acidic, hydrophobic, neutral, polar, and basic canonical amino acids (from left to right, top row) and one respective derivative each (bottom row). The pK_a of the carboxylic acid and the amino group of naturally occurring amino acids are below pH 3 and above pH 9, respectively. Side chains as shown for aspartate may have a higher (lower) pK_a, but none of them is in a range relevant for *in vivo* pH imaging. Around their pK_a, carbonyl carbons of canonical amino acids exhibit a pH dependent chemical shift (top row). Esterification, amide formation, and carbon chain length reduction lower the pK_a of amino acids toward the relevant range for *in vivo* pH imaging yielding derivatives such as SA and DAP (blue box), which show a strong chemical shift between pH 6.4 and pH 7.6 (bottom row). The pH range relevant for *in vivo* pH imaging is indicated with vertical dashed lines in each pH nuclear magnetic resonance (NMR) titration plot. NMR pH titrations curves were obtained from 250 mM amino acid solutions in 1 M KCl containing 10% D_2O. Spectra were reference to the resonance signal of 2.5 mM ^{13}C-urea set to 165 ppm.

In order to exploit the pH sensitivity of these moieties for hyperpolarized *in vivo* pH imaging, their pK_a needs to be adjusted to be in a range that is at the physiological pH (pH 7.0 ± 0.6[113]) or rather acidic.[28, 29, 166, 295, 296] The pK_a of histidine (His) and cysteine (Cys) are close to that range but their carbonyl chemical shift sensitivity is rather low (histidine: $\Delta\delta$ = 0.7 ppm, cysteine: $\Delta\delta$ = 0.2 ppm, for all other ^{13}C shifts of histidine and cysteine see **Figure S7.2**). Esterification or amidation removes the carboxylic acid proton and the pH sensitivity of the carboxylic acid group's carbon chemical shift, which leads to a lowering of the amino group's pK_a by up to more than four pH units (**Figures 7.1** and **S7.1**). For instance, aspartate has a pK_{a2} = 10.27, which is lowered to pK_a = 6.04 by esterification of both carboxylic acid groups. Glycine methyl ester has a pK_a = 7.52 that is two pH steps below the one of glycine (pK_a = 9.88). Serine amide (SA) has a pK_a = 7.35 and its carbonyl carbon shows a strong pH shift of $\Delta\delta$ = 4.2 ppm in the physiological pH range. A decreasing number of carbon atoms in the ester alkyl chain has negligible effects on the pK_a as observed for serine propyl (pK_a = 7.74, $\Delta\delta$ = 4.2 ppm), serine ethyl (pK_a =7.47, $\Delta\delta$ = 4.5 ppm), and serine methyl ester (pK_a = 7.32, $\Delta\delta$ = 3.8 ppm, see **Figure S7.1**). Shortening of a basic amino acid's chain length decreases the pK_a as measured for lysine (pK_{a2} = 9.48) > ornithine (pK_{a2} = 9.19) > 2,4-diaminobutyrate (pK_a = 8.38) > 2,3-diaminopropionic acid (DAP) (pK_a = 7.00). Notably, DAP has the same pH sensitivity ($\Delta\delta$ = 4.2 ppm) in the physiological pH range as SA. Although amino acid alkyl esters also exhibit a similarly high pH shift around this range, they hydrolyse in solution, forming the respective canonical amino acids and alcohols (**Figure S7.3**). In contrast, DAP and amino acid amides like SA are stable in aqueous solution. We therefore tested if their pH-dependent chemical shift is influenced by parameters that vary under *in vivo* conditions and that could thus affect the pH determination (**Figure 7.2**).

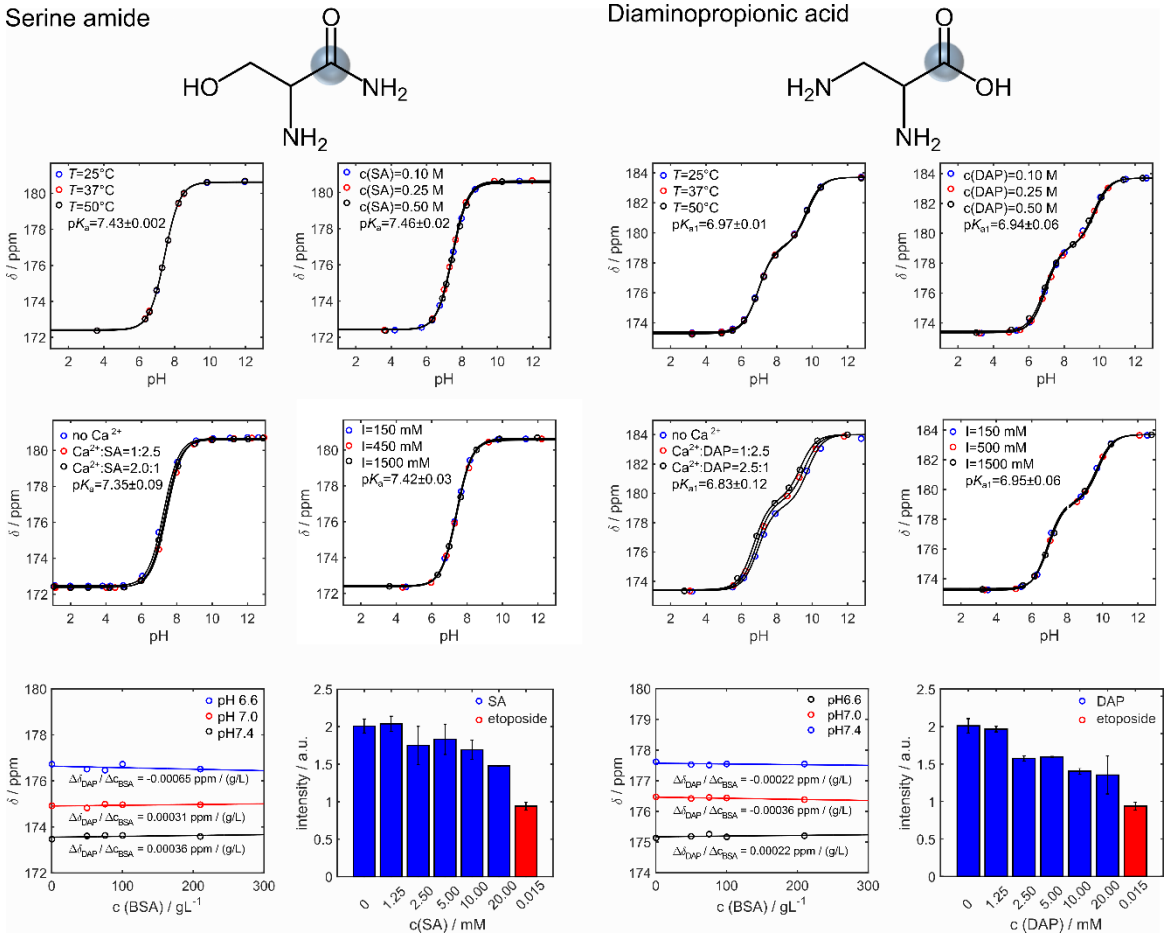

Figure 7.2. Dependency of pH sensitivity of serine amide (SA) and 2,3-diaminopropionic acid (DAP) under varying environmental conditions mimicking different physiological parameters. The ^{13}C chemical shift of SA (left two rows) and DAP (right two rows) are rather independent of temperature, sensor concentration, ionic strength, and the presence of proteins (BSA). DAP appears to slightly interact with Ca^{2+} ions, which was not observed for SA. Water-soluble tetrazolium (WST) cytotoxicity tests with EL4 tumor cells showed a slightly reduced metabolic activity at concentrations above 1.25 mM of DAP. At concentrations above 10 mM, a decrease in metabolic activity is observable for both DAP and SA, which is however not as prominent as for the positive control (etoposide). Note that the concentration of etoposide is 2 to 3 magnitudes lower than the one of DAP and SA. NMR pH titrations curves were obtained from 250 mM amino acid solutions except for experiments analyzing the effect of the sensor concentration on the pH-dependent chemical shifts. In that case, measured concentrations were 100 mM, 250 mM and 500 mM. Spectra were referenced to the resonance signal of 2.5 mM ^{13}C-urea set to 165 ppm.

Their chemical shift is not decisively altered or impeded by temperature, sensor concentration, ionic strength, or in presence of proteins. DAP appears to weakly interact with bivalent metal ions such as calcium, which was not observed for SA. WST cytotoxicity tests with EL4 tumor cells show a slightly reduced metabolic activity at concentrations above 1.25 mM of DAP. This is not observed for SA at concentrations relevant for *in vivo* applications (< 10 mM).

Figure 7.3 demonstrates that spin-½ nuclei other than ^{13}C exhibit a pH-sensitive chemical shift in the physiologically and pathologically relevant pH range. The nitrogen

chemical shifts of ^{15}N-labelled DAP are $\Delta\delta$ = 4.8 ppm (2-^{15}N) and $\Delta\delta$ = 4.6 ppm (3-^{15}N). Notably, we also observed pH-sensitive ^{31}P chemical shifts of P-Ser and P-Thr in that range ($\Delta\delta$ = 1.2 ppm and $\Delta\delta$ = 1.8 ppm), which were not observed for the ^{13}C-carbonyl (**Figure S7.4**).

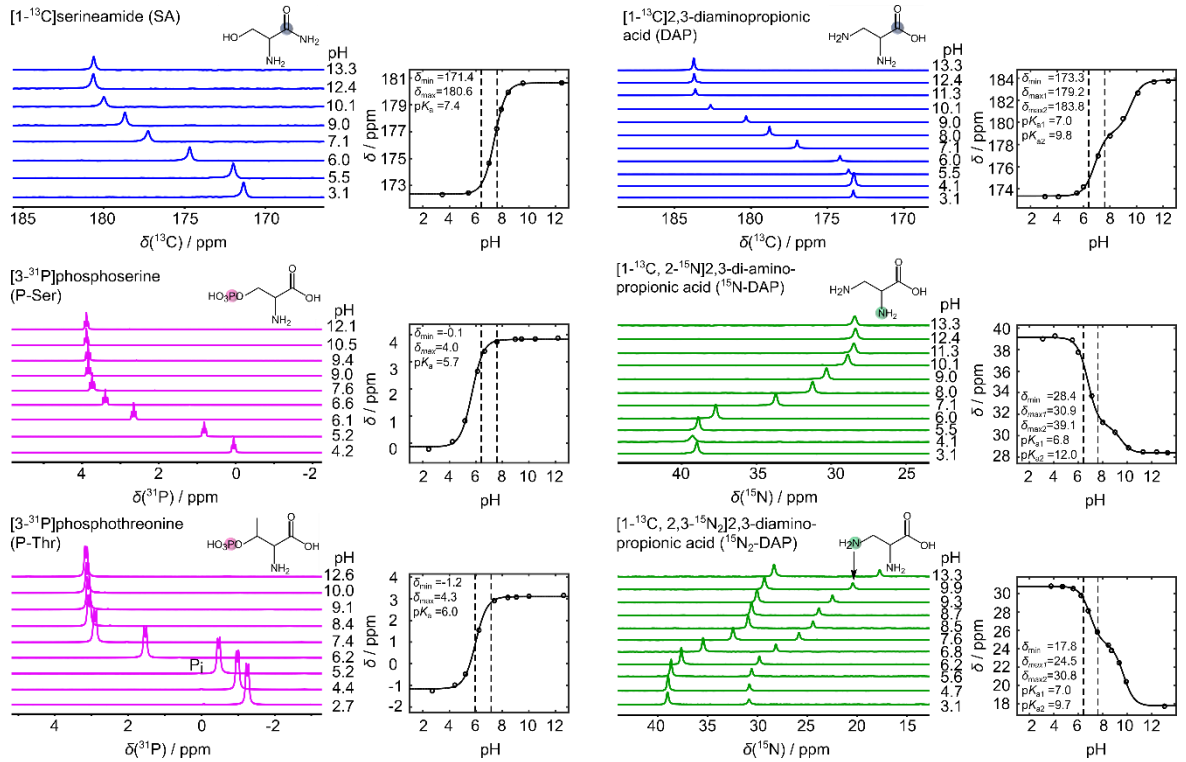

Figure 7.3. NMR titration curves of P-Ser, P-Thr, ^{13}C-SA, ^{13}C-DAP, ^{13}C-^{15}N-DAP, and ^{13}C-^{15}N$_2$-DAP. ^{13}C (blue), ^{31}P (purple), and ^{15}N (green) NMR pH titration series are shown for the respective amino acid given with their chemical structure. Measured nuclei are marked with filled circles of their respective colors. Fit curves and fitting parameters for pH-dependent chemical shifts are given next to each NMR series. Dashed lines mark the range pH 6.4 - 7.6. Concentrations of P-Ser, P-Thr, ^{13}C-DAP, ^{13}C-^{15}N-DAP, and ^{13}C-^{15}N$_2$-DAP were 300 mM. For, ^{13}C-SA, a 100 mM solution was measured. ^{13}C-spectra were referenced to the resonance signal of 250 mM ^{13}C-urea set to 165 ppm. ^{15}N- and ^{31}P-spectra were reference to the respective spectrometer frequency.

^{13}C-SA and ^{13}C-DAP hydrochloride form a glass at concentrations up to 6 M and 7 M, respectively, and show a 30% smaller maximum solid state polarization compared to [1-^{13}C]pyruvate (PA, **Figures 7.4** and **S7.5**). However, we observed that the HP signal of SA and DAP rapidly relaxed during the dissolution process in aqueous buffers yielding poor or no analyzable NMR spectra. Addition of vitamin C to the dissolution buffer allowed T_1 measurements with concentrations relevant for *in vivo* applications (20 - 30 mM) in aqueous solution (**Figure 7.4**, **Table S7.1** for vitamin C experiments) with reasonable liquid state polarization levels and signal enhancements ε (n = 3 measurements each): P(SA) = 9.5 ± 4.9%, ε(SA) = (1.1 ± 0.6) × 10^5 and P(DAP) = 7.5 ± 2.1%, ε = (0.8 ± 0.2) × 10^5 compared to P(PA) = 38.0 ± 1.4%. T_1 values were 13.8 ±

0.4 s and 18.8 ± 2.0 s for SA and DAP, respectively (T_1 (PA) = 62.3 ± 2.9 s). At pH values above neutral, the effect of vitamin C appeared to be weaker (**Table S7.1**).

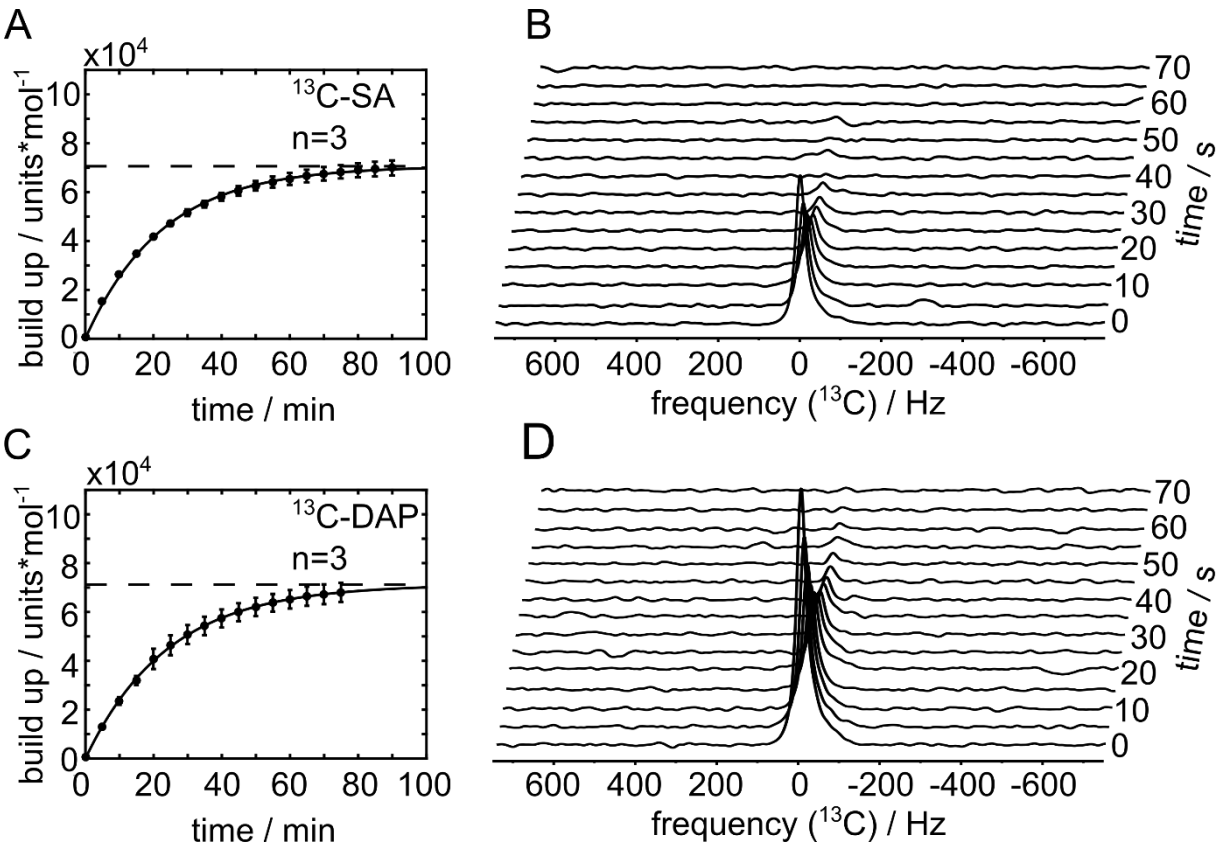

Figure 7.4. Molar solid-state polarization build-up (A, C) and polarization decay in aqueous solution (B, D) of DAP and SA. The maximum achievable molar solid-state polarization of DAP (A) and SA (C) were measured to 7.12 × 10^4 u.*mol^{-1} and 7.06 × 10^4 u.*mol^{-1}, respectively (from fit, horizontal dashed lines). After dissolution, the decaying ^{13}C NMR signal (B, D) was used to quantify T_1 = 13.8 s ± 0.4 s and T_1 = 18.8 s ± 2.0 s, for SA and DAP, respectively (B_0 = 1 T). The solid build up constants for SA and DAP were 22.5 ± 1.8 min and 24.2 ± 4.1 min, respectively. The build up constant of PA was 15.2 ± 0.5 min. Measured concentrations of DAP and SA were 20.9 ± 1.7 mM (pH 5.3 ± 0.8, n = 3) and 28.5 ± <0.1 mM (pH 5.8 ± 0.4, n = 3), respectively.

Finally, we acquired pH maps of thermally polarized, ^{13}C-labelled SA and DAP model solutions in 3D-printed, letter shaped compartments. SA solutions of distinct pH values were used to image the abbreviation of “Technical University of Munich does Magnetic Resonance Imaging” (TUM MRI, **Figure 7.5A**). DAP solutions were used to image a phantom shaped to resemble the Henderson-Hasselbalch equation (“pH = pK_a + log(A^-/HA)”, **Figure 7.5C**). The low ^{13}C-signal at the edges of the setup (“T”, “M” in **Figure 7.5A**, “p”, “a,”, “)” in **Figure 7.5C**) may be attributed to the low B_1 sensitivity of the coil in these regions (**Figure S7.6**). Nevertheless, pH values were recovered with a good accuracy except for those outside of the sensors range (pH < 6, **Table S7.2**).

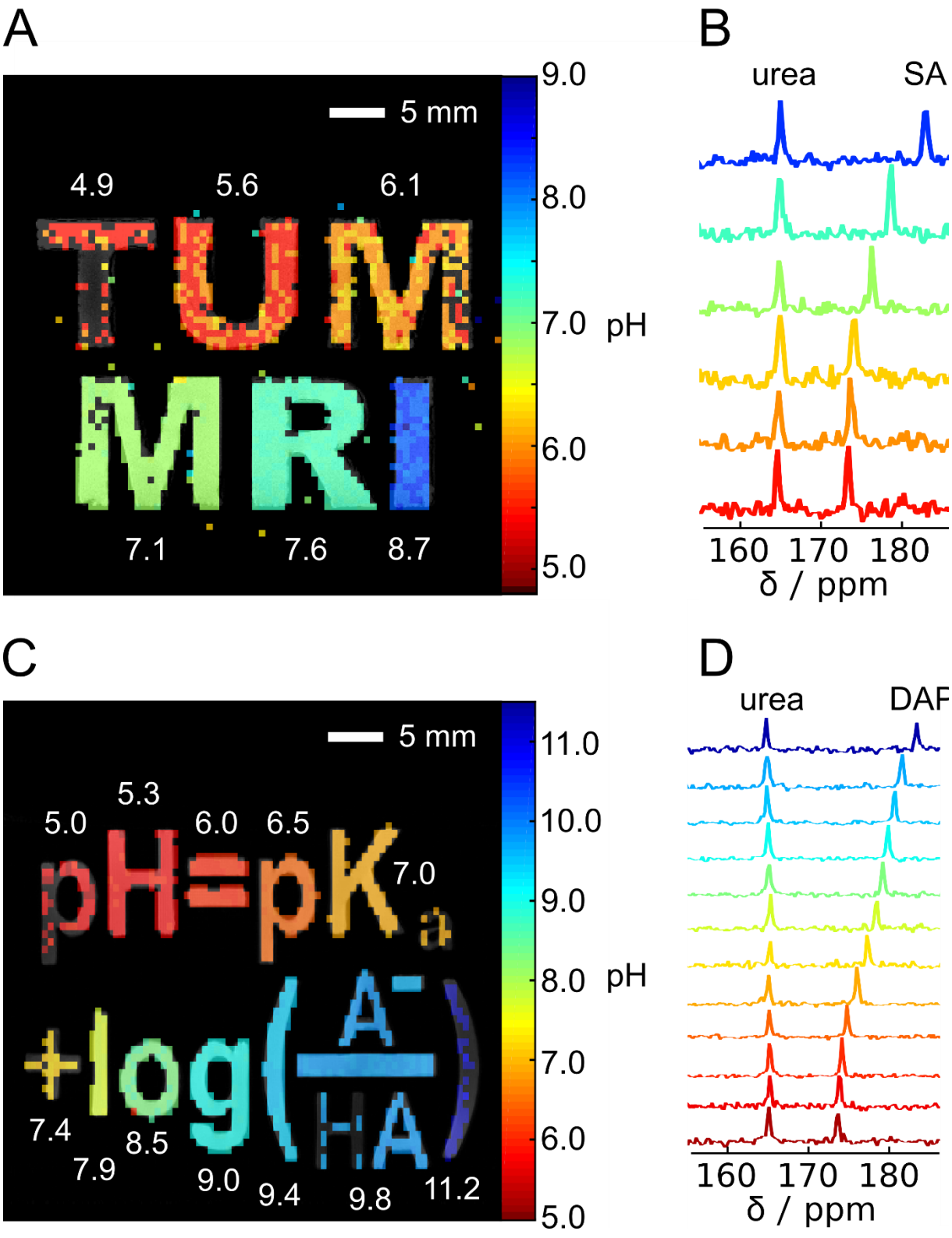

Figure 7.5. pH maps and ^{13}C-NMR spectra of thermally polarized SA and DAP. 3D-printed, letter-shaped compartments filled with solutions containing 250 mM ^{13}C-SA **(A)** or 250 mM ^{13}C-DAP **(C)** both with 250 mM ^{13}C-urea and 2 mM Dotarem at different pH. Chemical shift images were acquired and used to calculate pH maps ((A, C) color) co-registered with T_1-weighted ^{1}H images (gray). pH values measured with a pH electrode are written in white next to the respective compartment. NMR spectra of a representative voxel for each compartment are displayed for SA **(B)** and for DAP **(D)**

7.4 Discussion

Natural amino acids exhibit pH-dependent carbonyl carbon chemical shifts around the pK_a values of their carboxylic acid, their amino and their side chain groups. However, these pK_a values do not lie in the pH range that is useful for MR pH imaging, and the carbonyl chemical shift sensitivity of natural amino acids is small in that range (even for His and Cys). The physiological pH of blood and most bodily fluids is between pH 7.35 and pH 7.45 (up to pH 7.6), and diseases such as cancer exhibit an acidic extracellular tissue with pH as low as pH 5.8.[28, 29, 166, 295, 296] The ideal pK_a of an *in vivo* pH sensor should therefore be around pH 7.0 ± 0.6 in order to achieve maximum pH sensitivity. Amidation or esterification of amino acids removes the carboxylic acid proton and the molecule thus loses the pH sensitivity of its carboxylic acid. In effect, this lowers the pK_a of the amino group toward pH values of physiological relevance. The addition of groups with positive inductive effects increases the pK_a, which we demonstrated for basic and phosphorylated amino acids and that also applies for dicarboxylic acids, pyridine derivatives[218], and most probably for other pH-sensitive molecules like furanones[78]. On the other hand, addition of moieties or atoms with negative inductive effects (-I) decreases the pK_a.

Spectroscopy and MRI (^{1}H, ^{19}F, ^{31}P) with molecules bearing pH-sensitive chemical shifts are easily applicable approaches to measure pH *in vivo.* IEPA and ISUCA were used to measure pH in pre-clinical studies, and histidine could sense pH in human brain after oral loading. However, a main drawback of thermally polarized sensors is the requirement of high sensor doses and long scan times. In fact, concentrations were two[201, 204, 299] to three[202, 298] magnitudes higher, and scan times about one (for single voxel spectroscopy)[298] to two magnitudes (imaging)[201, 202] longer, compared to *in vivo* studies with hyperpolarized sensors.[78]

Hyperpolarization enables MR imaging with up to more than 10^4 - 10^5 fold signal enhancements. This reduces scan times to a few seconds yielding MRSI images with high signal to noise ratios and a comparable resolution as obtained with thermally polarized sensors (IEPA: (2 × 2 × 4) mm^{3}[201] ^{13}C-bicarbonate: (2 × 2 × 6) mm^3,[166] nominal resolution). Furthermore, HP allows low sensor doses of ≤ 0.05 mM/kg,[78] which potentially minimizes toxic side effects caused by the injection of highly concentrated exogenous compounds. Nevertheless, isotope enrichment and especially DNP instrumentation are rather expensive, whereas other HP techniques like PHIP can be implemented at lower costs.

Spin-½ nuclei can be polarized using various polarization techniques. Carbon- and nitrogen-bearing compounds can be isotopically enriched with ^{13}C and ^{15}N in amino acid derivatives, and ^{31}P is highly abundant in nature. Even though serine alkyl esters might form unhealthy alcohol degradation products, unsaturated precursors for pH sensors with a sensitivity up to $\Delta\delta$ = 4.5 ppm (e.g., serine allyl ester) could be

synthesized which are potentially amenable for parahydrogen (H_2) induced polarization (PHIP, **Figure S7.7**)[225]. In addition to ^{13}C, amino acid derivatives (and histidine) bear pH-sensitive ^{15}N and ^{31}P nuclei. ^{15}N could be a potential target for signal enhancement by reversible exchange (SABRE), which was already shown for imidazole - the side chain group of histidine.[119] This PHIP-based technique does not require chemical addition of H_2 but has so far mainly been applied to cyclic, unsaturated, and most probably unhealthy pH-sensitive ^{15}N-compounds.[113] Nevertheless, SABRE has already been used to enhance the proton NMR signal of amino acids, which could probably be extended to ^{15}N.[305] Recently, ^{31}P-phosphate and ^{31}P-phosphocreatine have been successfully polarized with DNP, suggesting that phosphoserine and phosphothreonine could be polarized as well and could potentially be used for *in vivo* applications.[300]

So far, two promising HP ^{13}C-labelled chemical shift-based pH sensors for pre-clinical applications have been presented in the literature. ^{13}C-diethyl malonic acid (DEMA) exhibits a long T_1 (≈106 s, B_0 = 11.7 T) and was used *in vitro* to sense pH,[216] while [1,5-^{13}C]zymonic acid (ZA) has already been applied for pH *in vivo* imaging in rodent kidneys and tumors.[78, 122] Serine derivatives and DAP ($\Delta\delta$ = 4.2 ppm) exhibit a 2.4 or 1.5-fold higher pH sensitivity than diethyl malonic acid ($\Delta\delta$ = 1.7 ppm) and zymonic acid ($\Delta\delta$ = 2.4 ppm), respectively. ^{13}C-SA and ^{13}C-DAP appear to be biocompatible and they are stable in solution. Both molecules exhibit a reasonable solid state polarization level when polarized with DNP, but we observed a rapid signal loss after dissolution. This has been observed earlier for polarizations with 4-hydroxy-2,2,6,6-tetramethylpiperidine-1-oxyl (TEMPOL) radicals,[307] for natural amino acids and molecules with amino groups directly attached to ^{13}C-carbonyls (e.g., urea).[243] Studies in absence and presence of vitamin C and at different pH values (**Table S7.1**) showed that vitamin C, which most likely scavenges[307] the radical, is essential to preserve hyperpolarization during the dissolution process or during transfer of the probe from the polarizer to the NMR spectrometer through transient Earth's magnetic field. At pH values above neutral, the quenching effect of vitamin C was weaker, and, in dissolutions without vitamin C, relaxation effects were reduced. Liquid state polarization of SA and DAP could be further improved, e.g., by filtration (radical and paramagnetic impurities) and the usage of magnetic transfer lines.[231-235, 242-245, 304, 308] Although the pH sensitivity of SA and DAP is higher than for diethyl malonic acid and zymonic acid, their T_1 is relatively short (up to ≈ 18 s at B_0 = 1 T) compared to DEMA (≈ 106 s, B_0 = 11.7 T)[216] and ZA (≈ 56 s at B_0 = 1 T).[78] Deuteration, dissolution in D_2O,[120, 122] or the use of long-lived singlet states[249-251] could enhance the HP signal lifetime and will be subject for further studies.

Future *in vivo* application of pH sensitive amino acid derivatives will require their co-polarization with an internal reference without chemical shift sensitivity to back-calculate the pH. As reported earlier[78], ^{13}C-urea is feasible, and we are seeking to

establish recipes for co-polarization to provide optimal protocols for *in vivo* pH measurements.

7.5 Conclusion

We systematically analyzed the effect of carbon chain length reduction and derivatization of naturally occurring amino acids on their pH-dependent chemical shift sensitivity. Thereby, we have found a strategy to tailor the pK_a of molecules toward the physiologically relevant pH range, which is necessary for the development of magnetic resonance pH biosensors. Notably, amino acid derivatives bear different spin-½ nuclei that exhibit a pH-dependent chemical shift in the physiological range and that can be polarized using DNP. Two novel pH sensors that can be potentially applied *in vivo*, namely [1-^{13}C]serine amide and [1-^{13}C]-2,3-diaminopropionic acid, have been identified. These molecules showed reasonable solid-state polarization levels and, to the best of our knowledge, exhibit the largest ^{13}C-chemical shift pH sensitivity known so far in the literature. Our findings elucidate the effect of chemical derivatization on MR pH sensitivity and are potentially transferable to other molecule classes.

7.6 Supplementary Information

7.6.1 Supplementary Figures

pH-dependent chemical shift of amino acids and derivatives

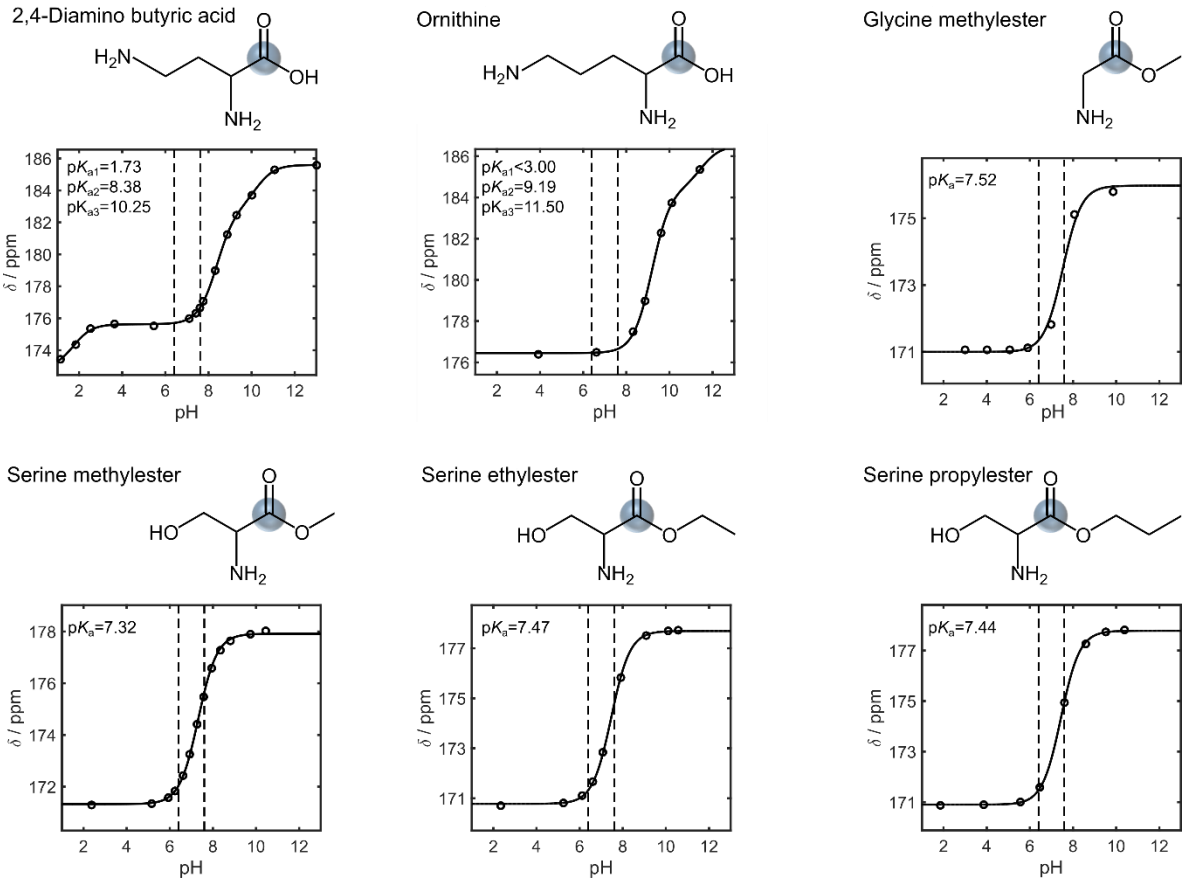

Figure S7.1: pH dependent chemical shift of carbonyl ^{13}C-atoms of 2,4-diamino butyric acid, ornithine, glycine methyl ester, serine methyl, ethyl and propyl ester. Chemical structures of the respective amino acids, NMR titration curves and pK_a values calculated from the fit are given. The pH range relevant for pH *in vivo* imaging is indicated with vertical dashed lines in each pH NMR titration plot.

pH-dependent chemical shifts of cysteine and histidine

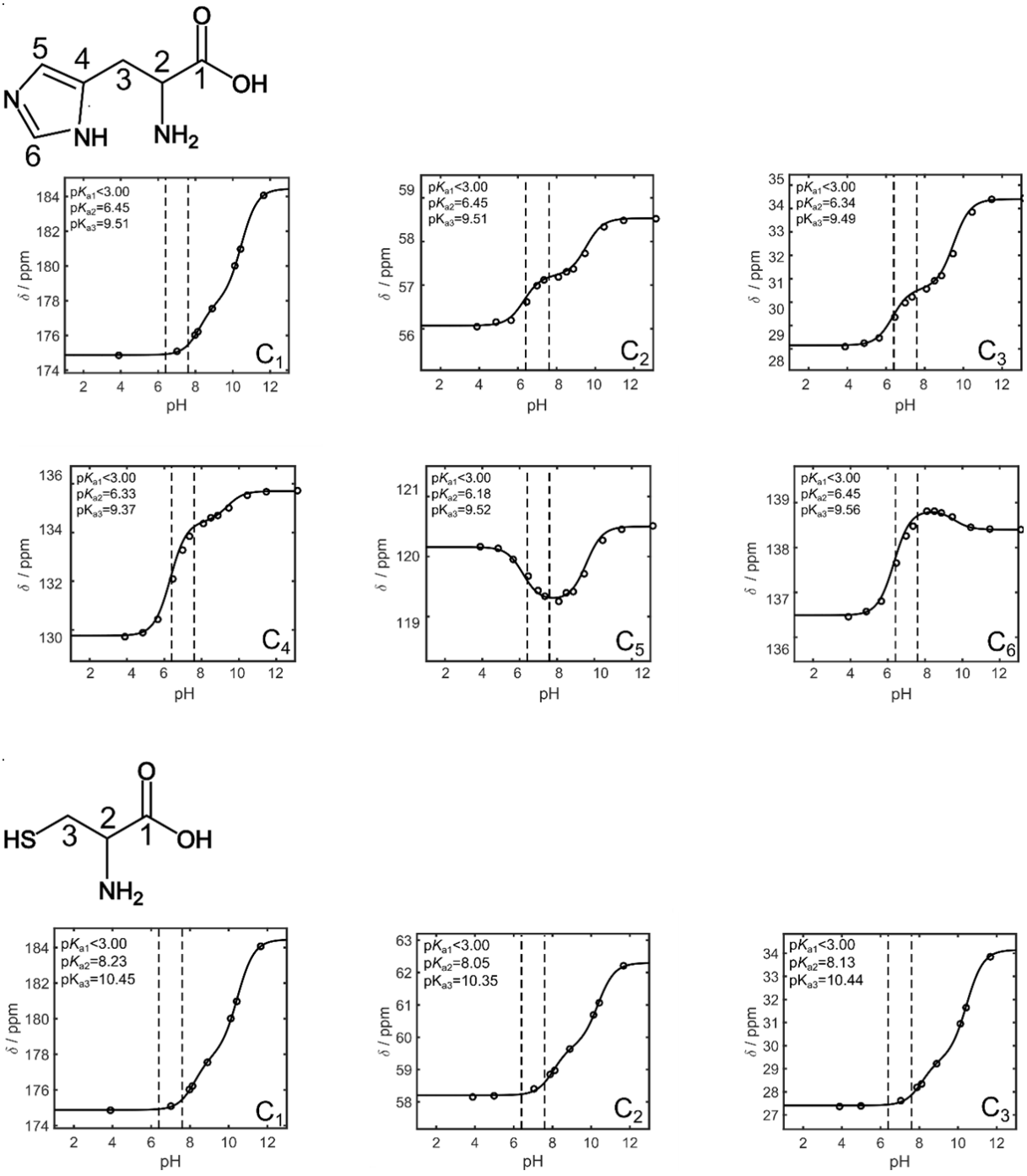

Figure S7.2: NMR pH titration curves of histidine (top) and cysteine (bottom). Chemical structures of both amino acids and the respective pH dependent chemical shifts are given. Histidine and cysteine bear side chains groups with a pK_a close to a range that is relevant for pH *in vivo* imaging. However, their chemical shift sensitivity between pH 6.4 and pH 7.6 of all carbon atoms is rather low.

Stability of amino acid esters in aqueous solution

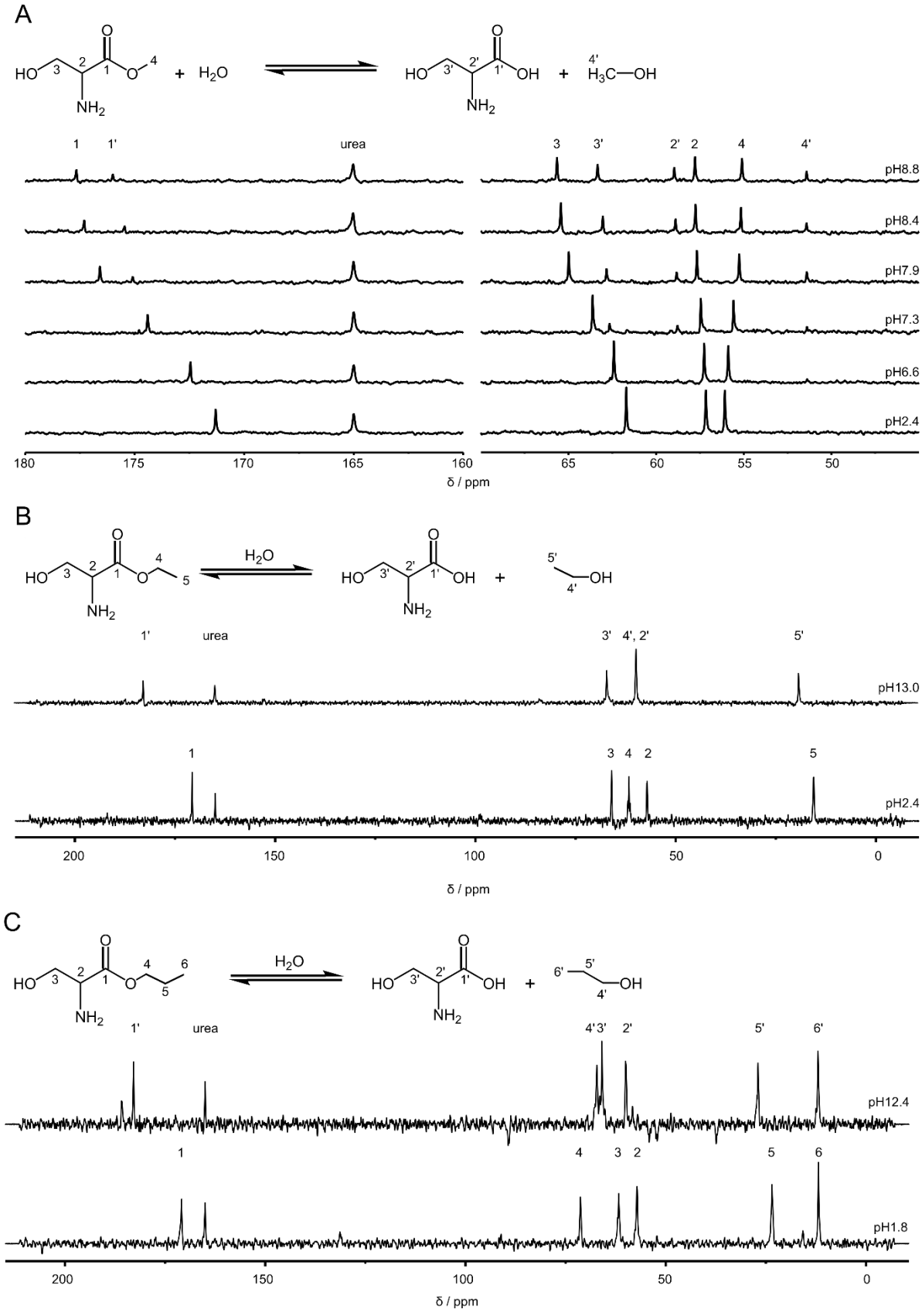

Figure S7.3: Stability of serine alkyl esters in aqueous solution. (A) NMR titration series of serine methyl ester shows that the molecule hydrolysis in aqueous solution forming serine and methanol. **(B)**

First and last spectrum of an NMR titration series of serine ethyl ester. The amino acid derivative is stable at low pH and starts hydrolyzing at pH > 10. The NMR titration series took less than 1 hour. **(C)** The same observation as in (B) was made for serine propyl ester.

^{13}C-spectra of NMR titration series of phosphoserine (P-Ser) and phosphothreonine (P-Thr)

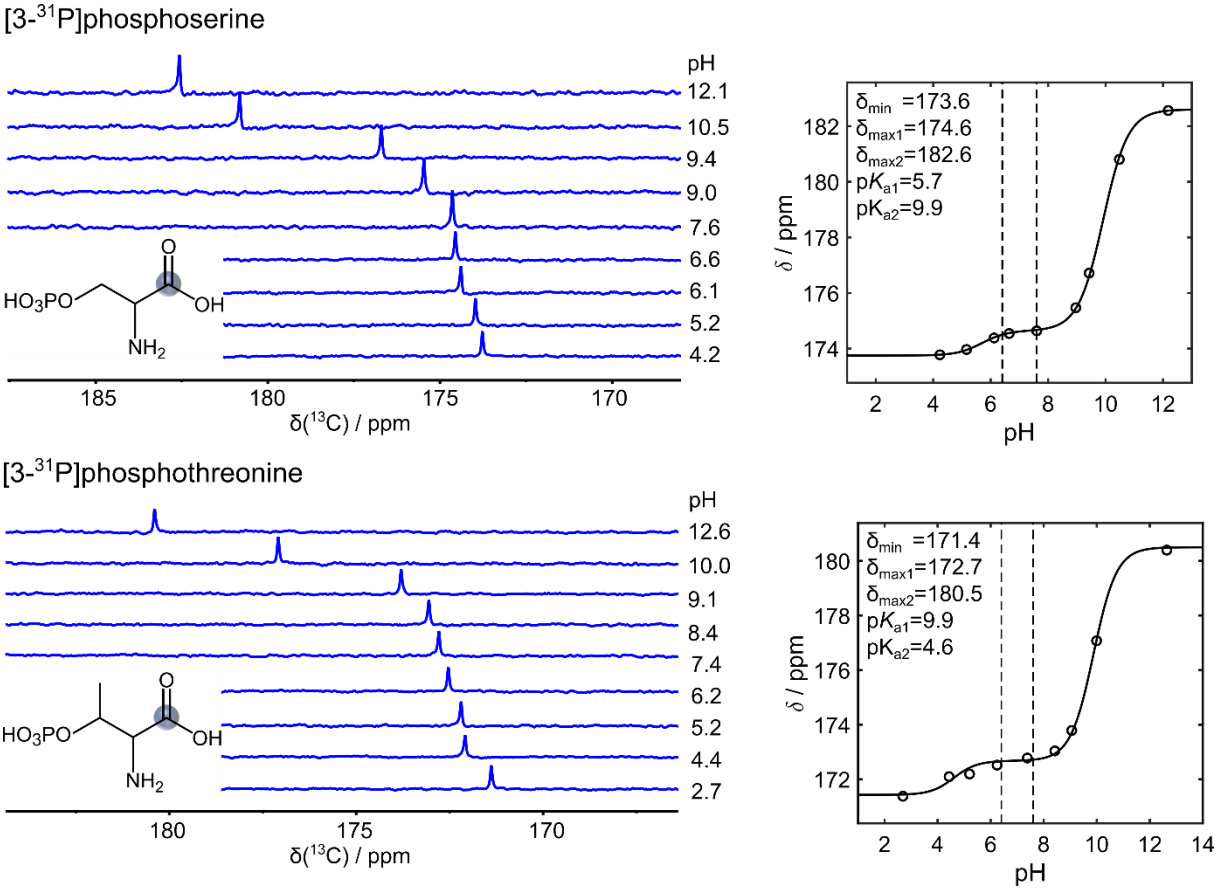

Figure S7.4: ^{13}C-NMR pH titration series of [3-^{31}P]phosphoserine (P-Ser) and [3-^{31}P]phosphothreonine (P-Thr). On the right side, the chemical structure and the respective NMR signal of the carboxyl carbon atom (circled in blue in the structure) of P-Ser and P-Thr shifting with pH is shown. On the left side, the pH-dependent chemical shifts are plotted against pH and fits are given with the respective fitting parameters. The pH range relevant for pH *in vivo* imaging is indicated with vertical dashed lines in each pH NMR titration plot.

Molar solid state polarization build ups of ^{13}C-DAP, ^{13}C-SA and [1-^{13}C]pyruvate

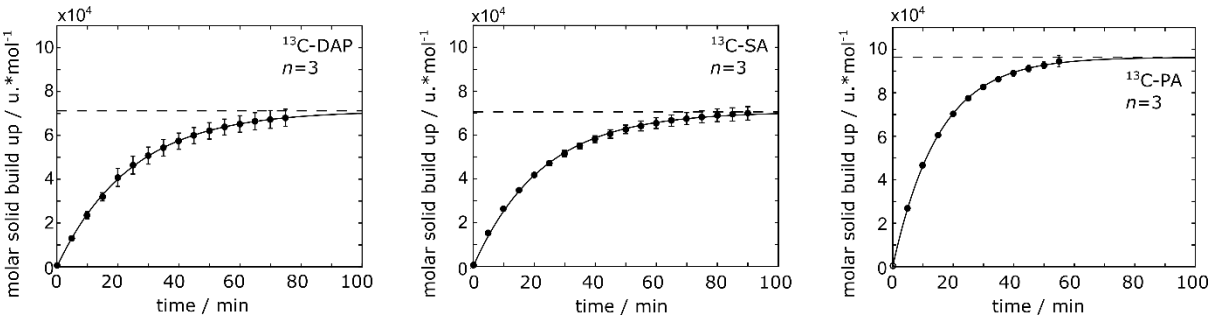

Figure S7.5: Molar solid state polarization build-up of ^{13}C-DAP and ^{13}C-SA compared and ^{13}C-pyruvate (^{13}C-PA). The maximum molar solid state polarization build-up of DAP and SA is about 30 % smaller than the one of pyruvate. The fitted maximum solid state polarization level is indicated by horizontal dashed lines. The solid build up constants for SA, DAP and PA were 22.5 ± 1.8 min, 24.2 ± 4.1 min and 15.2 ± 0.5 min, respectively.

B_1-field homogeneity of the ^{1}H/^{13}C volume coil

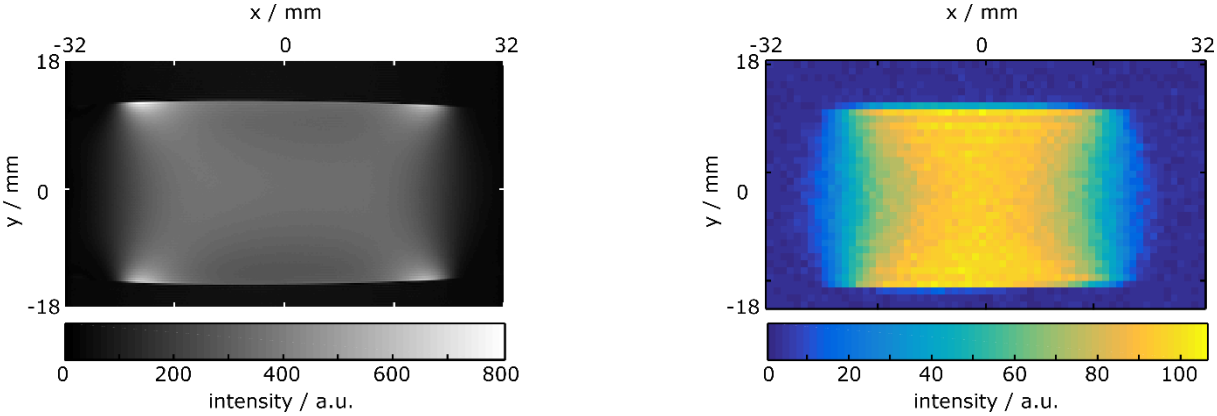

Figure S7.6: ^{13}C-Images of ^{13}C-urea in water uniformly filling the entire field of view of the ^{1}H/^{13}C volume coil. The left image shows a coronal proton image. The right image shows the ^{13}C-signal in the same orientation as the proton image indicating a lower B_1-field away from the axial center of the ^{1}H/^{13}C volume coil.

The spatially varying sensitivity of the ^{1}H/^{13}C volume coil was assessed for ^{13}C-CSI by acquiring an image of a uniform phantom containing 1.8 M ^{13}C-urea and 50 mM DOTA, with diameter 28.7 mm (50 mL Falcon tube), and length extending past both axial ends of the sensitive volume of the coil. A horizontal image was acquired with a 2D phase-encoded chemical shift imaging sequence, with repetition time 35 ms, flip angle 60°, matrix size 64x36, field of view (64x36) mm^2, slice thickness 2 mm, 9 averages, total scan time 2 min 6 s, receive bandwidth 2 kHz, 64 points acquired per phase-encode, spectral resolution 5.6 Hz, excitation bandwidth 12 kHz, and chemical shift offset 163.5 ppm. Automated linear shimming on the proton signal from the phantom was run prior to ^{13}C-image acquisition. ^{13}C-images were reconstructed in Matlab (The Mathworks, Natick, MA, USA), and then averaged over frequencies within +/- 50 Hz of the peak

frequency at the center of the phantom. The reconstructed sensitivity image covers the entire sensitive length and diameter of the volume coil, and the uniform phantom completely fills the sensitive volume.

The cause of intensity variation is the variation of transmit and receive B_1 of the coil with position. Within the axially central 20 mm, the sensitivity is relatively uniform, but further away from the center of the coil, the sensitivity drops substantially. The relationship between phantom T_1, scan repetition time and flip angle, and coil B_1-variation is more complicated than warrants a full discussion here. However, this image illustrates the cause - coil B_1 variation - of reduced image intensity in areas further away from the axial center of the letter shaped phantoms.

Amino acid esters as potential targets for ^{13}C parahydrogen induced polarization (PHIP)

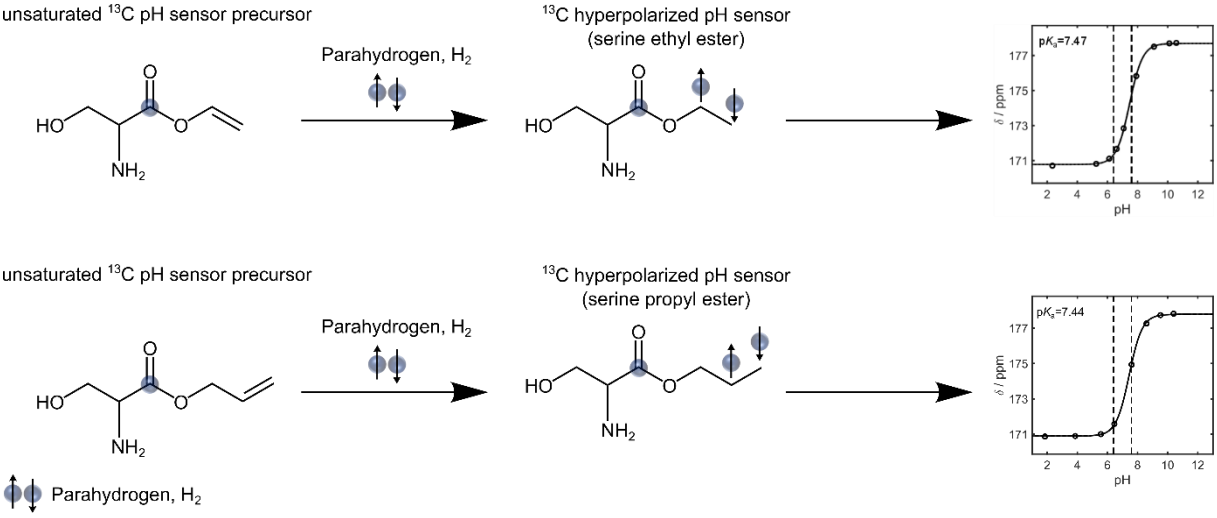

Figure S7.7: Amino acid esters as potential targets for ^{13}C parahydrogen induced polarization (PHIP). Unsaturated vinyl and allyl esters of serine are potentially amendable for chemical addition of parahydrogen yielding serine ethyl and propyl ester that are sensitive to pH at the physiological range.

The carbonyl carbon of pyruvate and acetate esters with unsaturated alkyl chains can be hyperpolarized by addition of parahydrogen.[225] Analogous to that, parahydrogen addition to unsaturated precursors of serine ethyl ester and serine propyl ester should yield the desired hyperpolarized pH sensors. Synthesis of amino acid allyl and vinyl esters has been described previously.[309, 310]

7.6.2 Supplementary Tables

Table S7.1: Hyperpolarization experiments of ^{13}C-DAP in absence and presence of vitamin C at varying pH.

Vitamin C							
pH	4.08	5.45	5.59	6.20	7.24	7.99	8.8
Pol. Level / %	11.99	8.99	5.23	7.49	0.08	3.52	0.19
T1 / s	20.45	21.2	17.5	17.8	Low signal	22.2	21.3
Time to polarizer / s	29	21	22	22	22	22	26
No Vitamin C							
pH	2.67	5.45	6.54	6.84 (n=2)	7.18	7.44	7.84
Pol. Level / %	No signal	No signal	No signal	No signal	No signal	No signal	0.32
T_1 / s	No signal	No signal	No signal	No signal	No signal	No signal	17.1
Time to polarizer / s	25	24	25	24.5±0.7	23	27	22

Table S7.2: Electrode and ^{13}C-calculated pH values of spatially resolved pH measurements with letter shaped 3D printed phantoms.

Letter	pH image*	Electrode pH (± 0.01 std.)	Letter	pH image*	Electrode pH (± 0.01 std.)
T	5.71 ± 0.17	4.88	p	5.62 ± 0.23	5.00
U	5.80 ± 0.26	5.62	H	5.7 ± 0.1	5.30
M	6.07 ± 0.28	6.11	=	6.0 ± 0.1	6.00
M	6.97 ± 0.12	7.06	p	6.4 ± 0.1	6.50
R	7.40 ± 0.11	7.56	K_a	6.9 ± 0.04	7.01
I	8.93 ± 0.24	8.70	+	7.2 ± 0.04	7.41
			I	7.7 ± 0.05	7.85
			o	8.4 ± 0.30	8.50
			g	9.0 ± 0.04	9.00
			(	9.4 ± 0.04	9.32
			A^- / HA	9.8 ± 0.07	9.81
			)	11.3 ± 0.13	11.22

*pH values calculated from the pH images are mean±*std* of all voxels from the respective letter excluding signals that were 20% smaller than the maximum intensity signal.

8. Summary and Outlook

This work presented the development of new imaging strategies to non-invasively study the tumor metabolism - namely the Warburg effect - with cutting edge techniques such as hybrid PET/MR and hyperpolarized ^{13}C-magnetic resonance spectroscopic imaging.

The key study of this thesis (**chapter 4**) showed that the simultaneous acquisition of augmented glucose uptake with FGD-PET and LDH activity with MRSI of hyperpolarized [1-^{13}C]pyruvate is feasible at a clinical PET/MR system and with tumor model sizes as small as a rat. A quantitative comparison of the data revealed that the analyzed breast tumor model follows the Warburg effect and reduces a major portion of consumed glucose to lactate. Besides the assessment of the first and the last step of the Warburg effect, metabolic data from PET and MRSI could be analyzed in the anatomic context at high resolution, which allowed for an accurate tumor localization and delineation. Furthermore, the tumor cellularity was addressed with diffusion-weighted imaging. This revealed that a variable cell density can introduce a bias for the quantification of image-derived metabolic data.

Future studies should focus on an improved quantification of metabolic information derived from PET and ^{13}C-data. The resolution of a clinical PET/MR is too low to accurately resolve small rodent structures like the vena cava, which is important to derive the dynamic glucose uptake of tumors. Limitations were partially overcome by the definition of correction factor using comparative measurements with a dedicated small-animal PET/CT. However, arterial sampling is more precise to quantify such correction factors and the feasibility to integrate this approach into the existing work-flow should be evaluated, even though this invasive and rather time consuming.

One of the most important parameters of hyperpolarized probes is their spin-lattice-relaxation time, which is in an order of a view tens of seconds thus limiting the time available for an experiment to a few minutes. This work used a regular free induction decay chemical shift imaging (FIDCSI) to generate metabolic images. However, FIDCSI requires a fairly high amount of hyperpolarized magnetization to visualize metabolic information. Furthermore, it is prone to point spread function artefacts that introduce a bias for the quantification of pyruvate-to-lactate conversion rates. More sophisticated and accelerated ^{13}C-imaging strategies such as IDEAL spiral CSI or multi-echo balanced steady state free precession (me-bSSFP) have been developed. These promising strategies yield higher spatial and temporal resolution thus increasing the accuracy of metabolic data. Me-bSSFP was recently implemented at the PET/MR that was used in this thesis and the evaluation of its performance is ongoing research.

Tumors that follow the Warburg effect produce an excess of lactate in their cytosol, which is finally co-exported with protons leading to an acidification of the extracellular space. This so called lactate acidification can be quantified non-invasively by several

techniques including hyperpolarized pH sensor molecules. The current literature on pH imaging was reviewed in this work (**chapter 5**), which revealed that ^{13}C-zymonic acid (ZA) is the only chemical shift based sensor that was so far able to sense the pH *in vivo*. Therefore, another part of this work was to improve the sensitivity of ZA by prolonging the hyperpolarized signal lifetime (**chapter 6**). This was achieved by deuteration of stably attached protons, which enabled sensitivity enhanced imaging of the acidic microenvironment of tumors in rats. Furthermore, we demonstrated that a longer signal life-time can generally be used to follow pH changes with spatial and temporal resolution at the same clinical PET/MR used in the study in **chapter 4**.

Zymonic acid is the dehydrated dimer of pyruvate and was so far only synthesized with two pH sensitive ^{13}C-labels at position one and five. As both resonance signals shift into the same direction with varying pH, a future improvement could be to selectively label ZA preferably at positon one, because it has a fairly high pH sensitivity and a rather long hyperpolarized signal life time.

Last, this thesis aimed to characterize hyperpolarized amino acids and their derivatives as new molecular class of chemical shift based pH sensors (**chapter 7**). In general, amino acids can be enriched with several spin-½ nuclei (^{13}C, ^{15}N) that exhibit a pH dependent chemical shift and might be amenable to hyperpolarization. The two most promising candidates ^{13}C-serine amide (SA) and ^{13}C-diaminopropionic acid (DAP) exhibit the highest ^{13}C-chemical shift pH sensitivity so far known in the literature. Furthermore, the molecules showed no cytotoxic effect in tumor cell experiments and could be hyperpolarized. However, they have a rather short T_1, which should in future be prolonged by deuterium enrichment as was shown for ZA.

In summary, the simultaneous acquisition of metabolic, cellular and anatomic data allowed for an accurate characterization of the initial and the last step of glycolysis in malignant tissues. In the future, a multimodal assessment of all key metabolic steps of the Warburg effect with FDG-PET, hyperpolarized ^{13}C-pyruvate MRSI and hyperpolarized pH imaging within one scan session could prove to be highly valuable for an even more accurate characterization of tumor biology.

Most of the experiments in this thesis were performed at a clinical PET/MR system combined with cutting edge hyperpolarized metabolic imaging. The application of these methods to bigger tumor models or their translation into the clinic are the most interesting outlooks to give. While FDG-PET and diffusion-weighted imaging are already clinically approved and used on a daily base, hyperpolarized MRSI requires the production of sterile and quality-controlled hyperpolarized probes, which was recently made possible with commercially available sterile polarizers.

The combination of PET, MRI, DWI and cutting-edge hyperpolarized MRSI on a clinical PET/MR is a promising approach to understand tumor biology in greater depth. Therefore, this work finally contributes to the concept of precision medicine, which aims to reduce the global burden of non-communicable diseases (**chapter 1**).

9. Bibliography

1. U.N. *Political declaration of the high-level meeting of the General Assembly on the prevention and control of non-communicable diseases. (accessed June, 2018)*. 2011; Available from: http://www.un.org/en/ga/ncdmeeting2011.
2. WHO. *Key facts on noncommunicable diseases. (accessed June, 2018).* 2018; Available from: http://www.who.int/news-room/fact-sheets/detail/noncommunicable-diseases.
3. Lee, K., *Tobacco control yields clear dividends for health and wealth.* Public Library of Science Medicine, 2008. **5**(9): p. e189.
4. Kircher, M.F., H. Hricak, and S.M. Larson, *Molecular imaging for personalized cancer care.* Molecular Oncology, 2012. **6**(2): p. 182-95.
5. Stewart, B.W. and C.P. Wild, *World cancer report*. 2014.
6. Kelloff, G.J., et al., *Progress and promise of FDG-PET imaging for cancer patient management and oncologic drug development.* Clinical Cancer Research, 2005. **11**(8): p. 2785-808.
7. Atri, M., *New technologies and directed agents for applications of cancer imaging.* Journal of Clinical Oncology, 2006. **24**(20): p. 3299-308.
8. Leonard, F., *Imaging and cancer: A review.* Molecular Oncology, 2008. **2**(2): p. 115-52.
9. Histed, S.N., et al., *Review of functional/anatomical imaging in oncology.* Nuclear Medicine Communications, 2012. **33**(4): p. 349-61.
10. Gordon, P.B. and L.S. Goldenberg, *Malignant breast masses detected only by ultrasound. A retrospective review.* Cancer, 1995. **76**(4): p. 626-30.
11. Brito, J.P., et al., *The accuracy of thyroid nodule ultrasound to predict thyroid cancer: Systematic review and meta-analysis.* The Journal of Clinical Endocrinology and Metabolism, 2014. **99**(4): p. 1253-63.
12. Moreno, C.C., et al., *Testicular tumors: What radiologists need to know-differential diagnosis, staging, and management.* RadioGraphics, 2015. **35**(2): p. 400-15.
13. Herth, F.J.F., et al., *Real-time endobronchial ultrasound guided transbronchial needle aspiration for sampling mediastinal lymph nodes.* Thorax, 2006. **61**(9): p. 795-8.
14. Puli, S.R., et al., *Accuracy of endoscopic ultrasound to diagnose nodal invasion by rectal cancers: a meta-analysis and systematic review.* Annals of Surgical Oncology, 2009. **16**(5): p. 1255-65.
15. Steiner, E., et al., *Transvaginal ultrasound for endometrial carcinoma screening-current evidence-based data.* Geburtshilfe und Frauenheilkunde, 2012. **72**(12): p. 1088-91.
16. Wesolowski, J.R. and M.H. Lev, *CT: History, technology, and clinical aspects.* Seminars in Ultrasound, CT, and MR, 2005. **26**(6): p. 376-9.
17. De Wever, W., J. Verschakelen, and J. Coolen, *Role of imaging in diagnosis, staging and follow-up of lung cancer.* Current Opinion In Pulmonary Medicine, 2014. **20**(4): p. 385-92.
18. Pearce, M.S., et al., *Radiation exposure from CT scans in childhood and subsequent risk of leukaemia and brain tumours: a retrospective cohort study.* Lancet, 2012. **380**(9840): p. 499-505.
19. Church, T.R., et al., *Results of initial low-dose computed tomographic screening for lung cancer.* New England Journal of Medicine, 2013. **368**(21): p. 1980-91.
20. Hutton, B.F., *The origins of SPECT and SPECT/CT.* European Journal of Nuclear Medicine and Molecular Imaging, 2014. **41 Suppl 1**: p. 3-16.
21. Rahmim, A. and H. Zaidi, *PET versus SPECT: Strengths, limitations and challenges.* Nuclear Medicine Communications, 2008. **29**(3): p. 193-207.
22. Van Dort, M.E., A. Rehemtulla, and B.D. Ross, *PET and SPECT imaging of tumor biology: New approaches towards oncology drug discovery and development.* Current Computer-Aided Drug Design, 2008. **4**(1): p. 46-53.
23. Hricak, H., et al., *Global trends in hybrid imaging.* Radiology, 2010. **257**(2): p. 498-506.
24. Khalil, M.M., et al., *Molecular SPECT imaging: An overview.* International Journal of Molecular Imaging, 2011. **2011**: p. 796025.
25. Rosenkrantz, A.B., et al., *Current status of hybrid PET/MRI in oncologic imaging.* American Journal of Roentgenology, 2016. **206**(1): p. 162-72.
26. García-Figueiras, R., et al., *Proton magnetic resonance spectroscopy in oncology: the fingerprints of cancer?* Diagnostic and Interventional Radiology, 2016. **22**(1): p. 75-89.
27. Khlebnikov, V., et al., *Chapter FIVE-^{31}P-MRSI studies in patients with cancer*, in *Annual Reports on NMR Spectroscopy*, G.A. Webb, Editor. 2016, Academic Press. p. 319-68.

28. Gillies, R.J., et al., *MRI of the tumor microenvironment.* Journal of Magnetic Resonance Imaging, 2002. **16**(4): p. 430-50.
29. Gillies, R.J., et al., *pH imaging. A review of pH measurement methods and applications in cancers.* IEEE Engineering in Medicine and Biology Magazine, 2004. **23**(5): p. 57-64.
30. van Zijl, P.C.M. and N.N. Yadav, *Chemical exchange saturation transfer (CEST): what is in a name and what isn't?* Magnetic Resonance in Medicine, 2011. **65**(4): p. 927-48.
31. Walker-Samuel, S., et al., *In vivo imaging of glucose uptake and metabolism in tumors.* Nature medicine, 2013. **19**(8): p. 1067-72.
32. Rivlin, M., et al., *Molecular imaging of tumors and metastases using chemical exchange saturation transfer (CEST) MRI.* Scientific Reports, 2013. **3**: p. 3045.
33. Zhou, J., et al., *Using the amide proton signals of intracellular proteins and peptides to detect pH effects in MRI.* Nature Medicine, 2003. **9**(8): p. 1085-90.
34. Patz, S., et al., *Hyperpolarized ^{129}Xe-MRI: A viable functional lung imaging modality?* European Journal of Radiology, 2007. **64**(3): p. 335-44.
35. Serrao, E.M. and K.M. Brindle, *Potential clinical roles for metabolic imaging with hyperpolarized [1-^{13}C]pyruvate.* Frontiers in Oncology, 2016. **6**.
36. Hesketh, R.L. and K.M. Brindle, *Magnetic resonance imaging of cancer metabolism with hyperpolarized ^{13}C-labeled cell metabolites.* Current Opinion in Chemical Biology, 2018. **45**: p. 187-94.
37. Ardenkjaer-Larsen, J.H., et al., *Dynamic nuclear polarization polarizer for sterile use intent.* NMR in Biomedicine, 2011. **24**(8): p. 927-32.
38. Cunningham, C.H., et al., *Hyperpolarized ^{13}C-metabolic MRI of the human heart: Initial experience.* Circulation Research, 2016. **119**(11): p. 1177-82.
39. Miloushev, V.Z., et al., *Metabolic imaging of the human brain with hyperpolarized ^{13}C-pyruvate demonstrates ^{13}C-lactate production in brain tumor patients.* Cancer Research, 2018. **78**(14): p. 3755-60.
40. Fatima, N., et al., *Hybrid imaging in oncology.* Asian Pacific Journal of Cancer Prevention, 2015. **16**(14): p. 5599-605.
41. Beyer, T., et al., *The future of hybrid imaging-part 1: Hybrid imaging technologies and SPECT/CT.* Insights Into Imaging, 2011. **2**(2): p. 161-9.
42. Sandulescu, D.L., et al., *Hybrid ultrasound imaging techniques (fusion imaging).* World Journal of Gastroenterology, 2011. **17**(1): p. 49-52.
43. Czernin, J., M. Allen-Auerbach, and H.R. Schelbert, *Improvements in cancer staging with PET/CT: Literature-based evidence as of September 2006.* Journal of Nuclear Medicine, 2007. **48 Suppl 1**: p. 78-88.
44. Hundshammer, C., et al., *Simultaneous characterization of tumor cellularity and the Warburg effect with PET, MRI and hyperpolarized ^{13}C-MRSI.* Theranostics, 2018. **8**(17): p. 4765-80.
45. Almuhaideb, A., N. Papathanasiou, and J. Bomanji, *^{18}F-FDG PET/CT imaging in oncology.* Annals of Saudi Medicine, 2011. **31**(1): p. 3-13.
46. Sauter, A.W., et al., *Combined PET/MRI: One step further in multimodality imaging.* Trends in Molecular Medicine, 2010. **16**(11): p. 508-15.
47. Gaertner, F.C., S. Fürst, and M. Schwaiger, *PET/MR: A paradigm shift.* Cancer Imaging, 2013. **13**: p. 36-52.
48. Kjaer, A. and D.A. Torigian, *Clinical PET/MR imaging in oncology: Future perspectives.* PET Clinics, 2016. **11**(4): p. 489-93.
49. Cabello, J. and S.I. Ziegler, *Advances in PET/MR instrumentation and image reconstruction.* British Journal of Radiology, 2018. **91**(1081): p. 20160363.
50. Yiping, S., et al., *Simultaneous PET and MR imaging.* Physics in Medicine and Biology, 1997. **42**(10): p. 1965.
51. Iagaru, A., et al., *Simultaneous whole-body time-of-flight ^{18}F-FDG PET/MRI: A pilot study comparing SUV_{max} with PET/CT and assessment of mr image quality.* Clinical Nuclear Medicine, 2015. **40**(1): p. 1-8.
52. Fraum, T.J., K.J. Fowler, and J. McConathy, *PET/MRI: Emerging clinical applications in oncology.* Academic Radiology, 2016. **23**(2): p. 220-36.
53. Pace, L., et al., *Comparison of whole-body PET/CT and PET/MRI in breast cancer patients: lesion detection and quantitation of ^{18}F-deoxyglucose uptake in lesions and in normal organ tissues.* European Journal of Radiology, 2014. **83**(2): p. 289-96.
54. Wu, H.B., et al., *^{18}F-FDG in conjunction with ^{11}C-choline PET/CT in the diagnosis of hepatocellular carcinoma.* Clinical Nuclear Medicine, 2011. **36**(12): p. 1092-7.

55. Gutte, H., et al., *Simultaneous hyperpolarized ^{13}C-pyruvate MRI and ^{18}F-FDG-PET in cancer (hyperPET): Feasibility of a new imaging concept using a clinical PET/MRI scanner.* American Journal of Nuclear Medicine and Molecular Imaging, 2015. **5**(1): p. 38-45.
56. Gutte, H., et al., *Simultaneous hyperpolarized ^{13}C-pyruvate MRI and ^{18}F-FDG PET (HyperPET) in 10 dogs with cancer.* Journal of Nuclear Medicine, 2015. **56**(11): p. 1786-92.
57. Warburg, O., F. Wind, and E. Negelein, *The metabolism of tumors in the body.* Journal of General Physiology, 1927. **8**(6): p. 519-30.
58. Warburg, O., *On the origin of cancer cells.* Science, 1956. **123**(3191): p. 309-14.
59. Potter, M., E. Newport, and K.J. Morten, *The Warburg effect: 80 years on.* Biochemical Society Transactions, 2016. **44**(5): p. 1499-505.
60. Xu, X.D., et al., *Warburg effect or reverse Warburg effect? A review of cancer metabolism.* Oncology Research and Treatment, 2015. **38**(3): p. 117-22.
61. Doherty, J.R. and J.L. Cleveland, *Targeting lactate metabolism for cancer therapeutics.* Journal of Clinical Investigation, 2013. **123**(9): p. 3685-92.
62. Liberti, M.V. and J.W. Locasale, *The Warburg effect: How does it benefit cancer cells?* Trends in Biochemical Sciences, 2016. **41**(3): p. 211-8.
63. Vander Heiden, M.G., L.C. Cantley, and C.B. Thompson, *Understanding the Warburg effect: the metabolic requirements of cell proliferation.* Science, 2009. **324**(5930): p. 1029-33.
64. Hsu, P.P. and D.M. Sabatini, *Cancer cell metabolism: Warburg and beyond.* Cell, 2008. **134**(5): p. 703-7.
65. Pavlova, Natalya N. and Craig B. Thompson, *The emerging hallmarks of cancer metabolism.* Cell Metabolism, 2016. **23**(1): p. 27-47.
66. Chiaradonna, F., et al., *Ras-dependent carbon metabolism and transformation in mouse fibroblasts.* Oncogene, 2006. **25**(39): p. 5391-404.
67. Cairns, R.A., I.S. Harris, and T.W. Mak, *Regulation of cancer cell metabolism.* Nature Reviews. Cancer, 2011. **11**(2): p. 85-95.
68. Romero-Garcia, S., et al., *Lactate contribution to the tumor microenvironment: Mechanisms, effects on immune cells and therapeutic relevance.* Frontiers in Immunology, 2016. **7**: p. 52.
69. Huber, V., et al., *Cancer acidity: An ultimate frontier of tumor immune escape and a novel target of immunomodulation.* Seminars in Cancer Biology, 2017. **43**: p. 74-89.
70. Kato, Y., et al., *Acidic extracellular microenvironment and cancer.* Cancer Cell International, 2013. **13**(1): p. 89.
71. Som, P., et al., *A fluorinated glucose analog, 2-fluoro-2-deoxy-D-glucose (F-18): Nontoxic tracer for rapid tumor detection.* Journal of Nuclear Medicine, 1980. **21**(7): p. 670-5.
72. Phelps, M.E., et al., *Tomographic measurement of local cerebral glucose metabolic rate in humans with (F-18)2-fluoro-2-deoxy-D-glucose: Validation of method.* Annals of Neurology, 1979. **6**(5): p. 371-88.
73. Larson, S.M., et al., *Positron imaging feasibility studies. II: Characteristics of 2-deoxyglucose uptake in rodent and canine neoplasms: Concise communication.* Journal of Nuclear Medicine, 1981. **22**(10): p. 875-9.
74. Jensen, M.M., et al., *^{18}F-FDG and ^{18}F-FLT positron emission tomography imaging following treatment with belinostat in human ovary cancer xenografts in mice.* BMC Cancer, 2013. **13**: p. 168.
75. Johnbeck, C.B., et al., *^{18}F-FDG and ^{18}F-FLT-PET imaging for monitoring everolimus effect on tumor-growth in neuroendocrine tumors: Studies in human tumor xenografts in mice.* Public Library of Science One, 2014. **9**(3): p. e91387.
76. Golman, K., et al., *Metabolic imaging by hyperpolarized ^{13}C-magnetic resonance imaging for in vivo tumor diagnosis.* Cancer Research, 2006. **66**(22): p. 10855-60.
77. Day, S.E., et al., *Detecting tumor response to treatment using hyperpolarized ^{13}C-magnetic resonance imaging and spectroscopy.* Nature Medicine, 2007. **13**(11): p. 1382-7.
78. Düwel, S., et al., *Imaging of pH in vivo using hyperpolarized ^{13}C-labelled zymonic acid.* Nature Communications, 2017. **8**: p. 15126.
79. Ziegler, S.I., *Positron emission tomography: Principles, technology, and recent developments.* Nuclear Physics A, 2005. **752**: p. 679-87.
80. Miele, E., et al., *Positron emission tomography (PET) radiotracers in oncology-utility of ^{18}F-fluoro-deoxy-glucose (FDG)-PET in the management of patients with non-small-cell lung cancer (NSCLC).* Journal of Experimental and Clinical Cancer Research, 2008. **27**(1): p. 52.
81. Wahl, R.L., *Principles and practice of PET and PET/CT 2nd edition*. 2008, Philadelphia: Lippincott Williams and Wilkins.
82. Grassi, I., et al., *The clinical use of PET with ^{11}C-acetate.* American Journal of Nuclear Medicine and Molecular Imaging, 2012. **2**(1): p. 33-47.

83. Yi, C., et al., *The combination of ^{13}N-ammonia and ^{18}F-FDG whole-body PET/CT on the same day for diagnosis of advanced prostate cancer.* Nuclear Medicine Communications, 2016. **37**(3): p. 239-46.
84. Fletcher, J.W., et al., *Whole-body PET/CT evaluation of tumor perfusion using generator-based ^{62}Cu-ethylglyoxal bis(thiosemicarbazonato)copper(II): Validation by direct comparison to ^{15}O-water in metastatic renal cell carcinoma.* Journal of Nuclear Medicine, 2015. **56**(1): p. 56-62.
85. Zyromska, A., et al., *^{15}O-H_2O PET/CT as a tool for the quantitative assessement of early post-radiotherapy changes of heart perfusion in breast carcinoma patients.* British Journal of Radiology. **91**(1088): p. 20170653.
86. Maurer, T., et al., *Current use of PSMA–PET in prostate cancer management.* Nature Reviews Urology, 2016. **13**: p. 226.
87. Karlberg, A.M., et al., *Quantitative comparison of PET performance-Siemens Biograph mCT and mMR.* European Journal of Nuclear Medicine and Molecular Imaging Physics, 2016. **3**: p. 5.
88. Pichler, B.J., M.S. Judenhofer, and H.F. Wehrl, *PET/MRI hybrid imaging: Devices and initial results.* European Radiology, 2008. **18**(6): p. 1077-86.
89. Levin, C.S., M. Dahlbom, and E.J. Hoffman, *A Monte Carlo correction for the effect of Compton scattering in 3D PET brain imaging.* IEEE Transactions on Nuclear Science, 1995. **42**(4): p. 1181-5.
90. Wagenknecht, G., et al., *MRI for attenuation correction in PET: Methods and challenges.* Magnetic Resonance Materials in Physics, Biology and Medicine, 2013. **26**(1): p. 99-113.
91. Min Sun, L., et al., *Prototype preclinical PET scanner with depth-of-interaction measurements using single-layer crystal array and single-ended readout.* Physics in Medicine and Biology, 2017. **62**(10): p. 3983.
92. Omidvari, N., et al., *PET performance evaluation of MADPET4: A small animal PET insert for a 7T MRI scanner.* Physics in Medicine and Biology, 2017. **62**(22): p. 8671-92.
93. Constantinescu, C.C. and J. Mukherjee, *Performance evaluation of an Inveon PET preclinical scanner.* Physics in Medicine and Biology, 2009. **54**(9): p. 2885-99.
94. Schug, D., et al., *Initial PET performance evaluation of a preclinical insert for PET/MRI with digital SiPM technology.* Physics in Medicine and Biology, 2016. **61**(7): p. 2851-78.
95. Moses, W.W., *Fundamental limits of spatial resolution in PET.* Nuclear Instruments and Methods in Physics Research Section A. Accelerators, Spectrometers, Detectors and Associated Equipment, 2011. **648** (S 1): p. 236-40.
96. Patlak, C.S., R.G. Blasberg, and J.D. Fenstermacher, *Graphical evaluation of blood-to-brain transfer constants from multiple-time uptake data.* Journal of Cerebral Blood Flow and Metabolism, 1983. **3**(1): p. 1-7.
97. Purcell, E.M., H.C. Torrey, and R.V. Pound, *Resonance absorption by nuclear magnetic moments in a solid.* Physical Review, 1946. **69**(1-2): p. 37-8.
98. Bloch, F., *Nuclear induction.* Physical Review, 1946. **70**(7-8): p. 460-74.
99. Lauterbur, P.C., *Image formation by induced local interactions: Examples employing nuclear magnetic resonance.* Nature, 1973. **242**: p. 190.
100. Mansfield, P., *Multi-planar image formation using NMR spin echoes.* Journal of Physics C: Solid State Physics, 1977. **10**(3): p. 55-8.
101. Hennig, J., A. Nauerth, and H. Friedburg, *RARE imaging: A fast imaging method for clinical MR.* Magnetic Resonance in Medicine, 1986. **3**(6): p. 823-33.
102. Haase, A., et al., *FLASH imaging. Rapid NMR imaging using low flip-angle pulses.* Journal of Magnetic Resonance, 1986. **67**(2): p. 258-66.
103. De Graaf, R.A., *In vivo NMR spectroscopy: Principles and techniques*. 2007, New York: John Wiley & Sons.
104. Keeler, J., *Understanding NMR spectroscopy*. 2013, New York: John Wiley & Sons.
105. Levitt, M.H., *Spin dynamics: Basics of nuclear magnetic resonance*. 2015, Chichester: Wiley.
106. Koechli, V.D., B. Marincek, and D. Weishaupt, *Wie funktioniert MRI?* 2006, New York: Springer Medizin Verlag Heidelberg.
107. Herneth, A.M., S. Guccione, and M. Bednarski, *Apparent diffusion coefficient: a quantitative parameter for in vivo tumor characterization.* European Journal of Radiology, 2003. **45**(3): p. 208-13.
108. Koh, D.M. and D.J. Collins, *Diffusion-weighted MRI in the body: Applications and challenges in oncology.* American Journal of Roentgenology, 2007. **188**(6): p. 1622-35.
109. Padhani, A.R., et al., *Diffusion-weighted magnetic resonance imaging as a cancer biomarker: Consensus and recommendations.* Neoplasia, 2009. **11**(2): p. 102-25.

110. Stejskal, E.O. and J.E. Tanner, *Spin diffusion measurements: Spin echoes in the presence of a time-dependent field gradient.* The Journal of Chemical Physics, 1965. **42**(1): p. 288-92.
111. White, N.S., et al., *Diffusion-weighted imaging in cancer: Physical foundations and applications of Restriction Spectrum Imaging.* Cancer Research, 2014. **74**(17): p. 4638-52.
112. Hirsch, M.L., et al., *Brute-force hyperpolarization for NMR and MRI.* Journal of the American Chemical Society, 2015. **137**(26): p. 8428-34.
113. Hundshammer, C., S. Düwel, and F. Schilling, *Imaging of extracellular pH using hyperpolarized molecules.* Israel Journal of Chemistry, 2017. **57**(9): p. 788-99.
114. Bowers, C.R. and D.P. Weitekamp, *Transformation of symmetrization order to nuclear-spin magnetization by chemical reaction and nuclear magnetic resonance.* Physical Review Letters, 1986. **57**(21): p. 2645-8.
115. Kirss, R.U., T.C. Eisenschmid, and R. Eisenberg, *Parahydrogen induced polarization in hydrogenation reactions catalyzed by ruthenium phosphine complexes.* Journal of the American Chemical Society, 1988. **110**(25): p. 8564-6.
116. Eisenschmid, T.C., et al., *Parahydrogen induced polarization in hydrogenation reactions.* Journal of the American Chemical Society, 1987. **109**(26): p. 8089-91.
117. Truong, M.L., et al., *^{15}N-hyperpolarization by reversible exchange using SABRE-SHEATH.* The Journal of Physical Chemistry C, 2015. **119**(16): p. 8786-97.
118. Theis, T., et al., *Microtesla SABRE enables 10% nitrogen-15 nuclear spin polarization.* Journal of the American Chemical Society, 2015. **137**(4): p. 1404-7.
119. Shchepin, R.V., et al., *^{15}N-hyperpolarization of $^{15}N_2$-imidazole for magnetic resonance pH sensing via SABRE-SHEATH.* ACS Sensors, 2016. **1**(6): p. 640-4.
120. Keshari, K.R. and D.M. Wilson, *Chemistry and biochemistry of ^{13}C-hyperpolarized magnetic resonance using dynamic nuclear polarization.* Chemical Society Reviews, 2014. **43**(5): p. 1627-59.
121. Ardenkjaer-Larsen, J.H., et al., *Increase in signal-to-noise ratio of > 10,000 times in liquid-state NMR.* Proceedings of the National Academy of Science USA, 2003. **100**(18): p. 10158-63.
122. Hundshammer, C., et al., *Deuteration of hyperpolarized ^{13}C-labeled zymonic acid enables sensitivity-enhanced dynamic MRI of pH.* ChemPhysChem, 2017. **18**(18): p. 2422-5.
123. Hundshammer, C., et al., *Hyperpolarized amino acid derivatives as multivalent magnetic resonance pH sensor molecules.* Sensors, 2018. **18**(2): p. 600.
124. Wiesinger, F., et al., *IDEAL spiral CSI for dynamic metabolic MR imaging of hyperpolarized [1-^{13}C]pyruvate.* Magnetic Resonance in Medicine, 2012. **68**(1): p. 8-16.
125. Reed, G.D., et al., *A method for simultaneous echo planar imaging of hyperpolarized ^{13}C-pyruvate and ^{13}C-lactate.* Journal of Magnetic Resonance, 2012. **217**: p. 41-7.
126. Durst, M., et al., *Comparison of acquisition schemes for hyperpolarised ^{13}C-imaging.* NMR in Biomedicine, 2015. **28**(6): p. 715-25.
127. Perman, W.H., et al., *Fast volumetric spatial-spectral MR imaging of hyperpolarized ^{13}C-labeled compounds using multiple echo 3D bSSFP.* Magnetic Resonance Imaging, 2010. **28**(4): p. 459-65.
128. Nelson, S.J., et al., *Metabolic imaging of patients with prostate cancer using hyperpolarized [1-^{13}C]pyruvate.* Science Translational Medicine, 2013. **5**(198): p. 198ra108.
129. Hill, D.K., et al., *Model free approach to kinetic analysis of real-time hyperpolarized ^{13}C-magnetic resonance spectroscopy data.* Public Library of Science One, 2013. **8**(9): p. e71996.
130. Gatenby, R.A. and R.J. Gillies, *Why do cancers have high aerobic glycolysis?* Nature Reviews. Cancer, 2004. **4**(11): p. 891-9.
131. Kurhanewicz, J., et al., *Analysis of cancer metabolism by imaging hyperpolarized nuclei: Prospects for translation to clinical research.* Neoplasia, 2011. **13**(2): p. 81-97.
132. Blodgett, T.M., C.C. Meltzer, and D.W. Townsend, *PET/CT: Form and function.* Radiology, 2007. **242**(2): p. 360-85.
133. Haberkorn, U., et al., *Molecular imaging of tumor metabolism and apoptosis.* Oncogene, 2011. **30**: p. 4141.
134. Glunde, K., Z.M. Bhujwalla, and S.M. Ronen, *Choline metabolism in malignant transformation.* Nature Reviews. Cancer, 2011. **11**(12): p. 835-48.
135. Serrao, E.M., et al., *Analysis of ^{13}C- and ^{14}C-labeling in pyruvate and lactate in tumor and blood of lymphoma-bearing mice injected with ^{13}C- and ^{14}C-labeled pyruvate.* NMR in Biomedicine, 2018. **31**(5): p. e3901.
136. Kettunen, M.I., et al., *Magnetization transfer measurements of exchange between hyperpolarized [1-^{13}C]pyruvate and [1-^{13}C]lactate in a murine lymphoma.* Magnetic Resonance in Medicine, 2010. **63**(4): p. 872-80.

137. Hansen, A.E., et al., *Simultaneous PET/MRI with ^{13}C-magnetic resonance spectroscopic imaging (hyperPET): Phantom-based evaluation of PET quantification.* European Journal of Nuclear Medicine and Molecular Imaging Physics, 2016. **3**(1): p. 7.
138. Hansen, A.E., et al., *Combined hyperpolarized ^{13}C-pyruvate MRS and ^{18}F-FDG PET (hyperPET) estimates of glycolysis in canine cancer patients.* European Journal of Radiology, 2018. **103**: p. 6-12.
139. Witney, T.H., et al., *A comparison between radiolabeled fluorodeoxyglucose uptake and hyperpolarized ^{13}C-labeled pyruvate utilization as methods for detecting tumor response to treatment.* Neoplasia, 2009. **11**(6): p. 574-82.
140. Menzel, M.I., et al., *Multimodal assessment of in vivo metabolism with hyperpolarized [1-^{13}C]MR spectroscopy and ^{18}F-FDG PET imaging in hepatocellular carcinoma tumor-bearing rats.* Journal of Nuclear Medicine, 2013. **54**(7): p. 1113-9.
141. Ravoori, M.K., et al., *In vivo assessment of ovarian tumor response to tyrosine kinaseinhibitor pazopanib by using hyperpolarized ^{13}C-pyruvate MR spectroscopy and ^{18}F-FDG PET/CT imaging in a mouse model.* Radiology, 2017. **285**(3): p. 830-8.
142. Greve, D.N., et al., *Different partial volume correction methods lead to different conclusions: An ^{18}F-FDG PET study of aging.* NeuroImage, 2016. **132**: p. 334-43.
143. Hamacher, K., H.H. Coenen, and G. Stocklin, *Efficient stereospecific synthesis of no-carrier-added 2-[^{18}F]-fluoro-2-deoxy-D-glucose using aminopolyether supported nucleophilic substitution.* Journal of Nuclear Medicine, 1986. **27**(2): p. 235-8.
144. Chen, H.H., et al., *Prognostic value of whole-body total lesion glycolysis at pretreatment FDG PET/CT in non-small cell lung cancer.* Radiology, 2012. **264**(2): p. 559-66.
145. Kim, T.M., et al., *Total lesion glycolysis in positron emission tomography is a better predictor of outcome than the International Prognostic Index for patients with diffuse large B cell lymphoma.* Cancer, 2013. **119**(6): p. 1195-202.
146. Doblas, S., et al., *Apparent diffusion coefficient is highly reproducible on preclinical imaging systems: Evidence from a seven-center multivendor study.* Journal of Magnetic Resonance Imaging, 2015. **42**(6): p. 1759-64.
147. Westin, C.F., et al., *Processing and visualization for diffusion tensor MRI.* Medical Image Analysis, 2002. **6**(2): p. 93-108.
148. Cohen, J., *Statistical power analysis for the behavioral sciences*. 1977, New York: Academic Press.
149. Longo, D.L., et al., *In vivo imaging of tumor metabolism and acidosis by combining PET and MRI-CEST pH imaging.* Cancer Research, 2016. **76**(22): p. 6463-70.
150. Thackeray, J.T., J.P. Bankstahl, and F.M. Bengel, *Impact of image-derived input function and fit time intervals on Patlak quantification of myocardial glucose uptake in mice.* Journal of Nuclear Medicine, 2015. **P56**(10): p. 1615-21.
151. Lanz, B., C. Poitry-Yamate, and R. Gruetter, *Image-derived input function from the vena cava for ^{18}F-FDG PET studies in rats and mice.* Journal of Nuclear Medicine, 2014. **55**(8): p. 1380-8.
152. Skoch, A., F. Jiru, and J. Bunke, *Spectroscopic imaging: Basic principles.* European Journal of Radiology, 2008. **67**(2): p. 230-9.
153. Delso, G., et al., *Performance measurements of the Siemens mMR integrated whole-body PET/MR scanner.* Journal of Nuclear Medicine, 2011. **52**(12): p. 1914-22.
154. Wu, C., et al., *PET imaging of inflammation biomarkers.* Theranostics, 2013. **3**(7): p. 448-66.
155. Seitz, B.M., et al., *Serial measurements of splanchnic vein diameters in rats using high-frequency ultrasound.* Frontiers in Pharmacology, 2016. **7**: p. 116.
156. Wang, H. and Y. Cao, *Correction of arterial input function in dynamic contrast-enhanced MRI of the liver.* Journal of Magnetic Resonance Imaging, 2012. **36**(2): p. 411-21.
157. Shimoji, K., et al., *Measurement of cerebral glucose metabolic rates in the anesthetized rat by dynamic scanning with ^{18}F-FDG, the ATLAS small animal PET scanner, and arterial blood sampling.* Journal of Nuclear Medicine, 2004. **45**(4): p. 665-72.
158. Kazan, S.M., et al., *Kinetic modeling of hyperpolarized ^{13}C-pyruvate metabolism in tumors using a measured arterial input function.* Magnetic Resonance in Medicine, 2013. **70**(4): p. 943-53.
159. Hay, N., *Reprogramming glucose metabolism in cancer: Can it be exploited for cancer therapy?* Nature Reviews. Cancer, 2016. **16**(10): p. 635-49.
160. Gu, J., et al., *Quantitative assessment of diffusion-weighted MR imaging in patients with primary rectal cancer: Correlation with FDG-PET/CT.* Molecular Imaging and Biology, 2011. **13**(5): p. 1020-8.
161. Schmidt, H., et al., *Correlation of simultaneously acquired diffusion-weighted imaging and 2-deoxy-[^{18}F] fluoro-2-D-glucose positron emission tomography of pulmonary lesions in a*

dedicated whole-body magnetic resonance/positron emission tomography system. Investigative Radiology, 2013. **48**(5): p. 247-55.
162. Brandmaier, P., et al., *Simultaneous [^{18}F]FDG-PET/MRI: Correlation of apparent diffusion coefficient (ADC) and standardized uptake value (SUV) in primary and recurrent cervical cancer.* Public Library of Science One, 2015. **10**(11): p. e0141684.
163. Andersen, L.W., et al., *Etiology and therapeutic approach to elevated lactate.* Mayo Clinic Proceedings, 2013. **88**(10): p. 1127-40.
164. Holz, M., S.R. Heil, and A. Sacco, *Temperature-dependent self-diffusion coefficients of water and six selected molecular liquids for calibration in accurate ^{1}H-NMR PFG measurements.* Physical Chemistry Chemical Physics, 2000. **2**(20): p. 4740-2.
165. Adrogue, H.J. and N.E. Madias, *Management of life-threatening acid-base disorders. First of two parts.* New England Journal of Medicine, 1998. **338**(1): p. 26-34.
166. Gallagher, F.A., et al., *Magnetic resonance imaging of pH in vivo using hyperpolarized ^{13}C-labelled bicarbonate.* Nature, 2008. **453**(7197): p. 940-3.
167. Hashim, A.I., et al., *Imaging pH and metastasis.* NMR in Biomedicine, 2011. **24**(6): p. 582-91.
168. Parks, S.K., J. Chiche, and J. Pouyssegur, *Disrupting proton dynamics and energy metabolism for cancer therapy.* Nature Reviews. Cancer, 2013. **13**(9): p. 611-23.
169. Raghunand, N., et al., *Enhancement of chemotherapy by manipulation of tumour pH.* British Journal of Cancer, 1999. **80**(7): p. 1005-11.
170. Raghunand, N., et al., *Acute metabolic alkalosis enhances response of C3H mouse mammary tumors to the weak base mitoxantrone.* Neoplasia, 2001. **3**(3): p. 227-35.
171. Collins, F.S. and H. Varmus, *A new initiative on precision medicine.* New England Journal of Medicine, 2015. **372**(9): p. 793-5.
172. Friedman, A.A., et al., *Precision medicine for cancer with next-generation functional diagnostics.* Nature Reviews. Cancer, 2015. **15**(12): p. 747-56.
173. Kearfott, K.J., L. Junck, and D.A. Rottenberg, *^{11}C-dimethyloxazolidinedione (DMO): biodistribution, radiation absorbed dose, and potential for PET measurement of regional brain pH: Concise communication.* Journal of Nuclear Medicine, 1983. **24**(9): p. 805-11.
174. Brooks, D.J., et al., *Studies on regional cerebral pH in patients with cerebral tumours using continuous inhalation of $^{11}CO_2$ and positron emission tomography.* Journal of Cerebral Blood Flow and Metabolism, 1986. **6**(5): p. 529-35.
175. Flavell, R.R., et al., *Caged ^{18}F-FDG glycosylamines for imaging acidic tumor microenvironments using positron emission tomography.* Bioconjugate Chemistry, 2016. **27**(1): p. 170-8.
176. Demoin, D.W., et al., *PET imaging of extracellular pH in tumors with ^{64}Cu- and ^{18}F-labeled pHLIP peptides: A structure-activity optimization study.* Bioconjugate Chemistry, 2016. **27**(9): p. 2014-23.
177. Vavere, A.L., et al., *A novel technology for the imaging of acidic prostate tumors by positron emission tomography.* Cancer Research, 2009. **69**(10): p. 4510-6.
178. Macholl, S., et al., *In vivo pH imaging with ^{99m}Tc-pHLIP.* Molecular Imaging and Biology, 2012. **14**(6): p. 725-34.
179. Zhang, X., Y. Lin, and R.J. Gillies, *Tumor pH and its measurement.* Journal of Nuclear Medicine, 2010. **51**(8): p. 1167-70.
180. Anderson, M., et al., *Probe for the measurement of cell surface pH in vivo and ex vivo.* Proceedings of the National Academy of Sciences USA, 2016. **113**(29): p. 8177-81.
181. Tapmeier, T.T., et al., *The pH low insertion peptide pHLIP Variant 3 as a novel marker of acidic malignant lesions.* Proceedings of the National Academy of Sciences USA, 2015. **112**(31): p. 9710-5.
182. Deliolanis, N.C., et al., *Performance of the red-shifted fluorescent proteins in deep-tissue molecular imaging applications.* Journal of Biomedical Optics, 2008. **13**(4): p. 044008.
183. Chen, Q., et al., *A self-assembled albumin-based nanoprobe for in vivo ratiometric photoacoustic pH imaging.* Advanced Materials, 2015. **27**(43): p. 6820-7.
184. Lowe, M.P., et al., *pH-dependent modulation of relaxivity and luminescence in macrocyclic gadolinium and europium complexes based on reversible intramolecular sulfonamide ligation.* Journal of the American Chemical Society, 2001. **123**(31): p. 7601-9.
185. Zhang, S., K. Wu, and A.D. Sherry, *A novel pH-sensitive MRI contrast agent.* Angewandte Chemie, 1999. **38**(21): p. 3192-4.
186. Mikawa, M., et al., *Gd^{3+}-loaded polyion complex for pH depiction with magnetic resonance imaging.* Journal of Biomedical Materials Research, 2000. **49**(3): p. 390-5.
187. Raghunand, N., et al., *Renal and systemic pH imaging by contrast-enhanced MRI.* Magnetic Resonance in Medicine, 2003. **49**(2): p. 249-57.

188. Frullano, L., et al., *Bimodal MR-PET agent for quantitative pH imaging.* Angewandte Chemie, 2010. **49**(13): p. 2382-4.
189. Chen, L.Q. and M.D. Pagel, *Evaluating pH in the extracellular tumor microenvironment using CEST MRI and other imaging methods.* Advances in Radiology, 2015. **2015**: p. 25.
190. Moritz, Z. and B. Peter, *Chemical exchange saturation transfer (CEST) and MR Z-spectroscopy in vivo: A review of theoretical approaches and methods.* Physics in Medicine and Biology, 2013. **58**(22): p. R221.
191. Zhang, S., et al., *PARACEST agents: Modulating MRI contrast via water proton exchange.* Accounts of Chemical Research, 2003. **36**(10): p. 783-90.
192. Aime, S., et al., *Paramagnetic lanthanide(III) complexes as pH-sensitive chemical exchange saturation transfer (CEST) contrast agents for MRI applications.* Magnetic Resonance in Medicine, 2002. **47**(4): p. 639-48.
193. Sheth, V.R., et al., *Improved pH measurements with a single PARACEST MRI contrast agent.* Contrast Media and Molecular Imaging, 2012. **7**(1): p. 26-34.
194. Hwang, T.L., P.C. van Zijl, and S. Mori, *Accurate quantitation of water-amide proton exchange rates using the phase-modulated CLEAN chemical EXchange (CLEANEX-PM) approach with a Fast-HSQC (FHSQC) detection scheme.* Journal of Biomolecular NMR, 1998. **11**(2): p. 221-6.
195. Snoussi, K., et al., *Sensitive CEST agents based on nucleic acid imino proton exchange: detection of poly(rU) and of a dendrimer-poly(rU) model for nucleic acid delivery and pharmacology.* Magnetic Resonance in Medicine, 2003. **49**(6): p. 998-1005.
196. Longo, D.L., et al., *A general MRI-CEST ratiometric approach for pH imaging: Demonstration of in vivo pH mapping with iobitridol.* Journal of the American Chemical Society, 2014. **136**(41): p. 14333-6.
197. Aime, S., et al., *Iopamidol: Exploring the potential use of a well-established x-ray contrast agent for MRI.* Magnetic Resonance in Medicine, 2005. **53**(4): p. 830-4.
198. Longo, D.L., et al., *Iopamidol as a responsive MRI-chemical exchange saturation transfer contrast agent for pH mapping of kidneys: In vivo studies in mice at 7T.* Magnetic Resonance in Medicine, 2011. **65**(1): p. 202-11.
199. Chen, L.Q., et al., *Evaluations of extracellular pH within in vivo tumors using acidoCEST MRI.* Magnetic Resonance in Medicine, 2014. **72**(5): p. 1408-17.
200. Moon, B.F., et al., *A comparison of iopromide and iopamidol, two acidoCEST MRI contrast media that measure tumor extracellular pH.* Contrast Media and Molecular Imaging, 2015. **10**(6): p. 446-55.
201. van Sluis, R., et al., *In vivo imaging of extracellular pH using ^{1}H-MRSI.* Magnetic Resonance in Medicine, 1999. **41**(4): p. 743-50.
202. Provent, P., et al., *Serial in vivo spectroscopic nuclear magnetic resonance imaging of lactate and extracellular pH in rat gliomas shows redistribution of protons away from sites of glycolysis.* Cancer Research, 2007. **67**(16): p. 7638-45.
203. Hunjan, S., et al., *Simultaneous intracellular and extracellular pH measurement in the heart by ^{19}F-NMR of 6-fluoropyridoxol.* Magnetic Resonance in Medicine, 1998. **39**(4): p. 551-6.
204. Gillies, R.J., Z. Liu, and Z. Bhujwalla, *^{31}P-MRS measurements of extracellular pH of tumors using 3-aminopropylphosphonate.* The American Journal of Physiology, 1994. **267**(1): p. C195-203.
205. Ojugo, A.S., et al., *Measurement of the extracellular pH of solid tumours in mice by magnetic resonance spectroscopy: A comparison of exogenous ^{19}F- and ^{31}P-probes.* NMR in Biomedicine, 1999. **12**(8): p. 495-504.
206. Wu, Y., et al., *Optical imaging of tumor microenvironment.* American Journal of Nuclear Medicine and Molecular Imaging, 2013. **3**(1): p. 1-15.
207. Chan, M. and A. Almutairi, *Nanogels as imaging agents for modalities spanning the electromagnetic spectrum.* Materials Horizons, 2016. **3**(1): p. 21-40.
208. Oishi, M., S. Sumitani, and Y. Nagasaki, *On-off regulation of ^{19}F-magnetic resonance signals based on pH-sensitive PEGylated nanogels for potential tumor-specific smart ^{19}F-MRI probes.* Bioconjugate Chemistry, 2007. **18**(5): p. 1379-82.
209. Wang, C.T., et al., *The effects of green tea (-)-epigallocatechin-3-gallate on reactive oxygen species in 3T3-L1 preadipocytes and adipocytes depend on the glutathione and 67 kDa laminin receptor pathways.* Molecular Nutrition and Food Research, 2009. **53**(3): p. 349-60.
210. Zabow, G., S.J. Dodd, and A.P. Koretsky, *Shape-changing magnetic assemblies as high-sensitivity NMR-readable nanoprobes.* Nature, 2015. **520**(7545): p. 73-7.

211. Ling, D., et al., *Multifunctional tumor pH-sensitive self-assembled nanoparticles for bimodal imaging and treatment of resistant heterogeneous tumors.* Journal of the American Chemical Society, 2014. **136**(15): p. 5647-55.
212. Gallagher, F.A., M.I. Kettunen, and K.M. Brindle, *Imaging pH with hyperpolarized ^{13}C.* NMR in Biomedicine, 2011. **24**(8): p. 1006-15.
213. Lee, Y., et al., *Chemical reaction-induced multi-molecular polarization (CRIMP).* Chemical Communications 2014. **50**(86): p. 13030-3.
214. Ghosh, R.K., et al., *Efficient production of hyperpolarized bicarbonate by chemical reaction on a DNP precursor to measure pH.* Magnetic resonance in Medicine, 2015. **74**(5): p. 1406-13.
215. Korenchan, D.E., et al., *Dynamic nuclear polarization of biocompatible ^{13}C-enriched carbonates for in vivo pH imaging.* Chemical Communications, 2016. **52**(14): p. 3030-3.
216. Korenchan, D.E., et al., *Dicarboxylic acids as pH sensors for hyperpolarized ^{13}C-magnetic resonance spectroscopic imaging.* Analyst, 2017. **142**(9): p. 1429-33.
217. Flavell, R.R., et al., *Application of Good's buffers to pH imaging using hyperpolarized ^{13}C-MRI.* Chemical Communications, 2015. **51**(74): p. 14119-22.
218. Jiang, W., et al., *Hyperpolarized ^{15}N-pyridine derivatives as pH-sensitive MRI agents.* Scientific Reports, 2015. **5**: p. 9104.
219. Jindal, A.K., et al., *Hyperpolarized ^{89}Y-complexes as pH sensitive NMR probes.* Journal of the American Chemical Society, 2010. **132**(6): p. 1784-5.
220. Riggle, B.A., Y. Wang, and I.J. Dmochowski, *A "smart" ^{128}Xe-NMR biosensor for pH-dependent cell labeling.* Journal of the American Chemical Society, 2015. **137**(16): p. 5542-8.
221. Appelt, S., et al., *Theory of spin-exchange optical pumping of ^{3}He and ^{129}Xe.* Physical Review A, 1998. **58**(2): p. 1412-39.
222. Berthault, P., et al., *Effect of pH and counterions on the encapsulation properties of xenon in water-soluble cryptophanes.* Chemistry-A European Journal, 2010. **16**(43): p. 12941-6.
223. Adams, R.W., et al., *Reversible interactions with para-hydrogen enhance NMR sensitivity by polarization transfer.* Science, 2009. **323**(5922): p. 1708-11.
224. Bowers, C.R. and D.P. Weitekamp, *Parahydrogen and synthesis allow dramatically enhanced nuclear alignment.* Journal of the American Chemical Society, 1987. **109**(18): p. 5541-2.
225. Reineri, F., T. Boi, and S. Aime, *Parahydrogen induced polarization of ^{13}C-carboxylate resonance in acetate and pyruvate.* Nature Communications, 2015. **6**: p. 5858.
226. Wolber, J., et al., *Generating highly polarized nuclear spins in solution using dynamic nuclear polarization.* Nuclear Instruments and Methods in Physics Research Section A. Accelerators, Spectrometers, Detectors and Associated Equipment, 2004. **526**(1): p. 173-81.
227. Johannesson, H., S. Macholl, and J.H. Ardenkjaer-Larsen, *Dynamic Nuclear Polarization of [1-^{13}C]pyruvic acid at 4.6 tesla.* Journal of Magnetic Resonance, 2009. **197**(2): p. 167-75.
228. Meyer, W., et al., *Dynamic polarization of ^{13}C-nuclei in solid ^{13}C-labeled pyruvic acid.* Nuclear Instruments and Methods in Physics Research Section A. Accelerators, Spectrometers, Detectors and Associated Equipment, 2011. **631**(1): p. 1-5.
229. Jannin, S., et al., *A 140 GHz prepolarizer for dissolution dynamic nuclear polarization.* The Journal of Chemical Physics, 2008. **128**(24): p. 241102.
230. Jannin, S., et al., *High field dynamic nuclear polarization at 6.7T: Carbon-13 polarization above 70% within 20min.* Chemical Physics Letters, 2012. **549**: p. 99-102.
231. Munoz-Gomez, J.L., et al., *A benzyl alcohol derivative of the BDPA radical for fast dissolution dynamic nuclear polarization NMR spectroscopy.* Organic an Biomolecular Chemistry, 2015. **13**(9): p. 2689-93.
232. Gajan, D., et al., *Hybrid polarizing solids for pure hyperpolarized liquids through dissolution dynamic nuclear polarization.* Proceedings of the National Academy of Sciences, 2014. **111**(41): p. 14693-7.
233. McCarney, E.R. and S. Han, *Spin-labeled gel for the production of radical-free dynamic nuclear polarization enhanced molecules for NMR spectroscopy and imaging.* Journal of Magnetic Resonance, 2008. **190**(2): p. 307-15.
234. Harris, T., C. Bretschneider, and L. Frydman, *Dissolution DNP NMR with solvent mixtures: Substrate concentration and radical extraction.* Journal of Magnetic Resonance, 2011. **211**(1): p. 96-100.
235. Eichhorn, T.R., et al., *Hyperpolarization without persistent radicals for in vivo real-time metabolic imaging.* Proceedings of the National Academy of Sciences, 2013. **110**(45): p. 18064-9.
236. Liepinsh, E. and G. Otting, *Proton exchange rates from amino acid side chains-implications for image contrast.* Magnetic Resonance in Medicine, 1996. **35**(1): p. 30-42.

237. Vuichoud, B., et al., *Measuring absolute spin polarization in dissolution-DNP by Spin PolarimetrY Magnetic Resonance (SPY-MR).* Journal of Magnetic Resonance, 2015. **260**: p. 127-35.
238. Hersman, F.W., et al., *Large production system for hyperpolarized ^{129}Xe for human lung imaging studies.* Academic Radiology, 2008. **15**(6): p. 683-92.
239. Allouche-Arnon, H., et al., *A hyperpolarized choline molecular probe for monitoring acetylcholine synthesis.* Contrast Media & Molecular Imaging, 2011. **6**(3): p. 139-47.
240. Meier, S., et al., *Metabolic pathway visualization in living yeast by DNP-NMR.* Molecular BioSystems, 2011. **7**(10): p. 2834-6.
241. Barb, A.W., et al., *Probing alanine transaminase catalysis with hyperpolarized $^{13}CD_3$-pyruvate.* Journal of Magnetic Resonance, 2013. **228**: p. 59-65.
242. Milani, J., et al., *A magnetic tunnel to shelter hyperpolarized fluids.* The Review of Scientific Instruments, 2015. **86**(2): p. 024101.
243. Chiavazza, E., et al., *Earth's magnetic field enabled scalar coupling relaxation of ^{13}C-nuclei bound to fast-relaxing quadrupolar ^{14}N in amide groups.* Journal of Magnetic Resonance, 2013. **227**: p. 35-8.
244. Shang, H., et al., *Handheld electromagnet carrier for transfer of hyperpolarized carbon-13 samples.* Magnetic Resonance in Medicine, 2016. **75**(2): p. 917-22.
245. Chattergoon, N., et al., *Field dependence of T_1 for hyperpolarized [1-^{13}C]pyruvate.* Contrast Media & Molecular Imaging, 2013. **8**(1): p. 57-62.
246. Ji, X., et al., *Transportable hyperpolarized metabolites.* Nature Communications, 2017. **8**: p. 13975.
247. Schmidt, A.B., et al., *Liquid-state carbon-13 hyperpolarization generated in an MRI system for fast imaging.* Nature Communications, 2017. **8**: p. 14535.
248. Scholz, D.J., et al., *Quantified pH imaging with hyperpolarized ^{13}C-bicarbonate.* Magnetic Resonance in Medicine, 2015. **73**(6): p. 2274-82.
249. Carravetta, M. and M.H. Levitt, *Long-lived nuclear spin states in high-field solution NMR.* Journal of the American Chemical Society, 2004. **126**(20): p. 6228-9.
250. Carravetta, M. and M.H. Levitt, *Theory of long-lived nuclear spin states in solution nuclear magnetic resonance. I. Singlet states in low magnetic field.* The Journal of Chemical Physics, 2005. **122**(21): p. 214505.
251. Chaumeil, M.M., C. Najac, and S.M. Ronen, *Studies of metabolism using ^{13}C-MRS of hyperpolarized probes.* Methods in Enzymololgy, 2015. **561**: p. 1-71.
252. Warren, W.S., et al., *Increasing hyperpolarized spin lifetimes through true singlet eigenstates.* Science, 2009. **323**(5922): p. 1711-4.
253. Pileio, G., M. Carravetta, and M.H. Levitt, *Storage of nuclear magnetization as long-lived singlet order in low magnetic field.* Proceedings of the National Academy of Sciences, 2010. **107**(40): p. 17135-9.
254. Vasos, P.R., et al., *Long-lived states to sustain hyperpolarized magnetization.* Proceedings of the National Academy of Sciences, 2009. **106**(44): p. 18469-73.
255. Laustsen, C., et al., *Hyperpolarized singlet NMR on a small animal imaging system.* Magnetic Resonance in Medicine, 2012. **68**(4): p. 1262-5.
256. Marco-Rius, I., et al., *Hyperpolarized singlet lifetimes of pyruvate in human blood and in the mouse.* NMR in Biomedicine, 2013. **26**(12): p. 1696-704.
257. Tayler, M.C., et al., *Direct enhancement of nuclear singlet order by dynamic nuclear polarization.* Journal of the American Chemical Society, 2012. **134**(18): p. 7668-71.
258. Scholz, D.J., et al., *Parameterization of hyperpolarized ^{13}C-bicarbonate dissolution dynamic nuclear polarization.* Magnetic Resonance Materials in Physics, Biology and Medicine, 2015. **28**(6): p. 591-8.
259. Stimmel, J.B., M.E. Stockstill, and F.C. Kull, Jr., *Yttrium-90 chelation properties of tetraazatetraacetic acid macrocycles, diethylenetriaminepentaacetic acid analogues, and a novel terpyridine acyclic chelator.* Bioconjugate Chemistry, 1995. **6**(2): p. 219-25.
260. Seward, G.K., Q. Wei, and I.J. Dmochowski, *Peptide-mediated cellular uptake of cryptophane.* Bioconjugate Chemistry, 2008. **19**(11): p. 2129-35.
261. Khan, N.S., et al., *Cryptophane-folate biosensor for ^{129}Xe-NMR.* Bioconjugate Chemistry, 2015. **26**(1): p. 101-9.
262. Rose, H.M., et al., *Development of an antibody-based, modular biosensor for ^{129}Xe-NMR molecular imaging of cells at nanomolar concentrations.* Proceedings of the National Academy of Sciences, 2014. **111**(32): p. 11697-702.
263. Yannai, S., et al., *Dictionary of food compounds with CD-ROM: Additives, flavors, and ingredients*. 2004, New York, USA: Boca Raton, Fla.: Chapman and Hall/CRC.

264. Brown, T.R., B.M. Kincaid, and K. Ugurbil, *NMR chemical shift imaging in three dimensions.* Proceedings of the National Academy of Sciences USA, 1982. **79**(11): p. 3523-6.
265. Mayer, D., et al., *Application of subsecond spiral chemical shift imaging to real-time multislice metabolic imaging of the rat in vivo after injection of hyperpolarized $^{13}C_1$-pyruvate.* Magnetic Resonance in Medicine, 2009. **62**(3): p. 557-64.
266. Yen, Y.F., et al., *Imaging considerations for in vivo ^{13}C-metabolic mapping using hyperpolarized ^{13}C-pyruvate.* Magnetic Resonance in Medicine, 2009. **62**(1): p. 1-10.
267. Wilson, D.M., et al., *Multi-compound polarization by DNP allows simultaneous assessment of multiple enzymatic activities in vivo.* Journal of Magnetic Resonance, 2010. **205**(1): p. 141-7.
268. Wojtkowiak, J.W., et al., *Drug resistance and cellular adaptation to tumor acidic pH microenvironment.* Molecular Pharmaceutics, 2011. **8**(6): p. 2032-8.
269. Tian, L. and Y.H. Bae, *Cancer nanomedicines targeting tumor extracellular pH.* Colloids and Surfaces B: Biointerfaces, 2012. **99**: p. 116-26.
270. Tung, C.H., et al., *A quick responsive fluorogenic pH probe for ovarian tumor imaging.* Theranostics, 2015. **5**(10): p. 1166-74.
271. Arnold, J.B., L. Junck, and D.A. Rottenberg, *In vivo measurement of regional brain and tumor pH using [^{14}C]dimethyloxazolidinedione and quantitative autoradiography.* Journal of Cerebral Blood Flow and Metabolism, 1985. **5**(3): p. 369-75.
272. Delli Castelli, D., et al., *In vivo maps of extracellular pH in murine melanoma by CEST-MRI.* Magnetic Resonance in Medicine, 2014. **71**(1): p. 326-32.
273. McVicar, N., et al., *Simultaneous in vivo pH and temperature mapping using a PARACEST-MRI contrast agent.* Magnetic Resonance in Medicine, 2013. **70**(4): p. 1016-25.
274. Vuichoud, B., et al., *Hyperpolarization of deuterated metabolites via remote cross-polarization and dissolution dynamic nuclear polarization.* The Journal of Physical Chemistry. B, 2014. **118**(5): p. 1411-5.
275. Blicharski, J.S., *Nuclear magnetic relaxation by anisotropy of chemical-shift.* Zeitschrift für Naturforschung Part A-Astrophysik Physik und Physikalische Chemie, 1972. **A 27**(10): p. 1456-8.
276. Som, A., et al., *Monodispersed calcium carbonate nanoparticles modulate local pH and inhibit tumor growth in vivo.* Nanoscale, 2016. **8**(25): p. 12639-47.
277. Kemp, G., *Lactate accumulation, proton buffering, and pH change in ischemically exercising muscle.* American Journal of Physiology-Regulatory, Integrative and Comparative Physiology, 2005. **289**(3): p. R895-R901.
278. Frisch, M.J., et al., *Gaussian 16 Rev. B.01*. 2016: Wallingford, CT.
279. Hanwell, M.D., et al., *Avogadro: an advanced semantic chemical editor, visualization, and analysis platform.* Journal of Cheminformatics, 2012. **4**(1): p. 17.
280. Halgren, T.A., *Merck molecular force field. I. Basis, form, scope, parameterization, and performance of MMFF94.* Journal of Computational Chemistry, 1996. **17**(5-6): p. 490-519.
281. Halgren, T.A., *Merck molecular force field. II. MMFF94 van der Waals and electrostatic parameters for intermolecular interactions.* Journal of Computational Chemistry, 1996. **17**(5-6): p. 520-52.
282. Halgren, T.A., *Merck molecular force field. III. Molecular geometries and vibrational frequencies for MMFF94.* Journal of Computational Chemistry, 1996. **17**(5-6): p. 553-86.
283. Halgren, T.A. and R.B. Nachbar, *Merck molecular force field. IV. conformational energies and geometries for MMFF94.* Journal of Computational Chemistry, 1996. **17**(5-6): p. 587-615.
284. Halgren, T.A., *Merck molecular force field. V. Extension of MMFF94 using experimental data, additional computational data, and empirical rules.* Journal of Computational Chemistry, 1996. **17**(5-6): p. 616-41.
285. Binkley, J.S., J.A. Pople, and W.J. Hehre, *Self-consistent molecular orbital methods. 21. Small split-valence basis sets for first-row elements.* Journal of the American Chemical Society, 1980. **102**(3): p. 939-47.
286. Becke, A.D., *Density-functional thermochemistry. III. The role of exact exchange.* The Journal of Chemical Physics, 1993. **98**(7): p. 5648-52.
287. Perdew, J.P., *Electronic structure of solids*. Vol. 11. 1991, Berlin: Akademie Verlag.
288. Lee, C., W. Yang, and R.G. Parr, *Development of the Colle-Salvetti correlation-energy formula into a functional of the electron density.* Physical Review B, 1988. **37**(2): p. 785-9.
289. Stephens, P.J., et al., *Ab Initio Calculation of Vibrational Absorption and Circular Dichroism Spectra Using Density Functional Force Fields.* The Journal of Physical Chemistry, 1994. **98**(45): p. 11623-7.
290. Schäfer, A., H. Horn, and R. Ahlrichs, *Fully optimized contracted Gaussian basis sets for atoms Li to Kr.* The Journal of Chemical Physics, 1992. **97**(4): p. 2571-7.

291. Kendall, R.A., T.H.D. Jr., and R.J. Harrison, *Electron affinities of the first-row atoms revisited. Systematic basis sets and wave functions.* The Journal of Chemical Physics, 1992. **96**(9): p. 6796-806.
292. Scalmani, G. and M.J. Frisch, *Continuous surface charge polarizable continuum models of solvation. I. General formalism.* The Journal of Chemical Physics, 2010. **132**(11): p. 114110.
293. Pople, J.A., *The theory of chemical shifts in nuclear magnetic resonance. I. induced current densities.* Proceedings of the Royal Society of London. Series A, Mathematical and Physical Sciences, 1957. **239**(1219): p. 541-9.
294. Pople, J.A., *The theory of chemical shifts in nuclear magnetic resonance. II. Interpretation of proton shifts.* Proceedings of the Royal Society of London. Series A, Mathematical and Physical Sciences, 1957. **239**(1219): p. 550-6.
295. Tannock, I.F. and D. Rotin, *Acid pH in tumors and its potential for therapeutic exploitation.* Cancer Research, 1989. **49**(16): p. 4373-84.
296. Wike-Hooley, J.L., J. Haveman, and H.S. Reinhold, *The relevance of tumour pH to the treatment of malignant disease.* Radiotherapy and Oncology, 1984. **2**(4): p. 343-66.
297. Pavuluri, K. and M.T. McMahon, *pH imaging using chemical exchange saturation transfer (CEST) MRI.* Israel Journal of Chemistry, 2017. **57**(9): p. 862-79.
298. Garcia-Martin, M.L., et al., *Mapping extracellular pH in rat brain gliomas in vivo by ^{1}H-magnetic resonance spectroscopic imaging: Comparison with maps of metabolites.* Cancer Research, 2001. **61**(17): p. 6524-31.
299. Vermathen, P., A.A. Capizzano, and A.A. Maudsley, *Administration and ^{1}H-MRS detection of histidine in human brain: Application to in vivo pH measurement.* Magnetic Resonance in Medicine, 2000. **43**(5): p. 665-75.
300. Nardi-Schreiber, A., et al., *Biochemical phosphates observed using hyperpolarized ^{31}P in physiological aqueous solutions.* Nature Communications, 2017. **8**(1): p. 341.
301. Rao, S.L., *Chemical synthesis of N-beta-oxalyl-L-alpha, beta-diaminopropionic acid and optical specificity in its neurotoxic action.* Biochemistry, 1975. **14**(23): p. 5218-21.
302. Bastiaans, H.M.M., J.L. van der Baan, and H.C.J. Ottenheijm, *Flexible and Convergent Total Synthesis of Cyclotheonamide B.* The Journal of Organic Chemistry, 1997. **62**(12): p. 3880-9.
303. Tredwell, G.D., et al., *Modelling the acid/base ^{1}H NMR chemical shift limits of metabolites in human urine.* Metabolomics, 2016. **12**(10): p. 152.
304. Jensen, P.R., et al., *Hyperpolarized amino acids for in vivo assays of transaminase activity.* Chemistry, 2009. **15**(39): p. 10010-2.
305. Gloggler, S., et al., *Parahydrogen induced polarization of amino acids, peptides and deuterium-hydrogen gas.* Physical Chemistry Chemical Physics, 2011. **13**(30): p. 13759-64.
306. Gloggler, S., S. Wagner, and L.S. Bouchard, *Hyperpolarization of amino acid derivatives in water for biological applications.* Chemical Science, 2015. **6**(7): p. 4261-6.
307. Mieville, P., et al., *Scavenging free radicals to preserve enhancement and extend relaxation times in NMR using dynamic nuclear polarization.* Angewandte Chemie, 2010. **49**(35): p. 6182-5.
308. Gajan, D., et al., *Solid-phase polarization matrixes for dynamic nuclear polarization from homogeneously distributed radicals in mesostructured hybrid silica materials.* Journal of the American Chemical Society, 2013. **135**(41): p. 15459-66.
309. Geckeler, K. and E. Bayer, *Copolymerisation von Aminosäure-Alkenylestern.* Die Makromolekulare Chemie, 1974. **175**(7): p. 1995-2001.
310. Friedrich-Bochnitschek, S., H. Waldmann, and H. Kunz, *Allyl esters as carboxy protecting groups in the synthesis of O-glycopeptides.* The Journal of Organic Chemistry, 1989. **54**(4): p. 751-6.

10. List of Publications

Peer-Reviewed Journal Articles

Köcher S S, Düwel S, **Hundshammer C**, Glaser S J, Schilling F, Granwehr J, Scheurer C. *Ab initio simulation of pH-sensitive biomarkers in magnetic resonance imaging*. The Journal of Physical Chemistry A. **2018**. 122, 40, 7983 - 7990. DOI: 10.1021/acs.jpca.8b04665.

Hundshammer C, Braeuer M, Müller C, Hansen A E, Schillmaier M, Düwel S, Feuerecker B, Glaser S J, Haase A, Cabello J, Schilling F, Hövener J B, Kjær A, Nekolla S G, Schwaiger M. *Simultaneous characterization of tumor cellularity and the Warburg effect with PET, MRI and hyperpolarized ^{13}C-MRSI*. Theranostics. **2018**. 8, 17, 4765 - 4780. DOI: 10.7150/thno.25162.

Hundshammer C, Düwel S, Ruseckas D, Topping G, Dzien P, Müller C, Feuerecker B, Hövener J B, Haase A, Schwaiger M, Glaser S J, Schilling F. *Hyperpolarized amino acid derivatives as multivalent magnetic resonance pH sensor molecules. Sensors* **2018**, 18, 2, 600. DOI:10.3390/s18020600.

Hundshammer C, Düwel S, Köcher S S, Gersch M, Feuerecker B, Scheurer C, Haase A, Glaser S J, Schwaiger M, Schilling F. *Deuteration of hyperpolarized ^{13}C-labeled zymonic acid enables sensitivity-enhanced dynamic MRI of pH*. ChemPhysChem, **2017**, 18, 18, 2422-2425. DOI: 10.1002/cphc.201700779.

Hundshammer C, Düwel S, Schilling F. *Imaging of extracellular pH using hyperpolarized molecules*. Israel Journal of Chemistry, **2017**, 57, 9, 788 - 799. DOI:10.1002/ijch.201700017.

Düwel S, **Hundshammer C**, Gersch M, Feuerecker B, Steiger K, Buck A, Walch A, Haase A, Glaser S J, Schwaiger M, Schilling F. *Imaging of pH in vivo using hyperpolarized ^{13}C-labeled zymonic acid*. Nature Communications **2017**, 15126. DOI:10.1038/ncomms15126.

Kubala E, Muñoz-Álvarez K A, Topping G, **Hundshammer C**, Feuerecker B, Gómez P A, Pariani G, Schilling F, Glaser S J, Schulte R F, Menzel Marion I, Markus Schwaiger. *Hyperpolarized ^{13}C-metabolic magnetic resonance spectroscopy and imaging*. Journal of Visualized Experiments **2016**, 118, e54751. DOI: 10.3791/54751.

Conference Contributions

Hundshammer C, Braeuer M, Müller C, Hansen A E, Schillmaier M, Düwel S, Feuerecker B, Glaser S J, Haase A, Cabello J, Schilling F, Hövener J B, Kjær A, Nekolla S G, Schwaiger M. *Simultaneous characterization of tumor cellularity and the Warburg effect with PET, MRI and hyperpolarized ^{13}C-MRSI*. **2018**. Paris, France. **Talk**.

Hundshammer C, Düwel S, Köcher S S, Gersch M, Feuerecker B, Scheurer C, Haase A, Glaser S J, Schwaiger M, Schilling F. *Deuteration of hyperpolarized ^{13}C-labelled zymonic acid enables sensitivity-enhanced dynamic MRI of pH*. European Molecular Imaging Meeting. **2018**. San Sebastian, Spain. **Talk**.

Hundshammer C, Braeuer M, Cabello J, Hansen A E, Mueller C, Feuerecker B, Schachoff S, Blechert B, Michalik M, Hövener J B, Glaser S J, Haase A, Schilling F, Kjaer A, Nekolla S, Schwaiger M. *Simultaneous PET/MR/^{13}C-MRSI imaging of subcutaneous MAT-B-III tumor*s. **2017**. Deutsche Gesellschaft für Nuklearmedizin. V141. Dresden, Germany. **Talk**.

Düwel S, **Hundshammer C**, Gersch M, Feuerecker B, Haase A, Glaser S J, Schwaiger M, Schilling F. I*maging of pH in vivo using hyperpolarized ^{13}C-labeled zymonic acid*. International Society of Magnetic Resonance in Medicine. **2017**, 25, 3341, Honolulu, USA. Oral Power Pitch.

Hundshammer C, Braeuer M, Müller C, Hansen A E, Schillmaier M, Düwel S, Feuerecker B, Glaser S J, Haase A, Cabello J, Schilling F, Hövener J B, Kjær A, Nekolla S G, Schwaiger M. *Multiparametric tumor characterization using simultaneous 1H-MRI, ^{18}F-FDG PET and hyperpolarized [1-^{13}C]pyruvate MRSI*. International Society of Magnetic Resonance in Medicine. 25, 6097, Honolulu, USA. Poster Presentation.

Düwel S, **Hundshammer C**, Gersch M, Feuerecker B, Haase A, Glaser S J, Schwaiger M, Schilling F. *Imaging of pH in vivo using hyperpolarized ^{13}C-labeled zymonic acid*. 4th International Workshop on Personalized Medicine. **2017**. Brisbane, Australia. Talk.

Hundshammer C, Düwel S, Gersch M, Feuerecker B, Haase A, Glaser S J, Schwaiger M, Schilling F. *Zymonic Acid – a novel ^{13}C enriched biosensor for in vivo pH imaging*. International Society of Magnetic Resonance in Medicine. **2016**, 24, 3674, Singapore, USA. Poster Presentation.

Hundshammer C, Düwel S, Gersch M, Feuerecker B, Steiger K, Buck A, Walch A, Haase A, Glaser S J, Schwaiger M, Schilling F. *Tumor pH mapping using*

hyperpolarized [1,5-$^{13}C_2$] zymonic acid, a novel pH biosensor for ^{13}C MR Imaging. 3rd International Workshop on Personalized Medicine. **2016**. Munich, Germany. **Talk**.

Düwel S, **Hundshammer C**, Gersch M, Feuerecker B, Haase A, Glaser S J, Schwaiger M, Schilling F. *Imaging of pH in vivo using hyperpolarized ^{13}C-labeled zymonic acid*. European Molecular Imaging Meeting. **2016**, Utrecht, Netherlands. Talk.

Joos A, Löwa N, Düwel S, **Hundshammer C**, Wiekhorst F, Gleich B, Haase A. *Size-dependent MR relaxivities of magnetic nanoparticles*. International Conference of the Scientifiic and Clinical Applications of Magnetic Carriers. **2016**. Vancouver USA. Poster Presentation.

Hundshammer C, Düwel S, Gersch M, Feuerecker B, Haase A, Glaser S J, Schwaiger M, Schilling F. *Tumor pH mapping using hyperpolarized [1,5-$^{13}C_2$] zymonic acid, a novel pH biosensor for ^{13}C-MR Imaging*. 2th International Workshop on Personalized Medicine. **2015**. Brisbane, Australia. **Talk**.

Düwel S, **Hundshammer C**, Gersch M, Feuerecker B, Haase A, Glaser S J, Schwaiger M, Schilling F. *A novel hyperpolarized biosensor for ^{13}C magnetic resonance spectroscopic imaging of pH in vivo*. World Molecular Imaging Congress. **2015**, Honolulu, Hawaii. Talk.

Hundshammer C, Düwel S, Gersch M, Feuerecker B, Haase A, Glaser S J, Schwaiger M, Schilling F. *Characterization and deuterium enrichment of a novel biosensor for pH imaging*. World Molecular Imaging Congress. **2015**, Honolulu, Hawaii. Poster Presentation.

Düwel S, **Hundshammer C**, Gersch M, Feuerecker B, Steiger K, Buck A, Walch A, Haase A, Glaser S J, Schwaiger M, Schilling F. *A novel hyperpolarized biosensor for ^{13}C magnetic resonance spectroscopic imaging of pH in vivo*. International Conference on Magnetic Resonance Microscopy. **2015**, Munich. Germany. Talk.

Düwel S, Gersch M, Feuerecker B, **Hundshammer C**, Schwaiger M, Glaser S J, Schilling F. *A novel hyperpolarized biosensor for magnetic resonance imaging and spectroscopy*. BioVaria. **2015**, Munich. Germany. Talk.

11. Grants, Awards and Scholarships

06 / 2018	Magna cum laude merit award for outstanding abstracts (scored in the top 15%) of the International Society of Magnetic Resonance in Medicine (ISMRM). 26th annual conference. Paris, France.
04 / 2017	Educational stipend for attending the 25th annual conference of the International Society of Magnetic Resonance in Medicine (ISMRM). Honolulu, Hawaii, USA.
03 / 2017	“NMR is Science” contest winner. Cambridge Isotope Laboratories, Inc.
12 / 2016	Cambridge Isotope Laboratories, Inc. Research Award (14,000 US $).
05 / 2016	2nd best multimedia electronic poster award. International Society of Magnetic Resonance in Medicine (ISMRM). Singapore.
05 / 2016	Educational stipend for attending the 24th annual conference of the International Society of Magnetic Resonance in Medicine (ISMRM). Singapore.
09 / 2015	*Deutscher Akademischer Austauschdienst* (DAAD) travel award for attending the summer school of the “German-Australian network for personalized cancer medicine. Brisbane, Australia.
10 / 2014	Trainee Grant for attendance of the COST training school on hyperpolarization techniques. Marseille, France.

12. Acknowledgements

During my time at the University Hospital of Mannheim, the University Hospital of Freiburg, the Graduate School of Bioengineering in Munich, the Department of Chemistry at the Technical University of Munich and the Department of Nuclear medicine at the Klinikum rechts der Isar in Munich, I received tremendous support from many people. This thesis would not have been possible without the contribution of these outstanding persons. Among many others, I therefore want to thank:

Prof. Dr. Steffen Glaser for his continuous support and scientific input for my research projects as well as for giving the freedom to freely pursue my own ideas.

Prof. Dr Axel Haase for sharing his knowledge of magnetic resonance imaging and spectroscopy and continuous support for my research projects.

Prof. Dr. Markus Schwaiger for the excellent conversations on tumor biology and biochemistry as well as PET and MR instrumentation. I further want to thank him for his fabulous support on the PET/MR project, for providing extensive financial funding of my research projects and for the great atmosphere that was created under his supervision at the Klinikum rechts der Isar.

Dr. Franz Schilling for his continuous support and great scientific input on MR imaging and hyperpolarization techniques and for being a great supervisor for all pH imaging projects.

Dr. Stephan Düwel for sharing his great scientific knowledge in the field of physics and programming and for the wonderful atmosphere he created inside and outside of the lab.

P.D. Dr. Stephan Nekolla and *Dr. Jorge Cabe*llo for providing deep insights into the field of PET instrumentation, acquisition and data analysis.

Dr. Miriam Braeuer and *Christoph Müller* for sharing endless night shifts with me and respectively for their outstanding work with animals and for sharing knowledge of MR instrumentation and MR pulse sequence design.

*Dr. Anna Bart*els, *Dr. Zohreh Varasteh*, *Dr. Nahid Yusufi*, *Dr. Benedikt Feuerecker*, *Michael Michalik*, *Mathias Schillmaier*, *Martin Grashei*, and *Luca Nagel* for the great atmosphere in the lab and the pleasant lunch hours under chestnuts in the canteen of the *Prinzregententheater*.

Simone Köcher for running the structural simulation work on zymonic acid.

Dr. Geoffrey Topping and *Dr. Piotr Dzien* respectively for their help with MR acquisitions and cell culture.

Birgit Blechert and *Sandra Schäfer* for their helpful lab assistance.

Sylvia Schachoff for her help at the PET/MR.

Sybille Reder and *Markus Mittelhäuser* for performing PET/CT measurements.

Dr. Raimund Marx for his outstanding and uncomplicated assistance for every chemistry related question and support for my NMR experiments as well as *Albert Schröder* for his help in the laboratory at the chemistry department of the Technical University of Munich.

Dr. Christoph Seidl for the opportunity to participate in the exchange program, “German-Australian network for personalized medicine” and the wonderful trip to Brisbane.

Alexandra Greiner and *David Ruseckas* for their Master theses.

Prof Dr. Wilko Weichert and *Dr. Katja Steiger* for the uncomplicated und fruitful cooperation with the Pathology Department of the Klinikum rechts der Isar.

Prof. Dr. Andreas Kjær and *Dr. Adam Espe Hansen* for the great cooperation with the Rigshospitalet Copenhagen.

Prof. Dr. Bernd Reif and *Prof. Dr. Bernd Sieber* for access to their laboratories and *Dr. Franziska Mandl* and *Dr*. *Wolfgang Heydenreuter* for their help with their HPLC system.

Prof. Dr. Jan-Bernd Hövener, Dr. Jason Skinner, Stephan Berner, Dr. Tabea Flügge, and *Matthias Hennings* for the fruitful cooperation with the University hospital in Freiburg*.*

Prof. Dr. Lothar Schad, *Dr. Nadja Meissner*, *Dr. Jascha Zapp* and *Dr. Mathias Davids* from the University hospital in Mannheim for their help with Siemens MR systems.

Dr. Malte Gersch for his assistance on the synthesis of zymonic acid.

Dr. Anja Drescher, *Dr. Petra Dorfner* and *Katharina Lang* for their excellent guidance of the Graduate School of Bioengineering (GSB).

Cambridge Isotope Laboratories, Inc., the *GSB*, the *deutsche Forschungsgemeinschaft* (DFG, German Research Foundation, Major Instrumentation Initiative, 391523415, 68647618, HO-4604/2-1, SFB 824), the *Bundesministerium für Bildung und Forschung* (BMBF, FKZ 13EZ1114) and the *European Union* (EU, 642773 and 294582) for financial funding of the projects presented in this thesis.

My *parents*, my *brother* and my *fiance* for their steady support during my time as a Ph. D. candidate.